Development of a Multi-field Two-fluid Approach for Simulation of Boiling Flows

Hamed Setoodeh

Dresden, 2022

Printed and published with the support of the German Academic Exchange Service.

Development of a Multi-field Two-fluid Approach for Simulation of Boiling Flows

von der Fakultät Maschinenwesen
der Technischen Universität Dresden
zur Erlangung des akademischen Grades

Doktoringenieur (Dr.–Ing.)

angenommene Dissertation
Von

M.Sc. Hamed Setoodeh

Tage der Einreichung: 07.09.2022
Tage der Verteidigung: 14.04.2023

Gutachter: Prof. Dr.–Ing. habil. Dr. h. c. Uwe Hampel
Prof. Dr. rer. nat. Stephan Leyer

Dresden, 2022

To my family

Fatemeh and Anahid

Abstract

Safe and reliable operation of nuclear power plants is the basic requirement for the utilization of nuclear energy since accidents can release radioactivity and with that cause irreversible damage to human beings. Reliability and safety of nuclear reactors are highly dependent on the stability of thermal hydraulic processes occurring in them. Nucleate boiling occurs in Pressurized Water Reactors (PWRs) and Boiling Water Reactors (BWRs) as well as in their passive safety systems during an accident. Passive safety systems are solely driven by thermal gradients and gravitational force removing residual heat from the reactor core independent of any external power supply in the case of accidents. Instability of flow boiling in these passive circuits can cause flow oscillations. These oscillations may induce insufficient local cooling and mechanical loads, which threatens the reactors' safety. Analysis of boiling two-phase flow and associated heat and mass transfer requires an accurate modeling of flow regime transitions and prediction of boiling parameters such as void fraction, steam bubble sizes, heat transfer coefficient, etc. Flow boiling has been intensively investigated through experiments, one-dimensional codes, and Computational Fluid Dynamics (CFD) methods. Costly hardware and no accessibility to all locations in complex geometries restrict the experimental investigation of flow boiling. Since one-dimensional codes such as ATHLET, RELAP and TRACE are "lumped parameter" codes, they are unable to simulate complex flow boiling transition patterns.

In the last decades, with the development of supercomputers, CFD has been considered as a useful tool to model heat and mass transfer occurring in flow boiling regimes. In many industrial applications and system designs, CFD codes and particularly the Eulerian-Eulerian (E-E) two-fluid model are quickly replacing the experimental and analytical methods. However, the application of this approach for flow boiling modelling poses a challenge for the development of bubble dynamics and wall boiling models to predict heat and mass transfer at the heating wall as well as phase-change mechanism. Many empirical and mechanistic models have been proposed for bubble dynamics modelling. Nevertheless, the validity of these models for only a narrow range of operating conditions and their uncertainties limit their applicability and consequently presently necessitate us to calibrate them for a given boundary condition via calibration factors. For that reason, the first aim of this thesis is the development of a bubble dynamics model for subcooled boiling flow, which needs no calibration factor to predict the bubble growth and detachment.

This mechanistic model is formulated based on the force balance approach, physics of a single nucleated bubble and several well-developed models to cover the whole bubble life cycle including formation, growth and departure. This model considers dynamic inclination angle and contact angles between the bubble and the heating wall as well as the contribution of microlayer evaporation, thermal diffusion and condensation around the bubble cap. Validation against four experimental flow boiling data sets was conducted with no case-dependent recalibration and yielded good agreement. The second goal is the implementation of the developed bubble dynamics model in the E-E two-fluid model as a sub-model to improve the accuracy of boiling flow simulation and reduce the case dependency. This implementation requires an extension of the nucleation site activation and wall heat-partitioning models. The bubble dynamics and heat-partitioning models were coupled with the Population Balance Model (PBM) to handle bubble interactions and predict the Bubble Size Distribution (BSD). In addition, the contribution of bubble sliding to wall heat transfer, which has been rarely considered in other modelling approaches, is considered. Validation for model implementation in the E-E two-fluid model was made with ten experimental cases including R12 and R134a flow boiling in a pipe and an annulus. These test cases cover a wide range of operating parameters such as wall heat flux, fluid velocity, subcooling temperature and pressure. The validated parameters were the bubble diameter, void fraction, bubble velocity, Interfacial Area Density (IAD), bubble passing frequency, liquid and wall temperatures.

Two-phase flow morphologies for an upward flow in a vertical heating pipe may change from bubbly to slug, plug, and annular flow. Since these flow patterns have a great impact on the heat and mass transfer rates, an accurate prediction of them is critical. The aim of this thesis is the implementation of the developed bubble dynamics and heat-partitioning models in the recently developed GENeralized TwO-Phase flow (GENTOP) framework for the modelling of these flow patterns transition as well. An adopted wall heat-partitioning model for high void fractions is presented and for a generic test case, flow boiling regimes of water in a vertical heating pipe were modelled using ANSYS CFX 18.2. Moreover, the impacts of wall superheat, subcooling temperature and fluid velocity on the flow boiling transition patterns and the effects of these patterns on the wall heat transfer coefficient were evaluated.

Keywords: subcooled flow boiling, passive safety systems, bubble dynamics, CFD simulation, flow boiling transition patterns, GENTOP

Zusammenfassung

Der sichere und zuverlässige Betrieb von Kernkraftwerken ist Voraussetzung für die Nutzung der Kernenergie, weil es bei Unfällen zur Freisetzung von Radioaktivität und damit zur irreversiblen Schädigung von Menschen kommen kann. Die Zuverlässigkeit und Sicherheit von Kernreaktoren hängt in hohem Maße von der Stabilität der in ihnen ablaufenden thermohydraulischen Prozesse ab. Siedevorgänge treten in Druckwasserreaktoren (DWR) und Siedewasserreaktoren (SWR) sowie in ihren passiven Sicherheitssystemen während eines Unfalls auf. Passive Sicherheitssysteme werden ausschließlich durch thermische Gradienten und die Schwerkraft angetrieben, die bei Unfällen unabhängig von einer externen Energieversorgung Restwärme aus dem Reaktorkern abführen. Die Instabilität des Strömungssiedens in diesen passiven Kreisläufen kann zu Strömungsoszillationen führen. Diese Oszillationen können zu einer unzureichenden lokalen Kühlung und mechanischen Lasten führen, die die Sicherheit des Reaktors gefährden. Die Analyse der siedenden Zweiphasenströmung und des damit verbundenen Wärme- und Stofftransfers erfordert eine genaue Modellierung der Übergänge zwischen den Strömungszuständen und die Vorhersage von Siedeparametern wie Gasvolumenanteil, Blasengrößen, Wärmeübergangskoeffizient usw. Das Strömungssieden wurde mit Hilfe von Experimenten, eindimensionalen Codes und Methoden der numerischen Fluiddynamik (CFD) eingehend untersucht. Kostspielige Versuchsstände und fehlende Zugänglichkeit zu allen Stellen in komplexen Geometrien schränken die experimentelle Untersuchung des Strömungssiedens ein. Da es sich bei eindimensionalen Codes wie ATHLET, RELAP und TRACE um "lumped parameter"-Codes handelt, sind sie nicht in der Lage, komplexe instationäre Strömungsmusterübergänge zu simulieren.

Mit der Entwicklung der Rechentechik in den letzten Jahrzehnten, hat sich CFD zunehmend als nützliches Werkzeug für die Simulation des Wärme- und Stofftransfers in siedenden Strömungsregimen entwickelt. In vielen industriellen Anwendungen und Systemdesigns ersetzen CFD-Simulationen die experimentellen und analytischen Methoden. Für Mehrphasenströmungen in mittleren und großen Skalen wird dabei meist das Euler-Euler (E-E)-Zwei-Fluid-Modell genutzt. Die Anwendung dieses Ansatzes für die Modellierung des Strömungssiedens erfordert jedoch die Entwicklung von Modellen für die Blasendynamik und das Wandsieden, um den Wärme- und Stoffübergang an der beheizten Wand sowie den Phasenwechselmechanismus vorherzusagen. Für die Modellierung der Blasendynamik sind

viele verschiedene empirische und mechanistische Modelle vorgeschlagen worden. Die begrenzte Gültigkeit dieser Modelle für einen engen Bereich von Betriebsbedingungen und ihre Unsicherheiten schränken jedoch ihre Anwendbarkeit ein und machen es bisher erforderlich, sie über Kalibrierungsfaktoren für eine bestimmte Randbedingung zu kalibrieren. Aus diesem Grund ist das erste Ziel dieser Dissertation die Entwicklung eines Modells für die Blasendynamik im Fall von Strömungen mit unterkühltem Sieden, das keinen Kalibrierungsfaktor für die Vorhersage des Blasenwachstums und der Ablösung benötigt. Dieses mechanistische Modell basiert auf dem Ansatz des Kräftegleichgewichts, der Physik einer einzelnen an einem Keim gebildeten Blase und mehreren Modellen, die den gesamten Lebenszyklus einer Blase, einschließlich Bildung, Wachstum und Zerfall, abdecken. Dieses Modell berücksichtigt die dynamischen Neigungwinkel und den Kontaktwinkel zwischen der Blase und der beheizten Wand sowie den Beitrag der Verdampfung der dünnen Flüssigkeitsschicht unterhalb der Blase, die thermische Diffusion und die Kondensation um die Blasenkappe. Die Validierung anhand von vier experimentellen Datensätzen zum Strömungssieden wurde ohne fallabhängige Rekalibrierung durchgeführt und ergab eine gute Übereinstimmung. Das zweite Ziel ist die Implementierung des entwickelten Blasendynamikmodells in das E-E-Zwei-Fluid-Modell, um die Genauigkeit der Simulation von siedenden Strömungen zu verbessern und die Fallabhängigkeit zu verringern. Diese Implementierung erfordert eine Erweiterung der Modelle für die Aktivierung der Siedekeime und die Wandwärmeverteilung. Die Modelle für die Blasendynamik und die Aufteilung des Wandwämestroms wurden mit dem Populationsbilanzmodell (PBM) gekoppelt, um Blaseninteraktionen zu berücksichtigen und die Blasengrößenverteilung (BSD) vorherzusagen. Darüber hinaus wird der Beitrag des Gleitens von Blasen an der Wand auf den Wandwärmeübergang berücksichtigt, der in anderen Modellierungsansätzen nur selten in Betracht gezogen wurde. Die Validierung der Modellimplementierung im E-E-Zwei-Fluid-Modell erfolgte anhand von zehn experimentellen Fällen, bei denen R12 und R134a in einem Rohr und einem Ringraum sieden. Diese Testfälle decken eine breite Palette von Betriebsparametern ab, wie z. B. den Wandwärmestrom, die Flüssigkeitsgeschwindigkeit, die Unterkühlungstemperatur und den Druck. Die validierten Parameter waren der Blasendurchmesser, der Gasvolumenanteil, die Blasengeschwindigkeit, die Grenzflächendichte (IAD), die Blasenfrequenz sowie die Flüssigkeits- und Wandtemperatur.

Die Morphologie der Zweiphasenströmung bei einer Aufwärtsströmung in einem vertikalen beheizten Rohr kann von einer Blasenströmung bis zu Schwallströmung, Pfropfenströmung und Ringströmung variieren. Da diese Strömungsmuster einen großen Einfluss auf die Wärme- und Stoffübergangsraten haben, ist eine genaue Vorhersage von entscheidender Bedeutung. Das Ziel dieser Dissertation ist die Implementierung der entwickelten Blasendynamikmodelle und der

Modelle für die Aufteilung des Wärmestroms in das kürzlich entwickelte GENeralized TwO-Phase flow (GENTOP) Framework zur Modellierung solcher Strömungsmusterübergänge. Es wird ein adaptiertes Modell für die Aufteilung des Wärmestroms im Fall hoher Gasvolumenanteile vorgestellt und für einen generischen Testfall das Strömungssieden von Wasser in einem vertikalen Heizungsrohr mit ANSYS CFX 18.2 modelliert. Darüber hinaus wurden die Auswirkungen der Wandüberhitzung, der Unterkühlungstemperatur und der Fluidgeschwindigkeit auf die Strömungsregimeübergänge beim Strömungssieden und die Auswirkungen dieser Übergänge auf den Wandwärmeübergangskoeffizienten untersucht.

Schlüsselwörter: Unterkühltes Strömungssieden, passive Sicherheitssysteme, Blasendynamik, CFD-Simulation, Strömungsregimeübergänge beim Sieden, GENTOP

Acknowledgement

This work presented here was funded by the Deutscher Akademischer Austauschdienst (DAAD) funding program number: 57299294. Therefore, I thank the DAAD to give me this opportunity for doing this research.

I would like to express my deep sense of thanks and gratitude to my supervisor Dr. Wei Ding who has been a great mentor for me. I profusely thank him for his timely and meticulous advice, motivation, immense knowledge and scientific guidance. It would not have been possible to conduct this research without his precious support.

I submit my deep gratitude and appreciation to my respected supervisors Dr. Dirk Lucas and Prof. Dr. -Ing. habil. Uwe Hampel for their support, patience and enthusiasm. I really appreciate them for their encouragement and educating me on how to become a researcher. Their immense knowledge and experience have encouraged me in all the time of my academic research. Moreover, I would like to extend my sincere thanks to Prof. Dr. rer. nat. Stephan Leyer for accepting to be a referee of this thesis.

I am very grateful to all my friends E. Mohseni, A. Moonesi, A. Echresh and M. Khastkhodaei for their invaluable assistance and cooperation throughout my research. Their timely suggestions and enthusiasm have helped me to complete my thesis.

I humbly extend my thanks and gratefulness to my mother and father for their continuous support throughout my life. Last but not least, I am unable to describe how thankful I am to have such a wonderful family. My wife and my baby, Fatemeh and Anahid, to whom I'm dedicating this work. I thank and appreciate them from the bottom of my heart for their endless love and support throughout my career. Accomplishment of my work would not have been possible without their tremendous understanding and encouragement in the past years.

Contents

Nomenclature

Abbreviations

AIAD	Algebraic Interfacial Area Density
BIT	Bubble Induced Turbulence
BSD	Bubble Size Distribution
BWR	Boiling Water Reactor
CCC	Containment Cooling Condenser
CFD	Computational Fluid Dynamics
CHF	Critical Heat Flux
EC	Emergency Condenser
E-E	Eulerian-Eulerian
E-L	Eulerian-Lagrangian
GasD	Dispersed Gas
GasC	Continuous Gas
GasT	Total Gas (GasD plus GasC)
GENTOP	GENeralized TwO-Phase flow
iMUSIG	Inhomogeneous MUltiple SIze Group
IAD	Interfacial Area Density
LWR	Light Water Reactor
MUSIG	MUltiple SIze Group
NVG	Net Vapor Generation
ONB	Onset of Nucleate Boiling
PBM	Population Balance Model
PPPT	Passive Pressure Pulse Transmitter
PWR	Pressurized Water Reactor
RPI	Rensselaer Polytechnic Institute
RPV	Reactor Pressure Vessel
SWR	”SiedeWasserReaktor”-German word for BWR

Latin symbols

A_{if}	Interfacial area density, $(\frac{1}{\mathrm{m}})$
$A_{c,g}$	Wall area fraction influenced by continuous gas, $(-)$
$A_{c,l}$	Wall area fraction influenced by liquid, $(-)$
A_q	Bubble influence area fraction, $(-)$
A_b	Heating wall area fraction influenced by dispersed bubbles, $(-)$

C_2	Microlayer constant, $(-)$
C_L	Lift force coefficient, $(-)$
C_p	Specific heat capacity, $(\frac{\mathrm{J}}{\mathrm{kg.K}})$
d_b	Bubble diameter, (m)
d_{cr}	Bubble critical diameter, (m)
d_d	Bubble departure diameter, (m)
d_l	Bubble lift-off diameter, (m)
d_{SM}	Bubble Sauter mean diameter, (m)
d_w	Bubble base diameter, (m)
D_h	Hydrodynamic diameter of channel, (m)
Eö	Eötvös number, $(-)$
f	Bubble occupation number, $(-)$
f_b	Bubble blending function, $(-)$
f_d	Droplet blending function, $(-)$
fr	Bubble departure frequency, $(\frac{1}{\mathrm{s}})$
f_{sub}	Portion of bubble surface in contact with subcooled liquid, $(-)$
$\boldsymbol{F}$	Force, (N)
$\boldsymbol{F}_b$	Buoyancy force, (N)
F_B	Breakup coefficient, $(-)$
F_C	Coalescence coefficient, $(-)$
$\boldsymbol{F}_{cp}$	Contact pressure force, (N)
$\boldsymbol{F}_{drag}$	Drag force, (N)
$\boldsymbol{F}_{growth}$	Bubble growth force, (N)
$\boldsymbol{F}_L$	Lift force, (N)
$\boldsymbol{F}_W$	Wall lubrication force, (N)
$\boldsymbol{F}_{sl}$	Shear lift force, (N)
$\boldsymbol{F}_{surf}$	Surface tension force, (N)
$\boldsymbol{F}_{TD}$	Turbulent dispersion force, (N)
$\boldsymbol{F}_{VM}$	Virtual mass force, (N)
$\boldsymbol{g}$	Gravity, $(\frac{\mathrm{m}}{\mathrm{s}^2})$
G	Mass flux, $(\frac{\mathrm{kg}}{\mathrm{m}^2.\mathrm{s}})$
h	Specific enthalpy, $(\frac{\mathrm{J}}{\mathrm{kg}})$
h_{bt}	Bubble bottleneck height, (m)
h_c	Height of bubble without bottleneck, (m)
h_{fc}	Forced-convection heat transfer coefficient, $(\frac{\mathrm{W}}{\mathrm{m}^2.\mathrm{K}})$
h_{fg}	Latent heat, $(\frac{\mathrm{J}}{\mathrm{kg}})$
H_t	Total enthalpy, $(\frac{\mathrm{J}}{\mathrm{kg}})$
Ja	Jakob number, $(-)$
k	Turbulent kinetic energy, $(\frac{\mathrm{m}^2}{\mathrm{s}^2})$
k_{int}	Interface curvature, $(-)$

K	Bubble influence area factor, $(-)$
k	Mass, (kg)
$\dot{m}$	Mass transfer rate, $(\frac{\mathrm{kg}}{\mathrm{s}})$
$\boldsymbol{n}$	Unit normal vector, $(-)$
N	Nucleation site density, (m^{-2})
N_{ref}	Reference nucleation site density, (m^{-2})
Nu	Nusselt number, $(-)$
P	Pressure, (Pa)
Q	Heat flux, $(\frac{\mathrm{W}}{\mathrm{m}^2})$
$\dot{Q}$	Heat transfer rate, (W)
Q_c	Single-phase convection heat flux, $(\frac{\mathrm{W}}{\mathrm{m}^2})$
Q_e	Evaporation heat flux, $(\frac{\mathrm{W}}{\mathrm{m}^2})$
Q_l	Heat flux to liquid, $(\frac{\mathrm{W}}{\mathrm{m}^2})$
Q_q	Quenching heat flux, $(\frac{\mathrm{W}}{\mathrm{m}^2})$
Q_w	Wall heat flux, $(\frac{\mathrm{W}}{\mathrm{m}^2})$
r_b	Bubble radius, (m)
r_c	Radius of curvature, (m)
r_{do}	Dryout radius, (m)
r_w	Bubble contact radius (base radius), (m)
R_i	Outer diameter of inner pipe in an annulus, (m)
R_o	Inner diameter of outer pipe in an annulus, (m)
R_p	Pipe radius, (m)
Re	Reynolds number, $(-)$
S_d	Bubble sliding length, (m)
S_n	Distance between two neighboring nucleation sites, (m)
$T_{w,ac}$	Cavity activation temperature, (K)
T_b	Fluid bulk temperature, (K)
T_{in}	Inlet liquid temperature, (K)
T_l	Liquid temperature, (K)
T_{sat}	Saturation temperature, (K)
T_w	Heating wall temperature, (K)
t	Time, (s)
t_d	Bubble departure time, (s)
t_w	Bubble waiting time, (s)
$\boldsymbol{u}$	Velocity in x-direction, $(\frac{\mathrm{m}}{\mathrm{s}})$
$\boldsymbol{v}$	Velocity in y-direction, $(\frac{\mathrm{m}}{\mathrm{s}})$
$\boldsymbol{w}$	Velocity in z-direction, $(\frac{\mathrm{m}}{\mathrm{s}})$
$\boldsymbol{U}$	Fluid velocity, $(\frac{\mathrm{m}}{\mathrm{s}})$
$\boldsymbol{U}_\tau$	Friction velocity, $(\frac{\mathrm{m}}{\mathrm{s}})$
Δt	Time step, (s)

ΔT_{ca}	Average wall superheat of a cavity, (K)
ΔT_{sup}	Wall superheat $(T_w - T_{sat})$, (K)
ΔT_{sub}	Subcooling temperature $(T_{sat} - T_l)$, (K)
Δx	Grid size, (m)
z	Axial position, (m)

Greek symbols

τ	Shear stress, (Pa)
τ_g	Maximal inertia-controlled growth time, (s)
α	Void fraction, $(-)$
α_C	GasC void fraction, $(-)$
α_D	GasD void fraction, $(-)$
α_T	GasT void fraction, $(-)$
α'	Thermal diffusivity, $(\frac{\mathrm{m}^2}{\mathrm{s}})$
δ	Dirac delta function, $(-)$
δ_{mi}	Microlayer thickness, (m)
δ_{th}	Thermal layer thickness, (m)
δ_{tl}	Thickness of turbulent hydrodynamic layer, (m)
δ_w	Wall thickness, (m)
φ_{surf}	Interface blending function, $(-)$
β	Bubble contact angle, (rad)
β_{ad}	Advancing contact angle of macrolayer, (rad)
β_{re}	Receding contact angle of macrolayer, (rad)
β_s	Bubble expected contact angle, (rad)
θ_b	Bubble inclination angle, (rad)
θ_w	Wall orientation angle, (rad)
σ	Surface tension, $(\frac{\mathrm{N}}{\mathrm{m}})$
$\boldsymbol{\Gamma}$	Torque of force, $(\mathrm{N.m})$
ρ	Density, $(\frac{\mathrm{kg}}{\mathrm{m}^3})$
λ	Thermal conductivity, $(\frac{\mathrm{W}}{\mathrm{m.K}})$
ϵ	Turbulence dissipation rate, $(\frac{\mathrm{m}^2}{\mathrm{s}^3})$
ω	Specific dissipation rate, $(\frac{1}{\mathrm{s}})$
γ	Interface surface tension, $(\frac{\mathrm{N}}{\mathrm{m}})$
ν	Kinematic viscosity, $(\frac{\mathrm{m}^2}{\mathrm{s}})$
μ	Dynamic viscosity, $(\mathrm{Pa.s})$

Subscripts

b	Bubble
c	Convection
$cond$	Condensation
$clust$	Cluster

dg	Dispersed gas
$drop$	Droplet
cg	Continuous gas
e	Evaporation
Ent	Entrainment
fc	Forced-convection
fs	Interface
g	Gas phase
in	Inlet (input)
int	Interface
j	Velocity group indicator in the iMUSIG model
l	Liquid phase
m	Mixture
ma	Macrolayer
mi	Microlayer
n	Surface normal direction
q	Quenching
sat	Saturation
sta	Static
t	Surface tangential direction
td	Thermal diffusion
w	Heating wall

Superscripts

eff	Effective
$turb$	Turbulence

1 Introduction

1.1 Background and motivation

Resource scarcity and environmental problems related to fossil fuels have made nuclear energy production a good alternative to meet the growing global energy demand [1]. At present, nuclear reactors generate about 15% of the world's electricity [2] and approximately 80% of nuclear power is generated by Pressurized Water Reactors (PWRs) and Boiling Water Reactors (BWRs) [3]. Despite the significance of nuclear energy for generating electricity, one of the most significant concerns about nuclear reactors has always been their safety since accidents like coolant leakage can release radioactive materials into the environment and cause an irreversible damage to living beings [4]. Therefore, safety and reliability of nuclear reactors have been under continuous development since the first commercial exploitation of a civil nuclear power plant in the 1950s [5].

In a BWR water as a coolant is evaporated in the reactor core with the nuclear fission heat generated in the fuel rods. The produced steam is then dried by a dryer and used to drive a turbine. It is then condensed and recycled back to the reactor core. In a PWR, the heat generated in the reactor core is transferred to the coolant flow in the primary loop. The secondary circuit then uses this heat to convert water into steam for turbine rotation and the steam is later condensed and recycled. High heat fluxes for the operation of both BWRs and PWRs are achieved by nucleate boiling under a high-pressure subcooled liquid flow condition [6]. Flow boiling occurs when a liquid flow is brought into contact with a heating wall at a temperature that exceeds the Onset of Nucleate Boiling (ONB) temperature. The ONB point refers to the primary formation of bubbles at the heating wall. At the beginning of nucleation, bubbles leave the heating wall and condense in the bulk since the bulk liquid temperature is below its saturation one. They heat the subcooled liquid and when the bulk liquid approaches the saturation temperature the void fraction increases. Further downstream, the two-phase flow morphologies may change from bubbly to slug, plug, and annular flow sequentially dependent on the boundary condition and channel geometry as shown in Figure 1.1 [7]. These two-phase flow regimes have a great impact on the heat and mass transfer rates. Further increase in void fraction develops annular flow in which the vapor phase accelerates and forms a "chimney" with a continuous liquid film on the heating wall. After some

distance, the liquid film on the heating wall may deplete. This liquid depletion, which leads to a dryout at a moderate wall heat flux and Departure from Nucleate Boiling (DNB) at a high heat flux, is named Critical Heat Flux (CHF) as shown in Figure 1.1 [8]. CHF sharply decreases the heat transfer coefficient with a rapid wall temperature excursion and burnout may occur due to the overheating of the heating surface [8]. Therefore, boiling crises such as dryout in BWRs and DNB in PWRs may have disastrous consequences and must be avoided.

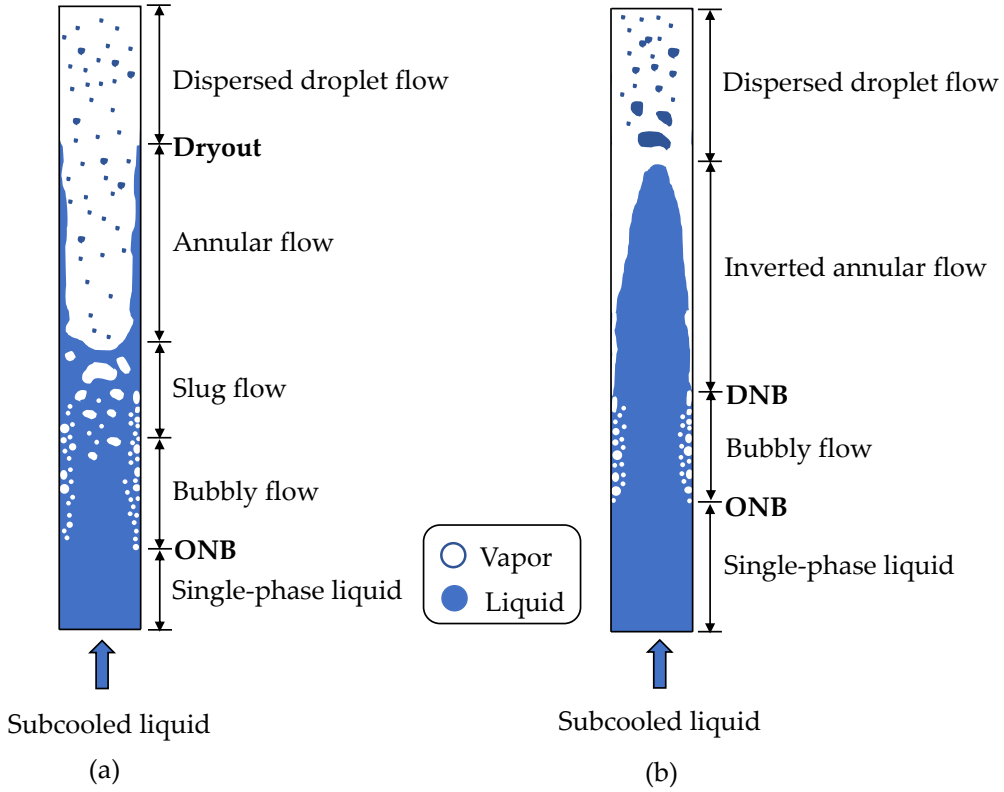

Figure 1.1: Two-phase flow regimes in a vertical heating pipe with a) moderate and b) high heat flux.

Nowadays one of the major research directions in reactors safety systems is stability analyses of two-phase flows occurring in passive safety systems of the third generation of BWRs. Passive safety systems remove the decay heat from the reactor core by taking advantage of gravitational force and thermal gradients in the event of an accident [9]. They operate without using active components such as pumps and emergency electrical supplies as well as manual intervention. These natural circulation loops eliminate the costs associated with installation, maintenance and operation of active safety systems like multiple pumps. However, they are susceptible to thermal-hydraulic instabilities. Although instabilities can occur in both forced and natural circulation loops, the latter is inherently more unstable than the former due to the relatively low driving force in natural systems (buoyancy)

compared to forced convection [10]. Instabilities of flow boiling in passive safety systems of nuclear reactors may cause flow oscillations [11]. These oscillations affect the local heat transfer characteristics and may induce insufficient local cooling and mechanical vibrations which threatens reactor's safety [10]. As a result, the parameters such as bubble size, void fraction, heat transfer coefficient as well as flow transition patterns play an important role in the stability of natural circulation flows in passive systems [10, 12]. Therefore, thermal-hydraulic parameters of flow boiling occurring in passive safety systems of nuclear reactors need to be accurately predicted.

An innovative BWR, the so-called KERENA (formerly called SWR-1000) was developed by Framatome [9] to meet the highest safety standards including control of core accidents by supplementing active safety systems with passive safety equipment [13]. The major parts of KERENA's passive systems include containment cooling condensers (CCCs), emergency condensers (ECs), passive pressure pulse transmitters (PPTs) and passive flooding lines as shown in Figure 1.2 [14].

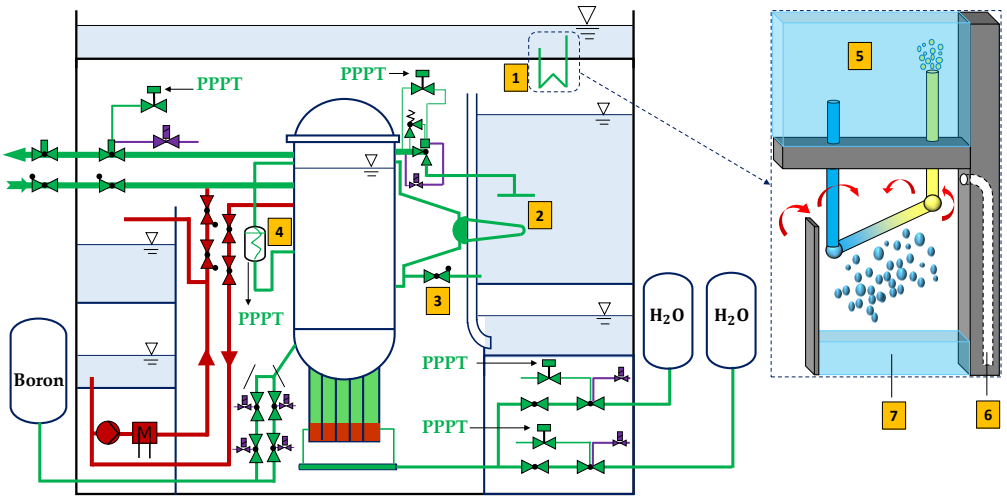

1- Containment cooling condenser (CCC)
2- Emergency condenser (EC)
3- Passive flooding lines
4- Passive pressure pulse transmitter (PPPT)
5- Storage pool
6- Overflow pipe
7- Core flooding pool

Figure 1.2: KERENA concept and the major parts of its passive safety system.

The function of the CCC is to transfer the residual heat from the containment to the storage pool located above it upon the failure of active residual heat removal system in the event of system malfunction [14]. The CCC system comprises of four heat exchangers hanged at the top of the containment vessel as shown in Figure 1.2. During normal operation mode, the condenser tubes are filled with subcooled water from the storage pool vessel and the CCC is not actuated [15]. Decay heat removal from the containment occurs by temperature rise in the containment (number 1 in

Figure 1.2) [9]. The temperature increases occurs due to two causes: firstly, the safety relief valve is opened and steam is simultaneously released and secondly, the flooding pool is heated up by the EC (number 2 in Figure 1.2) [9]. Due to a temperature difference between water inside the CCC tubes and steam in the containment, the heat transfer from the containment to the water in the tubes is initiated [15]. The surplus steam in containment condenses on the outer surface of tubes as shown in Figure 1.2. The heat released during the condensation is transferred by heat conduction through the tubes wall to the subcooled water inside the CCC. It leads to initiate subcooled boiling in the CCC [14–17] and drives another passive heat transfer to the storage pool through a natural circulation [16]. Different flow regimes, which are show in Figure 1.1 are formed in the CCC. These complex flow morphologies are prone to thermal hydraulic instabilities caused by the excursion of flow due to differences in the pressure drop characteristics of different flow patterns [10, 12, 18, 19]. Therefore, in order to avoid the occurrence of instabilities in the CCCs of KERENA it is required to accurately predict the thermal-hydraulic parameters of flow boiling regimes.

Flashing is another type of instability which may occur in the passive cooling loops of the KERENA concept [20]. During the naturally driven circulation loop, warm water coming from the CCC goes up through a long adiabatic rising pipe (discharge line in the storage pool). It is cooled in the storage pool vessel at the top of the circuit (number 5 in Figure 1.2) and then goes down back to the CCC again. If the water temperature entering the adiabatic rising pipe is high enough flashing boiling could occur there due to a reduction in hydrostatic pressure [20]. Steam formation increases circulation flow rates and causes a subsequent decrease of the water temperature. Consequently, flashing may eventually stop and the flow rate will be low again, so that the water temperature will raise leading to a new flashing cycle.

Another part of the KERENRA's passive cooling system is the ECs. They are tabular heat exchangers, which are designed for passive heat removal from the Reactor Pressure Vessel (RPV) to the core flooding pools in the event of an accident as shown in Figure 1.3. They remove heat from the core and thereby depressurize the reactor system after a scram with a heat-removal capacity of approximately 240 MW at a pressure of 71 bar [14]. The ECs consist of a steam line from the RPV, a condensate return line equipped with an anti-circulation loop back to the RPV and the condenser tubes as shown in Figure 1.3. They are connected to the RPV with no isolation pipes and are actuated when the level of water inside the RPV drops. Figure 1.3 shows the normal operation mode where the water level in the RPV is higher than in the EC (left side) and an accident mode where the water level in the RPV is lower than the one in the EC (right side). If the water level in the RPV

drops to a certain level due to an accident, steam from the RPV will flow into the condenser tubes. The steam then condenses inside the EC and the resulting condensate returns to the RPV due to gravity. Consequently, a passive heat removal loop is sustained and the heat released during the condensation is transferred by heat conduction through the EC tube wall. This heat transfer leads to initiate subcooled boiling on the outer surface of ECs' tubes as shown in Figure 1.3 [16]. The assessment of boiling heat transfer to determine the heat removal capacity of ECs is crucial.

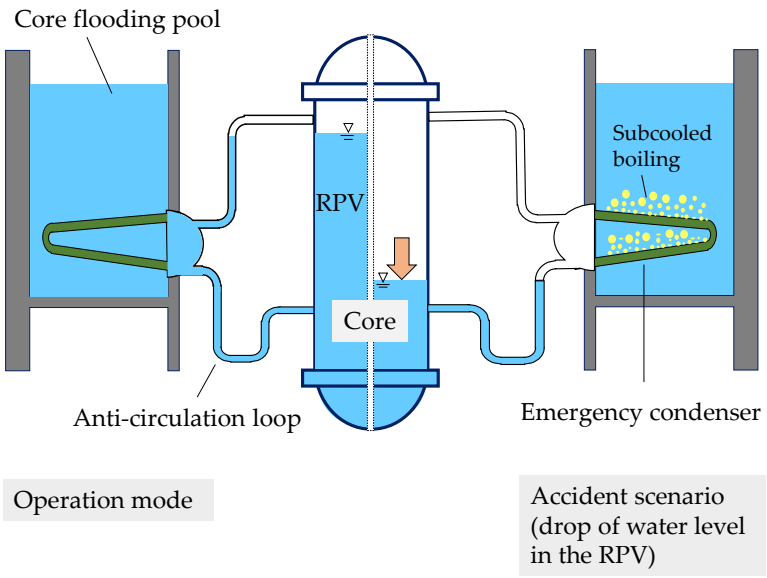

Figure 1.3: Schematic of the EC of the KERENA concept in the case of accident and operation mode.

Due to the passive and active safety systems, the core damage frequency of the KERENA concept is extremely low [13]. Nevertheless, to mitigate the consequence of a postulated core melt accident, the lower part of the RPV can be flooded with water coming from the core flooding pools via a drywell flooding line as shown in Figure 1.4 [21]. The water levels in the drywell and the core flooding pools equalize at a point well above the top edge of the reactor core and the RPV exterior surface is cooled by water [21]. Boiling occurs on the exterior surface of the RPV and the generated steam is condensed by the CCC as shown in Figure 1.4 [21]. The occurrence of CHF may result in the RPV overheating and consequently melting [13]. Therefore, an accurate prediction of boiling heat transfer prior to the CHF point is of a significant interest in the safety analysis of nuclear reactors in the event of a core melt.

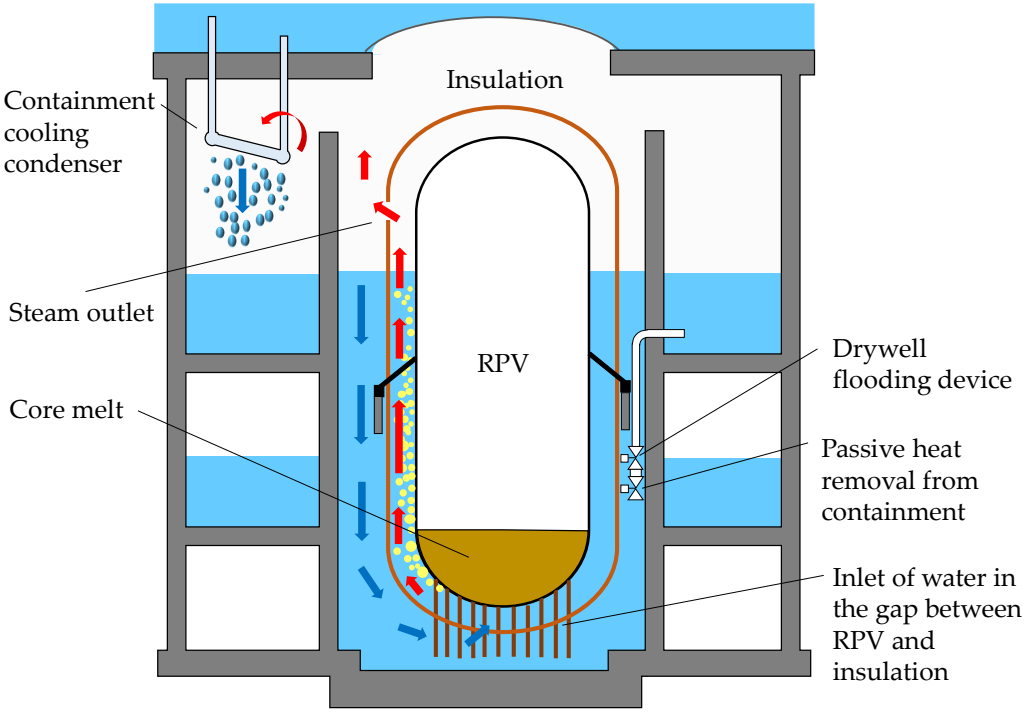

Figure 1.4: Control of the core melt in the KERENA concept.

Boiling occurs in nuclear reactors in normal operation condition as well as passive safety systems in the event of accidents as explained above. Therefore, it needs to be accurately modelled. Nucleate boiling is characterized by a higher heat transfer rate compared to single-phase convection due to the formation, growth, and detachment of bubbles from a heating wall. Its heat transfer is substantially more complex than single-phase convection because in addition to all of the variables associated with convection, those relevant to phase change and heating wall characteristics are also involved. Therefore, due to the large number of parameters involved in boiling, neither general analytical solutions nor general correlations for boiling heat transfer coefficient are available. The prediction of flow boiling heat transfer in nuclear reactors has been intensively investigated through experimental measurements, scale-down experimental models, one-dimensional codes, and CFD methods. Flow boiling modelling and the elucidation of boiling physics through experimental measurements require cost and time and accessibility to all locations in complex geometries may not be possible. Alternatively, scale-down experimental models can be employed. This method still needs expensive infrastructures as well and the obtained results have to be extrapolated to the full-size prototype and general rules to do this are often unavailable. One-dimensional system codes such as TRACE, ATHLET and RELAP have been widely employed to model the operation of thermal hydraulic circuits on the nuclear power plant scale [17]. Since these

codes are lumped parameter, which solve the balance equations on a rather coarse grid, they have limitations for the modelling of complex flow boiling regimes and heat transfer mechanisms [17]. Therefore, CFD methods are being considered as a helpful tool to provide a detailed view on the heat and mass transfer in flow boiling regimes.

CFD is a branch of fluid mechanics research that uses numerical methods to analyze and solve fluid flow problems. The most straightforward CFD technique is Direct Numerical Simulation (DNS), which involves the direct solution of the Navier-Stokes equations. Although the DNS method does not require any additional closure equations, very fine grids and small time steps need to be used in order to obtain accurate solutions. Boiling flows generally contain a large number of dispersed bubbles and involve many simultaneous physical processes taking place on widely different time and length scales. Therefore, the utilization of the DNS method in resolving such complex flows is computationally expensive and far beyond the capacity of computer resources [22]. Another CFD technique for multi-phase flows modelling is the Eulerian-Lagrangian (E-L) method. This model is based on a statistical description of the dispersed phase in terms of a stochastic point. It divides the fluid flow into a continuous phase and particles (dispersed phase) which are tracked individually in terms of a stochastic process. The trajectory of each particle is computed based on the Newton's second law and allows particle-particle and particle-fluid interactions modelling. It is evident that this model needs a lot of computational effort to keep track of large numbers of particles in a flow field. Another CFD method which has been widely employed to model two-phase flow with significant volume fractions of both phases is the Eulerian-Eulerian (E-E) two-fluid model. In the E-E two-fluid model, both dispersed and continuous phases are treated as interpenetrating continua and the balance equations of momentum, mass, and energy are separately solved for each phase based on the ensemble-averaged probability of occurrence for each phase in an Eulerian reference frame. In this model, the average behavior of particles is investigated instead of the behavior of each particle, which is being considered in the E-L model. Therefore, the E-E two-fluid model needs less computational effort. However, this model is not yet mature since it requires closure models for modelling mass, momentum, and energy exchanges between phases. The exchange terms are functions of average flow parameters and are expressed by analytical or empirical correlations. Moreover, in this model due to the averaged probability of occurrence for each phase in time and space all the information about the interfacial structures gets lost [23].

The E-E two-fluid model needs wall boiling and bubble dynamics models to describe the phase-change process as well as the partitioning of the wall heat flux between liquid and vapor phases at the heating wall. Many empirical correlations have

been proposed for the prediction of bubble dynamics parameters in flow boiling to be implemented in the E-E framework [24–26]. These parameters include bubble departure and lift-off diameters, waiting and lift-off times, sliding length, and generation frequency. The empirical correlations are only valid for specific conditions and the geometries applied in the experiments. Consequently, the uncertainties of these models limit their applicability. Mechanistic methods have been recently developed and employed for the prediction of bubble dynamics parameters. However, this methodology could not also be considered as a mature tool as none of the presented models are free of empirical parameters such as bubble inclination angle, contact angle, and base diameter. Therefore, the implementation of these models into the E-E model is debatable as they have to be calibrated for a given boundary condition via calibration factors.

1.2 Objectives

The application of the E-E two-fluid model for simulation of flow boiling in boiling systems is affected by closure models to describe the nucleate boiling process at the heating wall. Nucleate boiling is a complex process involving mass, momentum, and energy transfer at the liquid-vapor interface and frequently involves interaction with the heating wall. The physics of the phase-change process at the heating wall as well as the partitioning of wall heat flux between liquid and vapor phases are highly dependent on the bubble dynamics. The recently proposed empirical and mechanistic models for bubble dynamics need a recalibration of parameters. Therefore, this research aims to develop the E-E two-fluid approach for simulation of boiling flows by introducing improved mechanistic bubble dynamics and heat-partitioning models. The major objectives are summarized as follows:

- Prediction of bubble dynamics parameters with a mechanistic model that considers dynamic contact angle and base expansion and requires no calibration factors.
- Implementation of this mechanistic model in the E-E CFD framework as a sub-model to improve the accuracy of flow boiling simulations and reduce the case dependency.
- Analyzing the contribution of bubble sliding on the wall heat transfer mechanisms by introducing a new wall heat-partitioning model.
- Implementation of these bubble dynamics and heat-partitioning models in the GENTOP framework [27] for the modelling of flow boiling transition patterns in a vertical heating pipe.

– Investigation of the effects of flow boiling patterns on the wall heat transfer coefficient.

1.3 Outline of the thesis

The current thesis consists of 6 chapters and is structured as follows:

In Chapter 2, bubble formation mechanisms in nucleate boiling and a comprehensive review on the bubble growth modelling are presented. Moreover, CFD simulation of boiling flows with E-E two-fluid model and the governing equations are discussed. Then, the physical characteristics of flow boiling regimes including bubbly, slug, plug and annular flows in a vertical heating pipe are provided. Eventually, the application of the GENTOP concept and the Algebraic Interfacial Area Density (AIAD) model for simulation of flow boiling transition patterns are introduced.

Chapter 3 includes the introduction of a new mechanistic bubble dynamics model which is based on the force balance approach for a growing bubble in boiling flows. The governing equations of bubble dynamics model including applied forces on a growing bubble as well as the bubble departure and lift-off criteria are presented. Afterward, model validation against four experiments is discussed. Eventually, a model sensitivity analysis to evaluate the dependency of bubble departure and lift-off diameters on different parameters such as heat flux, subcooling temperature, pressure, heating wall inclination angle and mass flow rate are provided.

In Chapter 4, the implementation of the introduced bubble dynamics model in the E-E framework for simulating boiling flows is presented. This implementation introduces an activated temperature-dependent heat-partitioning model in which the contribution of bubble sliding to wall heat transfer is investigated. In addition, validation against two experimental cases including the subcooled boiling flow of R12 refrigerant in a vertical pipe and R134a in an annulus is given. These experimental tests include 10 experiments that cover a wide range of operating conditions including various heat flux, inlet subcooling, mass flow rate and pressure. The validated parameters are void fraction, vapor velocity, wall temperature, liquid temperature, bubble diameter, IAD and bubble passing frequency. Eventually, comparisons between the results of the conventional Rensselaer Polytechnic Institute (RPI) wall boiling model and the present model are provided.

Chapter 5 presents the implementation of the introduced bubble dynamics model in Chapter 3 in the GENTOP framework for simulation of flow boiling transition patterns in a vertical pipe. An adopted heat-partitioning model to consider the effect of continuous gas structures formation on the wall heat transfer is introduced

in this chapter. The test case is the water subcooled flow in a vertical heating pipe at ambient pressure. The impacts of wall temperature, velocity and subcooling temperature on the flow transition patterns are then investigated. Moreover, comparisons between the result of GENTOP and E-E two-fluid models are carried out. Eventually, the effects of flow morphologies on the wall heat transfer coefficient are discussed. Chapter 6 briefly summarizes this research outcomes and findings. Some recommendations for future works are also provided in this chapter.

2 State-of-the-art in modelling of subcooled flow boiling

Subcooled ow boiling occurs when a subcooled liquid enters a heating pipe and its temperature near the heating wall exceeds the Onset of Nucleate Boiling (ONB) temperature. Small bubbles are formed on the heating wall and condense in the bulk since the bulk liquid temperature is below its saturation point. They heat the subcooled liquid, causing the bulk liquid to reach saturation temperature. It increases the void fraction and further downstream, the two-phase flow morphologies may change from bubbly to slug, plug, and annular flow sequentially dependent on the boundary condition and channel. Since these flow patterns have a significant impact on the heat and mass transfer rates, an accurate prediction of them becomes critical. Figure 2.1 schematically illustrates the flow boiling regimes and heat transfer mechanisms occurring in a vertical heating pipe with an upward flow.

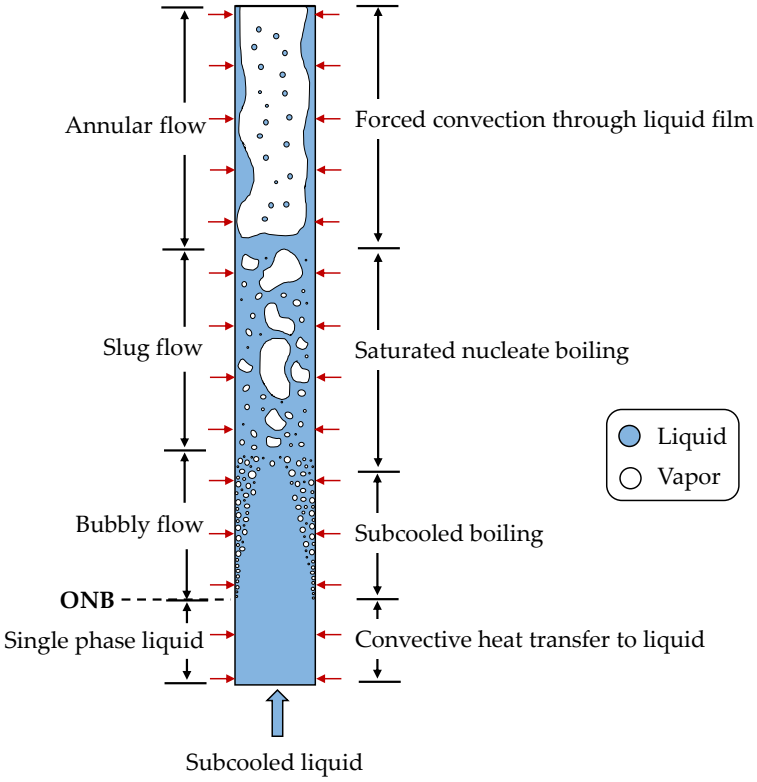

Figure 2.1: Flow boiling regimes in a vertical heating pipe.

This chapter will provide detailed information about the state-of-the-art related to the modelling of subcooled flow boiling. It consists of bubble dynamics modelling, CFD simulation of bubbly flow using E-E two-fluid model and pattern transition modelling in flow boiling using the GENTOP concept.

The following Section 2.1 introduces the bubble formation mechanism in nucleate boiling. In Section 2.2, the recently developed bubble growth models are reviewed. Physical characteristics and simulation of subcooled flow boiling by using the E-E two-fluid model are outlined in Section 2.3. The Population Balance Method (PBM) for bubble size distributions, the governing equations of the E-E two-fluid model, descriptions of the interfacial heat, mass and momentum transfers, the Rensselaer Polytechnic Institute (RPI) wall boiling model and its closure correlations are explained and discussed in this section as well. Section 2.4 gives an introduction to flow boiling regimes in a vertical heating pipe. The recently developed GENTOP concept and its application for the simulation of flow regimes are presented in Section 2.5. The interface detection using the Algebraic Interfacial Area Density (AIAD) model and handling of the potentially continuous gas phase is then explained. The interfacial exchange terms of continuous gas structures are reviewed in Section 2.6. Finally, a summary of this chapter is given in Section 2.7.

2.1 Physics of boiling

The enhancement of heat transfer during nucleate boiling compared to single-phase convection is determined by vapor bubbles, which grow and detach from the heating surface. Energy is transferred from the heating wall into the liquid layer adjacent to the wall, the so-called thermal boundary layer, by transient conduction. This stored energy is ultimately used to vaporize the liquid during the bubble inception, growth and decay. In addition, fluid motions induced by bubbles disrupt the thermal boundary layer, which results in enhancing the local heat transfer as well. Consequently, insight into responsible mechanisms for transporting energy away from the heating wall requires understanding the nature of bubble growth and detachment.

When a heating surface is submerged in a liquid, pockets of air are trapped into cavities, which create a gas-liquid interfacial area and can act as an embryo for bubble inception. The propagation, size, and geometric shapes of these cavities depend on the surface finishing methods and level of oxidation. These cavities are named nucleation sites and when the heating wall temperature (liquid layer adjacent to the heating wall) exceeds the ONB temperature, bubbles are initially formed in these crevices due to the expansion of entrapped gas as shown in Figure 2.2.

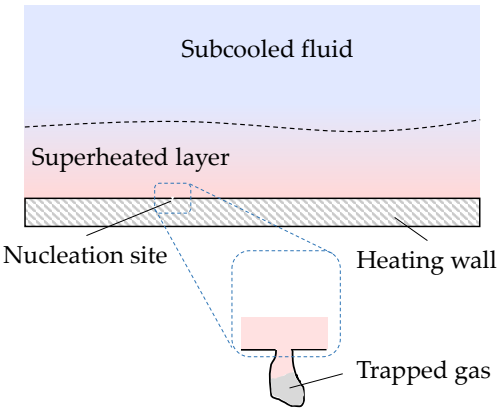

Figure 2.2: A cavity on the heating wall acts as a nucleation site.

Figure 2.3 illustrates the bubble growth on a heating wall in a sequence of stages [28]. After the bubble departure, the bulk liquid with temperature T_b, is brought into contact with the heating wall with $T_w > T_{sat}$, which results in the thermal boundary layer disruption as shown in Figure 2.3a. Afterward, a time period elapses at which transient conduction into the liquid adjacent layer takes place, but no bubble incepts. This time is referred to as waiting time, t_w, as depicted in Figure 2.3b.

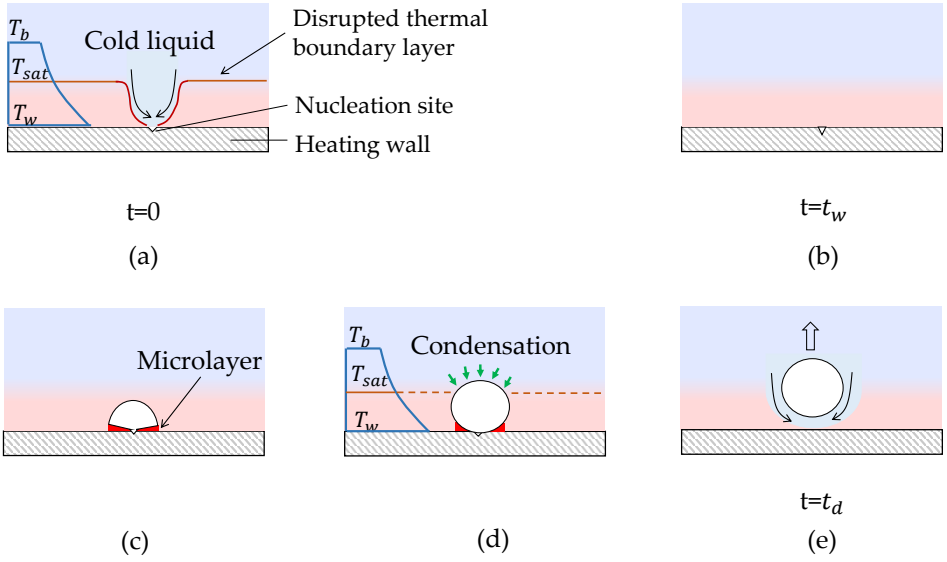

Figure 2.3: Bubble growth stages in nucleate boiling.

Bubble nucleation occurs when a microbubble, which resides inside or over the crevice grows from evaporation. At the beginning of bubble formation, its growth is primarily resisted by the inertia of liquid. In other words, the inertia-controlled growth is the initial stage of bubble formation at which the rate of bubble expansion

is primarily determined by its ability to push the surrounding liquid back. During this period, the bubble grows rapidly in nearly hemispherical shape and a thin liquid layer is left between the lower portion of bubble and the heating wall as shown in Figure 2.3c. This film is referred to as microlayer and its thickness varies from nearly zero in the nucleation site to a value at the edge of the hemispherical bubble. Due to the high pressure beneath the bubble induced by the bubble expansion at the early stage, the microlayer will not be evaporated until $T_w > T_{sat}\ (PV)$. Afterward, heat is transferred across the microlayer from the heating wall to the interface, which results in vaporizing the liquid at the surface and consequently contributing to the bubble growth. After a while, the heat transfer controlled period begins at which the heat flux supports the evaporation through the vapor-liquid interface. During this period, which is referred to as the thermal diffusion-controlled growth period, liquid inertia and pressure forces become smaller and the surface tension tends to pull the bubble into more spherical shape as shown in Figure 2.3d. When the bubble grows and its height becomes larger than the thermal layer thickness, condensation, which reduces the bubble size, occurs at the bubble surface (Figure 2.3d). Throughout the bubble growth process, interfacial tension acting along the contact line, where the solid wall meets the interface, tends to hold the bubble in place on the wall. On the opposite side, drag, lift, buoyancy, inertial forces associated with the motion of the surrounding fluid tend to pull the bubble away. As the bubble grows more, these detaching forces become stronger and eventually the bubble departures at t_d as depicted in Figure 2.3e. The thermal boundary layer is disrupted and cold liquid touches the heating wall and the cycle is repeated.

Figure 2.4 illustrates the principle of heat transfer mechanisms occurring in nucleate boiling [29]. As shown in Figure 2.4a, evaporation of superheated liquid surrounding the bubble and thin liquid film trapped beneath the bubble (microlayer) contribute to the bubble growth. Figure 2.4b shows a periodically disrupted thermal boundary layer and its later recovery due to the transient heat conduction to the liquid in the vicinity of the heating wall. Heat is transferred in a sensible form in the superheated liquid layer. The last heat transfer mechanism in boiling is the liquid motion induced by the growing and departing bubble, which enhances the convection heat transfer (Figure 2.4c).

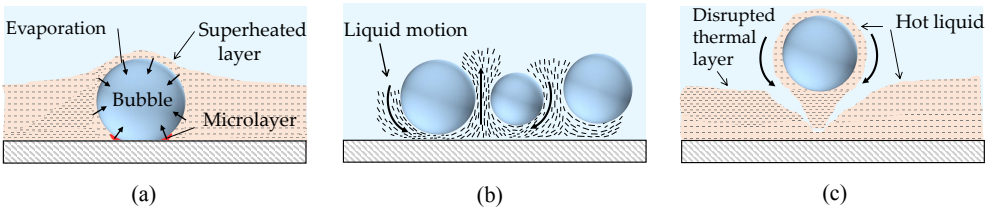

Figure 2.4: Different heat transfer mechanisms during bubble formation in the nucleate boiling.

2.2 Bubble growth modelling

The progression towards an accurate prediction of bubble dynamics is hampered by developing a solution method, which takes into account all parameters contributing to bubble growth and detachment. Nevertheless, recent theories for the prediction of bubble growth have significantly progressed and substantial insight into nucleate boiling has been provided by exploring the fundamental nature of bubble growth. In the early stage, the theoretical works on the bubble growth model was based on the idea of spherically symmetric bubble growth in a uniformly superheated pool of liquid. Nevertheless, these simplifications could not provide an exact solution to predict bubble dynamics parameters due to the complicated thermal and hydrodynamic interaction of vapor bubble and liquid.

In 1917, Rayleigh proposed the following equation for bubble growth rate in the inertia-controlled period [30].

$$r_b(t) = \left(\frac{2}{3}[\frac{T_b - T_{sat}}{T_{sat}}]\frac{h_{fg}\rho_g}{\rho_l}\right)^{\frac{1}{2}} t, \tag{2.1}$$

with T_b, T_{sat}, h_{fg}, ρ_g , ρ_l and t being the bulk liquid temperature, saturation temperature, latent heat, vapor density, liquid density and time. This model for the bubble inertia-controlled growth period was validated by the low pressure experiments of Lien [31] as well as numerical simulations of Robinson [32] and Lee [33]. Almost four decades later, Plesset and Zwick modelled the bubble growth in a uniform superheated liquid for the heat diffusion-controlled period in pool boiling [34]. The bubble growth modelling in the heat diffusion-controlled growth period was later extended to non-uniform temperature fields by others, such as Forster and Zuber [35], Grift [36], Savic [37] and Zuber [25]. A complete description of the bubble growth process represents a transition connecting the inertia-controlled growth and the later diffusion-controlled one. In 1970, Mikic et al. proposed the following equation for a growing bubble in a uniformly superheated liquid, which is applicable for the entire range of inertia-controlled and diffusion-controlled growth periods [38]. They [38] assumed that the bubble growth rate was bounded by the Rayleigh's analytical solutions [30] for inertia-controlled period and the model of Plesset and Zwick [34] for thermal diffusion-controlled one as:

$$R^+ = \frac{2}{3}\left[\left(t^+ + 1\right)^{\frac{3}{2}} - \left(t^+\right)^{\frac{3}{2}} - 1\right] \tag{2.2}$$

with

$$R^+ = \frac{r_b(t)A}{B^2},\ t^+ = \frac{tA^2}{B^2}, \tag{2.3}$$

and

$$A = \sqrt{b\frac{(T_w - T_{sat})h_{fg}\rho_g}{T_{sat}\rho_l}}, \qquad B = Ja\sqrt{\frac{12\alpha'_l}{\pi}}. \tag{2.4}$$

In Eq. (2.4), b is a constant with the values of $\frac{2}{3}$ and $\frac{\pi}{7}$ for the bubble growth in an infinite medium and on a surface. The term α'_l is the thermal diffusivity of liquid and Ja denotes the Jakob number defined as:

$$Ja = \frac{\rho_l C_{pl}\,(T_w - T_{sat})}{\rho_g h_{fg}}, \tag{2.5}$$

with C_{pl} being the liquid specific heat capacity.

In 1978, Prosperetti and Plesset derived dimensionless relations valid throughout both inertia controlled and diffusion-controlled growth [39]. Labuntsov further developed a model for bubble growth rate in the thermal diffusion-controlled period [40]. During the inertia-controlled period, the bubble growth is rapid and dominated by the inertia of the liquid being displaced due to the bubble formation. A microlayer postulated and proven by Cooper and Loyd in 1969 is formed underneath the bubble as illustrated in Figure 2.5 [41]. Then, Van Stralen et al. determined the initial thickness of the evaporating microlayer beneath a hemispherical vapor bubble on a horizontal heating wall and derived a heat and mass diffusion-type solution accounting for the contribution of relaxation microlayer and evaporation microlayer to the bubble growth [42]. Once the thermal-diffusion controlled period of bubble growth begins, the microlayer formed in the inertia-controlled period contributes to the bubble growth as it extends during the expansion of bubble base diameter (see Figure 2.6).

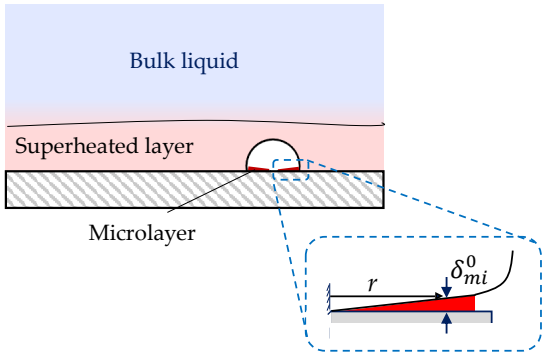

Figure 2.5: Illustration of the microlayer formation underneath a bubble.

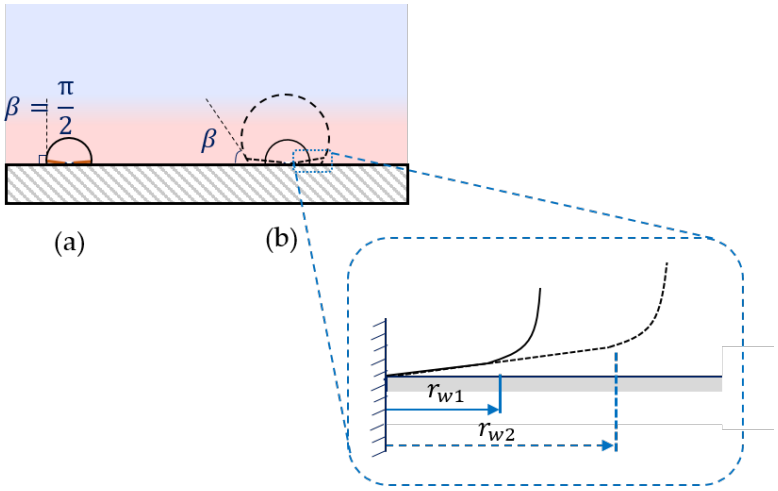

Figure 2.6: Schematic of bubble base diameter expansion during a) inertia and b) thermal-diffusion controlled period.

More recently, Klausner et al. developed a bubble growth model for the prediction of bubble departure and lift-off based on the balance of forces acting on a growing bubble [43]. They used the model of Mikic et al. [38] to predict the bubble growth rate and obtained a satisfactory predictive accuracy against their own experimental data for the refrigerant R113 flow boiling [43]. However, they considered a constant bubble base diameter (contact diameter), recommended as $d_w = 0.09$ mm and constant advancing and receding contact angles, $\beta_{ad} = \frac{\pi}{4}$ rad and $\beta_{re} = \frac{\pi}{5}$ rad which are shown in Figure 2.7. In reality, however, these parameters are not constant. In flow boiling, departure means that a bubble leaves the originating cavity and lift-off means that the bubble releases into bulk fluid. In other words, when a bubble does not slide on the heating wall, the departure means lift-off.

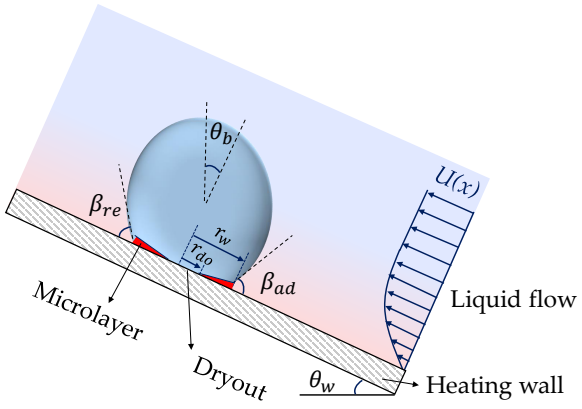

Figure 2.7: Schematic of a bubble formation in flow boiling. β_{ad}, β_{re}, θ_b and θ_w are the bubble advancing, receding, inclination and heating wall orientation angles. r_w and r_{do} denote the bubble base and dryout radii as well.

Thorncroft et al. [44], Situ et al. [45], Yeoh et al. [46], Wu et al. [47] and Sugrue and Buongiorno [48] coupled the force balance model of Klausner et al. [43] with the Zuber's bubble growth model [25] for prediction of bubble lift-off. The Zuber's bubble growth model is given as [25]:

$$r_b\left(t\right) = \frac{2b}{\sqrt{\pi}} Ja \sqrt{\alpha'_l t}. \tag{2.6}$$

The parameter b is used to account for the sphericity of the bubble and different values have been proposed based on the experimental data. The parameters b, β_{ad} and β_{re} were calibrated in these models as given in Table 2.1.

Yun et al. [49] improved the force balance model of Klausner et al. [43] by considering a bubble condensation and evaluating the model for a wider range of pressure, temperature, and low rates for water as well.

Table 2.1: Calibrated parameters in bubble dynamics models.

Reference	b	β_{ad}	β_{re}
Thorncroft et al. [44]	0.9	23.2°	8.4°
Situ et al. [45]	1.73	55°	35°
Yeoh et al. [46]	0.21	45°	35°
Wu et al. [47]	1.2	35°	45°
Sugrue and Buongiorno [48]	1.56	91°	8°

Chen et al. [50] coupled the following bubble growth rate model with the force balance model of Klausner et al. [43] for the prediction of bubble departure diameter. Their model is given as [50]:

$$r_b(t) = K \times t^n. \tag{2.7}$$

They [50] calibrated the values of K and n for different experimental conditions and proposed the ranges of 0.987-1.028 and 0.176-0.262 respectively. They also used the constant values of 130° and 65° for β_{ad} and β_{re}.

Recently Colombo and Fairweather presented the following equation for the bubble growth in flow boiling as [51]:

$$\begin{aligned}\frac{dr_b}{dt} =& \frac{1}{C_2} {Pr_l}^{-0.5} Ja \left(\frac{\lambda_l}{\rho_l C_{pl}}\right)^{0.5} t^{-0.5} \\ &+ \sqrt{\frac{3}{\pi}} \lambda_l \left(T_l - T_{sat}\right) \left(\frac{\lambda_l}{\rho_l C_{pl}}\right)^{0.5} t^{-0.5} \left(1 - f_{sub}\right) \\ &- \frac{\lambda_l (2 + 0.6 {Re_b}^{0.5} Pr_l^{0.3})(T_{sat} - T_b)}{d_b \rho_g h_{fg}} f_{sub},\end{aligned} \tag{2.8}$$

with Pr_l, d_b and λ_l being the liquid Prandtl number, bubble diameter and liquid thermal conductivity. The terms f_{sub} and Re_b denote the portion of the bubble surface in contact with the subcooled liquid and the bubble Reynolds number. T_l is the liquid temperature distribution in the superheated layer and C_2 is the microlayer constant which determined as $C_2 = 1.78$ [51]. Following the model of Klausner et al. [43] they set $\beta_{ad} = \frac{\pi}{4}$ rad and $\beta_{re} = \frac{\pi}{5}$ rad [51]. In addition, for the bubble base diameter they applied the model of Yun et al., that is, $d_w = \frac{d_b}{15}$ [49].

Raj et al. [52] employed Eq. (2.8) for bubble growth model prediction in flow boiling, but with the values of $\beta_{ad} = 89°$, $\beta_{re} = 9°$, $d_w = \frac{d_b}{15}$ and the bubble inclination angle of $\theta_b = 10°$. Most recently, Mazzocco et al. used this model with the values of $\beta_{ad} = \frac{\pi}{4}$ rad, $\beta_{re} = \frac{\pi}{5}$ rad and $d_w = 0.09$ mm as well [53]. In addition, they introduced and optimized a correlation factor to account for the effects of saturated and subcooled flows [53].

Many of the introduced bubble dynamics models consider constant values for bubble geometry parameters such as advancing, receding and inclination angles and base diameter as well. However, in reality, they are not constant. They contain parameters, which have to be calibrated for a given boundary condition. Table 2.2 gives a summary of proposed models for bubble growth and departure.

Table 2.2: Proposed models for calculating bubble growth and departure ("+" indicates that the respective physical mechanism is considered).

Reference	**Growth model**			**Departure model**		
	Microlayer	**Superheated layer**	**Condensation**	**Force balance**	**Contact angle/Base expansion**	**Geometry change**
Plesset and Zwick [34]		+				
Zuber [25]		+				
Cooper and Loyd [41]	+	+				
Mikic et al. [38]		+				
Prosperetti and Plesset [39]		+				
Klausner et al. [43]		+		+	+ constant/constant	
Situ et al. [45]		+		+	+ constant/constant	
Yeoh et al. [46]		+		+	+ constant/constant	
Wu et al. [47]		+		+	+ constant/constant	
Sugrue and Buongiorno [48]		+		+	+ constant/$\frac{d_w}{d_b} = 0.025$	
Colombo and Fairweather [51]	+ (no dryout)	+	+	+	+ constant/$d_w = \frac{d_b}{15}$	
Raj et al. [52]	+ (no dryout)	+	+	+	+ constant/$d_w = \frac{d_b}{15}$	
Mazzocco et al. [53]	+ (no dryout)	+	+	+	+ constant/constant	

2.3 CFD simulation of boiling flows

Figure 2.8 shows subcooled flow boiling in a vertical heating pipe along with a typical curve describing the void fraction distribution.

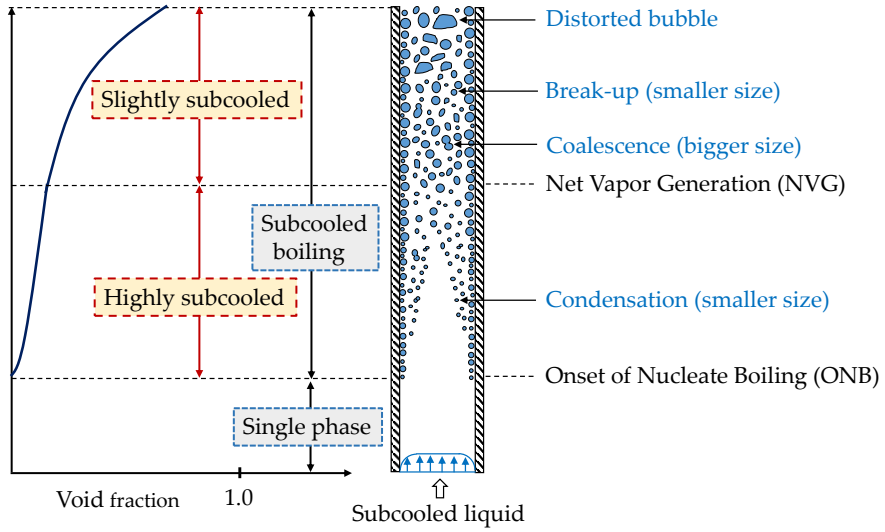

Figure 2.8: A phenomenological illustration of bubbly flow in subcooled flow boiling with a typical void fraction curve.

Bubble nucleation occurs at the ONB point. The subcooled boiling continues downstream of this point, but the void fraction can not significantly increase due to the high rate of condensation. Due to the increased bulk liquid temperature downstream, larger bubbles' departure size sharply enhances the void fraction at the location called Net Vapor Generation (NVG). This point indicates the transition between two regions: low void fraction with high subcooling and high void fraction region with slight subcooling. When bubbles leave the heating wall and move through the subcooled bulk liquid, where condensation happens, they shrink and sometimes disappear because of a high rate of condensation. Moreover, break-up and coalescence mechanisms can decrease or increase the size of bubbles and consequently the void fraction is affected. Normally, the big distorted bubbles move in the center of the pipe and small ones move near the heating walls.

2.3.1 The Eulerian-Eulerian two-fluid model

CFD simulation of subcooled flow boiling consists of two categories as shown in Figure 2.9. The first category is the wall heat transfer mechanism, which is predicted by bubble dynamics, nucleation site density and heat-partitioning models.

The second one involves two-phase flow and bubble interactions with other bubbles and liquid in the bulk flow away from the heating wall and is discussed in this chapter.

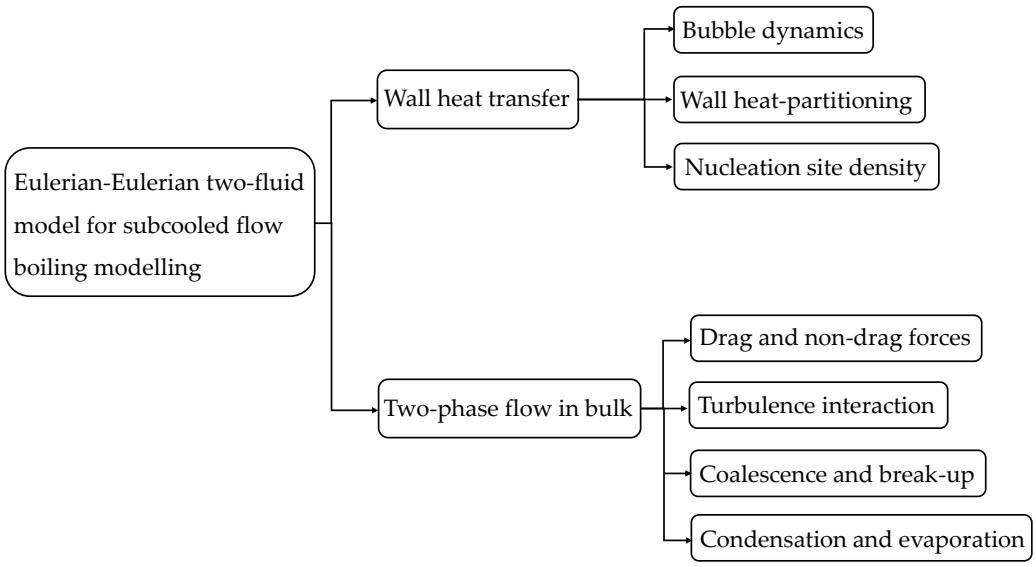

Figure 2.9: Schematic of CFD simulation of subcooled flow boiling including sub-models.

The two-fluid model based on the E-E framework represents a detailed macroscopic formulation of the thermal and hydrodynamic characteristics of two-phase systems. In this approach, the liquid and vapor phases are treated as interpenetrating continua. The equations of mass, momentum and energy are solved for each phase individually. The interaction terms including interfacial forces and heat and mass transfers are considered by adopting the additional sink/source terms for each of the governing equations. These terms are implemented by analytical or empirical models, which depend on average flow parameters. They are rather important as they determine the degree of thermal and mechanical non-equilibrium between liquid and vapor phases and the rate of phase change as well. The interfacial heat and mass transfers due to the condensation and evaporation are accounted in the governing equations. In the momentum conservation equation, the momentum exchange between phases due to the drag force and non-drag forces including the wall lubrication, turbulent dispersion, lift and virtual forces are incorporated.

2.3.2 The Population Balance Model (PBM)

In the E-E model, an accurate prediction of local bubble Sauter diameter is critical as it determines the interfacial area and further affects heat, mass and momentum transfers. The prediction of local bubble size is strongly influenced by the complex

bubble behaviors in two-phase flows. In the E-E framework, there are three main approaches in bubbly flow modelling. In the mono-disperse approach, it is assumed that all bubbles have the same size and move with a common velocity. In bi-disperse model, bubbles are divided into two velocity groups. The criterion for division is the critical bubble diameter, d_{cr}, where the lift force coefficient sign changes from positive to negative for small and large bubbles respectively (positive direction is assigned towards the wall). Two mean bubble diameters are allocated to small and large groups and two velocity groups are defined as well. For each distinct velocity group a set of conservation equations is solved. However, in reality, the BSD is neither mono-disperse nor bi-disperse. It is poly-disperse which is affected by other complex phenomena such as coalescence and breakup. Therefore, in order to take the effects of these phenomena on the BSD into account in CFD simulations a Population Balance Model (PBM) is employed. Two approaches are employed in ANSYS CFX 18.2 to use the PBM model. The first one is the homogenous Multiple Size Group (MUSIG) originally developed by Lo [54]. In this model, the BSD is divided into different size groups and it is assumed that all bubbles with different sizes move with a common velocity as shown in Figure 2.10.

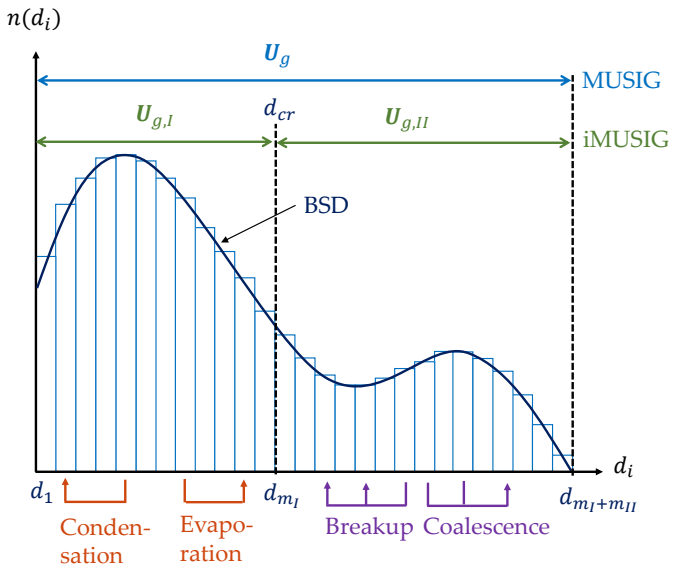

Figure 2.10: An illustration of a BSD with the MUSIG and iMUSIG models including phase transfer.

In the MUSIG model, the BSD is divided into different size groups, $k = 1 \ldots .m$, which represent the bubbles of size d_k. The void fraction of vapor phase in each size group is $\alpha_{g,k}$ and the total void fraction is calculated as:

$$\alpha_g = \sum_{k=1}^{m} \alpha_{g,k}. \tag{2.9}$$

$$f_k = \frac{\alpha_{g,k}}{\alpha_g}, \qquad \sum_{k=1}^{m} f_k = 1. \tag{2.10}$$

The bubble Sauter mean diameter, d_{SM}, is calculated as:

$$d_{SM} = \frac{1}{\sum_{k=1}^{m} \frac{f_k}{d_k}}. \tag{2.11}$$

The IAD is defined as the total interfacial surface between the phases per unit volume of mixture and is dominated by the number and size of vapor bubbles. Assuming spherical bubbles, the IAD is given as:

$$A_{if} = \frac{6\alpha_g}{d_{SM}}. \tag{2.12}$$

The MUSIG model is unable to predict the separation of small and large bubbles due to non-drag forces particularly for a heterogeneous bubble motion. In other words, the relation between the change of lift force coefficient sign and the BSD is not rightly modelled in this approach. The inhomogeneous Multiple Size Group (iMUSIG) model was developed by Krepper et al. to overcome the limitations of the MUSIG model [55]. In the iMUSIG model, bubbles are divided into two velocity groups and the d_{cr} is the criterion for division [55]. For each of small bubbles group ($d < d_{cr}$) and large one ($d > d_{cr}$) the MUSIG model is employed. In addition, each velocity group has its own common velocity and the conservation equations are solved for each of them separately. Figure 2.10 exhibits a discrete BSD including breakup, coalescence and phase transfer due to evaporation and condensation in the MUSIG and iMUSIG models. In the iMUSIG model, the total void fraction, α_g, and the equivalent d_{SM} are calculated as:

$$\alpha_{g,I} = \sum_{k=1}^{m_I} \alpha_k, \quad f_k = \frac{\alpha_{g,k}}{\alpha_{g,I}} \quad (k = 1,\ ..,\ m_I), \ \sum_{k=1}^{m_I} f_k = 1, \quad d_{SM,I} = \frac{1}{\sum_{k=1}^{m_I} \frac{f_k}{d_k}}, \tag{2.13}$$

$$\begin{aligned} &\alpha_{g,II} = \sum_{k=m_I}^{m_I+m_{II}} \alpha_k, \quad f_k = \frac{\alpha_{g,k}}{\alpha_{gII}} \quad (k = m_I + 1,\ ..,\ m_I + m_{II}), \\ &\sum_{k=m_I+1}^{m_I+m_{II}} f_k = 1,\ d_{SM,II} = \frac{1}{\sum_{k=m_I+1}^{m_I+m_{II}} \frac{f_k}{d_k}}, \end{aligned} \tag{2.14}$$

$$\alpha_g = \alpha_{g,I} + \alpha_{g,II}, \tag{2.15}$$

$$d_{SM} = \frac{\alpha_{g,I} + \alpha_{g,II}}{\frac{\alpha_{g,I}}{d_{SM,I}} + \frac{\alpha_{g,II}}{d_{SM,II}}}, \tag{2.16}$$

with m_I and m_{II} being the size group numbers of small ($d < d_{cr}$) and large ($d > d_{cr}$) bubbles. The $\alpha_{g,I}$ and $\alpha_{g,II}$ terms denote the total void fraction of first and second velocity groups as well. The IAD for each velocity group is given as:

$$A_{if,I} = \frac{6\alpha_{g,I}}{d_{SM,I}}, \tag{2.17}$$

$$A_{if,II} = \frac{6\alpha_{g,II}}{d_{SM,II}}. \tag{2.18}$$

2.3.3 Governing equations of the two-fluid model

In the E-E two-fluid model the liquid and vapor phases are treated as continuous and dispersed phases respectively. In this thesis, the vapor phase is assumed to be at saturation temperature corresponding to local pressure and the temperature distribution inside vapor bubbles is assumed to be uniform. In addition, as the interface is assumed to be at saturation temperature, the heat flux from the interface to the vapor phase is zero. Therefore, there is no need to solve the energy equation for the vapor phase. For the MUSIG model one set of conservation equations are solved for the vapor phase. The conservation equations of continuous liquid phase and vapor phase in the iMUSIG framework including two velocity groups (small and large bubbles) are given below [56].

Continuity equation of vapor phase:

$$\frac{\partial}{\partial t}(\alpha_{g,j}\rho_{g,j}) + \nabla.(\alpha_{g,j}\rho_{g,j}\boldsymbol{U}_{g,j}) = -\dot{m}_{l\leftrightarrow g,j} + S_j. \tag{2.19}$$

Momentum equation of vapor phase:

$$\begin{aligned}\frac{\partial}{\partial t}(\alpha_{g,j}\rho_{g,j}\boldsymbol{U}_{g,j}) + \nabla.(\alpha_{g,j}\rho_{g,j}\boldsymbol{U}_{g,j}\times\boldsymbol{U}_{g,j}) = -\alpha_{g,j}\nabla P + \alpha_{g,j}\,\rho_g\boldsymbol{g} \\ +\nabla.(\alpha_{g,j}\boldsymbol{\tau}_{g,j}) + \boldsymbol{F}_{g,j} - (\dot{m}_{g,j\leftrightarrow l}\boldsymbol{U}_l - \dot{m}_{l\leftrightarrow g,j}\boldsymbol{U}_{g,j}) + \boldsymbol{S}_{M,j}\end{aligned} \tag{2.20}$$

Continuity equation of liquid phase:

$$\frac{\partial}{\partial t}(\alpha_l\rho_l) + \nabla.(\alpha_l\rho_l\boldsymbol{U}_l) = \sum_{j=I}^{II}\dot{m}_{l\leftrightarrow g,j} \tag{2.21}$$

Momentum equation of liquid phase:

$$\frac{\partial}{\partial t}\left(\alpha_l \rho_l \boldsymbol{U}_l\right) + \nabla.\left(\alpha_l \rho_l \boldsymbol{U}_l \times \boldsymbol{U}_l\right) = -\alpha_l \nabla P + \alpha_l \rho_l \boldsymbol{g} + \nabla.(\alpha_l \boldsymbol{\tau}_l) + \boldsymbol{F}_l + \sum_{j=I}^{II} \left(\dot{m}_{g,j\leftrightarrow l}\boldsymbol{U}_l - \dot{m}_{l\leftrightarrow g,j}\boldsymbol{U}_{g,j}\right) \tag{2.22}$$

Energy equation of liquid phase:

$$\frac{\partial}{\partial t}\left(\alpha_l \rho_l H_{t,l}\right) + \nabla.\left(\alpha_l \rho_l H_{t,l}\boldsymbol{U}_l\right) = \alpha_l \frac{\partial P}{\partial t} + \nabla.(\alpha_l \lambda_l \nabla T_l) + \alpha_l \nabla.\left(\boldsymbol{U}_l.\boldsymbol{\tau}_l\right) + \sum_{j=I}^{II} \left(\dot{m}_{g,j\leftrightarrow l} H_{t,sat,l} - \dot{m}_{l\leftrightarrow g,j} H_{t,sat,g}\right) + Q_{int} \tag{2.23}$$

In the given equations, g and l subscripts indicate vapor and liquid phases. The subscript j is the indicator of two velocity groups in the iMUSIG model (for the MUSIG model, $j = 1$). In Eq. (2.19) the source or sink term $\dot{m}_{l\leftrightarrow g,j}$ represents the interfacial mass transfer due to the evaporation or condensation process and is expressed as:

$$\dot{m}_{l\leftrightarrow g,j} = \frac{h_{if,j} A_{if,j} (T_{sat} - T_l)}{h_{fg}}. \tag{2.24}$$

The term h_{if} is the interfacial heat transfer coefficient, which is commonly calculated by the model of Ranz-Marshal as [57]:

$$h_{if,j} = \frac{\lambda_l}{d_{SM,j}} \left(2 + 0.6\ Re_{g,j}^{0.5} Pr_l^{\frac{1}{3}}\right), \tag{2.25}$$

with $Re_{g,j}$ being the bubble Reynolds number given as:

$$Re_{g,j} = \frac{\rho_l |\boldsymbol{U}_{g,j} - \boldsymbol{U}_l| d_{SM,j}}{\mu_l}. \tag{2.26}$$

In this equation, $\boldsymbol{U}$ and μ_l are fluid velocity and the dynamic viscosity of liquid phase. Hughmark presented another equation for $h_{if,j}$ as [58]:

$$Nu_{D,j} = \begin{cases} 2 + 0.6 Re_{g,j}^{0.5} Pr_l^{0.33} & 1 < Re_{g,j} < 450 \\ 2 + 0.27 Re_{g,j}^{0.62} Pr_l^{0.33} & Re_{g,j} > 450, \end{cases} \tag{2.27}$$

with $Nu_{D,j}$ being the Nusselt number defined as:

$$Nu_{D,j} = \frac{h_{if,j} d_{SM,j}}{\lambda_l}. \tag{2.28}$$

The term $A_{if,j}$ in Eq. (2.24) denotes the IAD calculated by Eqs. (2.17) and (2.18).

In Eq. (2.23) the term Q_{int} is the heat flux from interface to liquid which is calculated as:

$$Q_{int} = \sum_{j=I}^{II} h_{if,j} A_{if,j} \left(T_{sat} - T_l\right). \tag{2.29}$$

In Eqs. (2.20), (2.22) and (2.23) the terms $\boldsymbol{\tau}_g$ and $\boldsymbol{\tau}_l$ indicate the shear stress vector acting on the vapor and liquid phases. They are given as:

$$\boldsymbol{\tau}_{g,j} = \mu_g \left[(\nabla \boldsymbol{U}_{g,j}) + (\nabla \boldsymbol{U}_{g,j})^T - \frac{2}{3}\delta \, \nabla . \boldsymbol{U}_{g,j} \right], \tag{2.30}$$

$$\boldsymbol{\tau}_l = \mu_l^{eff} \left[(\nabla \boldsymbol{U}_l) + (\nabla \boldsymbol{U}_l)^T - \frac{2}{3}\delta \, \nabla . \boldsymbol{U}_l \right], \tag{2.31}$$

with μ_g and δ being the vapor molecular viscosity and Dirac delta function. The term μ_l^{eff} is the liquid effective viscosity, which is defined as the sum of molecular and turbulent viscosity, i.e.:

$$\mu_l^{eff} = \mu_l + \mu_l^{turb}. \tag{2.32}$$

The liquid turbulent viscosity, μ_l^{turb}, is calculated as:

$$\mu_l^{turb} = \rho_l C_\mu \frac{k_l^2}{\epsilon_l}, \tag{2.33}$$

with C_μ being a constant with the value of 0.09. The terms k_l and ϵ_l are liquid turbulent kinetic energy and dissipation rate. The term H_t in Eq. (2.23) is the total enthalpy, which is given as:

$$H_t = h_{sta} + \frac{1}{2}\boldsymbol{U}^2, \tag{2.34}$$

with h_{sta} being the static enthalpy.

The term $\boldsymbol{F}_{g,j}$ in Eq. (2.20) denotes the forces acting on the vapor bubbles. Due to conservation of momentum the net force between vapor and liquid phase is equal to zero, i.e.:

$$\boldsymbol{F}_l = -\left(\boldsymbol{F}_{g,I} + \boldsymbol{F}_{g,II}\right). \tag{2.35}$$

Mass transfer between velocity groups caused by breakup and coalescence is modelled by the source terms S_j and $\boldsymbol{S}_{M,j}$ in Eqs. (2.19) and (2.20) respectively.

The total mass source for all velocity groups is equal to zero due to the mass conservation, i.e.:

$$S_I + S_{II} = 0. \tag{2.36}$$

The momentum source, $\boldsymbol{S}_{M,j}$, in Eq. (2.20) is calculated according to the default upwind scheme, which means that the interphase mass flux is assumed to have the velocity of the outgoing phase [59]. Therefore, they are given as:

$$\boldsymbol{S}_{M,I} = \max\left(S_I,\ 0\right) \boldsymbol{U}_{g,II} - \max\left(S_{II},\ 0\right) \boldsymbol{U}_{g,I}, \tag{2.37}$$

and

$$\boldsymbol{S}_{M,II} = \max\left(S_{II},\ 0\right) \boldsymbol{U}_{g,I} - \max\left(S_I,\ 0\right) \boldsymbol{U}_{g,II}. \tag{2.38}$$

The mass source term, S_j, in Eq. (2.19) for a velocity group is equal to the sum of that for all size groups that belong to it, i.e.:

$$S_I = \sum_{k=1}^{m_I} S_k, \quad S_{II} = \sum_{k=m_I+1}^{m_I+m_{II}} S_k. \tag{2.39}$$

2.3.4 Closure models for adiabatic bubbly flow

Closure models are applied to model bubble break-up and coalescence, bubble interaction forces and turbulence. These models have been developed for adiabatic bubbly flow and are used for simulation of boiling flows.

Break-up and coalescence

The source term, S_k, in Eq. (2.39) denotes the mass transfer between bubble size groups due to coalescence and breakup which is expressed via the population balance equation as:

$$S_k = B_{B,k} - D_{B,k} + B_{C,k} - D_{C,k}. \tag{2.40}$$

The terms $B_{B,k}$ and $B_{C,k}$ represent the birth rates of bubbles in size group k due to breakup of bubbles of larger size and the coalescence of smaller bubbles respectively. The terms, $D_{B,k}$ and $D_{C,k}$ denote the death rates of bubbles in size group k due to breakup into smaller bubbles and coalescence with other bubbles to form a larger one. These bubble birth and death rates are depicted in Figure 2.11.

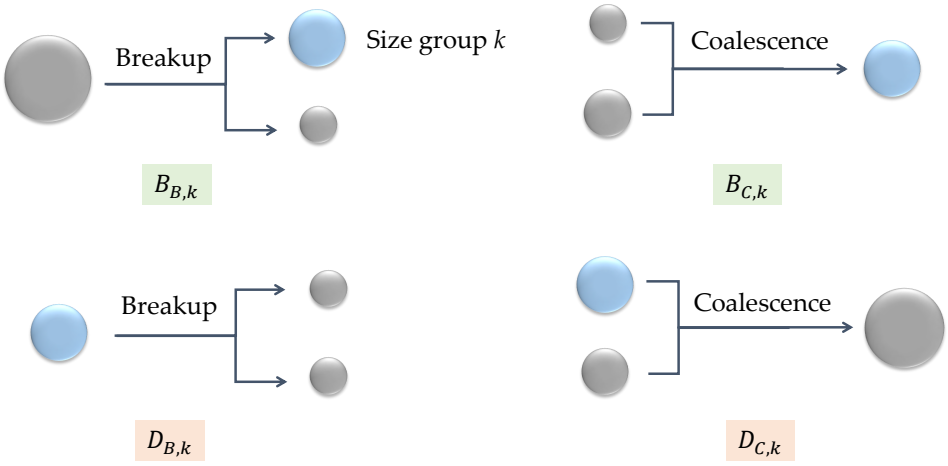

Figure 2.11: Schematic of bubble breakup and coalescence.

The birth and death rates are given as:

$$B_{B,k} = \rho_g \alpha_{g,j} \sum_{i>k} \Omega\left(m_i, m_k\right) f_i, \tag{2.41}$$

$$D_{B,k} = \rho_g \alpha_{g,j} f_k \sum_{i<k} \Omega\left(m_k, m_i\right), \tag{2.42}$$

$$B_{C,k} = \frac{1}{2}(\rho_g \alpha_{g,j})^2 \sum_{l<k} \sum_{i<k} \Gamma(m_l, m_i) X_{ilk} f_l f_i \frac{m_l + m_i}{m_l m_i}, \tag{2.43}$$

$$D_{C,k} = (\rho_g \alpha_{g,j})^2 f_k \sum_{n} \Gamma(m_k, m_i) f_i \frac{1}{m_i}, \tag{2.44}$$

with $\Omega(m_k, m_i)$ being the frequency of a bubble from size group, i breaking up into a daughter bubble in group k and its counterpart. The term $\Gamma(m_l, m_i)$ is the frequency of coalescence between two bubbles from size groups l and i respectively. The term f denotes the distribution of the size fraction of a certain velocity group calculated by Eqs. (2.13) and (2.14). The coalescence mass matrix, X_{ilk}, determines the mass fraction due to coalescence between group i and l going into group k and is given as:

$$X_{ilk} = \begin{cases} \frac{(m_l+m_i)-m_{k-1}}{m_k-m_{k-1}} & \text{if} \quad m_{k-1} < (m_l + m_i) < m_k \\ \frac{m_{k+1}-(m_i+m_l)}{m_{k+1}-m_k} & \text{if} \quad m_k < (m_l + m_i) < m_{k+1} \\ 0 & \text{Otherwise.} \end{cases} \tag{2.45}$$

The terms $\Gamma(m_l, m_i)$ and $\Omega(m_k, m_i)$ in Eqs. (2.41)-(2.44) should be provided by the coalescence and breakup models. Due to the availability of theses kernels in ANSYS CFX 18.2, the coalescence and breakup rates proposed by Prince and Blanch [60] and Luo and Svendsen [61] were adopted for the PBM source terms calculation in this thesis. In the Prince and Blanch model, it is assumed that the coalescence of two bubbles occurs at three stages [60]. First, two bubbles trap a small amount of liquid between them. Second, the trapped liquid film drains out until its thickness reaches a critical thickness. Finally, the bubbles rupture and coalesce together. Finally, the film ruptures and the bubbles coalesce together. Therefore, the coalescence kernel is modelled by a collision rate of two bubbles from size group i and j and a collision efficiency relating to the time required for coalescence. The equations of this model are given as:

$$\Gamma\left(m_i, m_j\right) = (\theta_{ij}^T + \theta_{ij}^B)\eta_{ij}, \tag{2.46}$$

$$\eta_{ij} = \exp\left(-\frac{t_{ij}}{\tau_{ij}}\right), \tag{2.47}$$

$$t_{ij} = \left(\frac{\rho_l r_{ij}^3}{16\sigma}\right)^{0.5} . \ln\left(\frac{h_0}{h_f}\right), \tag{2.48}$$

$$\tau_{ij} = \frac{r_{ij}^{\frac{2}{3}}}{\epsilon_l{}^{\frac{1}{3}}} \tag{2.49}$$

$$r_{ij} = \left(\frac{1}{2}\left(\frac{1}{r_i} + \frac{1}{r_j}\right)\right)^{-1}, \tag{2.50}$$

$$\theta_{ij}^T = F_C S_{ij}\left(\boldsymbol{u}_{ti}^2 + \boldsymbol{u}_{tj}^2\right)^{0.5}, \tag{2.51}$$

$$S_{ij} = \frac{\pi}{4}(d_i + d_j)^2, \tag{2.52}$$

$$\boldsymbol{u}_{ti} = \sqrt{2}\epsilon_l^{\frac{1}{3}} d_i^{\frac{1}{3}}, \tag{2.53}$$

$$\theta^B{}_{ij} = F_{CB} S_{ij}\left(\boldsymbol{U}_{rj} - \boldsymbol{U}_{ri}\right), \tag{2.54}$$

$$\boldsymbol{U}_{ri} = \left(\frac{2.14\sigma}{\rho_l d_i} + 0.505\boldsymbol{g} d_i \right)^{0.5}. \tag{2.55}$$

In the given equations, the terms θ_{ij}^T and θ_{ij}^B represent the turbulent and buoyancy contribution to the collision frequency with the efficiency of η_{ij}. This efficiency is modelled by comparing the time required for coalescence, t_{ij}, with the contact time during the collision, τ_{ij}. The terms h_0, h_f and r_{ij} denote the initial liquid film thickness, $h_0 = 1 \times 10^{-4}$ m, critical film thickness when rupture happens, $h_f = 1 \times 10^{-8}$ m, and the equivalent radius respectively. The cross-sectional area of the colliding bubbles and liquid eddy dissipation are given by S_{ij} and ϵ_l. The constant terms F_C and F_{CB} are coalescence and buoyancy calibration factors.

Luo and Svendsen developed a theoretical model for the breakup of drops and bubbles in turbulent suspensions based on the theory of isotropic turbulence and probability [61]. The formulations of this model are given as:

$$\Omega\left(m_i, m_j\right) = 0.923 F_B \left(1 - \alpha_g\right) \left(\frac{\epsilon_l}{d_i^2} \right)^{\frac{1}{3}} \int_{\zeta_{min}}^{1} \frac{\left(1+\zeta\right)^2}{\zeta^{\frac{11}{3}}} e^{-\aleph} d\zeta, \tag{2.56}$$

$$\aleph = \frac{12\left(f_{BV}^{\frac{2}{3}} + \left(1 - f_{BV}\right)^{\frac{2}{3}} - 1 \right)\sigma}{2\rho_l \epsilon_l^{\frac{2}{3}} d_i^{\frac{5}{3}} \zeta^{\frac{11}{3}}}, \tag{2.57}$$

$$f_{BV} = \frac{m_j}{m_i}, \tag{2.58}$$

$$\zeta_{min} = \frac{ER_{min}}{d_i}, \tag{2.59}$$

$$ER_{min} = 11.4\eta, \tag{2.60}$$

$$\eta = \left(\frac{\nu_l^3}{\epsilon_l} \right)^{0.25}. \tag{2.61}$$

In these equations, the terms σ and F_B denote surface tension and breakup calibration coefficient. The term ζ is the dimensionless size of eddies in the inertial subrange of isotropic turbulence.

After the solution of conservation Eqs. (2.19)-(2.23), an additional transport equation is solved for the determination of bubble occupation number, f_k, i.e.:

$$\frac{\partial}{\partial t}(\alpha_{g,j}\rho_{g,j}f_k) + \nabla.(\alpha_{g,j}\rho_{g,j}f_k\boldsymbol{U}_{g,j}) = S_k + {S_k}^{EC}, \tag{2.62}$$

with S_k being the mass transfer due to breakup and coalescence calculated by Eq. (2.40). The term ${S_k}^{EC}$ is the mass transfer due to evaporation and condensation given in Section 2.3.5.

Interaction forces modelling

For momentum exchange, the $\boldsymbol{F}_{g,j}$ term in Eq. (2.20), the forces of drag, lift, wall lubrication and turbulent dispersion and virtual mass are taken into account. Forces exerting on bubbles in group, j, are given as:

$$\boldsymbol{F}_{g,j} = \boldsymbol{F}_{g,D,j} + \boldsymbol{F}_{g,L,j} + \boldsymbol{F}_{g,W,j} + \boldsymbol{F}_{g,TD,j} + \boldsymbol{F}_{g,VM,j}. \tag{2.63}$$

There are no neither analytical nor theoretical expressions for the forces modelling, but experimental correlations are widely employed. In the present thesis, the selection of these models was based on the definition of the Helmholtz-Zentrum Dresden-Rossendorf (HZDR) baseline model. It was mainly based on experimental data for bubbly pipe flows in bubble columns [62].

The drag force reflects the resistance caused by the relative motion of bubbles to the surrounding liquid, which is calculated according to

$$\boldsymbol{F}_{g,D,j} = -\frac{3}{4d_{SM,j}}C_{D,j}\rho_l\alpha_{g,j}|\boldsymbol{U}_{g,j} - \boldsymbol{U}_l|(\boldsymbol{U}_{g,j} - \boldsymbol{U}_l), \tag{2.64}$$

with $C_{D,j}$ being the drag force coefficient. For this coefficient calculation, the Ishii and Zuber model, which takes into account different bubble shapes was used [63]. It is given as:

$$C_{D,j} = \max\left\{C_{D,j(\text{sphere})},\ \min\left[C_{D,j(\text{ellipse})}, C_{D,j(\text{cap})}\right]\right\}, \tag{2.65}$$

$$C_{D,j(\text{sphere})} = \frac{24}{Re,j}\left(1 + 0.1Re_{g,j}^{0.687}\right), \tag{2.66}$$

$$C_{D,j(\text{ellipse})} = \frac{2}{3}\sqrt{E\ddot{o}_j}, \tag{2.67}$$

$$C_{D,j(\text{cap})} = \frac{8}{3}, \tag{2.68}$$

with $E\ddot{o}_j$ being the Eötvös number defined as:

$$E\ddot{o}_j = \frac{g(\rho_l - \rho_g)d_{SM,j}^2}{\sigma}. \tag{2.69}$$

When a bubble moves in an unbounded shear flow it experiences a force perpendicular to the direction of its motion. The momentum source corresponding to this interaction of bubbles with the shear field of the liquid phase can be calculated as:

$$\boldsymbol{F}_{g,L,j} = -C_{L,j}\rho_l\alpha_{g,j}\left(\boldsymbol{U}_{g,j} - \boldsymbol{U}_l\right) \times rot\left(\boldsymbol{U}_l\right), \tag{2.70}$$

with $C_{L,j}$ being the lift force coefficient calculated by the model of Tomiyama et al. as [64]

$$C_{L,j} = \begin{cases} \min\left[0.288\tanh\left(0.121Re_{g,j}\right), f\left(E\ddot{o}_\perp\right)\right] & E\ddot{o}_{\perp,j} < 4 \\ f\left(E\ddot{o}_\perp\right) & 4 < E\ddot{o}_{\perp,j} < 10 \\ -0.27 & E\ddot{o}_{\perp,j} > 10, \end{cases} \tag{2.71}$$

$$f\left(E\ddot{o}_{\perp,j}\right) = 0.00105E\ddot{o}_{\perp,j}^3 - 0.0159E\ddot{o}_{\perp,j}^2 - 0.0204E\ddot{o}_{\perp,j} + 0.474, \tag{2.72}$$

with $E\ddot{o}_{\perp,j}$ being the modified Eötvös number given as:

$$E\ddot{o}_{\perp,j} = \frac{g\left(\rho_l - \rho_g\right)d_{\perp,j}^2}{\sigma}. \tag{2.73}$$

The $d_{\perp,j}$ term is the maximum horizontal dimension of the bubble (major axis) given as:

$$d_{\perp,j} = d_{SM,j}\sqrt[3]{1 + 0.163E\ddot{o}_j^{0.757}}. \tag{2.74}$$

According to the proposed model, the lift coefficient sign changes when the bubble deforms substantially. The bubble diameter at which the lift force coefficient changes is referred to as critical diameter, d_{cr}. Small bubbles with a diameter smaller than the d_{cr}, have a positive lift coefficient and the lift force direction is in direction of the negative velocity gradient (towards the wall). For large bubbles the lift force coefficient is opposite as shown in Figure 2.12.

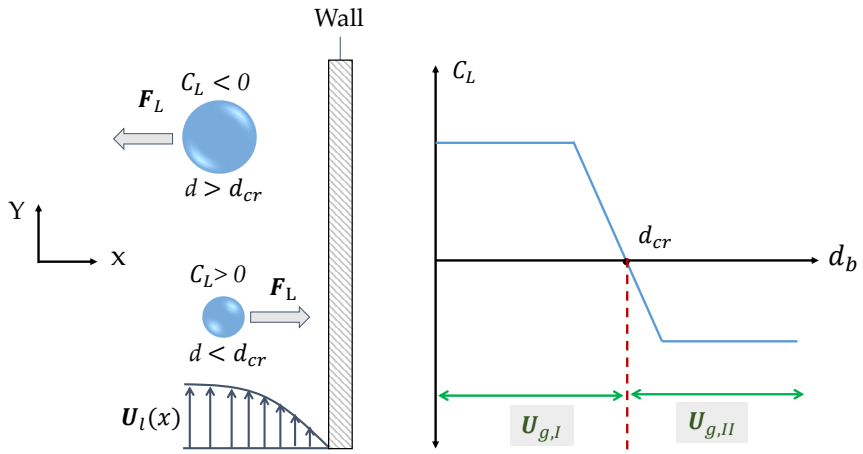

Figure 2.12: Schematic of lift force coefficient in the presence of a wall and velocity gradient.

In the bubbly upward flow in a vertical pipe, the dispersed phase is observed to concentrate in a region close to the wall, but not immediately adjacent to the wall. This effect may be modeled by the wall lubrication force, which prevents bubbles from penetrating the solid wall. For this force modelling, the model of Hosokawa et al. was employed [65]. It is given as:

$$\boldsymbol{F}_{g,W,j} = -C_{W,j}\rho_l\alpha_{g,j}\frac{2}{d_{SM,j}}|\boldsymbol{U}_{g,j} - \boldsymbol{U}_l|^2\left(\frac{d_{SM,j}}{2x}\right)^2\boldsymbol{n}_W, \tag{2.75}$$

with x and $\boldsymbol{n}_W$ being the distance to the wall and the unit normal pointing away from the wall. The wall force coefficient, $C_{W,j}$, depends on the Eötvös number and is given as:

$$C_{W,j} = 0.0217E\ddot{o}_j. \tag{2.76}$$

The turbulent dispersion force is due to the turbulent fluctuations of liquid and the interaction between bubbles and eddies. It is computed according to the Favre Average Drag (FAD) model proposed by Burns et al. as [66]:

$$\boldsymbol{F}_{g,TD,j} = -\frac{3}{4}C_{D,j}\frac{\alpha_{g,j}}{d_{SM,j}}|\boldsymbol{U}_g - \boldsymbol{U}_l|\frac{\mu_l^{turb}}{\sigma_{TD}}\left(\frac{1}{\alpha_l} + \frac{1}{\alpha_{g,j}}\right)\nabla\alpha_{g,j}, \tag{2.77}$$

with being σ_{TD} the Schmidt number and a value of 0.9 is typically used.

The virtual mass force is the inertia of the surrounding fluid that has to be taken into account when a bubble is accelerated relative to the surrounding continuous liquid phase. This force is modelled as:

$$\boldsymbol{F}_{g,VM,j} = -C_{VM}\rho_l\alpha_{g,j}\left(\frac{D\boldsymbol{U}_{g,j}}{Dt} - \frac{D\boldsymbol{U}_l}{Dt}\right), \tag{2.78}$$

with $\frac{D}{Dt}$ being the material derivatives. For the virtual mass coefficient, a value of $C_{VM} = 0.5$ is frequently used.

Turbulence modelling

A rising bubble agitates the liquid along its path and creates turbulence, which is called Bubble-Induced Turbulence (BIT). There are two approaches to account the liquid turbulence. The first one, which was proposed by Sato et al. adds an extra contribution to the effective viscosity [67]. Another approach is using the Shear Stress Transport (SST) $k-\omega$ model with additional bubble induced source terms. This approach considers the $k-\omega$ model for near the wall region and the $k-\epsilon$ one for the bulk flow [68, 69]. The conservation equations for k and ω including the BIT source terms are given as [62]:

$$\begin{aligned}\frac{\partial}{\partial t}\left(\alpha_l\rho_l k_l\right) + \nabla\left(\alpha_l\rho_l\boldsymbol{U}_l k_l\right) =& \nabla\left(\alpha_l\left(\mu_l + \frac{\mu_{tl}}{\sigma_k}\right)\nabla k_l\right) \\ &+\alpha_l\left(P_k - \rho_l\acute{\beta}\omega_l\right) + P_k^{\gamma} + S_l^k,\end{aligned} \tag{2.79}$$

$$\begin{aligned}&\frac{\partial}{\partial t}\left(\alpha_l\rho_l\omega_l\right) + \nabla\left(\alpha_l\rho_l\boldsymbol{U}_l\omega_l\right) = \nabla\left(\alpha_l\left(\mu + \frac{\mu_{tl}}{\sigma_\omega}\right)\nabla\omega_l\right) \\ &+2\alpha_l\rho_l\left(1-F_1\right)\frac{1}{\acute{\sigma}_\omega\omega_l}\nabla\omega_l\nabla k_l + \alpha_l\left(\frac{A\omega_l P_k}{k_l} - \beta\rho_l\omega_l^2\right) + P_\omega^{\gamma} + S_l^{\omega},\end{aligned} \tag{2.80}$$

with constant parameters,

$$\acute{\beta} = 0.09, \quad \beta = 0.075, \quad \sigma_k = 1, \quad \sigma_\omega = 2 \quad A = \frac{5}{9}, \quad \acute{\sigma}_\omega = \frac{1}{0.856}. \tag{2.81}$$

The term μ_{tl} is turbulent viscosity which is linked to the turbulence kinetic energy and turbulent frequency via the equation as:

$$\mu_{tl} = \frac{\rho_l k_l}{\omega_l}. \tag{2.82}$$

The term P_k is the turbulence generated due to the viscous force and is determined as:

$$P_k = \mu_{tl} \nabla \boldsymbol{U}_l . \left(\nabla \boldsymbol{U}_l + \nabla \boldsymbol{U}_l^T \right) - \frac{2}{3} \nabla . \boldsymbol{U}_l \left(3 \mu_{tl} \nabla . \boldsymbol{U}_l + \rho_l k_l \right) . \tag{2.83}$$

The source terms P_k^γ and P_ω^γ represent the buoyancy production turbulence which are defined as:

$$P_k^\gamma = - \frac{\mu_t \boldsymbol{g}_i}{\rho_l} . \nabla \rho_l, \tag{2.84}$$

$$P_\omega^\gamma = \frac{\omega_l}{k_l} \left[(A+1) \max(0, P_k^\gamma) - P_k^\gamma \right] . \tag{2.85}$$

In Eq. (2.80), the blending function, F_1, is defined as:

$$F_1 = \tanh \left(arg_1^4 \right) , \tag{2.86}$$

$$arg_1 = \min \left[\max \left(\frac{\sqrt{k_l}}{\acute{\beta} \omega_l x} , \frac{500 \nu_l}{x^2 \omega_l} \right) , \frac{4 \alpha_l k_l}{C D_{k\omega} x^2} \right] , \tag{2.87}$$

$$C D_{k\omega} = \max \left(2 \alpha_l \rho_l \frac{1}{\acute{\sigma}_\omega \omega_l} \nabla \omega_l \nabla k_l , \ 1.0 \times 10^{-10} \right) , \tag{2.88}$$

with x being the distance to the wall.

For the k-source, S_l^k, it is assumed that all energy lost by the bubble due to drag is converted into turbulence kinetic energy of the liquid in the wake of the bubble. Hence, it is calculated as:

$$S_l^k = \sum_{j=I}^{II} \left| \boldsymbol{F}_{g,D,j} \cdot \left(\boldsymbol{U}_{g,j} - \boldsymbol{U}_l \right) \right| , \tag{2.89}$$

with $\boldsymbol{F}_{g,D,j}$ being the drag force given by Eq. (2.64).

The ϵ-source term, S_l^ϵ, denotes the additional dissipation of turbulent kinetic energy due to the bubbles and is postulated to be proportional to the source in the k-equation divided by a time scale, τ, as:

$$S_l^\epsilon = C_{\epsilon B} \frac{S_l^k}{\tau} . \tag{2.90}$$

The term $C_{\epsilon B}$ is a constant with the value of 1 and the time scale is calculated as:

$$\tau = \frac{k_l}{\epsilon_l} . \tag{2.91}$$

The equivalent ω-source term is calculated as:

$$S_l^{\omega} = \frac{1}{C_{\mu} k_l} S_l^{\epsilon} - \frac{\omega_l}{k_l} S_l^{k}. \tag{2.92}$$

For vapor bubbles, a dispersed phase zero equation model is generally used. The turbulent viscosity of the vapor phase as a function of the turbulent viscosity of the continuous liquid phase is modelled as:

$$\mu_g = \frac{\rho_g}{\rho_l} \frac{{\mu_l}^{turb}}{Pr_t}, \tag{2.93}$$

with Pr_t being the turbulent Prandtl number relating the dispersed phase kinematic eddy viscosity to the continuous phase kinematic eddy viscosity which is considered $Pr_t = 1$ by default.

2.3.5 Phase transfer models

In addition to break-up and coalescence, direct mass transfer between bubbles and liquid due to evaporation and condensation changes the bubble size and consequently the size group. According to Lucas et al. [70] the total source term in the continuity equation, S_k^{EC}, due to evaporation ($\dot{m}_{l\leftrightarrow g} > 0$) and condensation ($\dot{m}_{l\leftrightarrow g} < 0$) is given as:

$$S_k^{EC} = \begin{cases} \frac{m_k}{m_k - m_{k-1}} \dot{m}_{l\leftrightarrow g,k} - \frac{m_k}{m_{k+1} - m_k} \dot{m}_{l\leftrightarrow g,k+1} & \text{for condensation} \\ \frac{m_k}{m_k - m_{k-1}} \dot{m}_{l\leftrightarrow g,k-1} - \frac{m_k}{m_{k+1} - m_k} \dot{m}_{l\leftrightarrow g,k} & \text{for evaporation,} \end{cases} \tag{2.94}$$

with $m_k = \frac{\rho_g \pi d_k^3}{6}$ being the mass of each bubble in k size group. The volumetric condensation and evaporation mass transfer rate of size group k, $\dot{m}_{l\leftrightarrow g,k}$, is given as:

$$\dot{m}_{l\leftrightarrow g,k} = f_k \frac{d_{SM,j}}{d_k} \dot{m}_{l\leftrightarrow g,j}, \tag{2.95}$$

with $j = I$ or II depending on which velocity group the bubble group k belongs to and $\dot{m}_{l\leftrightarrow g,j}$ is calculated by Eq. (2.24).

2.3.6 The Rensselaer Polytechnic Institute (RPI) wall boiling model

A number of wall boiling models have been developed to describe the phase-change process at the heating wall as well as the partitioning of the wall heat flux between the liquid and vapor phases. Among them, the RPI model developed by Kural and

Podowski [71] and adapted by Judd and Hwang [72] has been widely employed in CFD codes [73, 74]. In essence, this model entails the partitioning of applied wall heat flux into three components. They are: the heat fluxes owing to single-phase convection, Q_c, the evaporation heat flux, Q_e, and transient conduction due to quenching, Q_q, as shown in Figure 2.13a. The wall heat flux can be written as:

$$Q_w = Q_c + Q_e + Q_q. \tag{2.96}$$

This model divides the whole heating wall surface into two fractions: a fraction, which is influenced by the formed vapor bubbles on the wall, A_q, and the remaining wall surface, $1 - A_q$ as shown in Figure 2.13.

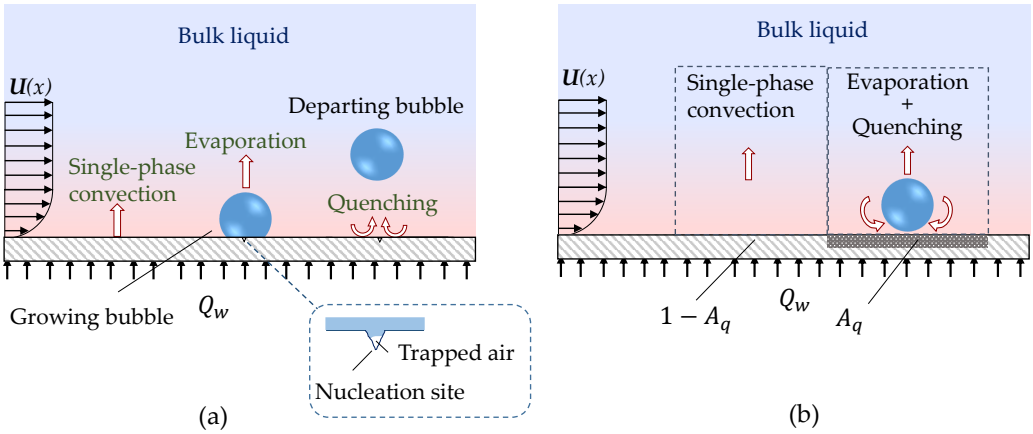

Figure 2.13: Schematic of a) heat transfer mechanisms in the RPI wall boiling model b) bubble influence area fraction.

The term Q_c in Eq. (2.96) is given as:

$$Q_c = (1 - A_q)\, h_{c,l}\, (T_w - T_l)\,, \tag{2.97}$$

with T_l being the liquid temperature adjacent to the heating wall and $h_{c,l}$ is the liquid heat transfer coefficient given as:

$$h_{c,l} = \frac{\rho_l C_{p,l} \boldsymbol{U}_\tau}{T_l^+}. \tag{2.98}$$

The term T_l^+ is the temperature wall function calculated by Kader's model [75] and $\boldsymbol{U}_\tau$ is the friction velocity given as:

$$\boldsymbol{U}_\tau = \sqrt{\frac{\boldsymbol{\tau}_w}{\rho}}, \tag{2.99}$$

with $\boldsymbol{\tau}_w$ being the wall shear stress.

The evaporation heat flux in Eq. (2.96), Q_e, can be calculated as:

$$Q_e = \dot{m}_g \left(h_{g,sat} - h_l \right), \tag{2.100}$$

with $h_{g,sat}$ and h_l being the specific enthalpies of the saturated vapor and subcooled liquid. The term $\dot{m}_g$ denotes the generated vapor mass at the heating wall and is expressed in terms of bubble departure diameter, d_d, bubble generation frequency, fr, and nucleation site density, N, as:

$$\dot{m}_g = \rho_g \frac{\pi}{6} d_d^3 fr N. \tag{2.101}$$

The quenching heat flux in Eq. (2.96), Q_q, is determined through the correlation as:

$$Q_q = \frac{2fr}{\sqrt{\pi}} \sqrt{\rho_l \lambda_l C_{pl} t_w} \;\; A_q \left(T_w - T_l \right), \tag{2.102}$$

with t_w being the bubble waiting time and is given by a simple assumption of Kural and Podowski [71]. It takes a fixed fraction of bubble departure period as:

$$t_w = \frac{0.8}{fr}. \tag{2.103}$$

The bubble influence area fraction in Eq. (2.102), A_q, is given in terms of d_d and N as:

$$A_q = \left(K \frac{\pi d_d}{2} \right)^2 N, \tag{2.104}$$

with K being the empirical constant used to account for the area of the heating wall influenced by the vapor bubbles and the value of $K = 2$ is often recommended [71]. However, Kenning specified ranging between 2 and 5 for it [76]. Judd and Hwang ascertained the value of $K = 1.8$ based on their experimental data [72].

In order to determine each term of the right-hand side of Eq. (2.96) an iterative procedure is normally employed to evaluate the wall superheat that fulfills the applied wall heat flux [56]. This algorithm starts with a guess of the wall superheat and then each component of the heat flux is calculated. The difference between the actual and the computed total applied wall heat flux provides a new wall superheat estimation for the next iteration procedure. The iteration continues until the difference between the applied and calculated wall heat flux falls below a predetermined value [56]. For the modelling of N, d_d and fr many empirical correlations have been proposed. Some of the most employed ones are summarized in Table 2.3, Table 2.4 and Table 2.5.

Table 2.3: Proposed correlations for nucleation site density, N.

Reference	**Correlation**
Gaertner [77]	$N = Q_w^{\frac{1}{m}}\ ,\ m = 0.48$
Kirby and Westwater [78]	$N = Q_w^{\frac{1}{m}}, m = 0.73$ for glass
	and $0.48 < m < 1$ for metal.
Lemmert and Chawla [79]	$N = N_{ref}\left(\frac{\Delta T_{sup}}{\Delta T_{ref}}\right)^m,$
	$N_{ref} = 7.94 \times 10^{+5}\ \mathrm{m}^{-2},\ m = 1.805.$
Kocamustafaogullari and Ishii [80]	$N = \frac{1}{d_l^2}\left[\frac{2\sigma T_{sat}}{\Delta T_{eff}\rho_g H_{lg}}\right]^{-4.4} f\left(\rho^*\right),$
	$\rho^* = \frac{(\rho_l - \rho_g)}{\rho_g},$
	$f\left(\rho^*\right) = 2.157 \times 10^{-7}(\rho^*)^{-3.2}(1 + 0.0049\rho^*)^{4.13}.$
Basu et al. [81]	$N = 0.34 \times 10^{+4}\left(1 - \cos\theta_b\right)\left(\Delta T_{sup}\right)^2,$
	$\Delta T_{ONB} < \Delta T_{sup} < 15\ \mathrm{K},$
	$N = 0.34 \times 10^{-1}\left(1 - \cos\theta_b\right)\left(\Delta T_{sup}\right)^{5.3},$
	$\Delta T_{sup} \geq 15\ \mathrm{K}.$

Table 2.4: Proposed correlations for bubble departure diameter, d_d.

Reference	**Correlation**
Fritz [24]	$d_d = 0.0208\theta_b\left(\frac{\sigma}{g(\rho_l-\rho_g)}\right)^{0.5}$
Zuber [82]	$d_d = \left(\frac{6\sigma}{g(\rho_l-\rho_g)}\frac{K\Delta T_{sup}}{Q_w}\right)^{\frac{1}{3}}$
Chi-Yeh and Griffth [83]	$d_d = 0.843\theta_b\left(\frac{\sigma}{g(\rho_l-\rho_g)}\right)^{0.5}$
Tolubinsky and Kostanchuk [26]	$d_d = \min\left(d_{ref}.\exp(-\frac{\Delta T_{sub}}{\Delta T_{ref}}),\ d_{max}\right),$
	$d_{ref} = 0.6$ mm , $\Delta T_{ref} = 45$ K,
	$d_{max} = 1.4$ mm.
Farajisarir [84]	$d_d = 10.02 \times 10^{+9} Ja^{-1.65} T^{*-1.65},$
	$T^* = \frac{T_w - T_b}{\Delta T_{sub}}.$

Table 2.5: Proposed correlations for bubble generation frequency, fr.

Reference	**Correlation**
Cole [85]	$fr = \left[\frac{4g(\rho_l-\rho_g)}{3d_d\rho_l}\right]^{0.5}$
Zuber [82]	$fr = \frac{1.18}{2d_d}\left[\frac{\sigma g(\rho_l-\rho_g)}{\rho_l^2}\right]^{0.25}$
Stephan [86]	$fr = \frac{1}{\pi}\sqrt{\frac{g}{2d_d}}\left[1+\frac{4\sigma}{d_l^2\rho g}\right]^{0.5}$
Kocamustafaogullari and Ishii [87]	$fr = \frac{1.18}{d_d}\left[\frac{\sigma g(\rho_l-\rho_g)}{\rho_l^2}\right]^{0.25}$

These correlations have been calibrated for different operating conditions. For example, Krepper et al. [88] employed the Tolubinsky and Kostanchuk [26] model for bubble departure diameter for simulation of DEBORA experiments [89]. They [88] calibrated the bubble reference diameter, d_{ref}, in the model of Tolubinsky and Kostanchuk [26] using 0.24 mm and 0.35 mm for DEBORA1-2 and DEBORA3-7 respectively. They [88] also used the model of Lemmert and Chawla [79] for nucleation site density modelling with the values of $N_{ref} = 3 \times 10^{+7}$ m^{-2} and $5 \times 10^{+6}$ m^{-2} for DEBORA1-2 and DEBORA3-7 respectively. More calibration of these parameters for different operating conditions can be found in [90, 91].

2.4 Flow boiling transition patterns in vertical pipes

In flow boiling applications, a wide range of interfacial scales between phases simultaneously occurs. The local hydrodynamic and heat transfer rate is related to the distribution of liquid and vapor phases, referred to as flow patterns or morphologies. The two-phase flow in a vertical heating pipe depicts different flow boiling regimes, depending on the void fraction and phases' velocities. Flow morphologies during upward flow boiling in a vertical heating pipe is shown in Figure 2.14.

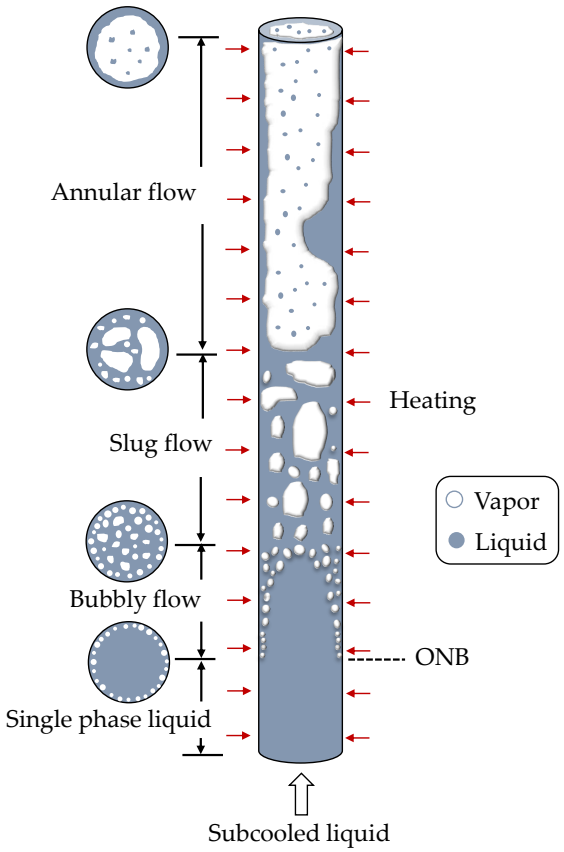

Figure 2.14: Flow boiling regimes in a vertical heating pipe.

A subcooled liquid flow enters the pipe from below and there is a single-phase convection as long as the liquid temperature near the heating wall stays below the ONB temperature. The ONB point refers to the primary formation of bubbles at the heating wall as shown in Figure 2.14. At the beginning, bubbles leave the heating wall and condense in the bulk since the bulk liquid temperature is below its saturation one. That is, they heat the subcooled liquid. Further along the pipe, the bulk liquid approaches the saturation temperature resulting in void fraction increases and bubbles agglomerate into larger slugs and plugs. These slugs may occupy nearly the whole pipe cross-section leaving only a thin liquid film on the heating wall. Further

increase in void fraction develops annular flow in which the vapor phase accelerates and forms a "chimney" with a continuous liquid film on the heating wall. The liquid film thickness usually varies with time and the continuous steam core may contain entrained liquid droplets and their evaporation provides a rather high heat transfer coefficient. In some cases, the annular flow regime is considered as a desired and specifically stable regime for heat transfer applications with high fluid velocity and steam quality. However, after some distance, the gradual depletion of liquid film due to the evaporation may cause dryout. At this liquid deficient point, the wall temperature sharply rises to dissipate the applied heat flux.

In order to determine these flow patterns, many flow regime maps have been developed based on the absolute or dimensionless mass flow rates of the gas and liquid phases. However, most such maps were presented for adiabatic two-phase flow [92, 93] and it can not be accurate for extrapolation to diabatic flow. Cheng et al. did a thorough review about the fundamentals and applications of flow pattern maps [93]. In general, different flow regime maps were developed depending on the operating conditions [94]. Thus, there is no universal flow regime map for all flow boiling problems. Besides the flow-patterns map, many numerical studies have been utilized for the flow boiling patterns modelling. Among them, the E-E two-fluid model has been extensively used to describe small-scale dispersed flows such as droplets and bubbles [95]. However, due to the averaging probability of each phase in time and space when their length scales are smaller than the grid cell size, the information about gas-liquid interface structure gets lost. Another model, so-called Volume of Fluid (VOF), has been introduced for the flow patterns modelling. However, this model is applicable for interfacial length scales several times larger than the grid size and requires phase-resolving approaches, with yet large computational costs [96]. Selecting the suitable CFD method for flow patterns modelling depends on its ability to resolve the wide range of interfacial scales between phases as illustrated in Figure 2.14 [97]. Cerne et al. coupled an interface-capturing model to the VOF method in order to deal with these multi-scale flow patterns and to eliminate the modelling restriction imposed by the grid density [98]. They defined a criterion according to the estimation of the local interface dispersion in each cell to switch between various models to simulate the Rayleigh-Taylor instability and a vortex flow [98]. Their modelling revealed a successful switch from the VOF model for initially stratified flow to the fully dispersed two-fluid model. Nevertheless, the reverse scheme for switching from the dispersed two-fluid model to the VOF model was not investigated.

Tomiyama and Shimada developed an $(N+2)$-field model including two continuous gas and liquid phases and N dispersed bubble fields [99]. They also combined a level-set approach for the interface capturing model and a multi-field

method for bubbly flow modelling [99]. Nevertheless, they employed a one-field formulation for the mixture velocity and an adjustable spatial resolution to the desired scale [99]. Maekawa et al. developed the $(N+2)$-field model for poly-dispersed bubble plumes modelling without considering bubble coalescence and break-up in their calculations [100]. Yan and Che introduced a model based on coupling the two-fluid model for the simulation of gas-liquid flow and the VOF method [101]. Their computational domain included liquid phase, large-length-scale-interface, small-length-scale-interface and a treatment called "Volume Fraction Redistribution", which was introduced for the momentum exchange modelling in the grid cells occupied by these three phases [101]. However, they only applied the coalescence of the small-scale-interface to the large one without considering the large-scale break-up to the small-scale [101].

The Standard Free Surface (SFS) is another model for simulation of flow morphologies in the E-E two-fluid framework [102]. In this model, liquid and gas are treated as two continuous phases and an advection discretization scheme is applied to the volume fraction equation [103]. Moonesi et al. used this model for simulation of flow morphologies (annular and stratified flows) occurring during high-pressure steam condensation in inclined pipes [104].

Höhne and Vallée proposed the Algebraic Interfacial Area Density (AIAD) model to distinguish between bubbles, droplets and the free surface based on the liquid volume fraction value in the computational domain [105]. This model allows the corresponding switching between these morphologies via a blending function and defines different IAD and momentum transfer models depending on the local flow morphologies. The AIAD has been widely employed for the detection of interfacial structures in different two-phase flows types such as stratified gas-liquid and counter-current flows [106, 107].

In 2012, Hänsch et al. introduced a new two-phase flow strategy, the so-called GENTOP, for the modelling of flow patterns transitions including the segregated and dispersed flow structures [27]. The GENTOP concept was mainly developed based on the extension of the iMUSIG model by adding an additional continuous gas phase to the computational domain in the E-E framework. They compared the simulation results obtained from the GENTOP concept with the experimental data for two test cases: the impingement of a liquid jet on a free surface and a vertical bubble column, which include a wide range of bubble sizes [27]. In 2014, Montoya et al. employed the GENTOP for modelling the flow patterns in an adiabatic co-current vertical gas-water pipe and compared with experimental data [108]. In 2017, Höhne et al. coupled the GENTOP and the conventional RPI wall boiling models for simulation of flow boiling morphologies in a vertical heating pipe [109]. Their simulation included evaporation, condensation, coalescence, break-up and

the small steam bubbles were handled as dispersed phases while the large interface structures were statistically resolved. However, they did not consider entrainment between dispersed bubbles and continuous gas structures.

2.5 The GENeralized TwO-Phase flow (GENTOP) concept

The GENTOP concept is defined based on the iMUSIG model in the E-E framework. The dispersed bubbles (GasD) is divided into two velocity groups based on the iMUSIG model [88]. One velocity group for small bubbles (GasD1) ($d < d_{cr}$) and one for large ones (GasD2) ($d > d_{cr}$) as shown in Figure 2.15. The exchange terms between GasD and liquid are modelled in the E-E two-fluid framework as described in Section 2.3.1. Then, a continuous gas (GasC) phase is added, i.e., the fluid flow domain is divided into phases including GasD, GasC and continuous liquid. The GasC velocity group includes only one size fraction and represents all gas structures larger than the maximum diameter of GasD, $d_{dg,max}$. This maximum diameter has to be selected according to the grid size using $d_{dg,max} = Z\Delta x$. The gas-liquid interface can be resolved only if the GasC structures occupy several grid cells and for this reason, $z = 5$ was recommended [109]. Moreover, the mass transfer between GasD and GasC is modelled based on the PBM described in Section 2.3.2.

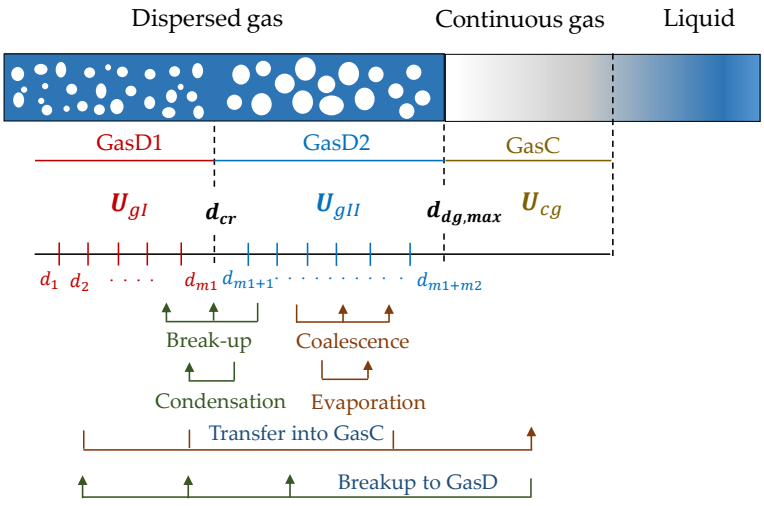

Figure 2.15: Schematic of extended iMUSIG model in GENTOP including phase transfers.

2.5.1 Treatment of the continuous gas

Large interfaces can be established between GasC and liquid phases and have to be localized in order to model the interface and interfacial mass and momentum exchanges. In the past, due to the lack of appropriate models, the developed correlations for 1D codes were mostly used to model the interfacial momentum transfer at the free surface, which do not properly reflect the physics of the phenomena. In the two-fluid approach, the detection of interfacial structure can only be determined by limited local information like void fraction, IAD or void fraction gradients [95]. An appropriate interface blending function based on the volume fraction gradient can realise the algebraic identification of the local interfacial structure. The GENTOP concept uses this function, ψ_{surf}, based on the volume fraction gradient of GasC, $|\nabla\alpha_{cg}|$, to detect the interface. The variation of $\nabla\alpha_{cg}$ from 0 to 1 over the number of n grid cells with the size of Δx which leads to the critical value of $|\nabla\alpha_{cg}|_{\text{crit}} = \frac{1}{n\Delta x}$ allows the interface definition [27]. One issue in the GENTOP concept is that the GasC may locally occur with low void fraction, e.g. in cases where GasC is generated out of GasD by coalescence. The ψ_{surf} function is given as [109]:

$$\psi_{surf} = \varphi_{surf}\left(f_b - f_d\right), \tag{2.105}$$

which reveals the information about the morphology by:

$$\psi_{surf} = \begin{cases} 1 & \text{Bubble region} \\ 0 & \text{Inteface} \\ -1 & \text{Droplet region.} \end{cases} \tag{2.106}$$

2.5.2 The Algebraic Interfacial Area Density (AIAD) model

The AIAD model provides the blending functions given in Eq. (2.105) for the bubbly regime, f_b, and droplet, f_d, as [109]:

$$f_b = \frac{1}{2}\left[1 + \cos(\pi\frac{\widetilde{\alpha^G} - (\alpha_{b,crit} - \delta_\alpha)}{2\delta_\alpha})\right], \tag{2.107}$$

$$f_d = \frac{1}{2}\left[1 + \cos(\pi\frac{\widetilde{\alpha^L} - (\alpha_{d,crit} - \delta_\alpha)}{2\delta_\alpha})\right]. \tag{2.108}$$

The terms $\widetilde{\alpha^G}$ and $\widetilde{\alpha^L}$ are defined as:

$$\widetilde{\alpha^G} = \min\left(\max\left[\alpha_{cg},\ \alpha_{b,crit} - \delta_\alpha\right],\ \alpha_{b,crit} + \delta_\alpha\right), \tag{2.109}$$

$$\widetilde{\alpha^L} = \min\left(\max\left[\alpha_l,\ \alpha_{d,crit} - \delta_\alpha\right],\ \alpha_{d,crit} + \delta_\alpha\right), \tag{2.110}$$

with α_{cg} and α_l being the GasC and liquid volume fraction. The critical gas phase fraction of the bubbles at the transition area, $\alpha_{b,crit}$, the critical liquid void fraction of the droplets at the transition area, $\alpha_{d,crit}$, and δ_α are given 0.3, 0.3 and 0.05 respectively [110]. The interface blending function, φ_{surf}, in Eq. (2.105) is calculated as [110]:

$$\varphi_{surf} = \frac{1}{2}\left[1 + \cos(\pi \frac{\widetilde{\nabla\alpha_{cg}} - (\nabla\alpha_{cg,crit} - \delta_\nabla)}{2\delta_\nabla})\right]. \tag{2.111}$$

Similar to f_b and f_d blending functions, the transition range of the void fraction gradient is $[\nabla\alpha_{cg,crit} - \delta_\nabla, \nabla\alpha_{cg,crit} + \delta_\nabla]$, where $\nabla\alpha_{cg,crit}$ denotes the value of critical void fraction gradient defined as $\frac{1}{n\Delta x}$, $n \geq 5$ [110]. Therefore, the term $\widetilde{\nabla\alpha_{cg}}$ is given as:

$$\widetilde{\nabla\alpha_{cg}} = \min\left(\max\left[|\nabla\alpha_{cg}|,\ \nabla\alpha_{cg,crit} - \delta_\nabla\right],\ \nabla\alpha_{cg,crit} + \delta_\nabla\right), \tag{2.112}$$

with δ_∇ being δ_∇=$0.1 \times \nabla\alpha_{cg,crit}$ [110].

2.6 Interfacial transfers of continuous gas

The AIAD model detects flow morphologies and distinguishes them as bubbles, droplets or the interface through the above blending functions. The interfacial mass and momentum transfers such as drag, lift, cluster and surface tension forces are modelled accordingly. These interfacial terms will be introduced in the next sections. Based on the values of ψ_{surf} function in Eq. (2.106), the IAD, A_i, is given as [110]:

$$A_i = (1 - |\psi_{surf}|)\, A_{i,fs} + a_{sign}\, |\psi_{surf}|\, A_{i,b} + (1 - a_{sign})\, |\psi_{surf}|\, A_{i,d}, \tag{2.113}$$

with

$$a_{sign} = \begin{cases} 1 & \text{if} \quad \text{sign}\,(\psi_{surf}) = 1 \\ 0 & \text{else.} \end{cases} \tag{2.114}$$

The A_i corresponding models for three different regimes including: bubble, droplet and interface in the AIAD model are given in Table 2.6.

Table 2.6: Interfacial area density for different flow morphologies in the AIAD model [110].

Regime	IAD
Bubble	$A_{i,b} = 6\frac{\alpha_g}{d_b}$
Droplet	$A_{i,d} = 6\frac{\alpha_l}{d_{drop}}$
Interface	$A_{i,fs} = \lvert\nabla\alpha_{cg}\rvert$

2.6.1 Drag and lift forces

For the modelling of drag force coefficient, C_D, it can be given based on the values of ψ_{surf} function as [110]:

$$C_D = (1 - |\psi_{surf}|)\, C_{D,fs} + a_{sign}\, |\psi_{surf}|\, C_{D,b} + (1 - a_{sign})\, |\psi_{surf}|\, C_{D,d}. \tag{2.115}$$

Three different drag coefficients, C_D, are applied dependent on the flow regimes. For calculation of bubble drag force coefficient, $C_{D,b}$, Eq. (2.65) is used and assuming the droplets are spherical, a constant value of $C_{D,d} = 0.44$ is employed [110]. The interface drag coefficient, $C_{D,fs}$, is calculated based on the tangential fraction of the stress vector, $\boldsymbol{t}_{fs}$, at the phase boundary as:

$$C_{D,fs} = \max\left(0.01,\ \frac{\alpha_l\, |\boldsymbol{t}_{fs,l}| + \alpha_g\, |\boldsymbol{t}_{fs,g}|}{\frac{1}{2}\rho_m |\boldsymbol{U}_{slip}|^2}\right), \tag{2.116}$$

with $\boldsymbol{t}_{fs}$ being the free surface stress vector calculated by the model of Porombka and Höhne [111] as:

$$\boldsymbol{t}_{fs} = \boldsymbol{t} - (\boldsymbol{n}.\boldsymbol{t})\boldsymbol{n}, \tag{2.117}$$

with $\boldsymbol{n}$ being the unit normal vector at the interface defined as:

$$\boldsymbol{n}_k = -\frac{\nabla\alpha_k}{|\nabla\alpha_k|}, \quad k = g,\ l \tag{2.118}$$

The term $\boldsymbol{t}$ in Eq. (2.117) is the stress vector given as:

$$\boldsymbol{t} = \frac{\mu}{|\nabla\alpha|}\begin{cases} 2\frac{\partial \boldsymbol{u}}{\partial x}\frac{\partial\alpha}{\partial x} + \left(\frac{\partial \boldsymbol{u}}{\partial y} + \frac{\partial \boldsymbol{v}}{\partial x}\right)\frac{\partial\alpha}{\partial y} + \left(\frac{\partial \boldsymbol{u}}{\partial z} + \frac{\partial \boldsymbol{w}}{\partial x}\right)\frac{\partial\alpha}{\partial z} \\ \left(\frac{\partial \boldsymbol{v}}{\partial x} + \frac{\partial \boldsymbol{u}}{\partial y}\right)\frac{\partial\alpha}{\partial x} + 2\frac{\partial \boldsymbol{v}}{\partial y}\frac{\partial\alpha}{\partial y} + \left(\frac{\partial \boldsymbol{v}}{\partial z} + \frac{\partial \boldsymbol{w}}{\partial y}\right)\frac{\partial\alpha}{\partial z} \\ \left(\frac{\partial \boldsymbol{w}}{\partial x} + \frac{\partial \boldsymbol{u}}{\partial z}\right)\frac{\partial\alpha}{\partial x} + \left(\frac{\partial \boldsymbol{w}}{\partial y} + \frac{\partial \boldsymbol{v}}{\partial z}\right)\frac{\partial\alpha}{\partial y} + 2\frac{\partial \boldsymbol{w}}{\partial z}\frac{\partial\alpha}{\partial z}. \end{cases} \tag{2.119}$$

The components of $\boldsymbol{t}_{fs}$ in Eq. (2.117) are given as:

$$\begin{aligned}
\boldsymbol{t}_{fs,x} &= \boldsymbol{t}_x \left(1 - \boldsymbol{n}_x^2\right) - \boldsymbol{t}_y \boldsymbol{n}_x \boldsymbol{n}_y - \boldsymbol{t}_z \boldsymbol{n}_x \boldsymbol{n}_z \\
\boldsymbol{t}_{fs,y} &= -\boldsymbol{t}_x \boldsymbol{n}_x \boldsymbol{n}_y + \boldsymbol{t}_y \left(1 - \boldsymbol{n}_y^2\right) - \boldsymbol{t}_z \boldsymbol{n}_z \boldsymbol{n}_y \\
\boldsymbol{t}_{fs,z} &= -\boldsymbol{t}_x \boldsymbol{n}_x \boldsymbol{n}_z - \boldsymbol{t}_y \boldsymbol{n}_y \boldsymbol{n}_z + \boldsymbol{t}_z \left(1 - \boldsymbol{n}_z^2\right).
\end{aligned} \tag{2.120}$$

In Eq. (2.116) the term ρ_m is the mixture density calculated by $\rho_m = \rho_l \alpha_l + \rho_g \alpha_g$ and $\boldsymbol{U}_{slip}$ denotes the slip velocity vector given by $\boldsymbol{U}_{slip} = \boldsymbol{U}_l - \boldsymbol{U}_g$.

Montoya et al. proposed a correlation to take into account the lift force of bubbles, which are larger than the maximum diameter of GasD, $d_{dg,max}$ but still have not reached the critical void fraction ($\alpha_{cg,crit} < 0.3$) [108]. Their lift force coefficient is given as:

$$C_{L,cg} = \left(1 - \varphi_{morph}\right) . \left(-0.27\right), \tag{2.121}$$

with φ_{morph} being a blending function given as [27]:

$$\varphi_{morph} = 0.5 \times \tanh\left[100(\alpha_{cg} - \alpha_{cg,crit})\right] + 0.5. \tag{2.122}$$

2.6.2 Cluster and surface tension forces

In order to minimize the occurrence of continuous gas with low volume fraction and to counteract the smearing of the resolved interfaces by numerical diffusion, a cluster force is modelled [27]. It acts between liquid and GasC in the opposition to the liquid volume fraction gradient. It supports the transition from the dispersed into the continuous gaseous morphology by causing aggregation of the continuous gas volume fraction as well. This force is given as [109]:

$$F_{l,clust} = -F_{cg,clust} = \max(0,\ \psi_{surf})\ C_{clust} . \rho_l \nabla \alpha_l, \tag{2.123}$$

with $C_{clust} = 1$ for GENTOP application [109].

Brackbill et al. proposed a model for surface tension force [112]. For a curved surface, this force is separated into normal and tangential components as [112]:

$$\boldsymbol{F}_{surf} = \boldsymbol{F}_{surf,n} + \boldsymbol{F}_{surf,t}. \tag{2.124}$$

The normal component is given as:

$$\boldsymbol{F}_{surf,n} = -\sigma k_{int} \boldsymbol{n}, \tag{2.125}$$

with σ being the surface tension coefficient. The term k_{int} is the curvature of interface, which is calculated as:

$$k_{int} = \nabla.\boldsymbol{n}, \tag{2.126}$$

with $\boldsymbol{n}$ being the interface normal vector calculated based on the void fraction of primary phase, i.e.:

$$\boldsymbol{n} = \frac{\nabla\alpha_{cg}}{|\nabla\alpha_{cg}|}. \tag{2.127}$$

From Eqs. (2.125)-(2.127), the normal component, $\boldsymbol{F}_{surf,n}$, is given as:

$$\boldsymbol{F}_{surf,n} = -\sigma \times \nabla.\left(\frac{\nabla\alpha_{cg}}{|\nabla\alpha_{cg}|}\right) \times \frac{\nabla\alpha_{cg}}{|\nabla\alpha_{cg}|}. \tag{2.128}$$

The tangential component of surface tension force, which is known as the Marangoni effect acts exclusively when the surface tension varies along the surface [112]. It is given as:

$$\boldsymbol{F}_{surf,t} = \nabla.\sigma. \tag{2.129}$$

For a constant value of σ, the tangential component is zero and the surface tension force acts only at the normal direction of interface.

2.6.3 Complete coalescence

In the GENTOP concept, when the critical void fraction of GasC is reached, a complete gaseous mass transfer to the GasC replaces the coalescence due to the averaged coalescence model. The complete coalescence avoids that GasD is present in regions occupied by GasC with a minimum volume fraction of 0.3 [27]. The mass transfer due to the complete coalescence is given as [109]:

$$\dot{m}_{GasD\rightarrow GasC} = (1 - |\psi_{surf}|)\,\frac{\rho_g.\alpha_{GasD}}{\tau_{GasD\rightarrow GasC}}, \tag{2.130}$$

with $\tau_{GasD\rightarrow GasC}$ being the time constant to regulate the mechanism rate and was recommended $20\Delta t$ [109].

2.6.4 Entrainment modelling

Entrainment, that is carry over of gas from GasC to GasD occurs when they are in a relative motion as shown in Figure 2.16.

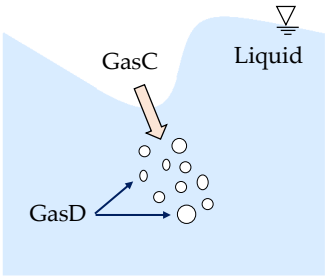

Figure 2.16: Schematic of entrainment phenomenon between GasC and GasD in the GENTOP concept.

Some models have been proposed for entrainment simulation [113, 114]. As an example, Ma et al. developed a model based on a simple argument that the turbulent kinetic energy, $k(x)$, near the liquid-gas interface with the velocity of $\boldsymbol{U}_n(x)$ causes the interface to develop air cavities [113]. The entrainment rate per unit volume and time, $\dot{m}_{Ent}$, occurs in a layer lies between the gas-liquid interface with the thickness of $\emptyset_{Ent} = C_1 a$ and is given as:

$$\dot{m}_{Ent} = (1 - |\psi_{surf}|) \frac{C_1 C_2}{\boldsymbol{g} \emptyset_{Ent}} k\,(x) \frac{\partial \boldsymbol{U}_n\,(x)}{\partial n}, \tag{2.131}$$

with C_1 being a non-dimensional constant. It is assumed that the interface is rough with the roughness of $a = \frac{C_2 k(x)}{\boldsymbol{g}}$ due to turbulence in the liquid and C_2 is the non-dimensional constant recommended to be 0.01 [115]. In the two-fluid model, the thickness of smeared interface, $\emptyset_{Ent}$, has to be determined by the user and recommended as $\emptyset_{Ent} = C_1 a = 4\Delta x$ [113–115].

2.6.5 Turbulence modelling

The effect of small waves created by Kelvin-Helmholtz instabilities on the turbulence kinetic energy of liquid phase needs to be modelled. Where the gradients of the local velocities and the liquid density are present, the specific turbulent kinetic energy is prescribed as a source term and added to the liquid total turbulent kinetic energym, k. This source term is given as [107]:

$$S_{k,SWT} = (1 - |\psi_{surf}|) \frac{2}{3} \frac{\partial \boldsymbol{U}_l}{\partial x} \rho_l k_l, \tag{2.132}$$

$$k_l = 0.5\left(q_u^2 - q_l^2\right), \tag{2.133}$$

$$q_u^2 = \frac{\pi}{24}\boldsymbol{g}_n L + \frac{\pi\sigma}{2L\rho_l}, \tag{2.134}$$

$$q_l^2 = \left(\frac{5}{3} - \frac{\pi}{2}\right)\frac{\boldsymbol{g}_n L}{125} + \frac{(\pi-2)\,\sigma}{5L\rho_l}, \tag{2.135}$$

with L being the length scale. The term $\boldsymbol{g}_n$ denotes the gravity vector defined as:

$$\boldsymbol{g}_n = \boldsymbol{g}.\boldsymbol{n}_{fs}, \tag{2.136}$$

with $\boldsymbol{n}_{fs}$ being the interface normal vector calculated as:

$$\boldsymbol{n}_{fs} = \frac{\nabla\alpha_l}{|\nabla\alpha_l|}. \tag{2.137}$$

The high-velocity gradients at the GasC and liquid interface generate levels of turbulence that are high especially in the gaseous phase when using eddy viscosity models like $k-\epsilon$ or $k-\omega$ [115]. The model of Egorov and Menter, which is based on a symmetric damping procedure, provides a solid wall-like damping of turbulence in both gas and liquid phases. It can be used for modelling the source term in the turbulence eddy frequency, ω equation as [116]:

$$S_{\omega,D} = A_i.\Delta x.\beta.\rho_l.\omega_D^2, \tag{2.138}$$

with $\beta = 0.075$ being a constant and ω_D is given as:

$$\omega_D = B.\frac{6\mu_l}{\beta.\rho_l.\Delta x^2}, \tag{2.139}$$

with $B = 100$ being a constant.

2.7 Summary

The state-of-the-art of the related topics of current research was reviewed in this chapter. First, the bubble formation mechanism in nucleate boiling and the recently developed bubble dynamics models were given. Then, CFD simulation of subcooled flow boiling using the E-E two-fluid model was provided. Afterward, the governing

equations of this model and closure models for interfacial heat, mass, and momentum transfers were given. Thereafter, the RPI wall boiling model and its closure models were reviewed. In the end, the GENTOP concept, its governing equations and application in the simulation of flow patterns transition were provided.

3 An improved bubble dynamics model for flow boiling

In this chapter, a mechanistic bubble dynamics model for flow boiling which requires no recalibration of parameters to predict the bubble growth and detachment is introduced [117]. This model is based on the force balance approach for a single growing bubble. Section 3.1.1 provides the bubble growth rate, which considers the evaporation of microlayer underneath the bubble, thermal diffusion and condensation around the bubble cap as well as dynamic inclination and contact angles. In Section 3.1.2, the force balance model for the prediction of bubble detachment is presented and Section 3.1.3 explains the bubble detachment criteria. In Section 3.1.4, the wall heat flux calculation during the formation of a single bubble for both constant heat flux and wall temperature is given. Section 3.1.5 provides the calculation of heating wall heat transfer. In Section 3.2, the discretization dependency, model validation against four experimental cases and sensitivity analysis are provided. Finally, Section 3.3 gives a short summary of this chapter.

3.1 Modelling of the bubble formation

The bubble growth is divided into two periods: the inertia-controlled and the thermal diffusion-controlled period [38]. In the inertia-controlled growth, a microlayer is formed underneath of the bubble and the bubble diameter evolution is given by a Rayleigh-type equation [41]. It is followed by the thermal diffusion-controlled growth for which the Labuntsov's model is used [40]. The evaporation of the microlayer is considered as an additional contribution of heat transfer in addition to the thermal-diffusion from the surrounding liquid. The microlayer depletion causes a dryout on the heating wall and its effect on the surface tension force will also be considered (see Section 3.1.1). During the thermal diffusion-controlled growth, the microlayer is expanded due to the expansion of the gas-liquid interface on the heating wall. The force acting on a growing bubble is taken from the work of Chen et al. [50] who developed it from the model of Klausner et al. [43] (see Section 3.1.2). Unlike the previous departure models, the bubble in the present model will not immediately depart from the heating wall when the force in perpendicular direction of the wall is balanced, but instead the formation of a bottleneck is considered. The

bottleneck connects the bubble's main body with the heating wall and enlarges until the bubble base diameter, r_w, becomes zero or the length of bottleneck becomes larger than what the internal pressure difference allows. With the occurrence of any of these conditions, the bubble lifts off (see Section 3.1.3). When the total height of the bubble (diameter of main body plus the bottleneck) becomes larger than the thermal layer thickness (Figure 3.1), condensation at the surface of the bubble occurs. For condensation, the model of Ranz and Marshall is used [57].

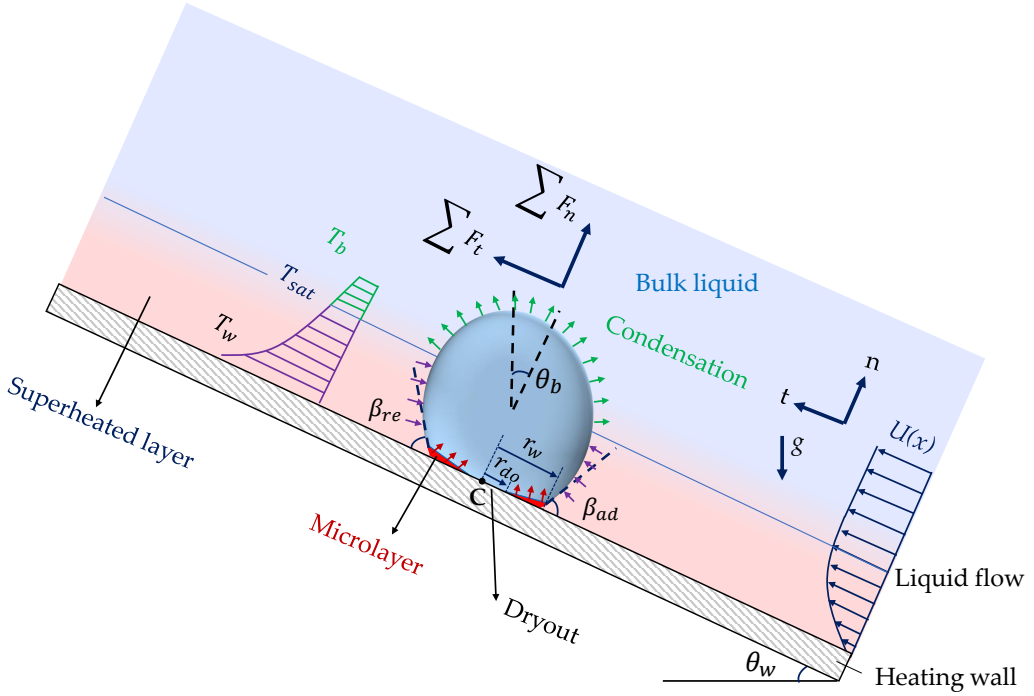

Figure 3.1: Schematic of the contributions of superheated liquid evaporation, microlayer evaporation and condensation to bubble growth during flow boiling.

The bubble starts sliding when the force in the tangential direction of the heating wall is balanced and the bubble inclination angle reaches its maximum value. This is called departure (see Section 3.1.3). Similar to the bottleneck formation that delays the bubble lift-off after the balance of forces in the perpendicular direction, the bubble inclination that comes from balanced forces in the tangential direction can also delay the bubble sliding. To calculate the expansion of the bubble base diameter, a hypothesis based on the work of Thorncroft et al. is adopted [44]. According to their hypothesis, the relation between bubble radius and bubble base radius is given as (see Section 3.1.3):

$$r_w = r_b \times \sin\beta. \tag{3.1}$$

3.1.1 Bubble growth rate

For bubble growth during flow boiling the correlations of two inertia-controlled and the thermal diffusion-controlled periods that have been proposed by Ding et al. for pool boiling are used [118]. Bubble growth in the inertia-controlled growth period is given as [38]:

$$r_b(t) = \left\{ \frac{\pi}{7} \left(\frac{T_w - T_{sat}}{T_{sat}} \right) \frac{h_{fg}\rho_g}{\rho_l} \right\}^{\frac{1}{2}} t. \tag{3.2}$$

In this model, the maximum bubble radius in the inertia-controlled period is calculated by the model of Mikic et al. as [38]:

$$r_{max,g} = \frac{B^2}{A}, \tag{3.3}$$

with B and A given by Eq. (2.4). The bubble growth rate in the thermal diffusion-controlled growth period is calculated as [117]:

$$\left.\frac{dr_b}{dt}\right|_{td} = \frac{\dot{V}_{mi,g}}{A_b} + \left.\frac{dr_b}{dt}\right|_{ma} (1 - f_{sub}), \tag{3.4}$$

with A_b being bubble surface area. The term $\dot{V}_{mi,g}$ denote the total volume of generated gas underneath of the bubble that by considering the mass balance between the generated gas and the evaporated liquid is given as [117]:

$$\dot{V}_{mi,g} = 2\frac{\rho_l}{\rho_g}\pi \int_0^{r_w} \frac{d\delta_{mi}}{dt} r dr. \tag{3.5}$$

The microlayer evaporation rate, $\frac{d\delta_{mi}}{dt}$, is given by considering the heat balance between conductive heat transfer through the microlayer with the thickness of δ_{mi} and the latent heat going into the bubble. It is given as [117]:

$$\rho_l h_{fg} \frac{d\delta_{mi}}{dt} = \frac{\lambda_l \Delta T_{sup}}{\delta_{mi}}, \tag{3.6}$$

with $\Delta T_{sup} = T_w - T_{sat}$ being the wall superheat.

Bubble growth rate due to the thermal layer in Eq. (3.4) is calculated by the model of Labuntsov as [40]:

$$\left.\frac{dr_b}{dt}\right|_{ma} = \frac{1}{2}\left[Ja \sqrt{\left(\frac{12\alpha'_l}{\pi}\right)\left[1 + \frac{1}{2}\left(\frac{\pi}{6Ja}\right)^{2/3} + \frac{\pi}{6Ja}\right]} \right] t^{-\frac{1}{2}}. \tag{3.7}$$

The contribution of condensation to the bubble growth when the bubble's height becomes larger than the thermal layer thickness is calculated by the model of Ranz and Marshal (Eq. (2.25)) [57].

According to the model of Cooper and Loyd, the initial microlayer thickness (see Figure 2.5) is given as [41]:

$$\delta_{mi}^{0}(t) = C_{mi}\sqrt{\nu_l.t} = \sqrt{C\alpha'_l.t} \qquad 0 \leq t \leq \tau_g, \tag{3.8}$$

with $C_{mi} = 0.8$ and $C = C^2{}_{mi} = 0.64 \times Pr$ and t is the time in the inertia-controlled period. The terms ν_l and τ_g are the liquid kinematic viscosity and the maximal inertia-controlled growth time which is given by the model of Zhao and Tsuruta as [119]:

$$\tau_g = C\alpha'_l \left[\frac{\rho_g h_{fg}.r_{max,g}}{2\lambda_l \Delta T_{sup}}\right]^2, \tag{3.9}$$

with $r_{max,g}$ being the maximum bubble radius in the inertia-controlled period calculated by Eq. (3.3). Zhao and Tsuruta calculated the initial microlayer thickness as [119]:

$$\delta_{mi}^{0}(r) = \frac{C\alpha'_l \rho_g h_{fg}}{2\lambda_l \Delta T_{sup}} r, \tag{3.10}$$

with r being the distance from the cavity. Recently, based on experimental observation, Utaka et al. proposed the initial microlayer thickness for water based on a linear slope to the bubble base diameter as [120]:

$$\delta_{mi}^{0}(r) = 4.46 \times 10^{-3} \times r. \tag{3.11}$$

In the thermal diffusion-controlled growth period, the microlayer will be extended with the expansion of the bubble contact base (Figure 2.6b). Therefore, it is better to adapt the formula of Cooper and Loyd [41](Eq. (3.8)) with the data of Utaka et al. [120] and a new constant $C = 0.075 \times Pr$ is given. During the inertia-controlled growth, the bubble has a semi-spherical shape and the conductive heat flux from the heating wall through the microlayer is calculated as [117]:

$$Q = \lambda_l \frac{\Delta T_{sup}}{\delta_{mi}^{0}}. \tag{3.12}$$

Based on the Eqs. (3.2)-(3.12), the bubble growth rate is given as [117]:

$$\frac{dr_b}{dt} = \begin{cases} \left\{ \frac{\pi}{7} \left(\frac{T_w - T_{sat}}{T_{sat}} \right) \frac{h_{fg}\rho_g}{\rho_l} \right\}^{\frac{1}{2}} & r \leq r_{max,g} \\ \frac{\dot{V}_{mi,g}}{A_b} + \left. \frac{dr_b}{dt} \right|_{ma} (1 - f_{sub}) - \left. \frac{dr_b}{dt} \right|_{cond} f_{sub} & r > r_{max,g}. \end{cases} \tag{3.13}$$

When the bubble radius reaches the maximum inertia-controlled bubble radius, $r_{max,g}$, the thermal diffusion-controlled growth period starts. During this period, the bubble growth is mainly caused by the evaporation of the microlayer underneath and superheated liquid around the bubble. The consumption of liquid in the microlayer determines the growth rate of the bubble during microlayer evaporation. In the present work, the effect of surface tension and inertia effect on the pressure of the bubble is neglected. In order to simplify the model, the concept of a fixed saturation thermal layer thickness, $\delta_{th,sat}$ between T_w and T_{sat} is employed (Figure 3.2). Condensation on the bubble cap starts when the height of bubble becomes larger than the saturation thermal layer thickness, $\delta_{th,sat}$ (Figure 3.2).

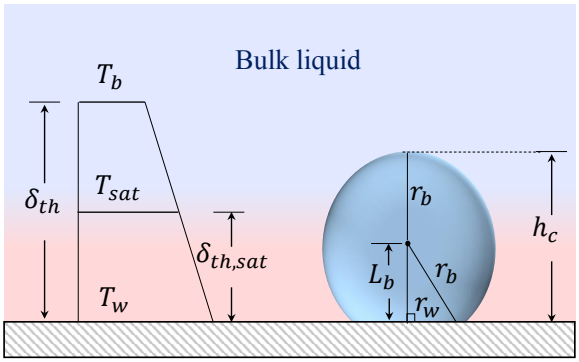

Figure 3.2: Temperature distribution in the thermal layer (left) and bubble geometry without bottleneck (right).

The total thermal layer thickness, δ_{th}, is defined as $\frac{\delta_{tl}}{\delta_{th}} = Pr^{\frac{1}{3}}$ for flow boiling [121]. Assuming a linear distribution of temperature in the thermal layer (Figure 3.2) one gets:

$$\delta_{th,sat} = \frac{T_w - T_{sat}}{T_w - T_{sub}} \delta_{th}. \tag{3.14}$$

The turbulent hydrodynamic layer thickness, δ_{tl}, which is defined when $\boldsymbol{U} = 0.99 \times \boldsymbol{U}_{max}$, can be calculated from the one-seventh power law for pipes, that is [121],

$$\frac{\boldsymbol{U}}{\boldsymbol{U}_{max}} = \left(1 - \frac{R_p - \delta_{tl}}{R_p} \right)^{\frac{1}{7}} \stackrel{\text{def}}{=} 0.99, \tag{3.15}$$

with $\boldsymbol{U}_{max}$ and R_p being the centerline velocity and the pipe's radius. The turbulent hydrodynamic layer thickness is also dependent on the distance to the inlet, that is [121],

$$\delta_{tl}\left(x\right) \cong 0.37x\left(\frac{\boldsymbol{U}_{max} \times x}{\nu_l}\right)^{-\frac{1}{5}}. \tag{3.16}$$

The height of the bubble without bottleneck (Figure 3.2) is calculated as:

$$h_c = \sqrt{r_b^2 - r_w^2} + r_b, \tag{3.17}$$

and the bubble growth velocity in the perpendicular direction is given as:

$$\boldsymbol{v}_{b,n} = \frac{dh_c}{dt}. \tag{3.18}$$

3.1.2 Force balance

The force balance analysis for a bubble growing on a superheated wall was taken from the models of Klausner et al. [43] and Chen et al. [50] as depicted in Figure 3.3.

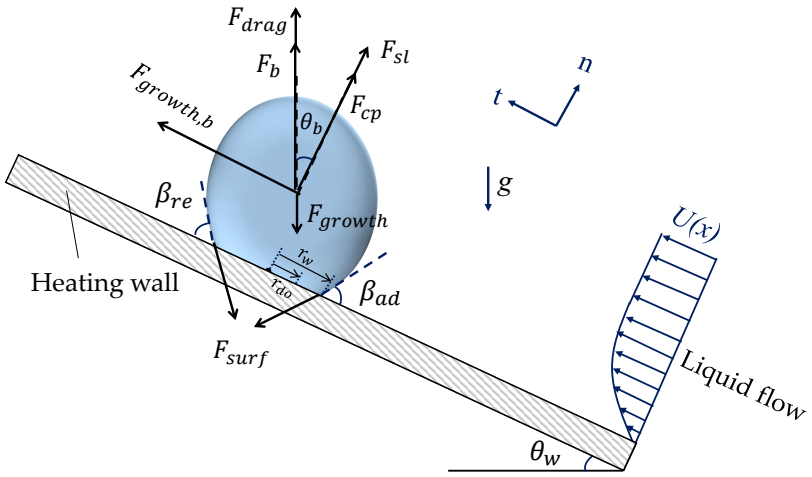

Figure 3.3: Schematic diagram of forces on a growing bubble in flow boiling.

Based on the conservation of momentum, the forces acting on the bubble in perpendicular (normal: n) and parallel (tangential: t) directions of the heating wall are balanced according to:

$$\boldsymbol{F}_{total,n} = \boldsymbol{F}_{growth,n} + \boldsymbol{F}_{drag,n} + \boldsymbol{F}_{surf,n} + \boldsymbol{F}_{b,n} + \boldsymbol{F}_{cp,n} + \boldsymbol{F}_{sl,n} \tag{3.19}$$

$$\boldsymbol{F}_{total,t} = \boldsymbol{F}_{growth,t} + \boldsymbol{F}_{drag,t} + \boldsymbol{F}_{surf,t} + \boldsymbol{F}_{b,t} + \boldsymbol{F}_{growth,b}. \tag{3.20}$$

$\boldsymbol{F}_{growth}$ is the bubble growth force, $\boldsymbol{F}_{drag}$ is the quasi-steady drag force due to the viscous fluid flow around the bubble. $\boldsymbol{F}_{cp}$ is the contact pressure force due to the effect of the heating wall and $\boldsymbol{F}_{b}$ is the buoyancy force. $\boldsymbol{F}_{sl}$ is the shear lift force resulting from the asymmetrical flow distribution in the tangential direction of the heating wall, and $\boldsymbol{F}_{surf}$ is the surface tension force due to the contact surface on the heating wall. $\boldsymbol{F}_{growth,b}$ is added mass force due to bubble growth in the bulk liquid velocity field.

The bubble growth force due to an asymmetrical growing bubble on a heating wall can be evaluated by integrating the pressure distribution over the bubble surface. It is expressed in both heating wall directions as [50]:

$$\boldsymbol{F}_{growth,n} = -\rho_l \pi {r_w}^2 \left(r_b \ddot{r}_b + \frac{3\dot{r}_b^2}{2} \right) \cos\left(\theta_b\right) \tag{3.21}$$

$$\boldsymbol{F}_{growth,t} = -\rho_l \pi {r_w}^2 \left(r_b \ddot{r}_b + \frac{3\dot{r}_b^2}{2} \right) \sin\left(\theta_b\right). \tag{3.22}$$

Due to the relative motion between liquid flow and bubble, the drag force on the bubble in perpendicular direction can be evaluated as [117]:

$$\boldsymbol{F}_{drag,n} = \frac{1}{2} \rho_l {\boldsymbol{v}_b}^2 \pi {r_b}^2 C_D, \tag{3.23}$$

with $\boldsymbol{v}_b$ being the velocity of the bubble in perpendicular direction of the heating wall. The term C_D is the drag force coefficient, which is dependent on turbulence intensity, bubble Reynolds number and bubble shape. Because of the pre-assumption of spherical bubble shape, C_D, is simplified with the models of Clift et al. [122] and Moore as [123]:

$$C_D = \frac{16}{Re_b} \left(1 + 0.15 {Re_b}^{0.5} \right). \tag{3.24}$$

The drag force in the tangential direction is calculated by the same equation as perpendicular direction. The difference is only $\boldsymbol{v}_b$ that is replaced by relative velocity $\boldsymbol{v}_{re} = \boldsymbol{v}_{sl} - \boldsymbol{v}_f$ with $\boldsymbol{v}_{sl}$ being the sliding velocity of bubble and $\boldsymbol{v}_f$ is the velocity of the supposed stream line through the mass center of the bubble. The term $\boldsymbol{v}_{sl}$ is calculated by the tangential forces applied on the bubble and $\boldsymbol{v}_f$ is computed

by the one-seventh power law of the turbulent flow. The tangential drag force is calculated as:

$$\boldsymbol{F}_{drag,t} = \frac{1}{2}\,\rho_l(v_{sl} - v_f)^2 \pi {r_b}^2 C_D. \tag{3.25}$$

The surface tension force, which originates from bubble contact with the heating wall can be expressed according to the models of Klausner et al. [43] and Chen et al. [50]. This force in the perpendicular and tangential directions of heating wall can be expressed as [50]:

$$\boldsymbol{F}_{surf,n} = -2 \times r_{do}\sigma \frac{\pi}{(\beta_{ad} - \beta_{re})} \left(\cos\beta_{re} - \cos\beta_{ad}\ \right), \tag{3.26}$$

$$\boldsymbol{F}_{surf,t} = -1.25 \times 2 \times r_{do}\sigma \frac{\pi\left(\beta_{ad} - \beta_{re}\right)}{\pi^2 - \left(\beta_{ad} - \beta_{re}\right)^2} \left(\sin\beta_{ad}\ + \sin\beta_{re}\right), \tag{3.27}$$

with σ being the surface tension. The buoyancy force acts on the bubble in the opposite direction of gravitational acceleration and it can be defined in the perpendicular and tangential direction of heating wall as [50]:

$$\boldsymbol{F}_{b,n} = \left(\rho_l - \rho_g\right)\mathbf{g} V_b \cos(\theta_w), \tag{3.28}$$

$$\boldsymbol{F}_{b,t} = \left(\rho_l - \rho_g\right)\mathbf{g} V_b \sin(\theta_w). \tag{3.29}$$

The contact pressure force, which acts only perpendicular to the heating wall is calculated by the model of Thorncroft et al. as [44]:

$$\boldsymbol{F}_{cp} = \frac{1}{2}\pi {d_w}^2 \frac{\sigma}{r_c}, \tag{3.30}$$

with r_c being the radius of curvature at the reference point and $r_c = 5 \times r_b$ was recommended by Klausner et al. [43]. The shear lift force, $\boldsymbol{F}_{sl}$, acts only in perpendicular direction of the heating wall and is partially due to Bernoulli suction and vortices in the approaching flow. It is given by the models of Van Helden et al. [124] and Chen et al. [50] as:

$$\boldsymbol{F}_{sl} = \frac{1}{2} C_{L1} \frac{0.5 d_w}{R} A \rho_l \boldsymbol{U}_c \widehat{\boldsymbol{e}}_{\boldsymbol{n}} + C_{L2}\rho_l V_b \left|\left(\boldsymbol{U}_c - \boldsymbol{U}_b\right) \times \boldsymbol{\omega}\right| \widehat{\boldsymbol{e}}_{\boldsymbol{n}}, \tag{3.31}$$

with $\boldsymbol{U}_c$ being the velocity of the supposed streamline through the mass center of the bubble. $\boldsymbol{U}_b$ is the bubble sliding velocity in the mass center and C_{L1} is a constant of Bernoulli suction, which is equal to $\frac{11}{8}$ according to the model of Van Helden et al. [124] , A is the bubble cross-section area perpendicular to the flow and V_b is the bubble volume. The term C_{L2} is an empirical constant, which was

recommended as 0.53 by Auton [125] and $\boldsymbol{\omega} = \frac{\boldsymbol{U}_{(n)}}{\boldsymbol{n}}$ is the vorticity effective only in perpendicular direction of the wall.

Chen et al. [50] and Thorncroft et al. [44] considered an additional growth force, which is referred as growth force bulk, $\boldsymbol{F}_{growth,b}$. It acts in the wall tangential direction due to bubble growth in a bulk liquid velocity field and is given as [50]:

$$\boldsymbol{F}_{growth,b} = 2\pi\rho_l {r_b}^2 \left(\boldsymbol{U}_c - \boldsymbol{U}_b\right) \dot{r}_b. \tag{3.32}$$

3.1.3 Detachment criteria

Though the bubble contact angle plays a key role in the calculation of acting forces, experimental data and reliable models are rather scarce. Mukherjee and Kandlikar proved that the contact angle does vary during the ebullition cycle and it depends on the heating wall material and liquid and vapor properties as well [126]. The contact angle is not constant even in equilibrium conditions. However, it is possible to calculate the value based on the analysis of acting forces on the bubble. Ding et al. investigated the bubble growth for horizontal pool boiling by using a mechanistic model based on the force balance and considered the dynamic contact angle and bubble base diameter [118]. In this bubble dynamics model, the dynamic deformation of the bubble is considered. At the transition from the inertia-controlled period to thermal diffusion-controlled one the contact angle is $\frac{\pi}{2}$ rad and the surface tension force is zero because the dryout radius, r_{do}, is zero (Eqs. (3.26) and (3.27)). If in this period, the mass center velocity of the bubble is larger than the expansion speed of bubble radius the bubble will detach from the surface. However, in most cases this will not happen due to the fast expansion of bubble. In this period the dryout radius, r_{do}, increases when sum of the negative forces that point toward the heating wall (mainly surface tension force and sometimes also growth force) is much higher than the sum of positive forces. The resulting net negative force leads to a deformation of the bubble and determines the contact angle and curvature. This in turn reduces the surface tension force in the negative direction until the acting forces are balanced. From the force calculation, the expected contact angle (see Figure 3.4) is given as:

$$\beta_s = 2 \times \arcsin\left(\frac{\boldsymbol{F}_{growth,n} + \boldsymbol{F}_{drag,n} + \boldsymbol{F}_{cp,n} + \boldsymbol{F}_{sl,n} + \boldsymbol{F}_{b,n}}{\boldsymbol{F}_{surf}}\right). \tag{3.33}$$

The constant 2 in this equation means that the contact angle, β, is twice the microlayer contact angle, θ, which is used to calculate the surface tension force. In this thesis, the force in perpendicular direction is considered as the dominant force that

effectively determines the contact angle. The effect of tangential forces which are influenced by roughness and wettability on the contact angle is still not clear and more investigations are needed. The expected contact angle, β_s, is changing with time due to the continued changing of forces during the bubble growth.

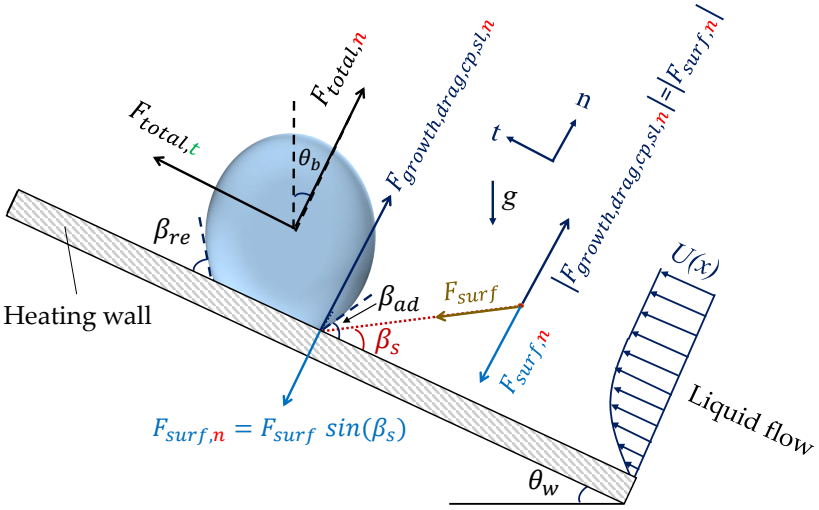

Figure 3.4: Schematic of a growing bubble on an inclined heating wall with dynamic contact angle, β, and expected contact angle, β_s, during flow boiling.

The bubble deformation causes an expansion of the base radius, r_w, so that its growth becomes different from the growth rate of the bubble radius, $\dot{r}_b$. Klausner et al. [43] considered $d_w = 0.09$ mm as being constant and later Thorncroft et al. adopted $d_w = d_b \times \sin(\beta_{re})$ with the receding side contact angle, β_{re}, to improve the modelling prediction accuracy [44].

Due to the consideration of a dynamic contact angle a correlation between the expansion rate of base radius, $\dot{r}_w$ and bubble radius, $\dot{r}_b$, instead of their fixed values is proposed. During the bubble growth, when the contact angle, β, is $\frac{\pi}{2}$ rad, the difference between $\dot{r}_w$ and $\dot{r}_b$ should be largest. Later, with decreasing β, this difference should become smaller and smaller as the value of driving force becomes smaller and smaller. The applied approach in this work is based on the work of Thorncroft et al. [44] and so the expansion rate of r_w is given as:

$$\dot{r}_w = \dot{r}_b \times \sin\left(\frac{\pi}{2} - \beta\right). \tag{3.34}$$

During the bubble deformation the contact angle, β, decreases until it becomes equal to the expected contact angle, β_s, and after that it will increase with the increase of β_s. When the net force in perpendicular direction becomes positive, the bubble starts departing and a bottleneck is formed.

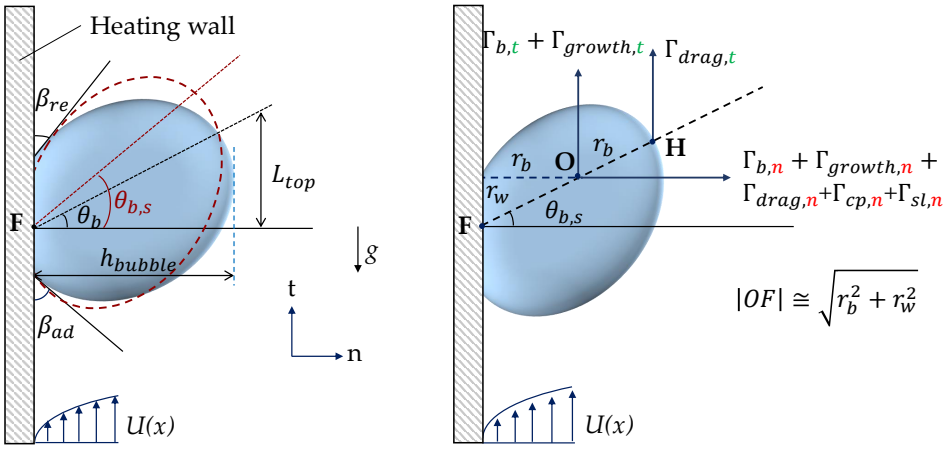

(a) (b)

Figure 3.5: a) Bubble with dynamic inclination angle, θ_b, and expected inclination angle, $\theta_{b,s}$, for an upward flow boiling in a vertical pipe b) torques due to the acting forces on the bubble.

During the bubble growth the bubble inclination angle, θ_b, is also here considered as being dynamic, depending, however, not on force but on torque (see Figure 3.5). The fulcrum of the torque is the center of the contact surface on the heating wall (point **F** in Figure 3.5) and the expected inclination angle, $\theta_{b,s}$, is calculated as:

$$\theta_{b,s} = \arctan\left(\frac{\boldsymbol{\Gamma}_{b,t} + \boldsymbol{\Gamma}_{drag,t} + \boldsymbol{\Gamma}_{growth,t}}{\boldsymbol{\Gamma}_{b,n} + \boldsymbol{\Gamma}_{drag,n} + \boldsymbol{\Gamma}_{growth,n} + \boldsymbol{\Gamma}_{cp,n} + \boldsymbol{\Gamma}_{sl,n}}\right) + \frac{\pi}{2} - \beta_w. \tag{3.35}$$

The terms $\boldsymbol{\Gamma}_b$, $\boldsymbol{\Gamma}_{growth}$, $\boldsymbol{\Gamma}_{cp}$ and $\boldsymbol{\Gamma}_{sl}$ are the torques of buoyancy, growth, contact pressure and shear lift forces that act at the mass center of the bubble (point **O** in Figure 3.5b). $\boldsymbol{\Gamma}_{drag}$ is the torque of drag force that acts at the bubble surface which contacts with the fluid and the part in contact with the heating wall. The torque is computed from the acting forces as $\boldsymbol{\Gamma}_x = \boldsymbol{F}_x \times \boldsymbol{r}_x$, where x stands for the respective type of forces/torque (see Figure 3.5b), and $\boldsymbol{r}$ is the radius vector, that is, $\boldsymbol{r} = \boldsymbol{OF}$ except for the tangential drag force/torque, for which $\boldsymbol{r} = \boldsymbol{FH}$.

The influence of surface roughness is neglected and β_w is the liquid contact angle in equilibrium state [127] (see Figure 3.6). Both horizontal and vertical forces are balanced at the contact point, which is known as equilibrium. The horizontal component of the gas-liquid surface tension force is balanced by the adhesive force and the vertical one is balanced by the difference of the forces along the heating wall as:

$$\gamma_{gl} \cos \beta_w = \gamma_{sg} - \gamma_{sl}, \tag{3.36}$$

with γ_{gl} , γ_{sg} and γ_{sl} being the interphase gas-liquid, solid-gas and solid-liquid surface tension.

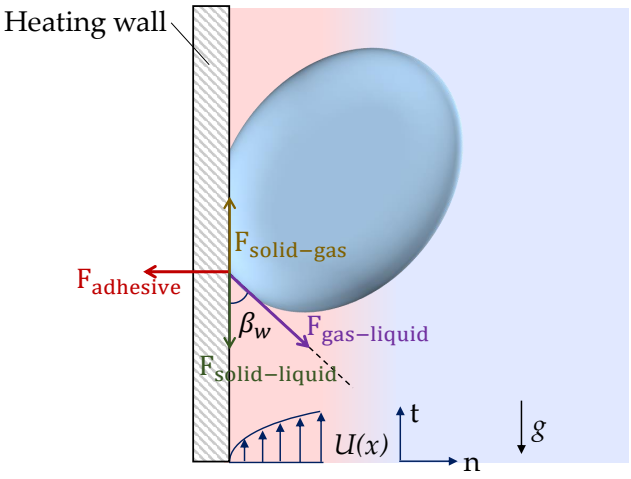

Figure 3.6: Acting forces at the contact point.

The drag force acting on the top of the bubble causes the formation of bubble inclination angle, θ_b. It is calculated by using the Newton's law with the displacement of the top part of the bubble as:

$$\theta_b = \arctan(\frac{L_{top}}{h_{bubble}}), \tag{3.37}$$

with L_{top} being the movement of the bubble top side with respect to its horizontal position and h_{bubble} is the bubble's height (see Figure 3.5a).

The bubble will not detach from the heating wall until $\theta_b \geq \theta_{b,s}$, even when the force in the tangential direction becomes positive. In this work, the calculation of advancing and receding contact angles is based on the contact angle, β, for horizontal pool boiling and an additional bubble inclination for flow boiling. As during the formation of inclination angle the bubble shape in the model is assumed to be hemispherical or perfectly spherical, the impact of buoyancy force, $\boldsymbol{F}_{b,n}$, is neglected when $\boldsymbol{F}_{b,n} < 0$, $\beta_{ad} = \beta$ and $\beta_{re} = \beta - \theta_b$, which is restricted by $\beta_{ad} \leq \frac{\pi}{2}$ rad and $\beta_{re} \geq 0$.

The contact angle changes due to the force balance and when the force in perpendicular direction, $\boldsymbol{F}_{total,n}$, becomes positive, the contact angle becomes $\frac{\pi}{2}$ rad at both sides during horizontal pool boiling, while for flow boiling it occurs only at the advancing side. The reason is the dominance of the force in perpendicular direction at both bubble's sides in horizontal pool boiling while for flow boiling it is only at the advancing one. At the same time, the bottleneck is formed due to the

microlayer evaporation and the bubble is stretched by adhesion force on the heating wall. For flow boiling, the bubble contact angle at the advancing side, β_{ad}, can also reach $\frac{\pi}{2}$ rad when the total force along the tangential direction is large enough, $\boldsymbol{F}_{total,t} > 0$.

Due to the difference between β_{ad} and β_{re}, the bubble has different base diameter expansion velocities at both bubble sides based on the Eq. (3.34). The dynamic bubble shape is considered as close to the observed physics as possible in order to avoid the case-dependent parameter tuning. The bubble starts with a hemispherical shape during the inertia-controlled growth, and then changes from hemispherical to spherical one during the thermal diffusion-controlled period. It continues with an inclined bubble to end in a sphere plus a bottleneck as depicted in Figure 3.7 and eventually after lift-off it becomes spherical. The force balance in perpendicular direction leads to the bottleneck formation. At this moment, the bubble can still be in contact with the heating wall if the velocity of bubble's main body, $\boldsymbol{v}_b$, is less than the bubble expansion velocity, which comes from the microlayer evaporation. The bottleneck formation occurs only when the bubble moves faster in perpendicular direction. When the evaporation of microlayer becomes less, the bubble base diameter (now it is that of the bottleneck) starts to shrink. Unlike in the conventional bubble dynamics model that the criterion of lift-off is the force balance in perpendicular direction, here, the bubble lifts off when the bottleneck breakage or the base diameter shrinks to zero.

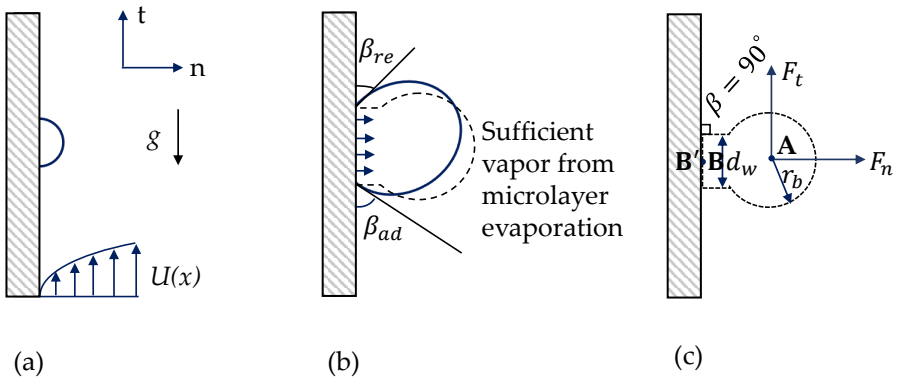

Figure 3.7: Bubble bottleneck formation in a vertical subcooled boiling flow a) bubble in the inertia-controlled growth period b) a moment after the force balance c) after bottleneck formation and before departure.

The bubble base radius, r_w, shrinks when $\boldsymbol{v}_b \pi r_w^2 > \dot{V}_{mi,g}$ and the volume conservation gives:

$$\frac{d(\pi r_w^2 h_{bt})}{dt} = \dot{V}_{mi,g} - \boldsymbol{v}_b \pi r_w^2, \tag{3.38}$$

with h_{bt} being the bottleneck's height (Figure 3.8). It is calculated from the velocity of bubble mass center, $\boldsymbol{v}_b$, and the time difference between the time when force in perpendicular direction becomes positive, t_{fp}, and the time from this moment, t as:

$$h_{bt} = \boldsymbol{v}_b(t - t_{fp}). \tag{3.39}$$

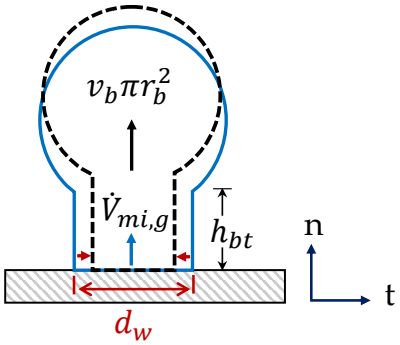

Figure 3.8: Bottleneck shrinkage after the moment of force balance in perpendicular direction.

Ding et al. claimed that in pool boiling the bottleneck breaks when the microlayer underneath the bubble is completely consumed or the pressure difference along the bottleneck reaches its limit [118]. Here also, this methodology for bottleneck breakage is applied. The required pressure to hold up the bubble on the heating wall, $P_{B'}$ differs from the pressure inside the bubble on the heating wall, P_B (Figure 3.7) which is strongly dependent on the base radius, r_w, and decreases with its shrinkage. The pressure difference is estimated as [118]:

$$\Delta P_{B'B} = 2\sigma \left(\frac{1}{r_w} - \frac{1}{r_b} \right). \tag{3.40}$$

When $\Delta P_{B'B}$ is larger than the pressure due to acting total force in the perpendicular direction on the bubble base area, that is:

$$\Delta P_{B'B} \geq \frac{|\boldsymbol{F}_{total,n}|}{A_{base}}, \tag{3.41}$$

the bubble will return back to a spherical shape and detach from the heating wall. Of course, if the bubble base radius shrinks to zero before $\Delta P_{B'B}$ reaches the limit, the bubble will also depart. The chart of bubble formation and detachment models for subcooled flow boiling is summarized in Figure 3.9.

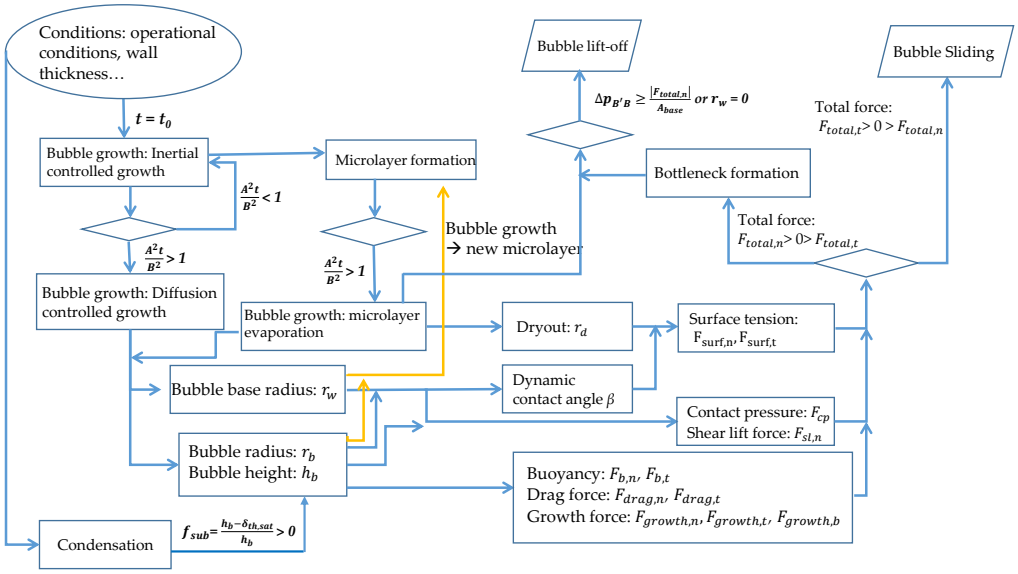

Figure 3.9: Schematics of the bubble growth model for flow boiling including sub-models.

3.1.4 Wall heat flux model

In this model, it is not necessary to calculate the heat flux as it will be calculated in the CFD simulation directly. However, it is required for validation against experimental data, for which only heat fluxes but no wall superheat are available. It is necessary to calculate the wall superheat under different heat fluxes as the bubble growth rate is strongly dependent on the wall superheat. The heat flux is divided into different terms similar to the heat-partitioning model: evaporation of microlayer (Figure 3.10a), evaporation of thermal layer (macrolayer) (Figure 3.10b), heat transfer from the heating wall to vapor in the dryout region (Figure 3.10c), quenching (Figure 3.10d) and forced-convection (Figure 3.10e). Quantitatively, it is given as:

$$Q_{out} = \left\{ \begin{array}{ll} Q_{e,mi} = \dot{m}_{mi} h_{fg} = \frac{k_l \Delta T_{sup}}{\delta_{mi}} & r_d < r < r_w \\ Q_{e,ma} = \dot{m}_{ma} h_{fg} & r_w < r < r_b \\ Q_{dryout} = \frac{\lambda_g \Delta T_{sup}}{\sqrt{\pi \alpha'_g \tau_d}} & r < r_d \\ Q_q = \frac{\lambda_l \Delta T_{sup}}{\sqrt{\pi \alpha'_l \tau_q}} & t > t_d \text{ (uniform } T_w\text{) or} \\ Q_q = \frac{\lambda_l \Delta T_{sup} \sqrt{\pi}}{2\sqrt{\alpha'_l \tau_q}} & t > t_d \text{ (uniform } Q_{in}\text{)} \\ Q_{fc} = h_{fc}(T_w - T_b) & r > r_b \end{array} \right\}. \quad (3.42)$$

Here, $\dot{m}_{mi}$ and $\dot{m}_{ma}$ are mass rates of evaporated liquid in the microlayer and macrolayer. The terms τ_d and τ_q denote the start time of dryout and quenching. The

term t_d is the time of departure as well. The quenching heat flux is calculated from the model of Zhao and Tsuruta [119] and h_{fc} is forced-convection heat transfer coefficient calculated by the Dittus-Boelter model as [121]:

$$h_{fc} = 0.023\ Re_l^{0.8} Pr_l^{0.4} \left(\frac{\lambda_l}{D_h}\right), \tag{3.43}$$

with Re_l, Pr_l and D_h being liquid flow Reynolds number, liquid Prandtl number and the hydrodynamic diameter of channel.

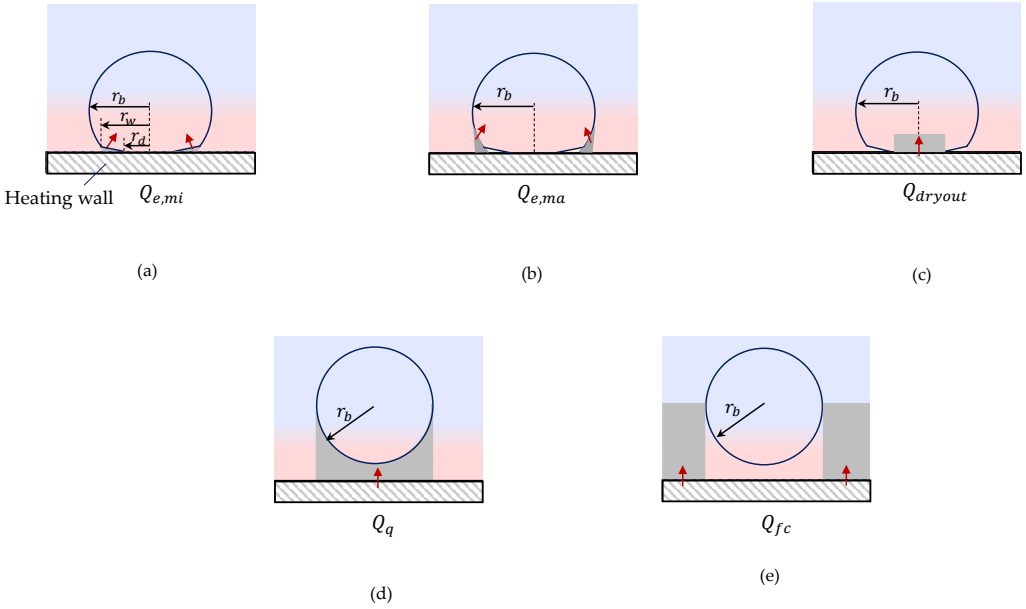

Figure 3.10: Different heat transfer mechanisms during bubble growth and detachment a) evaporation of microlayer b) evaporation of macrolayer c) dryout heat transfer d) quenching heat transfer e) forced convection heat transfer. The gray color highlights volumes from which the heat is being transferred.

3.1.5 Heat transfer in the heating wall

The impact of heating wall material and thickness on the heat transfer in the boiling process has usually not been considered in the previous studies. However, the heating wall can act as a thermal buffer and affects the heat transfer near hot spots caused by the dryout underneath the bubble. The energy equation gives:

$$\dot{Q}_{in}dt + \dot{Q}_{out}dt + \dot{Q}_{n,w}dt = \rho_w V_w C_{p,w} dT_w, \tag{3.44}$$

with $\dot{Q}_{in}$, $\dot{Q}_{out}$ and $\dot{Q}_{n,w}$ being the heat transfer rate into the heating wall, from the heating wall and conduction heat rate between two neighboring segments of wall as shown in Figure 3.11. These terms are calculated as:

$$\dot{Q}_{in} = Q_{in} \times \Delta L_w, \tag{3.45}$$

$$\dot{Q}_{out} = Q_{out} \times \Delta L_w, \tag{3.46}$$

$$\dot{Q}_{n,w} = Q_{n,w} \times \delta_w. \tag{3.47}$$

In these equations, Q_{in} is the heat flux into the heating wall, Q_{out} is provided by Eq. (3.42) and $Q_{n,w}$ denotes the tangential heat flux in the heating wall given as:

$$Q_{n,w} = \lambda_w \frac{\Delta T_w}{\Delta L_w}, \tag{3.48}$$

with λ_w being the heating wall thermal conductivity and ΔT_w is the temperature difference between two neighboring cells in the heating wall (Figure 3.11).

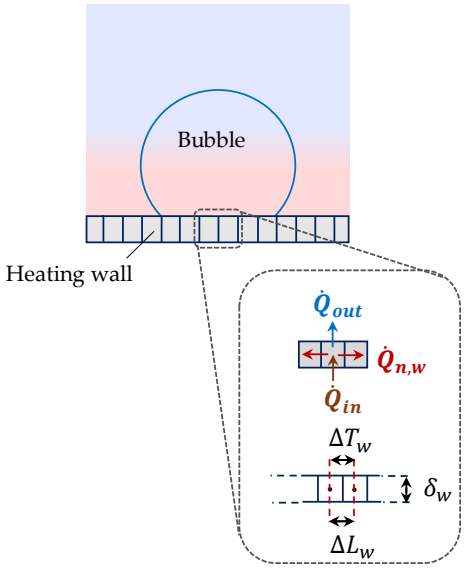

Figure 3.11: Schematic of heat transfer along the heating wall underneath the bubble.

From Eq. (3.44), the temperature change in the heating wall is given as:

$$\frac{dT_w}{dt} = \frac{\dot{Q}_{in} + \dot{Q}_{out} + \dot{Q}_{n,w}}{\rho_w V_w C_{pw}}, \tag{3.49}$$

with C_{pw} and ρ_w being the heating wall specific heat capacity and density. For the heating wall with the thickness of δ_w and unit depth ($1\ \mathrm{m}$), the volume of one cell, V_w, is calculated as:

$$V_w = \Delta L_w \times \delta_w. \tag{3.50}$$

3.2 Results and discussions

3.2.1 Discretization dependency study

The heat-partitioning sub-model requires a proper time discretization for bubble dynamics and a spatial discretization for the microlayer and the heat transfer inside the heating wall. Both space and time were discretized using a central differences scheme and in order to do the mesh independency, some cases with time steps from 1 μs to 30 μs and mesh sizes from 10 μm to 50 μm were tested. It was found that the mesh size less than 50 μm and a time step less than 30 μs yield a stable model convergence. In addition, the deviation from the average predicted value of bubble departure diameter from these cases were less than 2% and the Courant-Friedrichs-Lewy (CFL) number was controlled to be less than 1.

3.2.2 Model validation

For model validation, the published data from different experiments were used. One is from Klausner et al. who designed an experimental facility with a horizontal 25×25 mm square cross section for the subcooled flow boiling of refrigerant R113 [43]. They measured the mean bubble departure diameter, d_d, at different wall heat flux, Q_w, wall superheat, ΔT_{sup}, and mass flux, G, for a stratified two-phase flow in the boiling section. Prodanovic et al. investigated an upward water flow boiling in a vertical annular (quartz glass, 22 mm inner diameter) [128]. The boiling geometry was a heated hollow stainless-steel tube with 12.7 mm outer diameter welded to copper rods. The diameter of the heated rod was 22 mm downstream of the inlet to provide a fully developed turbulent flow. A high-speed camera at 6,000 to 8,000 frames per second was installed at the location 0.44 m downstream of the heated section start point to monitor the bubble behavior. They observed the bubble behavior from beginning to collapse and obtained bubble shapes during the lifetime, times of detachment and typical bubble size. Situ et al. [45] conducted different investigations for a vertical upward subcooled flow boiling in an annular channel with 38.1 mm inner diameter and 19.1 mm heater rod's diameter. They

also used a high-speed camera to assess bubble growth rate, lift-off diameter, and velocity after lift-off at different wall heat fluxes from 54 to 206 $\frac{\mathrm{kW}}{\mathrm{m}^2}$ and mass fluxes between 466 to 900 $\frac{\mathrm{kg}}{\mathrm{m}^2.\mathrm{s}}$ at ambient pressure. Sugrue studied the effect of the heating wall orientation angle on bubble departure diameter for subcooled boiling at different pressures, P, mass flux and wall heat fluxes with a high-speed camera [129]. The test section was a rectangular stainless-steel channel with 14.3 mm width and 19.9 mm height and a one-sided heater. The author carefully controlled the Reynolds number between 11,800 and 34,500 and the Froude number (based on the channel hydraulic diameter) between 0.42 to 1.06 and to eliminate the impacts of buoyancy and wall orientation angle. In addition, the author controlled the subcooled fluid flow and wall heat flux to provide an isolated bubbles regime for which interactions between bubbles at neighboring nucleation sites can be neglected. All the experiments introduced above cover nearly all physical parameters, which can affect the bubble behavior. The present model has been validated for the departure or lift-off diameter with these data as shown in Table 3.1. In flow boiling, the bubble departure diameter is not equal to the lift-off diameter when the bubble slides on the heating wall. In other words, departure means that the bubble leaves the originating cavity while lift-off means that the bubble leaves the wall. The calculated departure diameters are compared against the experimental data of Klausner et al. [43] and Sugrue [129].

Figure 3.12 shows the comparison with the data from Klausner et al. [43] for R113 subcooled flow boiling. The average deviation is 21%, which can be considered as a good agreement. In the model calculation, fully developed turbulent flow was considered because of the open channel in the experimental setup. In addition, the wettability of R113 has also been taken into account by considering the contact angle at the equilibrium state $\beta_w = 0.174$ rad [130].

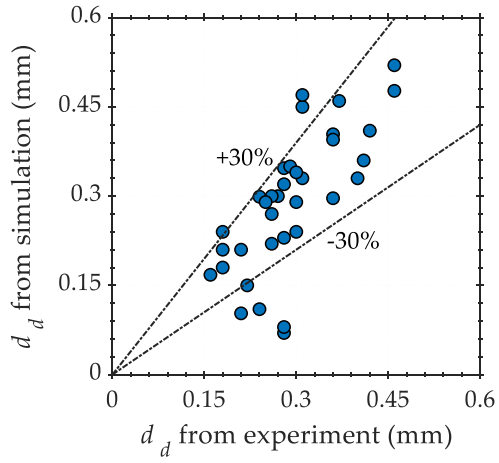

Figure 3.12: Comparison between model predictions and experimental data of Klausner et al. [43].

Table 3.1: Experimental data used for validation of the bubble dynamics model.

Reference	**Klausner et al.** [43]	**Prodanovic et al.** [128]	**Situ et al.** [45]	**Sugrue** [129]
Fluid	R113	Water	Water	Water
Heating wall orientation	Horizontal	Vertical	Vertical	$0°$, $30°$, $45°$, $60°$, $90°$, $180°$
Geometry of channel	Rectangular; $D_h = 25$ mm	Rectangular; $D_h = 9.3$ mm	Annular; $D_h = 19.1$ mm	Rectangular; $D_h = 16.7$ mm
	no full filled		Observation points at different positions	
G $(\frac{\text{kg}}{\text{m}^2.\text{s}})$	112 – 287	76.6 – 766	466 – 900	250 – 400
Q_w $(\frac{\text{kW}}{\text{m}^2})$	11 – 26	200 – 1000	54 – 206	50, 100
ΔT_{sub} (K)	Saturated	10, 20 , 30	2 – 20	10, 20
P (bar)	1.5	1.05; 2	1.01	1.01; 2.02; 5.05
Measured uncertainties	$\pm$0.03 mm	-	$\pm$0.016 mm	$\pm$0.113 mm

A better agreement for bubble departure diameter is achieved for the data of Sugure [129]. The average deviation is 12.44% as shown in Figure 3.13. These experiments [129] cover a wide range of parameters including mass flux, G, wall orientation angle, θ_w, wall heat flux, Q_w, and subcooling temperature, ΔT_{sub}. The model of Klausner et al. [43] has a reasonable agreement with their own experimental data for R113 flow boiling. However, it predicts the bubble departure diameter for Sugure's experiments [129] of water with an average deviation of 65.5%. The modified version of the model, which was introduced by Yun et al. [49] for water presents a better agreement but still has an average deviation of 37.9%. Both models can predict the experimentally observed trends but they overpredict the bubble departure diameter and only at 5 bar pressure a small overprediction is seen (see Figure 3.14).

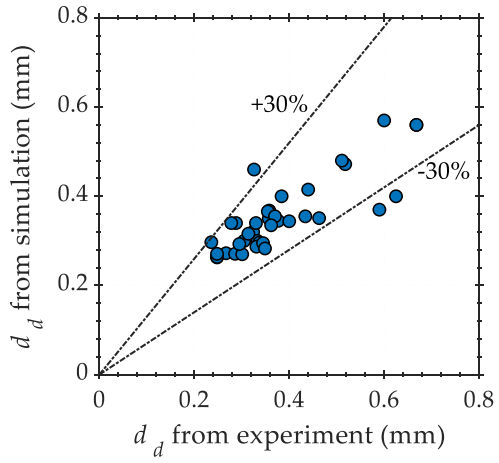

Figure 3.13: Comparison between model predictions and Sugrue's experimental data [129].

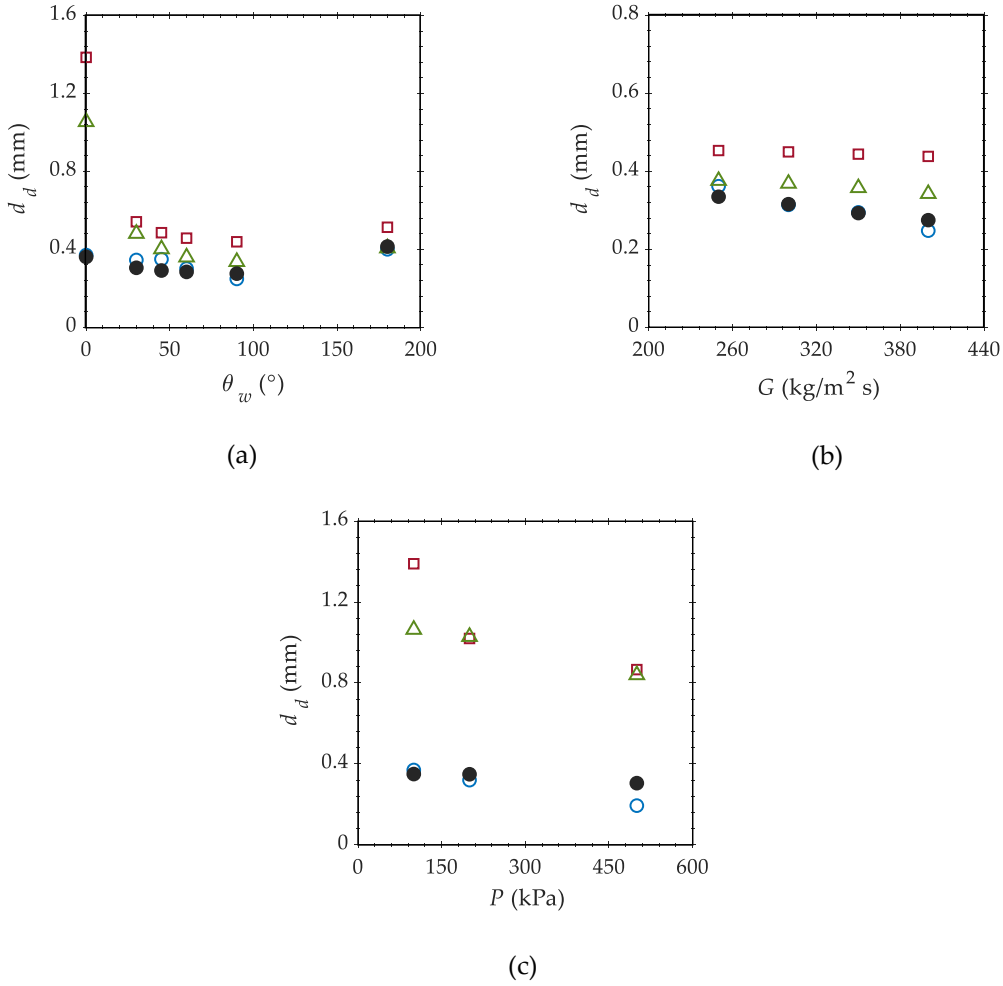

Figure 3.14: Comparison between the present model and Sugrue's experimental data [129], the model of Klausner et al. [43] and the modified model of Yun et al. [49] for departure diameter as a function of I) heating wall orientation angle, θ_w II) mass flux, G, and III) pressure, P. Conditions are $\Delta T_{sub} = 10$ K and $Q_w = 0.05\ \frac{\text{mW}}{\text{m}^2}$ as well as a) $G = 400\ \frac{\text{kg}}{\text{m}^2.\text{s}}$ and $P = 101$ kPa b) vertical heating wall, $\theta_w = 90°$ and $P = 101$ kPa c) downward-facing horizontal heating wall, $\theta_w = 0°$ and $G = 400\ \frac{\text{kg}}{\text{m}^2.\text{s}}$ (legend: ○ Sugrue's experiment [129] □ Model of Klausner et al. [43] △ Model of Yun et al. [49] • Present model.)

The dynamic inclination and contact angles for one test case of Klausner et al. [43] are depicted in Figure 3.15. The advancing contact angle, β_{ad}, strongly reduces from $\frac{\pi}{2}$ rad in the hemisphere shape to ~ 0.65 rad due to bubble growth and then increases back to $\frac{\pi}{2}$ rad because of the acting forces on the bubble in the tangential direction. The receding contact angle, β_{re}, firstly decreases like the advancing one due to bubble growth and then it increases because of the bubble inclination and also the acting forces in the perpendicular direction. Further, it reduces again due to the force acting on the bubble in the tangential direction, which results in the bubble inclination. Finally, it increases again to $\frac{\pi}{2}$ rad because of the acting forces in

the perpendicular direction. The bubble inclination angle, θ_b, increases from zero when the bubble is formed as a symmetric hemisphere until 1.43 rad when the forces acting on the bubble in the tangential direction are still not balanced. Then it slightly reduces because of the base diameter expansion. Eventually, it decreases back to zero due to bubble sliding, speed up and the reduced drag force, which results from the relative velocity between liquid and bubble. Since the dynamic inclination and contact angles are obtained from the present model there is no need to predetermine them like the works done by Klausner et al. [43], Colombo and Fairweather [51], Hong et al. [131] and Raj et al. [52].

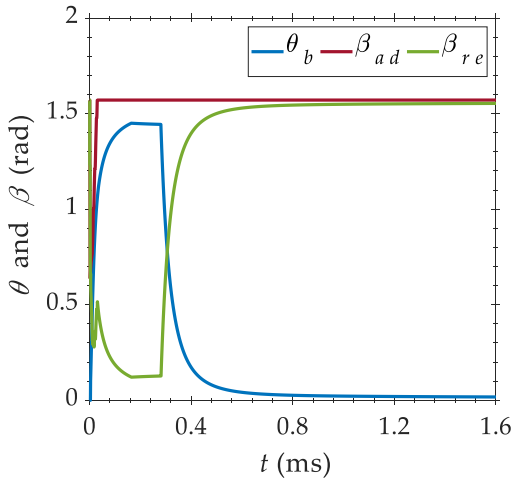

Figure 3.15: Calculated dynamic inclination and contact angles for one test case of Klausner et al. [43] with $G = 287\ \frac{\mathrm{kg}}{\mathrm{m^2.s}}$, 0.061 inlet vapor quality, liquid surface height of 0.0061 m, $\Delta T_{sub} = 13.6$ K and $Q_w = 20.2\ \frac{\mathrm{kW}}{\mathrm{m^2}}$.

Krepper et al. [88] assessed the application of Lemmert and Chawla [79] correlation to model the active nucleation site density in CFD simulations (see Eq. (3.51)). Nucleation site density is too complex to predict as it is strongly dependent on the heating wall material, roughness, etc. The model of Lemmert and Chawla is given as [79]:

$$N = N_{ref}\left(\frac{\Delta T_{sup}}{\Delta T_{ref}}\right)^{P}, \tag{3.51}$$

with N_{ref}= 7.94×10^5 m^{-2}, ΔT_{ref}= 10 K and $P = 1.805$. However, Krepper et al. stated that N_{ref} is a case-dependent parameter that should be calibrated for the given applications [88]. This correlation was employed in the present model to calculate the wall heat flux based on the known wall temperature for the experimental data of Klausner et al. [43]. The recalibration gives N_{ref}= 7.0×10^{+4} m^{-2} and the calculated wall heat fluxes and measured ones are compared by Figure 3.16

which proves the applicability of the Lemmert and Chawla equation [79] and the assessment of Krepper et al. [88].

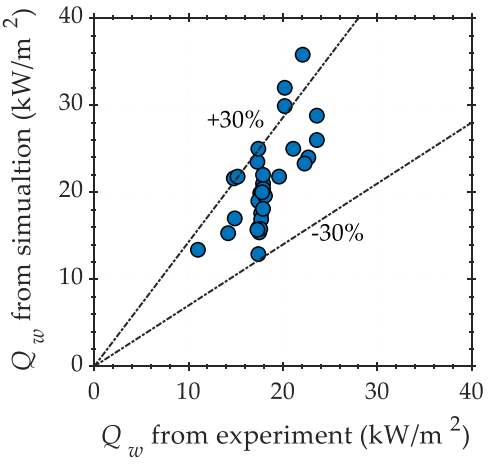

Figure 3.16: Comparison between experimental data of Klausner et al. [43] and the model calculation for wall heat flux.

For the present model the wall superheat is a necessary parameter for the calculation of active nucleation site density. However, both Prodanovic et al. [128] and Situ et al. [45] did not measure the local wall superheat in their experiments. The recalibration of N_{ref} are considered $4.8{\times}10^{+4}$ m^{-2} for the case of Prodanovic et al. [128] and $9.0{\times}10^{+4}$ m^{-2} for the case of Situ et al. [45]. The comparison for lift-off and departure diameters are illustrated in Figure 3.17. The average deviation from the test case of Situ et al. [45] for more than 90 data points is 35%. The location of the observation point where the flow was observed by a high-speed camera affects the data values since the turbulent layer thickness on the heating wall is changed [45]. For the experiments of Situ et al. [45] the location of observation points were specified which are helpful for interpretation and analysis.

The maximum average deviation of 37% is found for the experiment of Prodanovic et al. [128]. At low velocity ($\boldsymbol{U}_{in} = 0.08$ $\frac{\mathrm{m}}{\mathrm{s}}$) the model strongly overpredicts the departure diameter which is up to 3 times of the experimental value and similar findings were achieved by Sugrue and Buongiorno [48] and Colombo and Fairweather [51]. Evidently, the experimental data of Prodanovic et al. [128] is the most difficult one to predict. A possible reason may be the location of observation point, which is not considered in this work. Another reason maybe is the high subcooling that can lead to bubble collapse or merging [51].

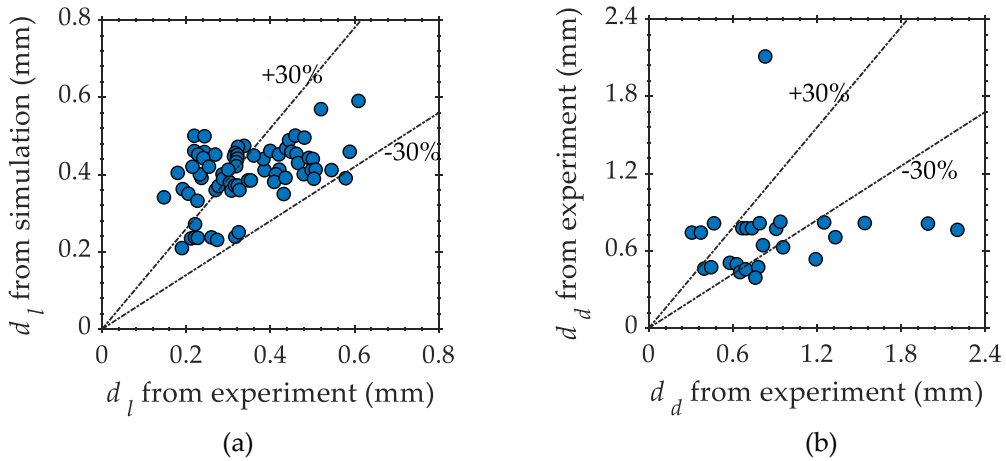

Figure 3.17: Comparison between the model predictions and experimental data at different conditions for a) Situ et al. [45] b) Prodanovic et al. [128] test cases.

3.2.3 Sensitivity analysis

In this section, the effect of different parameters such as subcooling temperature, boiling geometry, mass flux, wall heat flux, heating wall orientation angle and pressure on the bubble departure and lift-off diameters for flow boiling are analysed.

Mass flux increase (inlet velocity) usually causes the bubble departure diameter decrease (see Figure 3.18a) which is also confirmed by Sugrue [129], Klausner et al. [43] and Yun et al. [127] as depicted in Figure 3.14b. It is due to the enhancement of drag and lift forces with mass flux, which decreases lift-off diameter. This trend is confirmed by the present model as shown in Figure 3.19b.

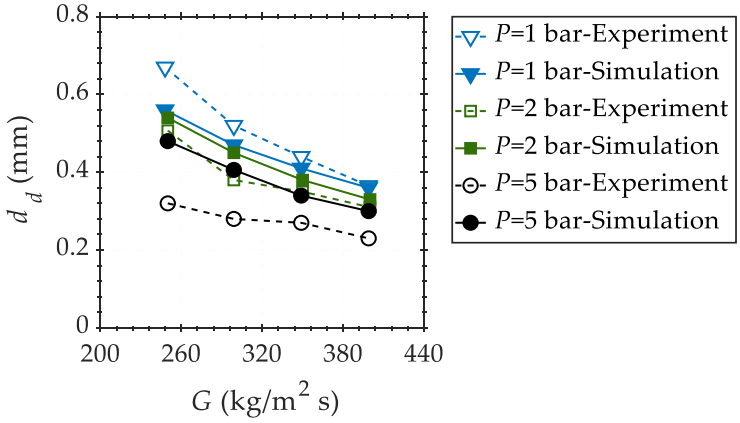

(a)

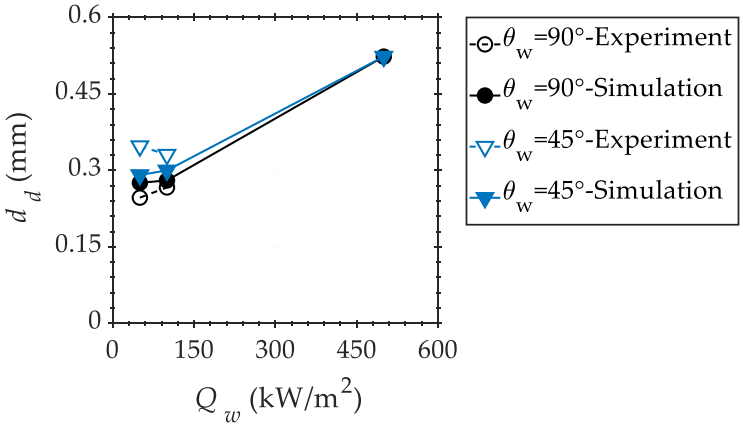

(b)

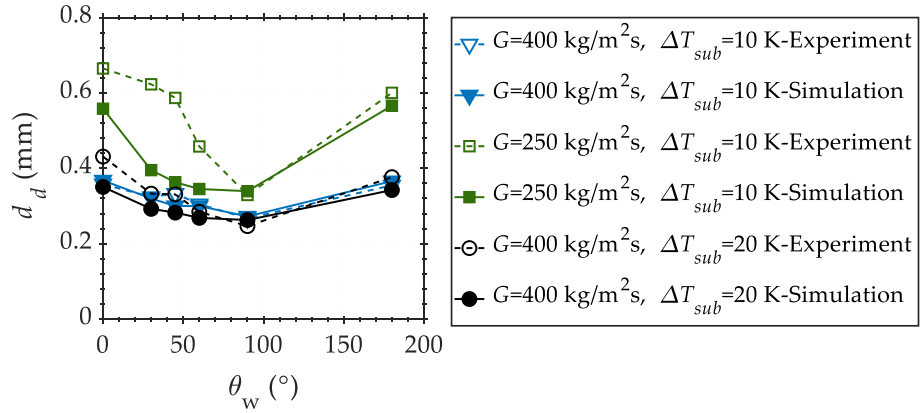

(c)

Figure 3.18: Comparison of the predicated and measured (from Sugrue's experiment [129]) departure diameters for a) $\theta_w = 0°$, $\Delta T_{sub} = 10$ K and $Q_w = 100$ $\frac{\text{kW}}{\text{m}^2}$ b) P=1 bar, $G = 400$ $\frac{\text{kg}}{\text{m}^2.\text{s}}$ and $\Delta T_{sub} = 10$ K c) $P = 1$ bar, $\Delta T_{sub} = 10 \sim 20$ K and $Q_w = 100$ $\frac{\text{kW}}{\text{m}^2}$.

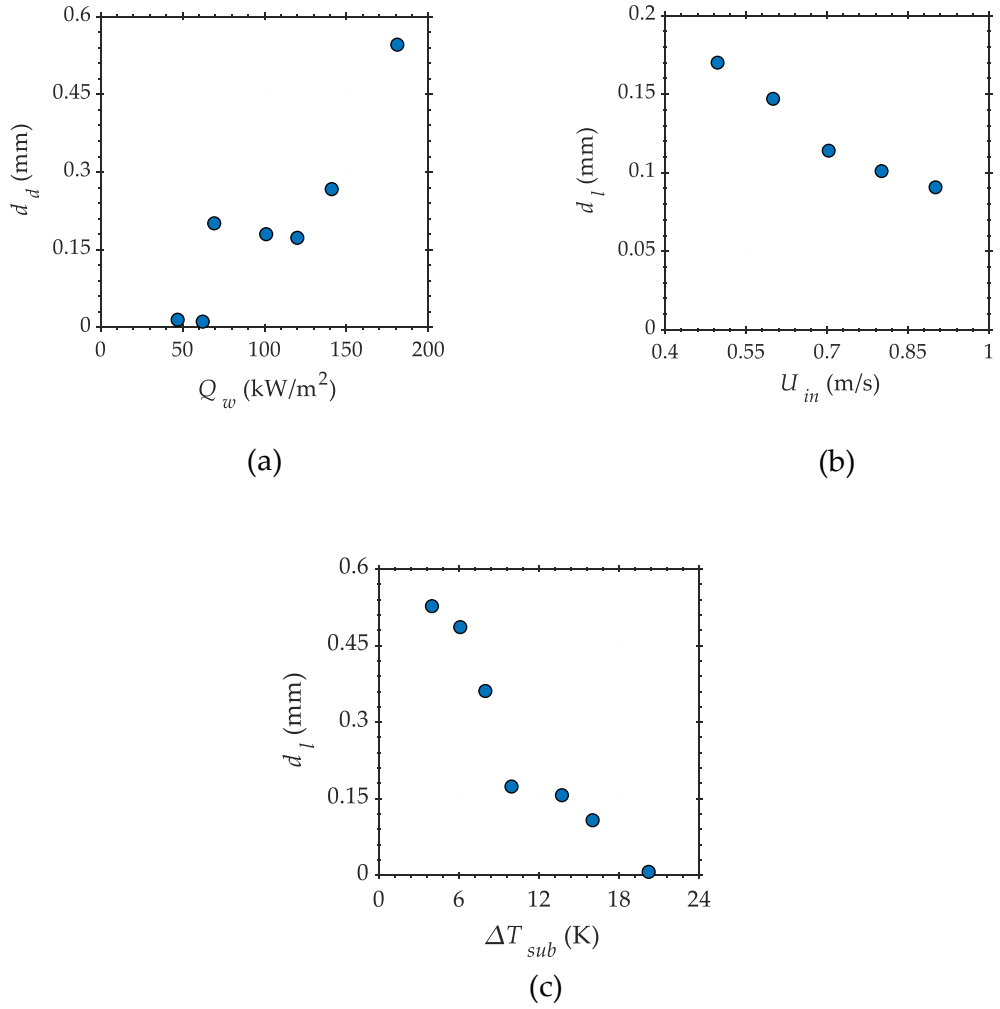

Figure 3.19: Calculated lift-off diameter for the experiment of Situ et al. [45], $\theta_w = 90°$, $P = 1$ bar, location of observation point is 0.57 m from the inlet pipe a) $\boldsymbol{U}_{in} = 0.5\ \frac{\mathrm{m}}{\mathrm{s}}$ and $\Delta T_{sub} = 10$ K b) $Q_w = 100\ \frac{\mathrm{kW}}{\mathrm{m}^2}$ and $\Delta T_{sub} = 10$ K c) $\boldsymbol{U}_{in} = 0.5\ \frac{\mathrm{m}}{\mathrm{s}}$ and $Q_w = 100\ \frac{\mathrm{kW}}{\mathrm{m}^2}$.

The growth speed of bubble is determined by the applied wall heat flux on the heating wall. A higher wall heat flux leads to a faster bubble growth, which influences the growth force that opposes the bubble departure. Therefore, a high wall heat flux leads to larger bubble departure diameter. Moreover, during the flow boiling the pressure on the distorted bubble is decreased in the direction facing the flow. This leads to a delay in the bubble lift-off, which has been verified by the model prediction. The increase is even relatively small which can be seen in Figure 3.18b. However, this effect is confirmed by the Sugrue's experiments only at a wall orientation angle of 90° [129]. At a wall orientation angle of 45 ° it is even the other way round when the applied wall heat flux enhances from 50 to 100 $\frac{\mathrm{kW}}{\mathrm{m}^2}$ as shown in Figure 3.18b. The departure diameter significantly increases in the model calculation for both 45 ° and 90 ° orientation angles when the wall heat

flux increases to 500 $\frac{\mathrm{kW}}{\mathrm{m}^2}$. The same impact was found in the model calculations results based on the setup of Situ et al. [45] for a wider range of wall heat flux and an axial location of 0.57 m from the inlet as shown in Figure 3.19a. The bubble even does not leave the heating wall at low wall heat flux, i.e., $Q_w \leq 60\ \frac{\mathrm{kW}}{\mathrm{m}^2}$. The bubble lift-off diameter slightly decreases from 0.2 mm to 0.17 mm when the wall heat flux is between 60-120 $\frac{\mathrm{kW}}{\mathrm{m}^2}$. Afterward, the bubble lift-off diameter rapidly increases to 0.54 mm with an increase of the wall heat flux to 180 $\frac{\mathrm{kW}}{\mathrm{m}^2}$. A credible explanation for these findings is the dynamic contact and inclination angles. The dynamic inclination angle of a bubble is not only determined by the bubble size but also by the flow velocity. A high wall heat flux can lead to fast bubble growth, but the forming time of inclination angle can be about the same due to the same flow conditions. In other words, the bubble lift-off time is more or less the same while the growth speed is much higher at high wall heat flux, which results in a larger lift-off diameter. However, from Eq. (3.34) the base diameter expansion is dependent on the bubble contact angle, β, and the bubble diameter expansion rate, $\dot{r}_b$. A smaller contact angle leads to a faster base diameter expansion. A higher wall heat flux leads to a larger contact angle, β, and a smaller lift-off diameter but also a higher bubble expansion rate, $\dot{r}_b$, and a larger lift-off diameter, d_l. A high wall heat flux results in two opposite impacts on the base diameter, which determines the bubble lift-off and departure. These different effects of wall heat flux on contact and inclination angles are the reasons that the lift-off diameter slightly reduces and further increases with the increase of wall heat flux as displayed in Figure 3.19a.

The effect of wall orientation angle on the bubble departure diameter in Sugrue's experiment [129] is also accurately reproduced by the present model as shown in Figure 3.18c. The smallest bubble departure diameter occurs in the vertical case, while the maximum occurs in the downward facing horizontal configuration. For example, for $\Delta T_{sub} = 10\ K$ and $G = 250\ \frac{\mathrm{kg}}{\mathrm{m}^2.\mathrm{s}}$, the departure diameter is maximum (0.668 mm) when the heating wall is downward facing ($\theta_w = 0°$). It decreases to 0.33 mm at $\theta_w = 90°$ and then increases again to 0.6 mm at $\theta_w = 180°$. The force difference between the upward and downward facing heating wall is just the direction of buoyancy force relative to the heating wall orientation. In the downward facing orientation, the total force in the positive perpendicular direction is smaller than that in the upward facing one. It means that the expected inclination angle, $\theta_{b,s}$, (Figure 3.5 and Eq. (3.35)) is smaller in the upward facing case than in the downward facing case when all other conditions are same. Therefore, sliding occurs later and the bubble size is larger in the downward facing case. In the vertical test case, the buoyancy force enforces bubble sliding which results in departure diameter decrease. However, the model predicts the departure diameter reduction from 0.56 mm to 0.351 mm and further increases to 0.57 mm. The difference between model calculation and experimental data may be due to the impact

of bubble geometry. In the experiment, the bubble is an ellipsoid which is pushed by buoyancy force against the heating wall, while in the model calculation it is still spherical or hemispherical. The liquid subcooling temperature affects the bubble size in such a way that higher subcooling reduces the bubble departure and lift-off diameters due to the high rate of condensation. In the Sugrue's case [129] this effect is small (see Figure 3.18c) as the bubble remains in the thermal boundary layer after detachment and so no condensation happens. The thickness of the thermal boundary layer is $\sim$1 mm for the case of Situ et al. [45] while it is $\sim$ 6 mm for Sugrue's case [129]. This impact becomes obvious in the model's results for the case of Situ et al. [45] where the effective parameters include a wider range. Higher subcooling reduces the lift-off diameter (see Figure 3.19c). It decreases from 0.52 mm at 4 K subcooling to 0 at 20 K subcooling. The second case means that the bubble shrinks and collapses due to condensation before leaving the heating wall.

Pressure significantly affects the bubble departure and lift-off diameters. Pressure enhancement predominantly increases the vapor to liquid density ratio. That is, at the same mass flux the bubble's volume is smaller at higher pressure which results in a smaller departure diameter as confirmed by the model calculations and Sugrue [129] (see Figure 3.18a). As an example, in Figure 3.18a at the mass flux of 250 $\frac{\mathrm{kg}}{\mathrm{m^2.s}}$ and 1 bar pressure the departure diameter is 0.79 mm and reduces to 0.51 mm at 2 bar and 0.33 mm at 5 bar in the Sugrue's experiments [129]. The model results (0.56 mm at 1 bar, 0.55 mm at 2 bar and 0.48 mm at 5 bar) does not show such a sharp reduction but the trend is correctly predicted.

In addition, the location of the observation point influences the thickness of the thermal boundary layer, which plays a key role in the bubble dynamics. In this model, the turbulent layer thickness was calculated based on the one-seventh power law. The effect of the observation point location on the bubble lift-off diameter is depicted in Figure 3.20. With an observation point distance between 0 to 0.3 m from the channel's inlet, the lift-off diameter increases correspond to the growth of the turbulent layer. When it is fully developed ($x > 0.3$ m) the lift-off diameter is no longer affected by the axial position as shown in Figure 3.20. In this figure, all conditions except the location of the observation point are the same.

The average relative deviation for prediction of the bubble lift-off diameter for the whole database of four different cases is 23% as summarized in Table 3.2. It proves the good predictability of the present model and the most important issue is that no recalibration parameter is necessary for the prediction of bubble growth except the nucleation site density which is due to the lack of wall superheat data.

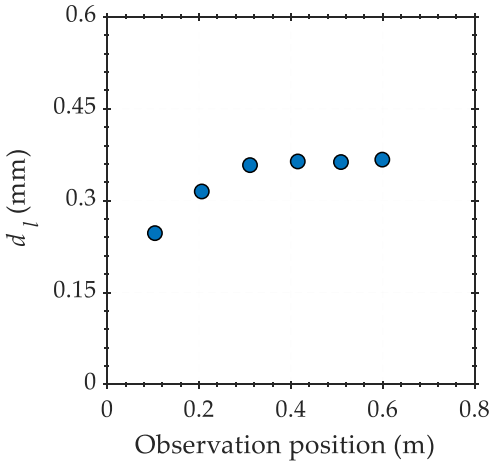

Figure 3.20: Effect of the axial location of observation point exemplarily for $D = 20$ mm, $P = 1$ bar, $\Delta T_{sup} = 8$ K, $\boldsymbol{U}_{in} = 0.752$ $\frac{\text{m}}{\text{s}}$ and $\Delta T_{sub} = 14$ K.

Table 3.2: Summary of the agreement between model and experimental data for the different data sets.

Experimental data	**Average deviation** (%)
Klausner et al. [43]	21%
Situ et al. [45]	35%
Sugrue [129]	12%
Prodanovic et al. [128]	36%
Whole database	26%

3.3 Summary

This chapter introduced a mechanistic bubble dynamics model for flow boiling based on the balance of forces on a single growing bubble. This model considers the contributions of microlayer evaporation underneath the bubble, thermal diffusion, and condensation around the bubble cap. It applies dynamic inclination and contact angles between the bubble and the heating wall as well as different criteria for bubble departure and lift-off. Wall heat flux calculation during the formation of a single bubble was given. Finally, validation against four experimental test cases as well as a sensitivity analysis were provided.

4 An improved wall heat-partitioning model

In this chapter, the previously introduced bubble dynamics model in Chapter 3 is implemented in the E-E two-fluid CFD framework as a sub-model to improve the accuracy of flow boiling simulations and reduce the case dependency [132]. Its implementation needs an extension of the current nucleation site activation and heat-partitioning models, which is discussed in Section 4.1. The prediction of bubble movement on the heating wall during flow boiling, the calculation of bubble sliding length and influence area are provided in Section 4.1.1. In Section 4.1.2, the implementation of the improved wall heat-partitioning and the cavity group activation models in the E-E framework is presented. Section 4.2 gives the results of this implementation for two validation cases, which are subcooled flow boiling in a vertical pipe and an annulus. Finally, Section 4.3 provides a short summary of this chapter.

4.1 The cavity group activation model

In the conventional RPI wall boiling model, the bubble departure model is dependent on the subcooling temperature as given by the model of Tolubinsky and Kostanchuk (Table 2.4) [26]. However, the bubble dynamics model introduced in Chapter 3 is dependent on the activated wall superheat but not the actual wall superheat, which is used for nucleation site density calculation in the RPI model. Therefore, the implementation of the bubble dynamics model in the E-E framework requires an extension of the nucleation site density and heat-partitioning models.

The model of Lemmert and Chawla [79] for nucleation site density modelling is given as:

$$N = N_{ref} \left[\frac{\Delta T_{sup}}{\Delta T_{ref}} \right]^{m}, \tag{4.1}$$

with $N_{ref} = 7.94 \times 10^{+5}$ m^{-2}, $\Delta T_{ref} = 10$ K, $m = 1.805$ and its distribution is shown in Figure 4.1a. In the RPI model, for a given position with an actual wall superheat, the nucleation site density is calculated without considering the

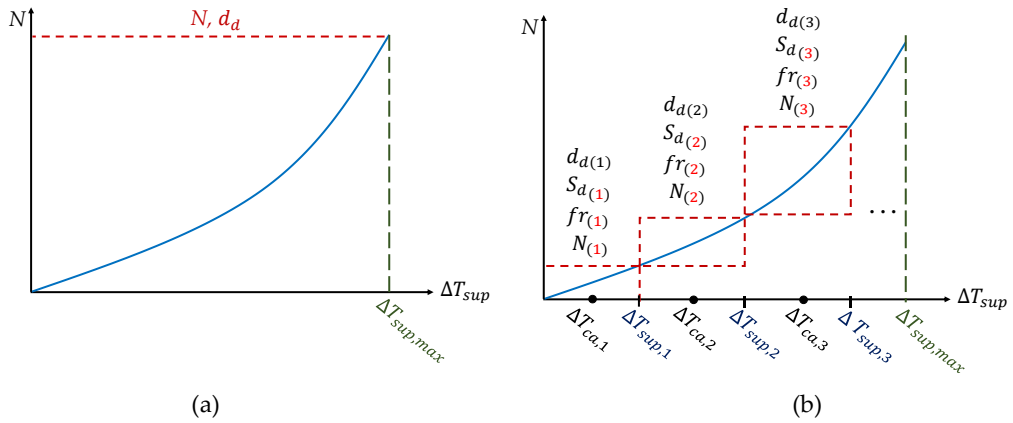

Figure 4.1: Nucleation site density distribution in: a) the conventional RPI model (Eq. (4.1) b) the group activation model (Eq. (4.2)).

effect of activated wall superheat on the bubble dynamics. That is, all the activated nucleate bubbles have same bubble dynamics such as the departure diameter and frequency.

In order to consider the dependency of bubble dynamics on the activated wall superheat, the activated nucleation site density method is employed. This method divides the nucleation site density into different groups with different activated wall superheat as shown in Figure 4.1b. Each activated cavity has a specific wall superheat as a result of specific bubble dynamics parameters. For instance, the first cavity has an average wall superheat of $\Delta T_{ca,1}$ which is used for the calculation of the bubble dynamics parameters and this continues for the 2^{nd}, 3^{rd} ,... and k^{th} cavity. The nucleation site density is given as:

$$N_{(i)} = N_{ref}\left(\frac{\Delta T_{sup,i}}{\Delta T_{ref}}\right)^{m} - N_{ref}\left(\frac{\Delta T_{sup,i-1}}{\Delta T_{ref}}\right)^{m} = N^{(i)} - N^{(i-1)}, \tag{4.2}$$

with $N_{(i)}$ being the nucleation site density of group i with the activation superheat of $\Delta T_{sup,i}$ and $N^{(i)}$ is calculated by Eq. (4.1). The nucleation site density of first group, N_1, is still calculated by Eq. (4.1) and N_2, N_3,..., N_k by Eq. (4.2). In each activated group, the bubble dynamics parameters are the same for the given boundary conditions such as fluid bulk temperature and flow velocity. In this model, different bubble dynamics parameters are calculated for a given position with different activated superheat.

When the group activation is employed, the heat-partitioning model can be simplified. The total applied wall heat flux, Q_w, is transferred to the liquid, Q_l, and vapor bubbles, Q_e, i.e.:

$$Q_w = Q_l + Q_e, \tag{4.3}$$

The liquid heat flux is the summation of quenching heat flux, Q_q, and single-phase convection, Q_c as (see Figure 2.13):

$$Q_l = Q_c + Q_q \tag{4.4}$$

In steady state, the total time-averaged heat flux due to evaporation, Q_e, and quenching, Q_q, must be equal to the applied heat flux as [132–134]:

$$Q_q + Q_e = A_b Q_w. \tag{4.5}$$

In other words, due to the steady state boiling in the bubble influence area (quenching and evaporation areas as shown in Figure 4.2) the average wall superheat is constant in each activation group. Therefore, the heat-partitioning model can be given as:

$$Q_w = A_b Q_w + Q_c, \tag{4.6}$$

with A_b being the heating wall area fraction influenced by a bubble which is defined as the bubble influence area divided by total heating wall area as shown in Figure 4.2.

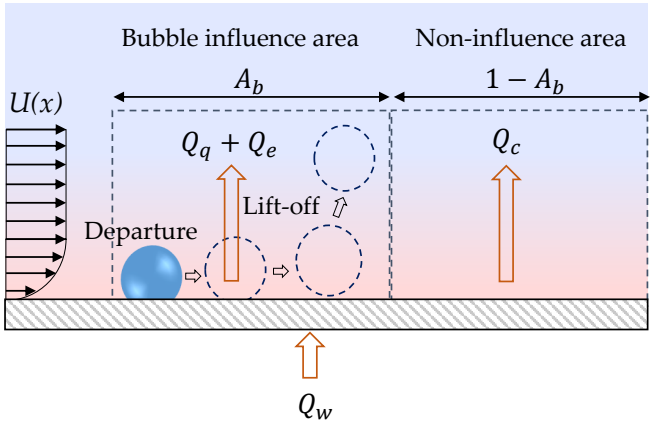

Figure 4.2: Schematic of heat-partitioning model and bubble influence area.

The single-phase convection, Q_c, in Eq. (4.6) is calculated as:

$$Q_c = (1 - A_b)\, h_{c,l}\, (T_{w,ac} - T_l)\,, \tag{4.7}$$

with $T_{w,ac}$ being the cavity activation temperature ($\Delta T_{sup} + T_{sat}$) from Figure 4.1b and the term $h_{c,l}$ denotes the liquid heat transfer coefficient given by Eq. (2.98).

4.1.1 Bubble sliding length and influence area

We refer to departure when a bubble leaves its originating cavity, while lift-off means that it leaves the heating wall. As discussed in Chapter 3, when the net force in the heating wall normal direction becomes positive, the bottleneck will be formed. The criterion for bubble lift-off is the bottleneck breakage or the shrinkage of base diameter to zero. When the bubble inclination angle reaches its maximum value and the force in the tangential direction of the heating wall is balanced, the bubble starts to slide. It travels a distance called sliding length, S_d, on the wall until the point at which the criteria for lift-off are fulfilled. Three different cases for bubble detachment from the heating wall are discussed here. In the first case, the bubble goes into the bulk liquid without sliding (Figure 4.3a). In the second case, the bubble travels the distance, S_d, and lifts off before reaching the neighboring nucleation site (Figure 4.3b). In the latter case, the bubble slides until reaching the neighboring bubble and then lifts off. Bubble merging on the heating wall is not considered and can be the subject of future studies (Figure 4.3c).

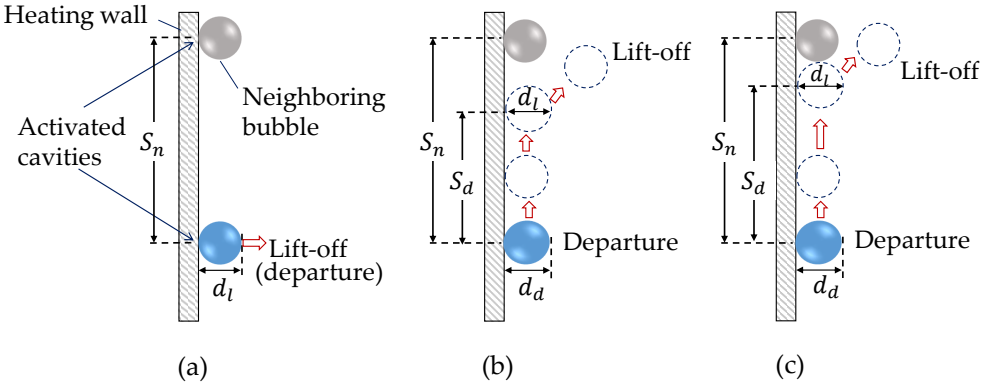

Figure 4.3: Different types of bubble detachment in flow boiling.

The bubble influence area fraction is a significant parameter in the prediction of wall heat transfer. Figure 4.4 shows the calculation of this parameter according to the bubble detachment from the heating wall.

The bubble influence area fraction for the first case is given as:

$$A_{b(i)} = \pi \left(K \frac{d_{d(i)}}{2} \right)^2 N_{(i)}, \tag{4.8}$$

with K being the influence area factor for which $K = 2$ has been recommended [71]. The parameter $d_{l(i)}$ is the bubble lift-off diameter which is equal to the departure diameter, $d_{d(i)}$, in this case and $N_{(i)}$ is calculated by Eq. (4.2).

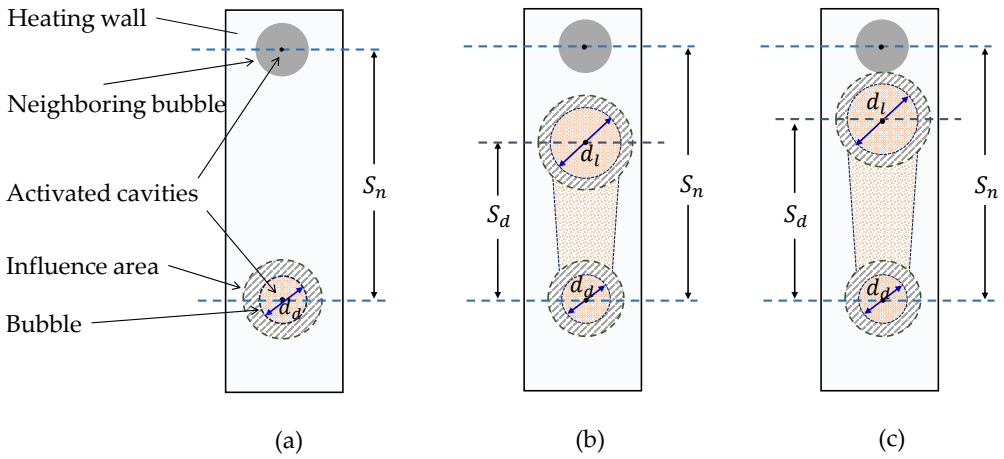

Figure 4.4: Top view of bubble influence area.

The second and third cases are unified as it is assumed that the bubbles lift off before reaching the neighboring cavities. For these cases, the bubble influence area fraction is given as:

$$A_{b(i)} = K^2 \Bigg\{ \left[\frac{\pi}{8} \left(d_{d(i)}^2 + d_{l(i)}^2 \right) \right] + \Bigg\{ \left[\frac{1}{2} (d_{d(i)} + d_{l(i)}) \right] \times \min \left(S_{d(i)}, \left| S_{n(i)} - d_{l(i)} \right| \right) \Bigg\} \Bigg\} N_{(i)}, \tag{4.9}$$

with $d_{d(i)}, S_{d(i)}$ and $S_{n(i)}$ being the bubble departure diameter, bubble sliding length and the distance between two neighboring nucleation sites. As it is assumed that nucleation sites are homogenously distributed and bubbles slide only in the direction of fluid flow, the $S_{n(i)}$ is given as [135]:

$$S_{n(i)} = \frac{1}{\sqrt{N_{(i)}}}. \tag{4.10}$$

4.1.2 Model implementation in the Eulerian-Eulerian framework

In order to implement these models into an E-E framework, the nucleation site density is divided into n size groups (for the next two validation cases, $n = 6$ was considered). Then, for each cavity group, the bubble dynamics parameters were calculated as functions of wall superheat, subcooling temperature and fluid velocity by the CFD code of bubble dynamics model introduced in Chapter 3. These parameters include bubble departure or lift-off diameters, sliding length (in the case of sliding), influence area, waiting and growth times and generation frequency. Afterward, they were implemented in ANSYS CFX 18.2 as tables. The mass generation

of vapor bubbles and heat transfer to both phases (Q_e and Q_l) in each activated group need to be calculated. The heat flux to the vapor bubbles, Q_e, (evaporation heat flux) is obtained via the evaporation mass flux at the heating wall as:

$$Q_e = \dot{m}_g h_{fg}, \tag{4.11}$$

with $\dot{m}_g$ being the mass generation of vapor bubbles. The latter is calculated in terms of the bubble lift-off diameter, bubble generation frequency and nucleation site density as:

$$\dot{m}_g = \rho_g \frac{\pi}{6} d_l^3 frN. \tag{4.12}$$

The heat flux to the liquid phase on the heating wall, Q_l, is calculated by Eqs. (4.4) and (4.5) as:

$$Q_l = A_b Q_w - Q_e + Q_c. \tag{4.13}$$

The single-phase convection, Q_c, is calculated by Eq. (4.7) as well.

4.2 Results and discussions

The introduced bubble dynamics and heat-partitioning models were implemented in the CFD code ANSYS CFX 18.2 together with the MUSIG and iMUSIG models in the E-E framework. To validate the numerical results and check the geometry-independency, two experimental cases, that are subcooled boiling flow of R12 refrigerant in a vertical pipe (DEBORA experiments [89]) and R134a in an annulus [136] were chosen. These two experiments include a wide range of operating conditions such as mass flow rate, applied wall heat flux, inlet subcooling and pressure. The simulation results for the bubble Sauter mean diameter, void fraction, bubble velocity, IAD, bubble passing frequency, liquid and wall temperatures are validated against the experimental data. In addition, the DEBORA experiments were simulated by the conventional RPI wall boiling model.

4.2.1 DEBORA experiments

The first validation case is the DEBORA experiments in which the test facility is a vertical heated pipe with an inner diameter of 19.2 mm and a total pipe length of 5 m [89]. It includes two unheated inlet and outlet sections with a length of 1 m and 0.5 m respectively. A constant wall heat flux is applied on the middle part

Table 4.1: Boundary conditions of the DEBORA experiments.

Case No.	P (MPa)	G ($\frac{\text{kg}}{\text{m}^2.\text{s}}$)	Q_w ($\frac{\text{kW}}{\text{m}^2}$)	T_{in} (K)	ΔT_{sub} (K)
DEB1	2.62	1996	73.89	341.67	17.91
DEB2	2.62	1985	73.89	343.68	15.9
DEB3	1.46	2028	76.2	301.67	29.58
DEB4	1.46	2030	76.24	304.31	26.94
DEB5	1.46	2028	76.19	308.75	22.5
DEB6	1.46	2023	76.26	312.82	18.43
DEB7	1.46	2024	76.26	317.36	13.89

with a length of 3.5 m. The measuring plane is located at the end of this section (4.485 m from the inlet). The pipe geometry and the CFX model setup are shown in Figure 4.5. Table 4.1 gives the experimental boundary conditions. The radial distribution of bubble diameter, void fraction, gas velocity and liquid temperature are calculated in the measuring plane. The wall temperature along the pipe is given as well.

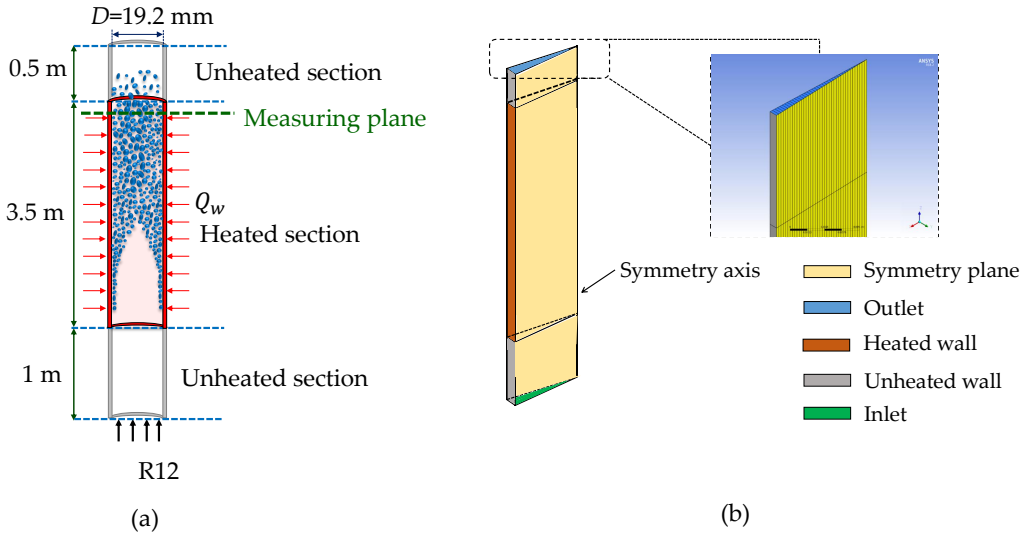

Figure 4.5: Sketch of a) DEBORA experiment geometry b) the model setup in CFX.

The numerical calculations were conducted in ANSYS CFX 18.2 with the Finite Volume Method (FVM) under steady-state conditions. The test section was modelled as a 2° sector in a quasi-2D cylindrical geometry as shown in Figure 4.5b. Symmetry boundary conditions were applied on the side faces of the narrow cylindrical sector. The validity of this simplification was verified by comparison with a 3D simulation

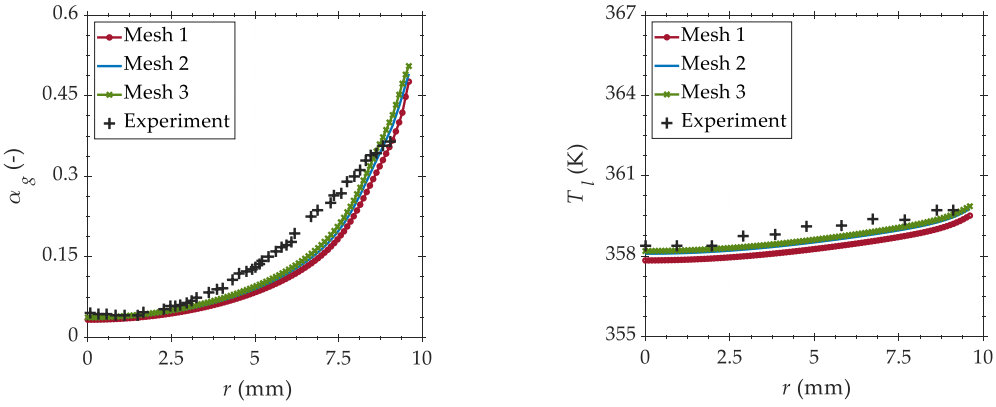

(a) (b)

Figure 4.6: Comparison of the CFD results with three different mesh resolutions with experimental data for DEB1 a) void fraction b) liquid temperature.

representing a 30° sector of the pipe. For the vapor phase the poly-disperse model with free slip on the wall and no-slip boundary condition for the continuous liquid phase was employed. For the pipe inlet, liquid flow with a typical turbulent profile and uniform temperature and for the outlet a pressure boundary condition was set. A constant wall heat flux was applied on the heating wall and the center of the grid cells adjacent to the wall had a non-dimensional coordinate of $y^+ = 250$ for the liquid adjacent temperature. The calculated bubble dynamics parameters were implemented by user functions for wall superheat, liquid subcooling and liquid velocity.

To investigate mesh independency, three uniform grids Mesh 1 (30×300), Mesh 2 (40×400) and Mesh 3 (50×500) were tested. The numbers 30, 40 and 50 denote the number of cells in lateral and 300, 400 and 500 are the ones in the axial direction. As an example, the calculation results of void fraction and liquid temperature in the measuring plane for DEB1 for these three grid cells are depicted in Figure 4.6. The grid refinement showed no change of the calculation results after the grid number has increased to 40 and 400 in lateral and axial directions. Therefore, the test section was modelled by Mesh 2 (40×400).

In this thesis, the break-up and coalescence models of Luo and Svendsen [61] and Prince and Blanch [60] which were adjusted by using break-up and coalescence coefficients, F_B and F_C, to match the measured bubble size were used. Krepper et al. proved that for the same system pressure, the same calibration parameters can be used and further model developments to overcome such tuning procedures are required [88]. To obtain an agreement for both validation cases, $F_B = 0$ and $F_C = 0.1$ were employed. For interaction forces and turbulence modelling, the

"baseline" and BIT models introduced in Section 2.3.4 were used. For the bubble size discretization, an equidistant bubble diameter, Δd_B, was used. It was checked that the calculation results do not change anymore when the width of bubble size groups is less than 0.1 mm. Therefore, for both the iMUSIG and MUSIG models the width of $\Delta d_B = 0.1$ mm was considered.

For $P = 2.62$ MPa and $P = 1.46$ MPa the critical bubble diameter, d_{cr}, at which the sign of lift force coefficient is changed are 1.0 mm and 1.5 mm respectively (see Section 2.3.4). In order to correctly capture the lift force effect for the cases in which the bubble sizes are larger than the critical value, it is necessary to use the iMUSIG model. Otherwise, the MUSIG model, which needs less computational efforts, is used. For the MUSIG approach 20 size groups in the range of 0 to 2 mm were used. From the BSD, it was concluded that just for the DEB6 case, the iMUSIG model is needed. For this case, two velocity groups, the first one (gas1) with 15 size groups for small bubbles, $d_b < d_{cr}$ (0-1.5 mm) and for the large bubbles (gas2) with 20 size groups, $d_b > d_{cr}$ (1.5-3.5 mm) were employed. The physical properties of R12 liquid and vapor were taken from the National Institute of Standards and Technology (NIST) [88].

The nucleation site density is strongly dependent on the heating wall material and finishing process which still requires a clear description [133]. Therefore, it is still necessary to do a calibration for N_{ref} in the model of Lemmert and Chawla [79]. For all DEBORA cases, $N_{ref} = 1.5 \times 10^{+10}$ m^{-2} and for the second cases $N_{ref} = 1.5 \times 10^{+8}$ m^{-2} yielded satisfactory results.

The measured and calculated distribution of bubble diameter, d_b, void fraction, α_g, bubble velocity, $\boldsymbol{U}_b$, and liquid temperature, T_l, in the measuring plane as well as wall temperature, T_w, with both RPI and the described model are shown in Figure 4.7 to Figure 4.13. The heat flux contribution due to bubble sliding, $\frac{Q_{sliding}}{Q_w}$, is also presented.

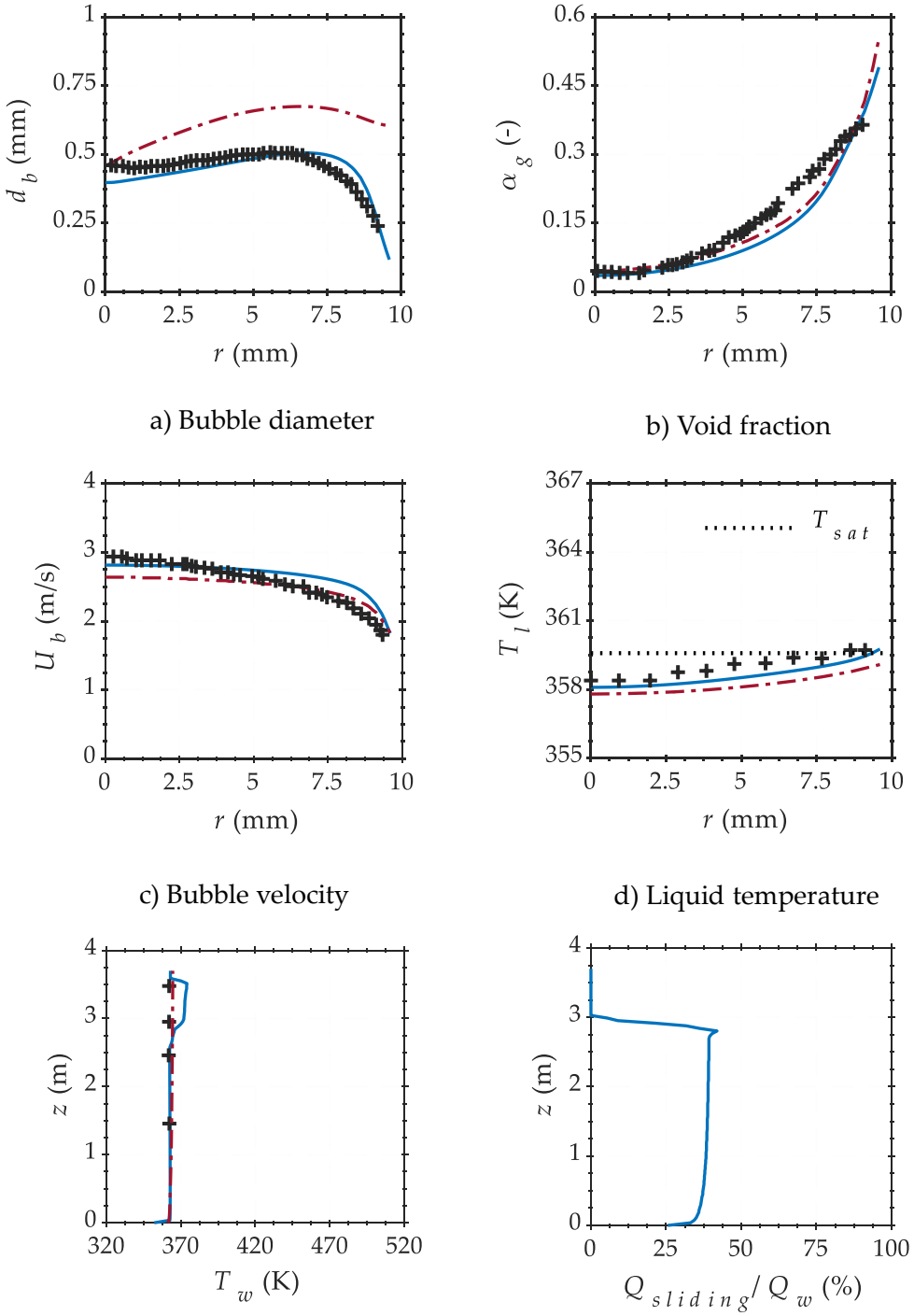

Figure 4.7: Comparison of measured and calculated values of bubble diameter, void fraction, bubble velocity, liquid, wall temperature and heat flux contribution due to bubble sliding for DEB1 (legend: — Present model, - - RPI, + Experiment).

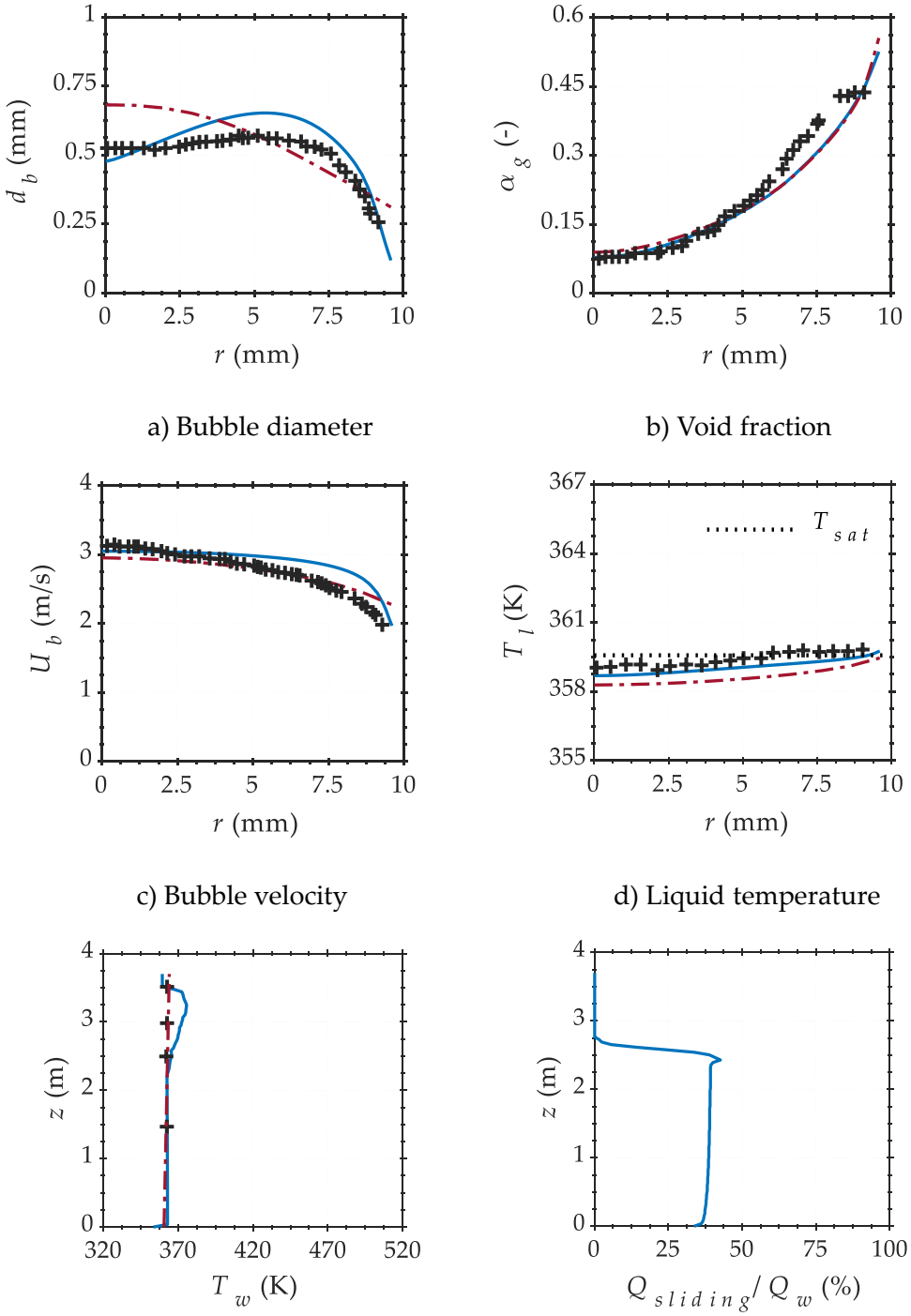

Figure 4.8: Comparison of measured and calculated values of bubble diameter, void fraction, bubble velocity, liquid, wall temperature and heat flux contribution due to bubble sliding for DEB2 (legend: — Present model, – – RPI, + Experiment).

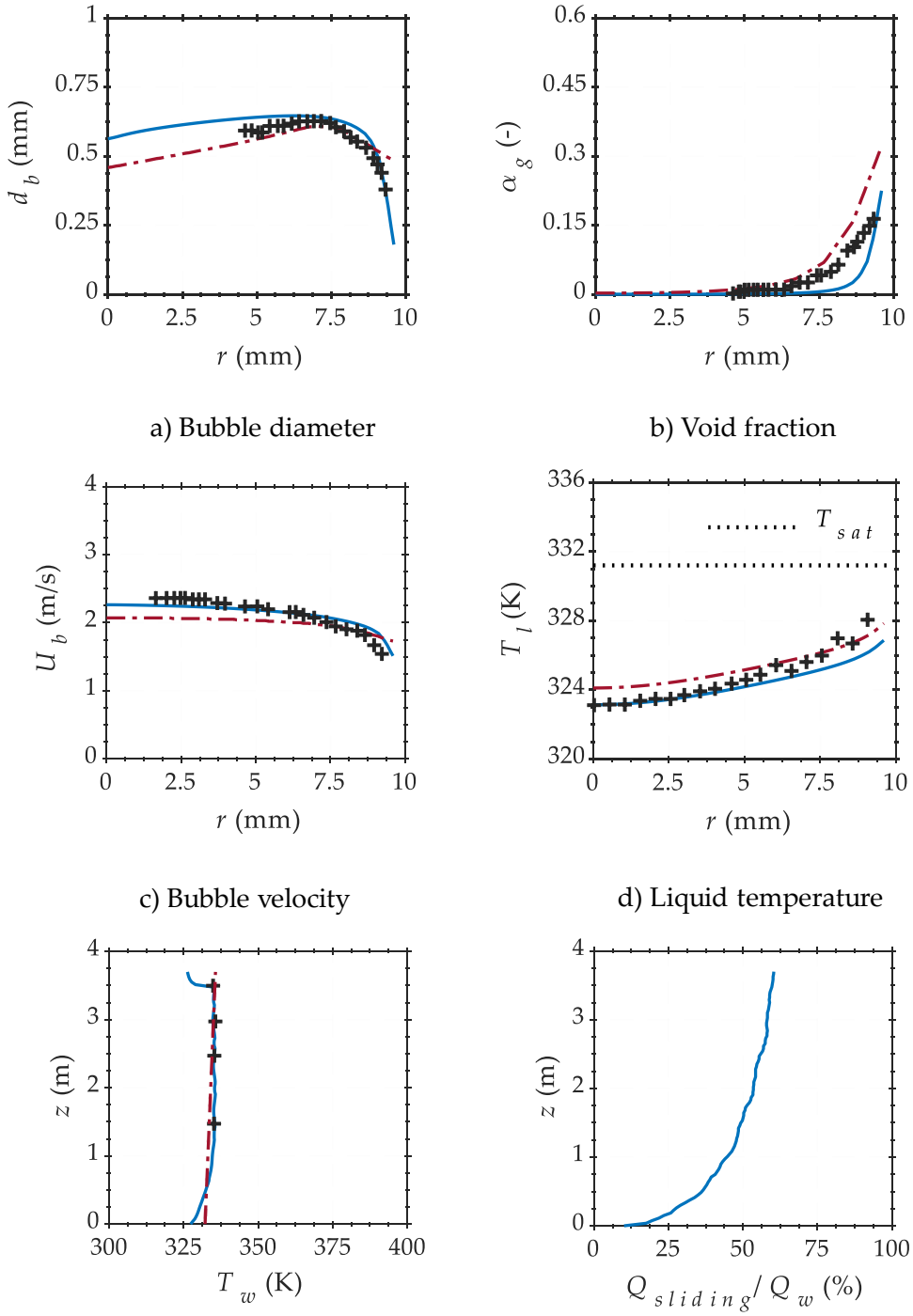

Figure 4.9: Comparison of measured and calculated values of bubble diameter, void fraction, bubble velocity, liquid, wall temperature and heat flux contribution due to bubble sliding for DEB3 (legend: — Present model, – – RPI, + Experiment).

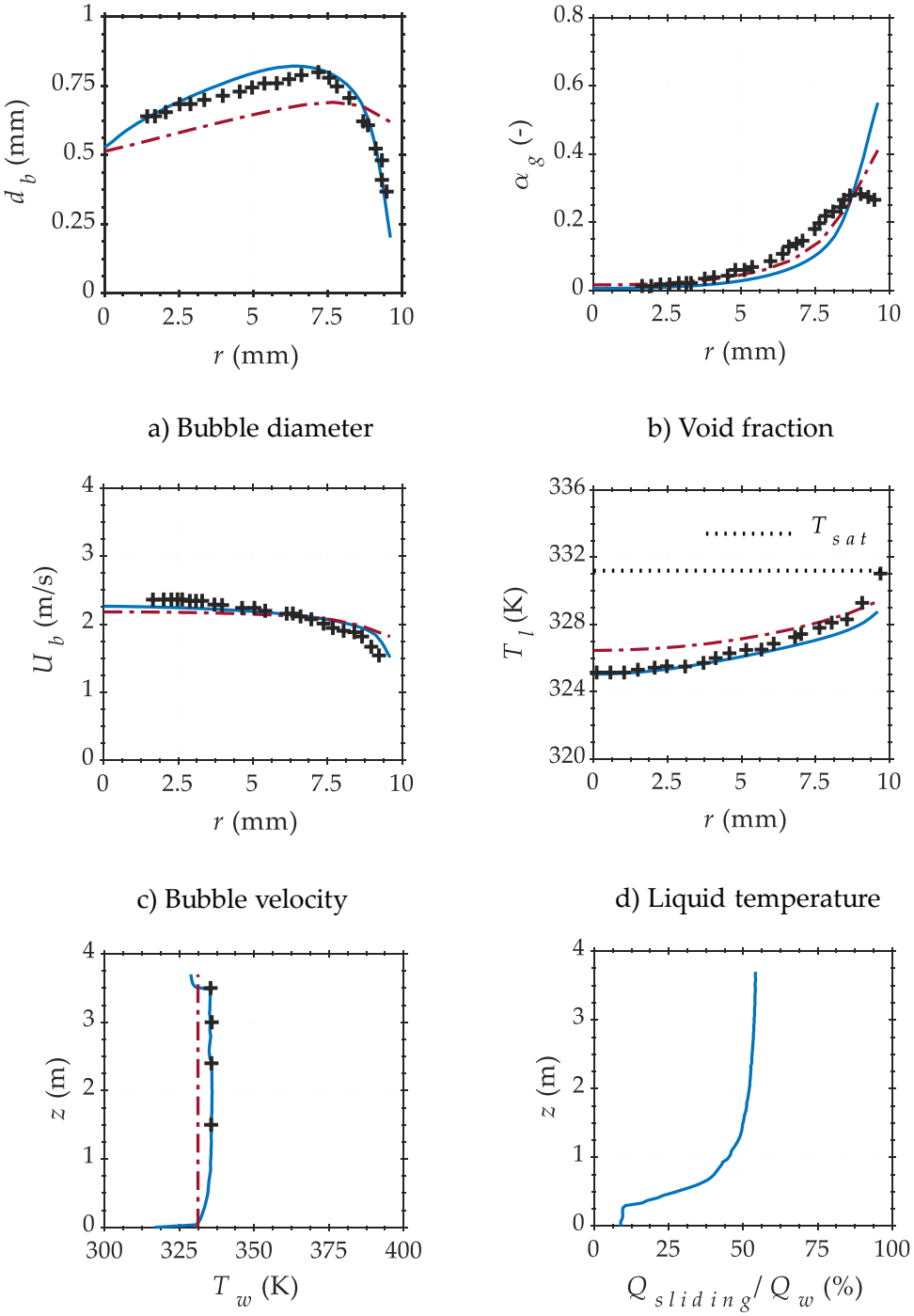

Figure 4.10: Comparison of measured and calculated values of bubble diameter, void fraction, bubble velocity, liquid, wall temperature and heat flux contribution due to bubble sliding for DEB4 (legend: — Present model, – – RPI, + Experiment).

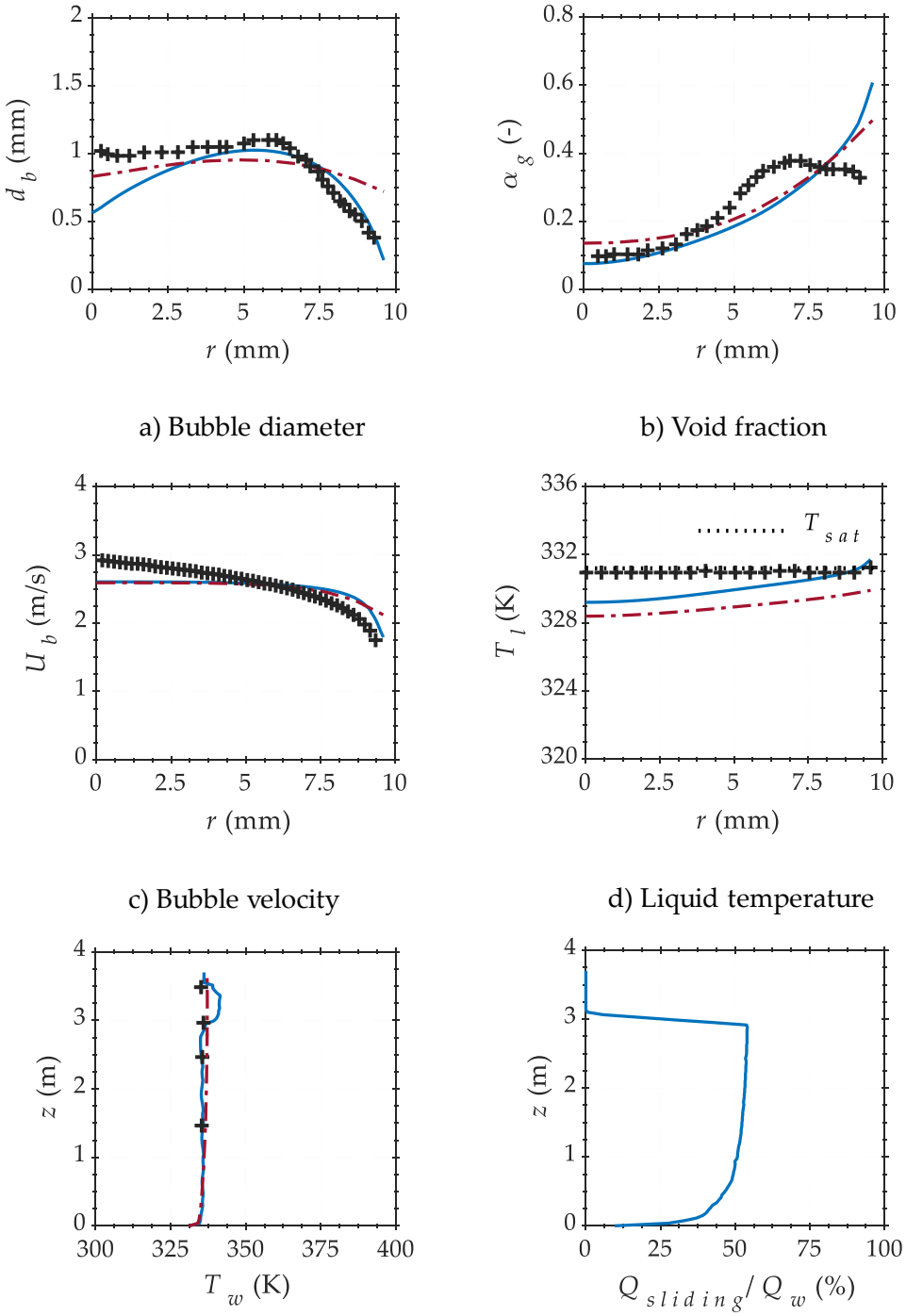

Figure 4.11: Comparison of measured and calculated values of bubble diameter, void fraction, bubble velocity, liquid, wall temperature and heat flux contribution due to bubble sliding for DEB5 (legend: — Present model, – – RPI, + Experiment).

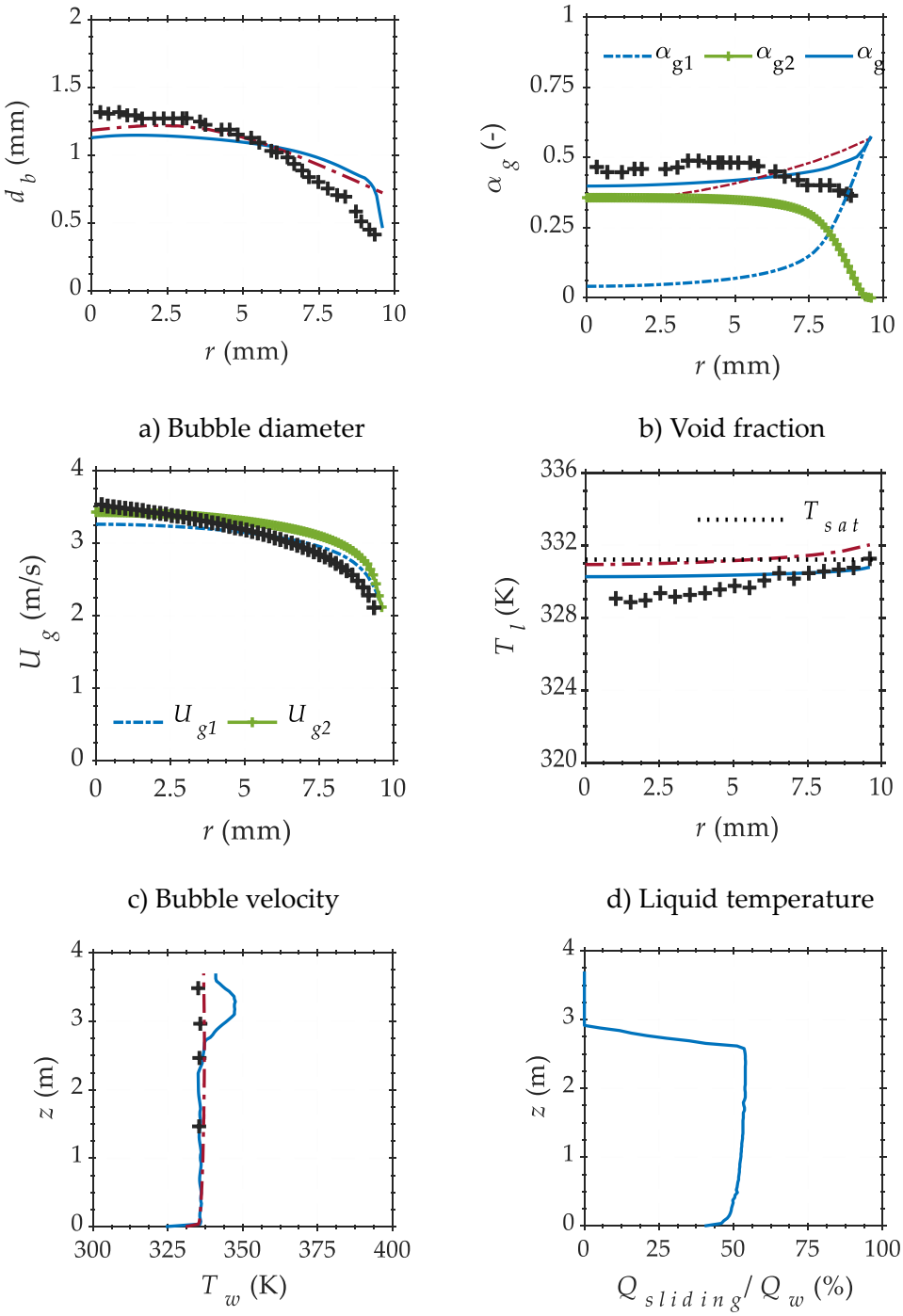

Figure 4.12: Comparison of measured and calculated values of bubble diameter, void fraction, bubble velocity, liquid, wall temperature and heat flux contribution due to bubble sliding for DEB6 (legend: — Present model, - - RPI, + Experiment).

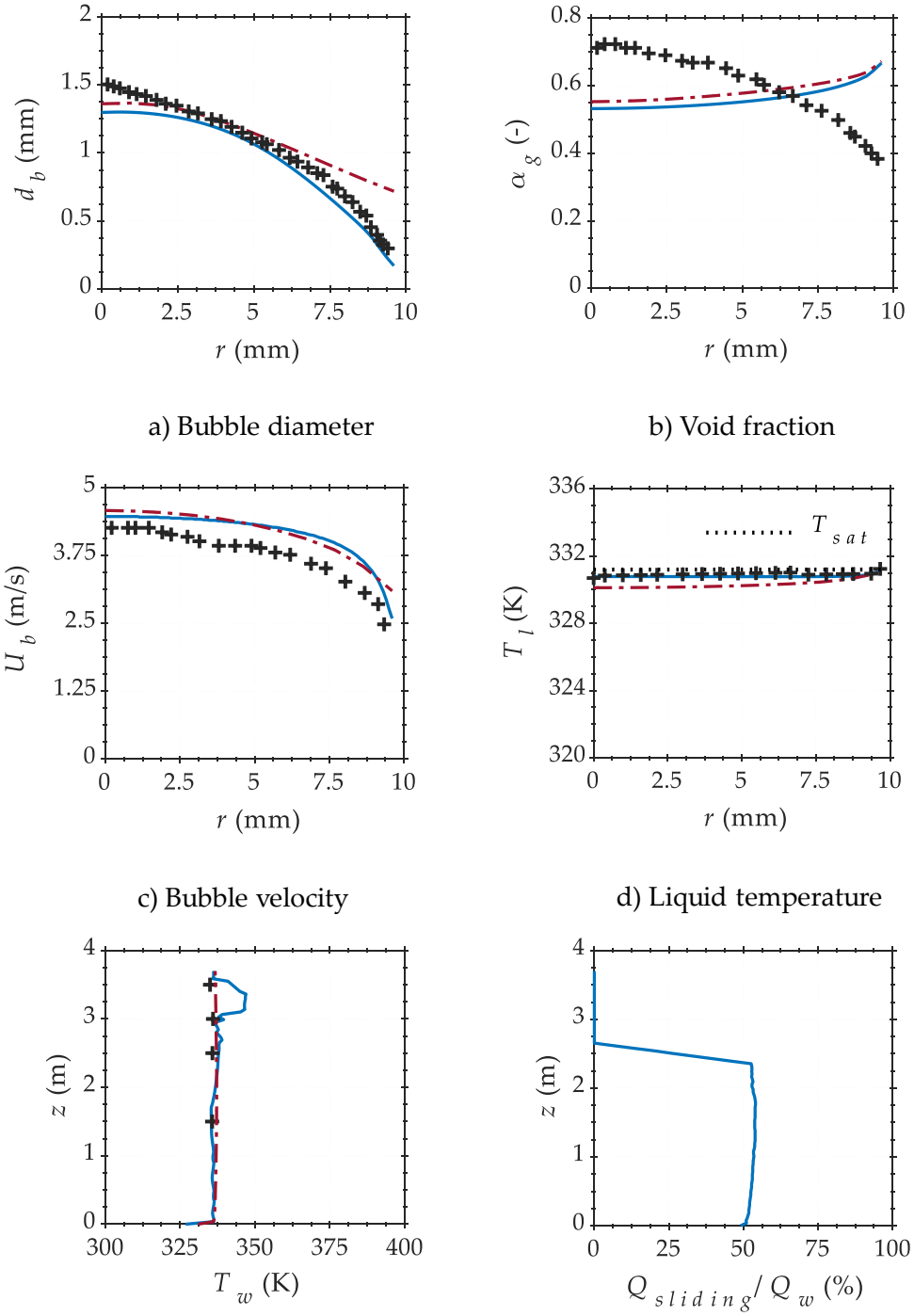

Figure 4.13: Comparison of measured and calculated values of bubble diameter, void fraction, bubble velocity, liquid, wall temperature and heat flux contribution due to bubble sliding for DEB7 (legend: — Present model, – – RPI, + Experiment).

Figure 4.7a to Figure 4.13a exhibit the radial bubble size distribution for DEB1 to DEB7 in the measuring plane. Smaller bubbles are found in the region near the heating wall since it is assumed that bubbles leave the heating wall with their lift-off diameter. The bubble size increases with increasing radial distance from the heating wall due to the high rate of bubble coalescence. This proves that the effect of bubble growth due to bubble coalescence exceeds the effect of bubble shrinkage due to condensation. For DEB6 where the iMUSIG model was used, the equivalent bubble diameter is calculated by Eq. (2.16) and shown in Figure 4.12a. The results of the present model provide a good agreement with the experimental data and it should be noted that the increase of RPI model prediction accuracy requires calibration of parameters as investigated by Krepper et al. [88].

The radial profiles of the predicted and measured void fraction in the measuring plane are depicted in Figure 4.7b to Figure 4.13b. The calculated void fraction in the near wall region is large and it is particularly obvious in the cases of DEB3 to DEB7 with a pressure of 1.46 MPa. The void fraction distribution is highly affected by non-drag forces such as turbulent dispersion and lift forces, whereby the lift force has the strongest effect. As stated before, the model of Tomiyama et al. [64] was used for lift force modelling. It is based on the migration of a single bubble in bulk liquid of a laminar flow and the swarm effects of bubbles are neglected in this model. More investigations on the bubble forces especially in the region near the heating wall are necessary. In addition, the applicability of the simple Ranz and Marshall [57] model for condensation modelling might be questionable [88]. The total void fraction, α_g, and the contribution of the two different velocity groups (α_{g1} and α_{g2}) for the DEB6 where the iMUSIG model was employed, are plotted separately in Figure 4.12b. According to the model of Tomiyama et al. [64], for small bubbles ($d_b < d_{cr}$) the lift force coefficient is positive which means that bubbles are pushed toward the heating wall. Conversely, for the large bubbles group ($d_b > d_{cr}$) the lift force coefficient is negative which means that they are pushed away from the heating wall. Therefore, small bubbles accumulate near the wall and the large ones transfer to the center of the pipe as depicted in Figure 4.12b.

Figure 4.7c to Figure 4.13c display the radial profiles of measured and calculated bubble velocity in the measuring plane. The minimum bubble velocity is observed in the region near the heating wall. Small bubbles at nucleation sites on the heating wall have a lower axial velocity compared to the large bubbles coming from the upstream of the flow. In addition, another explanation can be the wall shear effect, which results in a hydrodynamic drag on bubbles and reduce the velocity of bubbles adjacent to the heating wall. The predicted results by the present model provide a reasonable agreement with the experimental data.

The radial profiles of the predicted and measured liquid temperature in the measuring plane are depicted in Figure 4.7d to Figure 4.13d. It can be observed that the liquid temperature decreases with increasing distance from the heating wall. For the cases DEB4 to DEB6 the liquid temperature difference between the center of the pipe and near wall region is lower than for other cases, due to the lower inlet subcooling temperatures in these cases.

Figure 4.7e to Figure 4.13e show the wall temperature profile along the heating wall. As stated before, the dependency of the bubble dynamics parameters on the wall temperature were considered. As it is evident in all cases except DEB3 and DEB4, at the end of pipe there is a wall temperature increase. It proves that almost all of this area is covered by vapor bubbles and less subcooled liquid contacts the heating wall. For DEB3 and DEB4 this increase does not occur which can be due to the high inlet subcooling temperature.

The heat flux contribution due to bubble sliding for DEB1 to DEB7 is depicted in Figure 4.7f to Figure 4.13f. At the end of pipe for all cases except DEB3 and DEB4 the heat flux contribution due to bubble sliding is very small. For the cases there is a wall superheat increase at the end of the pipe and the nucleation site density increases too. It decreases the distance between the nucleation sites (Eq. (4.10)). Consequently, in these areas, bubbles cannot slide and therefore the heat flux contribution due to bubble sliding is very low.

4.2.2 Subcooled flow boiling of R134a in an annulus

The second validation case is subcooled flow boiling of R134a refrigerant in an annulus [136]. The inner diameter of the outer pipe and the outer diameter of the inner pipe are 27.2 mm and 9.5 mm. The annulus combines of three parts and its total length is 3.9 m. The length of the first unheated part that is an inlet section for the flow regulation is 1.35 m. The second part is a heated section with a 1.75 m length in which a constant heat flux is applied on the outer wall of the inner pipe. The last part is an unheated one located at the top with a length of 0.8 m. The measuring planes are located at different axial positions of $z = 0.48, 0.73, 0.98, 1.23, 1.48$ and 1.73 m from the start point of the heated section. The geometry of the pipe and the model setup in CFX are shown in Figure 4.14. Table 4.2 gives the boundary conditions.

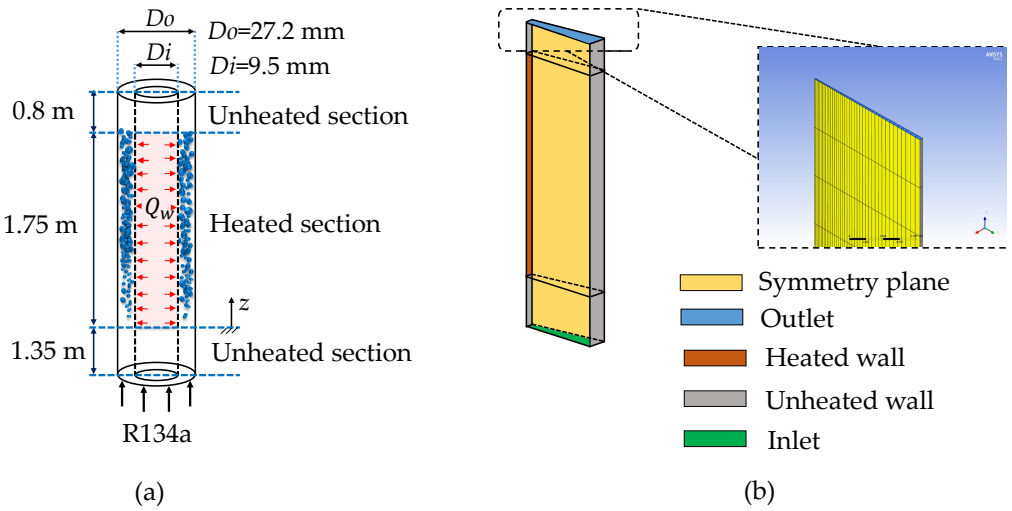

Figure 4.14: Sketch of a) R134a experiment geometry b) the model setup in CFX.

Table 4.2: Boundary conditions of the R134a subcooled flow boiling experiments.

Case No.	P (MPa)	G ($\frac{\text{kg}}{\text{m}^2.\text{s}}$)	Q_w ($\frac{\text{kW}}{\text{m}^2}$)	T_{in} (K)	ΔT_{sub} (K)
Test1	1.29	998	120.4	309.93	12.4
Test2	1.49	149	60.6	300.7	27.4
Test3	2.69	999	120.7	325.35	8.0

The radial profiles of void fraction, α_g, bubble Sauter mean diameter, d_{SM}, bubble velocity, $\boldsymbol{U}_b$, bubble passing frequency, fr and IAD, A_{if}, in the measuring planes are provided by the experiments [136]. The void fraction, bubble Sauter mean diameter and IAD are non-dimensionalized (α^*, $d^*{}_{SM}$, and $A^*{}_{if}$) as:

$$\alpha^* = \frac{\alpha_g}{\alpha_{ref}}, \quad d^*{}_{SM} = \frac{d_{SM}}{d_{SM,ref}}, \quad A^*{}_{if} = \frac{A_{if}}{A_{i,ref}}, \tag{4.14}$$

with α_{ref}, $d_{SM,ref}$ and $A_{i,ref}$ being the reference values of void fraction, bubble Sauter mean diameter and IAD in test1 at a radial position of 0.7 mm and an axial position of 1.73 m. The radial position, r, is non-dimensionalized by $r^* = \frac{r-R_i}{R_o-R_i}$ that R_i and R_o are the outer diameter of inner pipe and the inner diameter of outer pipe. $r^* = 1$ corresponds to the inner surface of the outer pipe and $r^* = 0$ to the outer surface of the heating wall.

The test section was modelled as a 2° sector in a quasi-2D cylindrical geometry in ANSYS CFX 18.2 and the numerical calculations were conducted with steady-

state conditions. To investigate mesh independency, three uniform grids, Mesh 1 (30×500), Mesh 2 (40×600) and Mesh 3 (50×700) were tested. The numbers 30, 40 and 50 denote the number of cells in lateral and 500, 600 and 700 are the ones in the axial direction. The grid refinement proved no change of the calculation results after the grid number has increased to Mesh 2. Therefore, the test section was modelled with 40 and 600 uniform grid cells and the model setup and boundary conditions were similar to the DEBORA cases. The MUSIG model with 20 bubble size groups from 0 to 2 mm ($\Delta d_B = 0.1\ \mathrm{mm}$) with the break-up and coalescence coefficients of $F_B = 0$ and $F_C = 0.1$ were used. The measured and calculated profiles of the non-dimensionalized void fraction, α^*, bubble Sauter mean diameter, ${d^*}_{SM}$, and IAD, ${A^*}_{if}$, in measuring planes that are located at different axial positions are shown. The distribution of calculated and measured bubble velocity, $\boldsymbol{U}_b$, and bubble passing frequency, fr, are given as well.

Figure 4.15 to Figure 4.17 show the radial profiles of the non-dimensional void fraction, α^*, in different measuring planes for all test cases. The general trend of the radial profiles of void fraction at different axial positions in all cases is similar. It has a maximum value in the region close to the heating wall and reduces as the measurement position moves toward the outer pipe. It is due to this fact that bubbles are generated on the heating wall with high frequencies causing severe coalescence in the bubble layer and transfer to the bulk liquid by the non-drag forces such as lift and turbulent dispersion and condense in the subcooled liquid bulk. In these cases, it is also evident that the calculated void fraction in the region near the wall is large. The possible reasons were explained in Section 4.2.1 for DEBORA cases. Comparing the results of void fraction profile for test1 and test3 (Figure 4.15 and Figure 4.17) proves that the effect of pressure (1.29 to 2.69 MPa) on the radial and axial distribution of void fraction does not seem to be significant when the liquid subcooling, mass flux and applied heat flux are similar. The predicted results of void fraction by the present model show a good agreement with the experimental data.

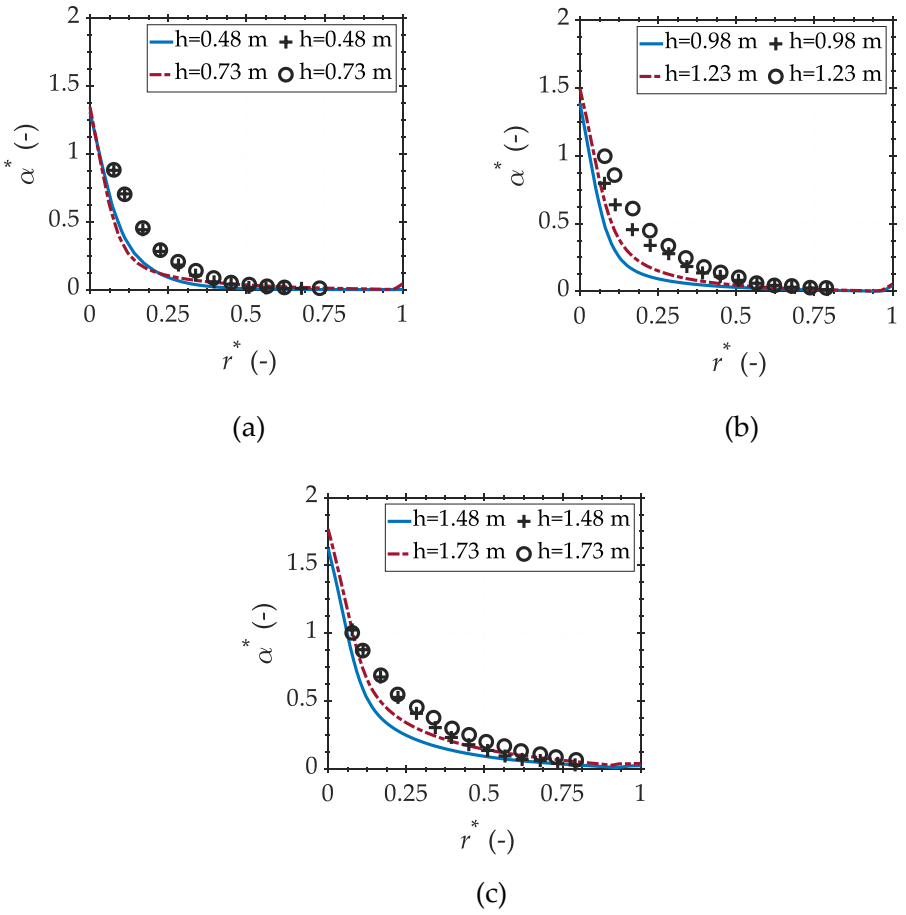

Figure 4.15: Comparison of measured and calculated values of void fraction at different axial positions of the annulus for test1 (legend: — - - Present model, +○ Experiment).

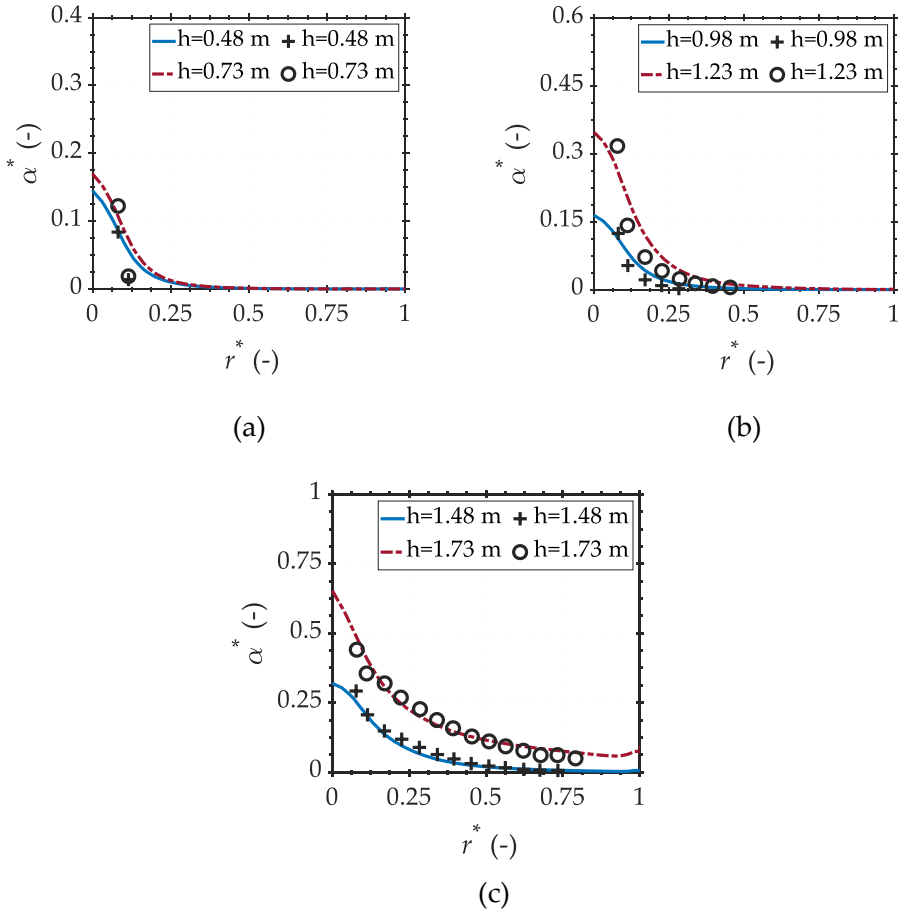

Figure 4.16: Comparison of measured and calculated values of void fraction at different axial positions of the annulus for test2 (legend: — — Present model, +∘ Experiment).

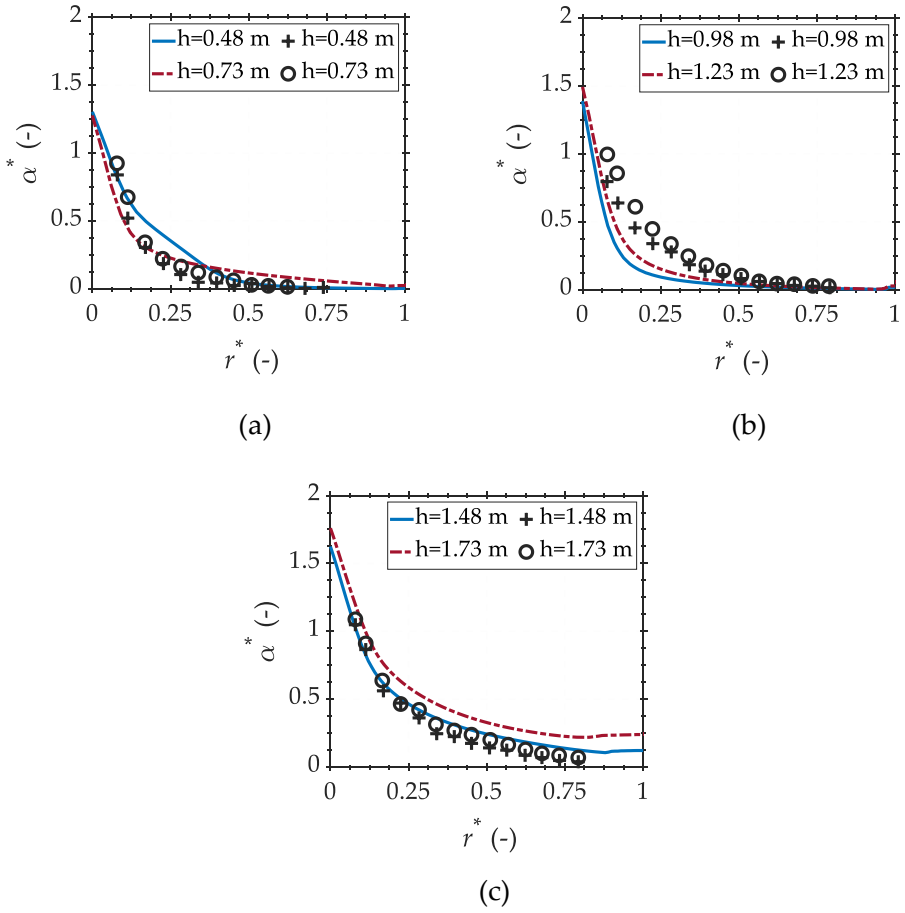

Figure 4.17: Comparison of measured and calculated values of void fraction at different axial positions of the annulus for test3 (legend: — - - Present model, +○ Experiment).

Figure 4.18 to Figure 4.20 exhibit the radial distribution of the non-dimensional bubble Sauter mean diameter, d^*_{SM}, and its propagation in different measuring planes for all tests. As it is assumed that bubbles are spherical, the bubble Sauter mean diameter is given as:

$$d_{SM} = \frac{6\alpha_g}{A_{if}}. \tag{4.15}$$

The bubble size in the regions near the heating wall is governed by the bubble lift-off and it is affected by break-up, coalescence and condensation when bubbles move toward the outer pipe. In test1 the bubble Sauter mean diameter increases toward the adiabatic outer pipe and shows a peak at the radial distance of around $r^* = 0.3$. From the bubble size distribution, it is deduced that at the position less than $r^* = 0.3$ the effect of bubble coalescence is dominant over the effect of condensation. For regions with radial position larger than this value, the coalescence becomes minor due to the decrease in bubble population and high rate of condensation. In test2 at

an axial position of 0.98 m, 1.23 m and 1.48 m the results exhibit maximum values in the region near the heating wall and a reduction toward the outer pipe. This is because of the high rate of condensation due to the high subcooling temperature. The trend of the radial profile of bubble Sauter mean diameter in test3 is similar to test1 although the bubble size in test1 is two times larger than in test3. This is due to the significant effect of pressure on the bubble size when the subcooling, mass flux and applied heat flux are similar

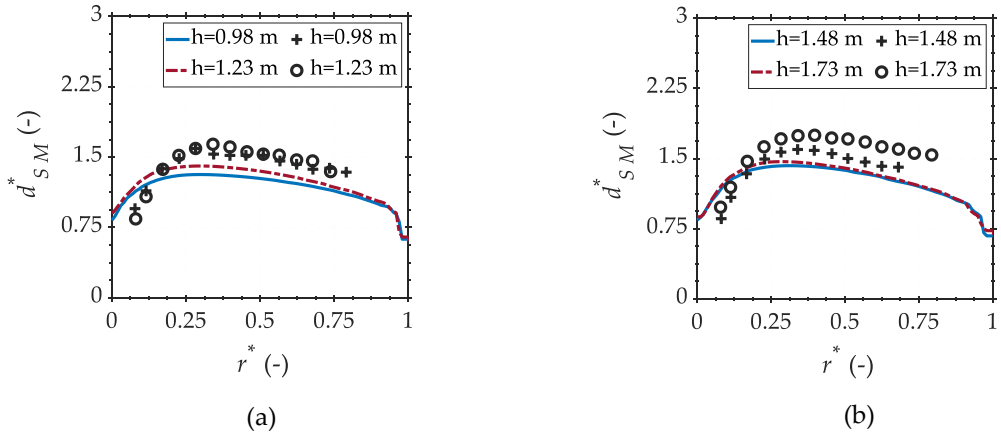

Figure 4.18: Comparison of measured and calculated values of bubble Sauter mean diameter at different axial positions of the annulus for test1 (legend: — – – Present model, +○ Experiment).

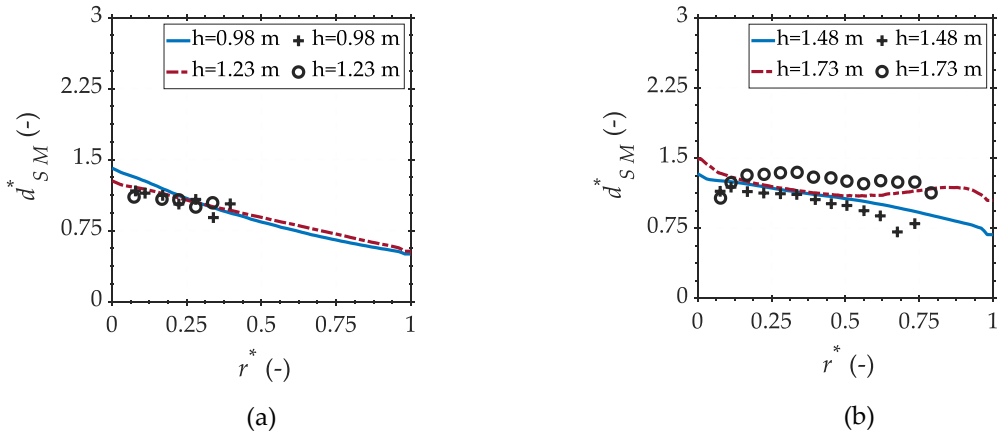

Figure 4.19: Comparison of measured and calculated values of bubble Sauter mean diameter at different axial positions of the annulus for test2 (legend: — – – Present model, +○ Experiment).

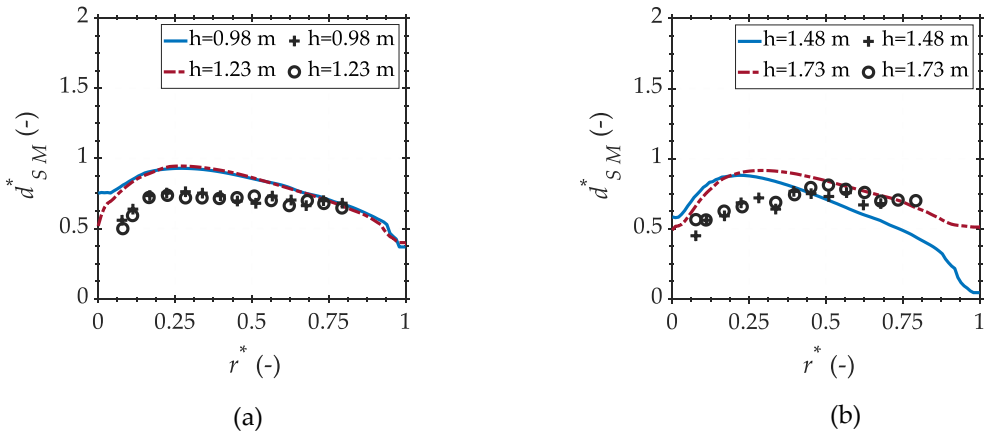

Figure 4.20: Comparison of measured and calculated values of bubble Sauter mean diameter at different axial positions of the annulus for test3 (legend: — - - Present model, +○ Experiment).

Figure 4.21 to Figure 4.23 illustrate the radial profiles of bubble velocity, $\boldsymbol{U}_b$, at different axial positions. The maximum bubble velocity is observed at some distance from the heating wall in all cases. Small generated bubbles at nucleation sites on the heating wall have a very low axial velocity compared to the relatively large bubbles coming from the upstream of the flow. Another explanation can be the wall shear effect, which results in a hydrodynamic drag on bubbles and decreases the velocity of bubbles adjacent to the heating wall. The calculated bubble velocity is overestimated in the regions near the wall due to the bubbles free slip boundary condition on the heating wall in CFD simulations. Comparing the bubble sizes and bubble velocities in test1 and test3 (Figure 4.18, Figure 4.20, Figure 4.21, and Figure 4.23) proves that increase in pressure reduces the bubble size causing high acceleration by drag, which results in a bubble velocity decrease. There is a noticeable difference between bubble velocities in test1 and test2 (Figure 4.21 and Figure 4.22) due to the difference between mass flux and void fraction.

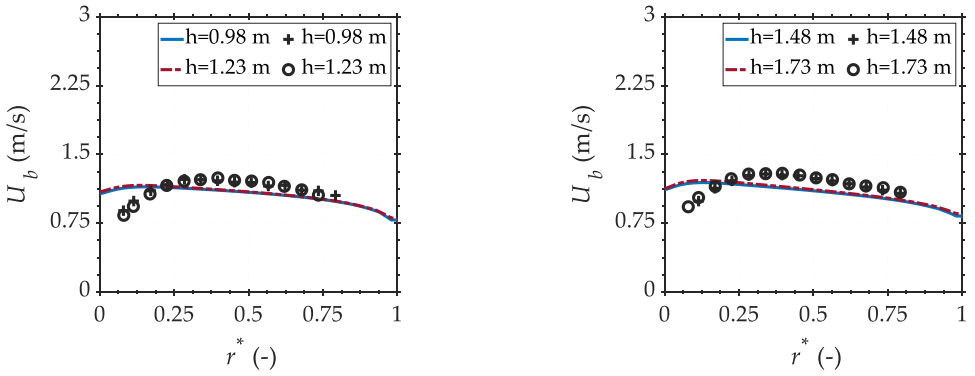

Figure 4.21: Comparison of measured and calculated values of bubble velocity at different axial positions of the annulus for test1 (legend: — — Present model, +○ Experiment).

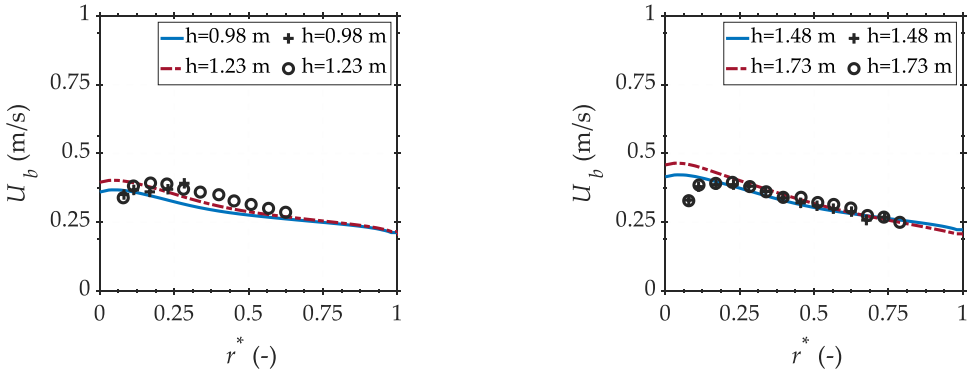

Figure 4.22: Comparison of measured and calculated values of bubble velocity at different axial positions of the annulus for test2 (legend: — — Present model, +○ Experiment).

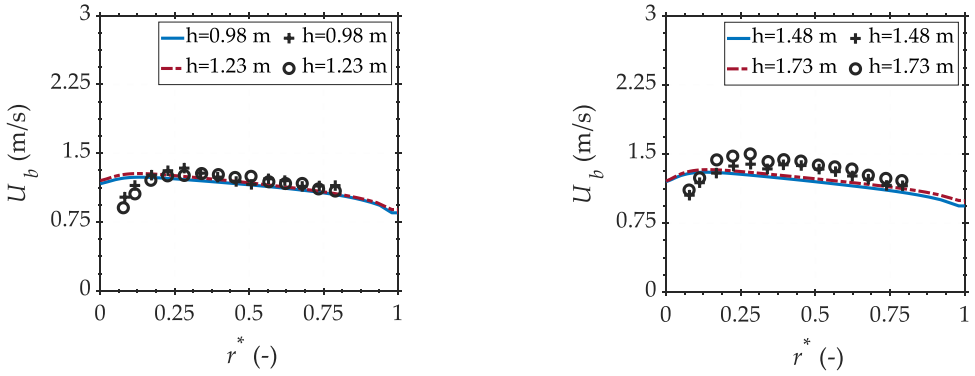

Figure 4.23: Comparison of measured and calculated values of bubble velocity at different axial positions of the annulus for test3 (legend: — — Present model, +○ Experiment).

The radial profiles of bubble passing frequency at different annulus axial positions are shown in Figure 4.24 to Figure 4.26. For calculation of bubble passing frequency the following equation is used [136],

$$fr = \frac{A_{if} \times \boldsymbol{U}_b}{4}. \tag{4.16}$$

The general trend of bubble passing frequency is similar to the void fraction but different in quantity. From Eqs. (4.15) and (4.16) the bubble passing frequency is proportional to the void fraction, bubble size and velocity according to,

$$fr = \frac{3\alpha_g \times \boldsymbol{U}_b}{2d_{SM}}. \tag{4.17}$$

The bubble passing frequencies in test1 are about 7 times higher than in test2 due to the impact of void of fraction and bubble velocity. Compared to test1, the bubble passing frequency of test3 provides about twofold increase, which is mainly because of the bubble size decrease.

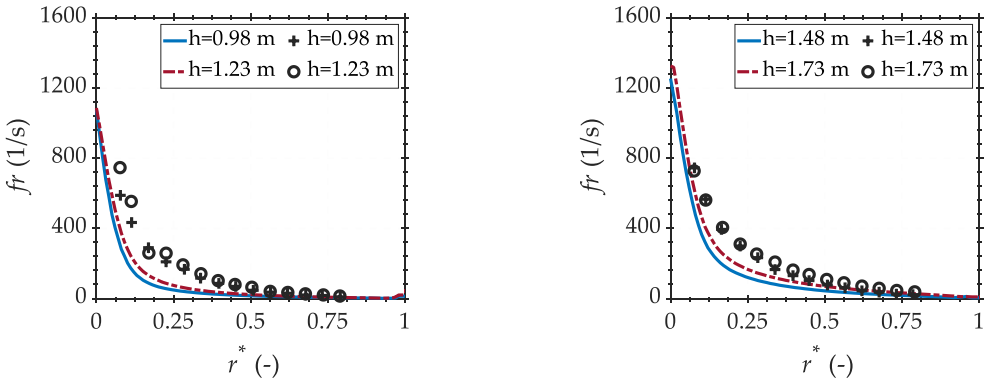

Figure 4.24: Comparison of measured and calculated values of bubble passing frequency at different axial positions of the annulus for test1 (legend: — — - Present model, +○ Experiment).

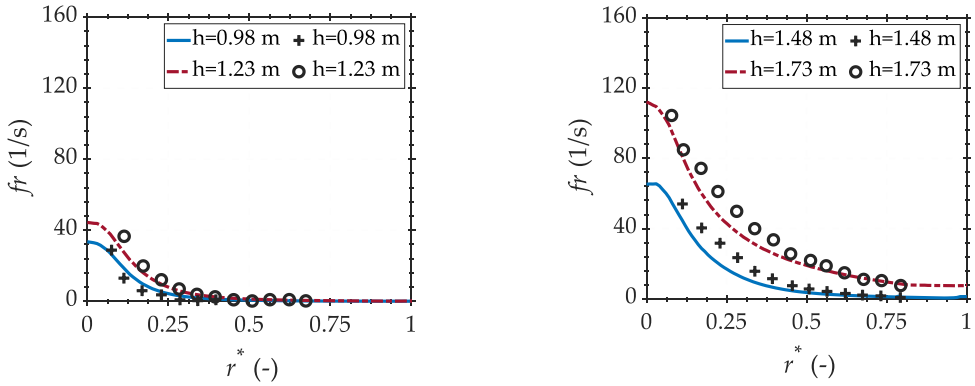

(a) (b)

Figure 4.25: Comparison of measured and calculated values of bubble passing frequency at different axial positions of the annulus for test2 (legend: — — Present model, +○ Experiment).

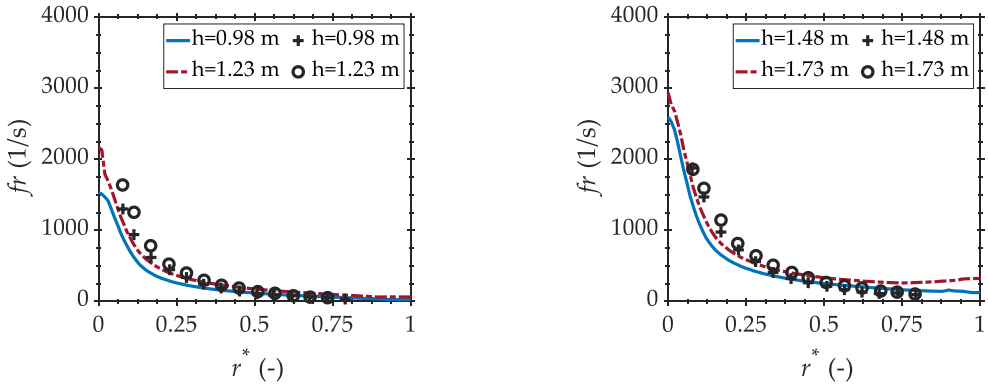

(a) (b)

Figure 4.26: Comparison of measured and calculated values of bubble passing frequency at different axial positions of the annulus for test3 (legend: — — Present model, +○ Experiment).

Figure 4.27 to Figure 4.29 depict the radial distributions of the non-dimensional IAD, A^*_{if}, at different axial positions for each case. The comparison of IAD in test2 and test3 proves that the axial evaluation of IAD in test2 is much more remarkable. This is because of the fact that test2 has a high inlet subcooling and therefore the significant change of liquid temperature in axial flow direction. This results in lower void fraction as shown in Figure 4.15 to Figure 4.17. The IAD of test3 shows about twofold increase compared to test1, which is mainly because of this fact that the bubble size reduces to half with the increase of pressure (Eq. (4.14)).

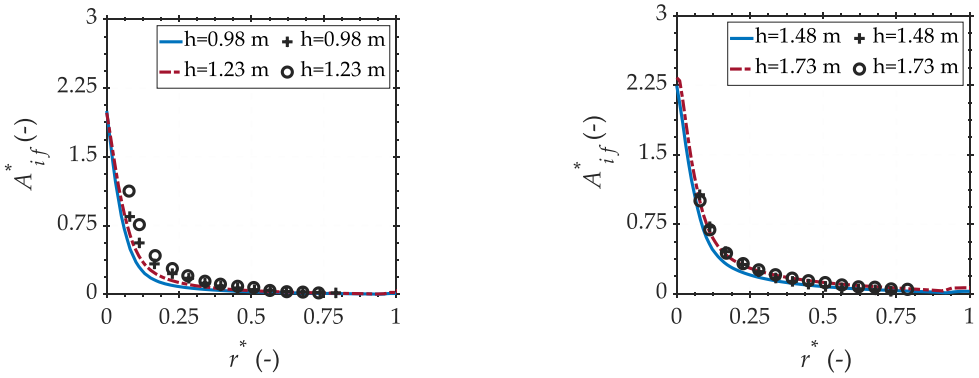

(a) (b)

Figure 4.27: Comparison of measured and calculated values of IAD at different axial positions of the annulus for test1 (legend: — – – Present model, +∘ Experiment).

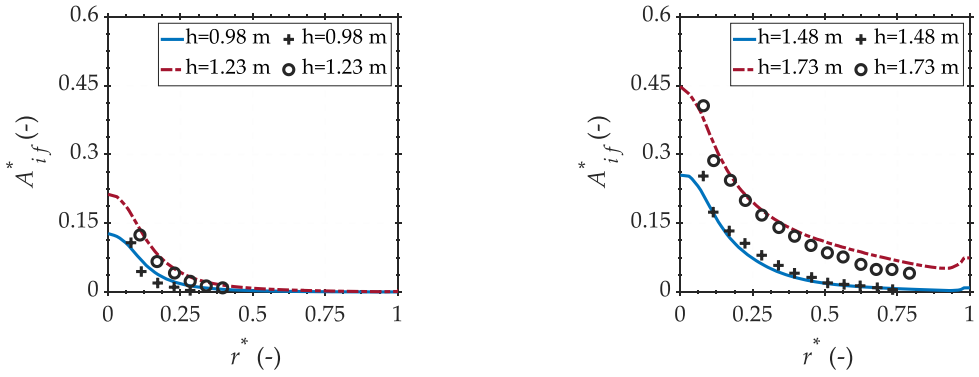

(a) (b)

Figure 4.28: Comparison of measured and calculated values of IAD at different axial positions of the annulus for test2 (legend: — – – Present model, +∘ Experiment).

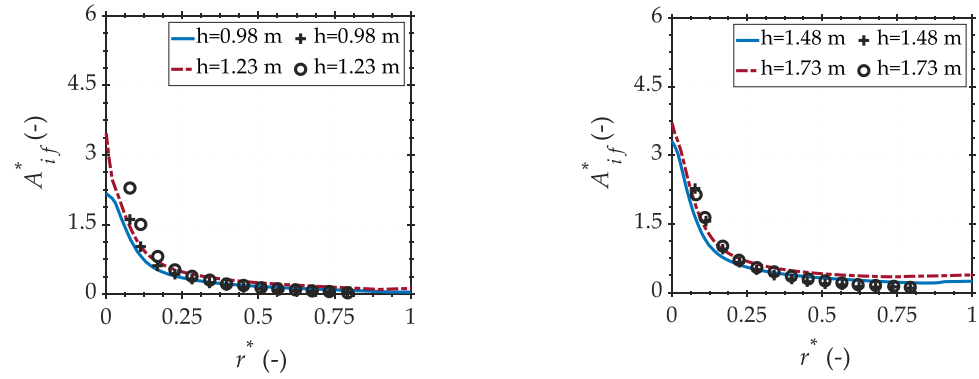

(a) (b)

Figure 4.29: Comparison of measured and calculated values of IAD at different axial positions of the annulus for test3 (legend: — – – Present model, +∘ Experiment).

4.3 Summary

This chapter provides the implementation of the bubble dynamics model introduced in Chapter 3 into the E-E framework as a sub-model for flow boiling modelling. This implementation requires an extension of nucleation site activation and heat-partitioning models. The prediction of bubble movement on the heating wall, the calculation of bubble sliding length and influence area during flow boiling were provided. The contribution of bubble sliding to the wall heat transfer was assessed and validation was made with ten experimental cases including subcooled flow boiling in a pipe and an annulus.

5 Modelling of flow boiling patterns in vertical pipes

In this chapter, the bubble dynamics model from Chapter 3 is implemented in the GENTOP framework for a simulation of transition patterns during the upward subcooled flow boiling inside a vertical heating pipe. The developed heat-partitioning model in Chapter 4 is adopted for modelling of high void fractions and given in Section 5.1. Section 5.2 discusses the impact of wall superheat, subcooling temperature and fluid velocity on the flow boiling transition patterns. The effects of flow morphologies on the wall heat transfer coefficient and the comparison of GENTOP and E-E two-fluid models results are given in this section as well. In the end, Section 5.3 provides the summary of this chapter.

5.1 Adopted wall heat-partitioning model for high void fractions

The wall heat-partitioning model introduced in Chapter 4 (Section 4.1) is given as:

$$Q_w = A_b Q_w + Q_{c,l}, \tag{5.1}$$

with A_b and $Q_{c,l}$ being the bubble influence area and convection heat flux to the liquid phase. For high void fraction flows where the continuous gas (GasC) structures are formed in the regions near the heating wall, this heat-portioning model has to be adopted. Therefore, it is adopted as [137]:

$$Q_w = A_b Q_w + Q_{c,l} + Q_{c,g}, \tag{5.2}$$

with $Q_{c,g}$ being the heat flux to the GasC structures on the heating wall as shown in Figure 5.1. The term A_b is the heating wall area fraction influenced by dispersed bubbles (GasD), which was discussed and calculated in Chapter 4, Section 4.1.1.

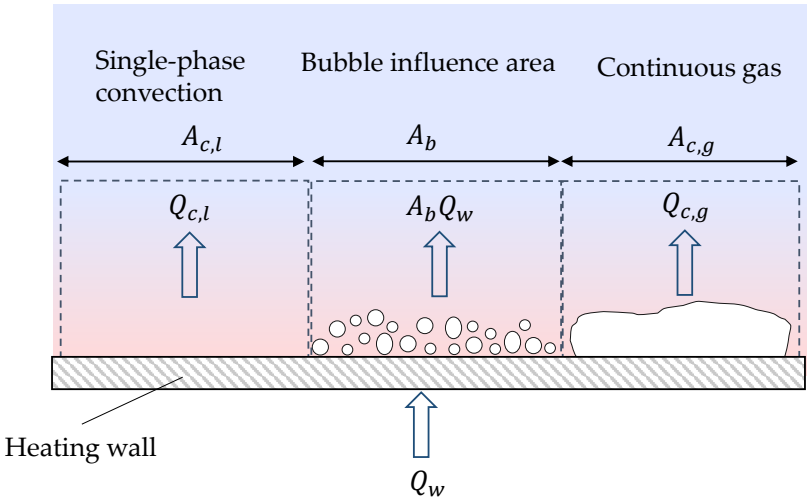

Figure 5.1: Schematic of the adopted heat-partitioning model for high void fraction flows.

The single-phase convection heat flux to liquid, $Q_{c,l}$, in Eq. (5.2) is given as:

$$Q_{c,l} = h_{c,l} A_{c,l} \left(T_{w,ac} - T_l\right), \tag{5.3}$$

with $h_{c,l}$ being the liquid heat transfer coefficient given by Eq. (2.98). The total wall area fractions influenced by GasD, A_b, GasC, A_{cg}, and liquid phase, A_{cl}, is equal to 1. Therefore, in Eq. (5.3), the term $A_{c,l}$ is calculated as:

$$A_{c,l} = 1 - A_b - A_{c,g}, \tag{5.4}$$

with $A_{c,g}$ being the GasC area fraction on the heating wall which is evaluated as its void fraction in the control volume adjacent to the wall [137]. In Eq. (5.2), $Q_{c,g}$ denotes the single-phase convection from the heating wall to GasC and is given as:

$$Q_{c,g} = A_{c,g} h_{c,g} \left(T_{w,ac} - T_{sat}\right), \tag{5.5}$$

with $h_{c,g}$ being the gas phase convection heat transfer coefficient and is calculated as:

$$h_{c,g} = \frac{\rho_g C_{p,g} \boldsymbol{U}_\tau}{T_g{}^+}. \tag{5.6}$$

As a demonstration example, an upward subcooled water flow in a vertical heating pipe was modelled by ANSYS CFX 18.2. The length and diameter of the pipe are 0.5 m and 0.025 m and the water flow enters the pipe at a pressure of 1 atm. In order to investigate the impacts of wall superheat, subcooling temperature and

fluid velocity on the flow patterns, seven cases were defined as summarized in Table 5.1.

Table 5.1: Boundary conditions of the test cases.

Case No.	ΔT_{sup} (K)	ΔT_{sub} (K)	$\boldsymbol{U}_{in}$ ($\frac{\mathrm{m}}{\mathrm{s}}$)
1	8	3	0.2
2	10	3	0.2
3	12	3	0.2
4	10	4	0.2
5	10	5	0.2
6	10	3	0.3
7	10	3	0.4

The simulations were carried out with a transient scheme for 10 seconds. The heating pipe was modelled as a full 3D geometry with 103653 hexahedral elements. The grid spacing was on average 2 mm with $y^+ = 250$ for the temperature of liquid adjacent to the wall. Table 5.2 summarizes the numerical scheme.

Table 5.2: Employed solver set up for GENTOP test cases.

Analysis type	Transient, $\Delta t = 0.002$ s
Transient scheme	First Order Backward Euler
Convergence control	Timescale control, Min./Max. coefficients loops: 4/40
Residual type	RMS
Residual target	10^{-4}

The gas phase was described in the iMUSIG framework by two GasD (GasD1 and GasD2) and a GasC. For the water-vapor fluid flow at $P = 1$ atm the critical bubble diameter which refers to the one for lift force sign change is $d_{cr} = 5.4$ mm. For each of GasD1 ($d < d_{cr}$) and GasD2 ($d > d_{cr}$), five size fractions were used. For the bubble size discretization, an equidistant bubble diameter of 1 mm was used and all gaseous phases were assumed at saturation temperature. All gas structures with

a spherical equivalent diameter equal or larger than 10 mm were assigned to GasC. For GasD interaction forces and turbulence modelling the ”baseline” and BIT models introduced in Section 2.3.4 were used. The models of Luo and Svendsen [61] and Prince and Blanch [60] for GasD breakup and coalescence modelling with coefficients $F_B = 0.01$ and $F_C = 2$ were used. Table 5.3 summarizes the employed correlations for the modelling of GasC interfacial transfers (see Section 2.5 for the mathematical formulations of given models).

Table 5.3: Interfacial exchange terms for GasC.

Exchange term	**Model**
Drag force coefficient	Höhne and Vallée [110] (Eq. (2.116))
Surface tension force	Brackbill et al. [112] (Eq. (2.124))
Clustering force	Höhne et al. [109] (Eq. (2.123))
Lift force coefficient	Montoya et al. [108] (Eq. (2.121))
Complete coalescence	Hänsch et al. [27] (Eq. (2.131))
Entrainment	Ma et al. [113] (Eq. (2.132))
Phase transfer	Hughmark [58] (Eq. (2.27))
Sub-grid wave turbulence	Höhne and Mehlhoop [107] (Eq. (2.133)
Damping turbulence	Höhne and Mehlhoop [107] (Eq. (2.139)

5.2 Results and discussions

5.2.1 Effect of wall superheat on the flow boiling transition patterns

Figure 5.2 shows the time course of averaged volume fractions of GasD, GasC, total gas (GasT) and liquid for case1, case2, and case3. The GasD volume fraction is defined as the sum of GasD1 and GasD2 volume fractions and similar GasT is the summation of GasD and GasC ones.

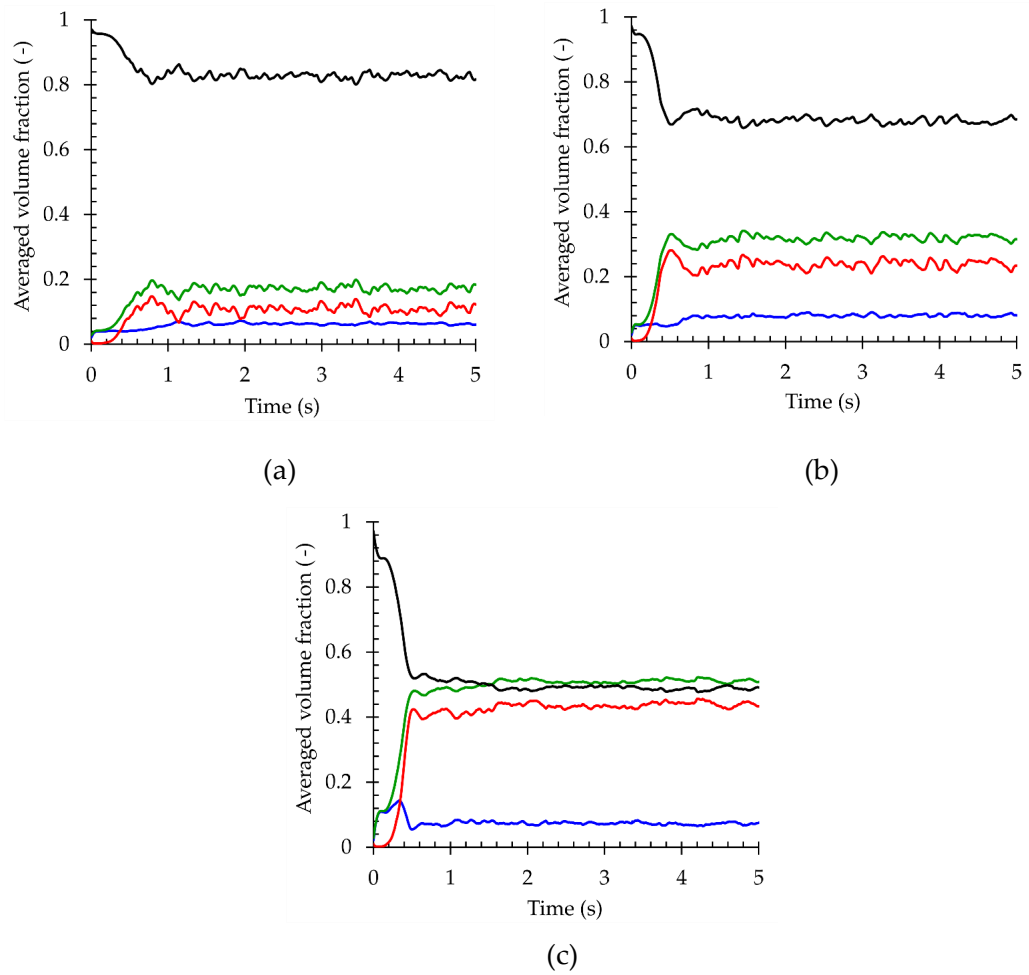

Figure 5.2: Averaged volume fractions of GasD, GasC, GasT and liquid for a) case1 ($\Delta T_{sup} = 8$ K) b) case2 ($\Delta T_{sup} = 10$ K) c) case3 ($\Delta T_{sup} = 12$ K)(legend: GasD GasC GasT Liquid).

At the beginning of the heating up process, GasD is generated on the heating wall. Next, approximately after 0.2 s, GasC is formed because of the GasD coalescence and the evaporation at the bubble interface. Later on, more liquid is converted into vapor and consequently, the vapor volume fraction reaches an almost constant value with lower oscillations. As expected, increasing the wall superheat in case1, case2, and case3 leads to higher GasC and consequently higher GasT formation.

The time course of the averaged liquid temperature in the flow domain for case1, case2, and case3 is shown in Figure 5.3. Increasing the wall superheat leads to an increase of the averaged liquid temperature and after 1 s and 0.6 s, the domain averaged temperature reaches saturation in case2 and case3 respectively. However, the average liquid temperature in case1 remains constantly below saturation temperature in the whole domain. From Figure 5.2 and Figure 5.3 it can be seen that steady state is reached after 2 s problem time.

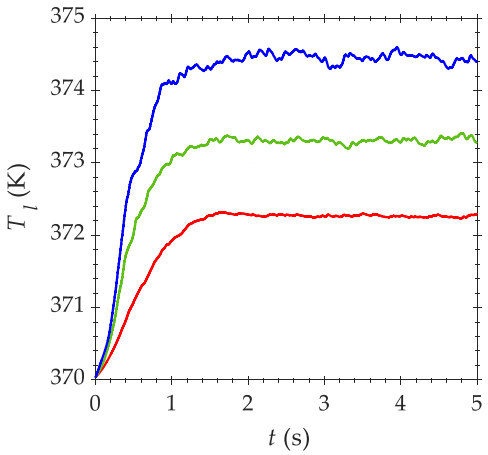

Figure 5.3: Time course of the average liquid temperature for case1 ($\Delta T_{sup} = 8$ K) case2 ($\Delta T_{sup} = 10$ K), and case3 ($\Delta T_{sup} = 12$ K)(legend: case1 case2 case3).

Figure 5.4 to Figure 5.6 show the distribution of GasD, GasC and GasT void fractions in a vertical plane at the center of pipe after 2 s. The acceleration of flow which results in varying vapor and liquid velocities creates a series of changes in the flow regime patterns. At the inlet, pure liquid enters the pipe and small bubbles are generated on the heating wall (see Figure 5.4a to Figure 5.6a). Because of the bubbles coalescence and evaporation, the size of bubbles increases until GasC formation. When mass transfer to GasC begins and its void fraction exceeds the threshold value ($\alpha_c > 0.5$ [109]), the cluster force agglomerates the GasC void fraction and large gas structures become resolved. With further coalescence, these structures form distorted slugs which rise to the top of the pipe due to buoyancy and upward flow.

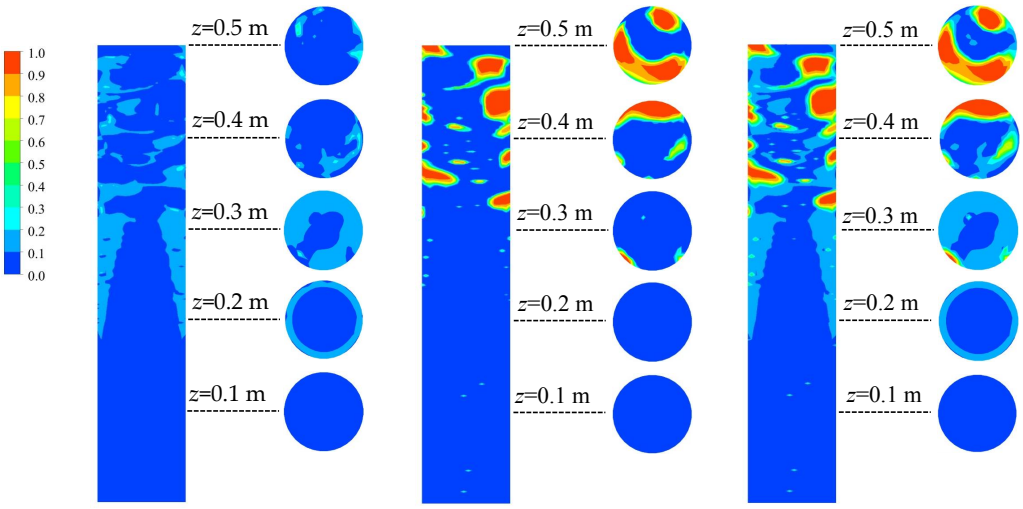

Figure 5.4: a) GasD b) GasC and c) GasT void fraction in transition from bubbly flow to slug flow for case1 ($\Delta T_{sup} = 8$ K) at $t = 2$ s (not to scale).

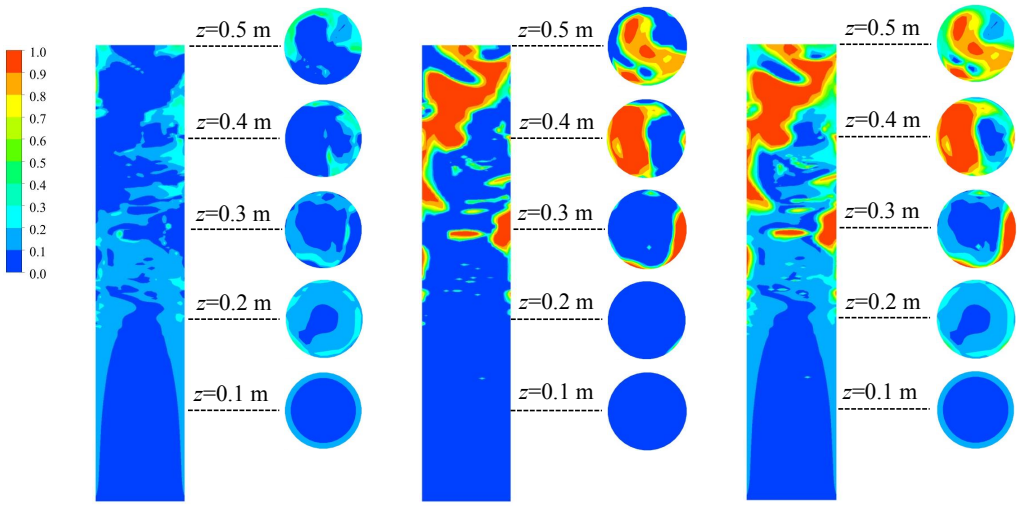

Figure 5.5: a) GasD b) GasC and c) GasT void fraction in transition from bubbly flow to slug flow for case2 ($\Delta T_{sup} = 10$ K) at $t = 2$ s (not to scale).

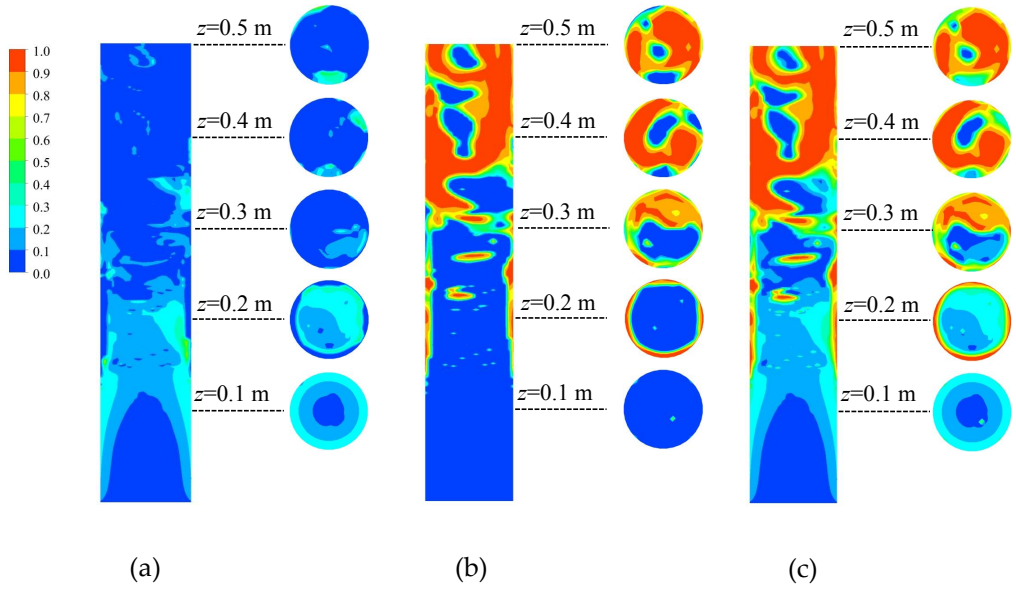

Figure 5.6: a) GasD b) GasC and c) GasT void fraction in transition from bubbly flow to slug flow for case3 ($\Delta T_{sup} = 12$ K) at $t = 2$ s (not to scale).

Figure 5.7a shows the cross-sectional and time-averaged (2 to 10 s) values of the GasT void fraction, α_T, along the pipe for case1, case2, and case3. For case1, at axial positions lower than 0.2 m, there is a region of very low void fraction ($\alpha_T < 0.1$). For cases2 and 3 this transition point is lower (0.12 m and 0.03 m) which is because of higher wall superheat.

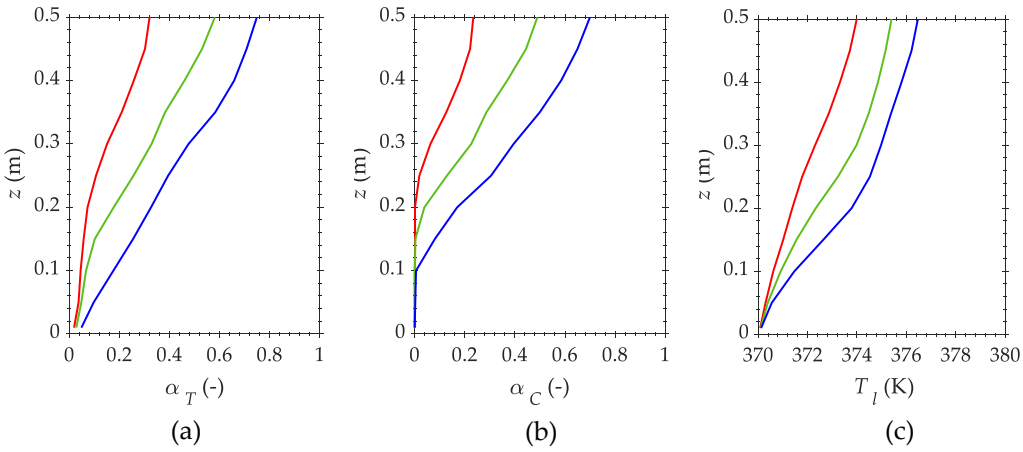

Figure 5.7: Distribution of cross-sectional and time-averaged values of a) GasT void fraction b) GasC void fraction c) liquid temperature for case1 ($\Delta T_{sup} = 8$ K), case2 ($\Delta T_{sup} = 10$ K), and case3 ($\Delta T_{sup} = 12$ K)(legend: case1 case2 case3).

Figure 5.7b shows the cross-sectional and time-averaged values of GasC void fraction, α_C, along the pipe. GasC originates for case1, case2, and case3 at axial positions of 0.2 m, 0.16 m and 0.1 m respectively. This can be explained by this fact that

increasing wall superheat leads to a higher evaporation rate and consequently an earlier formation of GasC. The cross-sectional and time-averaged values of liquid temperature is depicted in Figure 5.7c. With raising the wall superheat from case1 to case3, the average temperatures reach saturation at axial positions of 0.37 m, 0.24 m, and 0.17 m respectively.

Figure 5.8 shows the cross-sectional averaged values of GasD1, GasD2, GasD, GasC and GasT void fractions for case1, case2, and case3 after 2 s. For case1, it shows that between pipe inlet until the axial position of 0.24 m, only GasD is generated. For case2 and case3 the axial positions are 0.18 m and 0.1 m as wall superheat is higher. Because of the higher subcooling in the lower part of the pipe there is more bubble condensation and formation of smaller bubbles. However, by increasing the liquid temperature along the pipe and consequently more evaporation bubbles become larger until GasC is formed. In addition, increasing wall superheat in case1, case2, and case3 leads to more GasC formation in the whole domain.

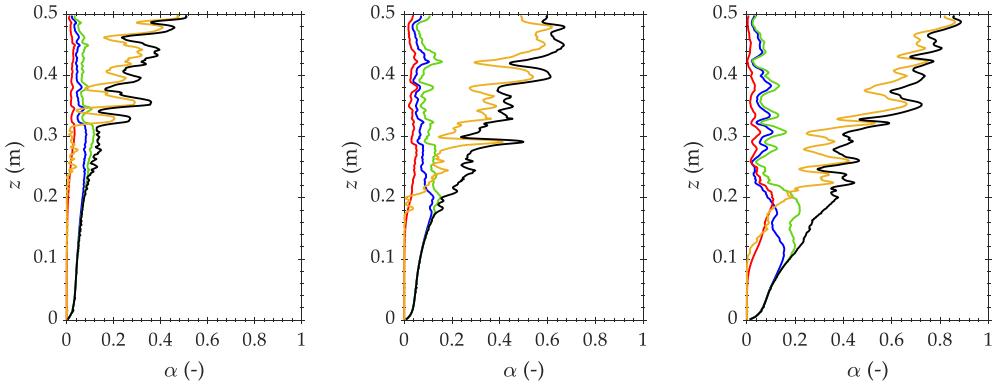

Figure 5.8: Cross-sectional averaged profiles of GasD1, GasD2, GasD, GasC and GasT void fractions for a) case1 ($\Delta T_{sup} = 8$ K) b) case2 ($\Delta T_{sup} = 10$ K) c) case3 ($\Delta T_{sup} = 12$ K) at $t = 2$ s (legend: GasD1 GasD2 GasD GasC GasT).

The time-averaged distribution of GasT void fraction for case1, case2, and case3 are depicted in Figure 5.9. It shows that wall superheat increase shifts the starting point of GasT void fraction accumulation to lower axial positions. Figure 5.10 shows the time-averaged distribution of the liquid superheating temperature ($T_l - T_{sat}$). As expected, regions near the heating wall have the highest superheating. In addition, by increasing the wall superheat, the maximum liquid superheating (3 K) point occurs at lower axial positions. Comparing Figure 5.9 and Figure 5.10 reveals that in the regions of high liquid superheating, high evaporation rate and consequently high void fraction occurs.

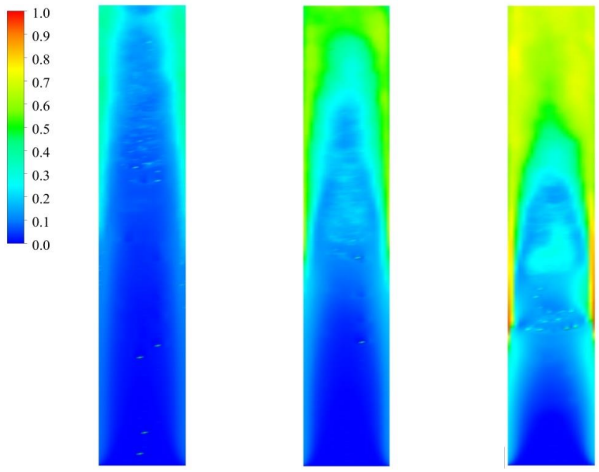

Figure 5.9: Distribution of the time-averaged GasT void fraction for a) case1 ($\Delta T_{sup} = 8$ K) b) case2 ($\Delta T_{sup} = 10$ K) c) case3 ($\Delta T_{sup} = 12$ K).

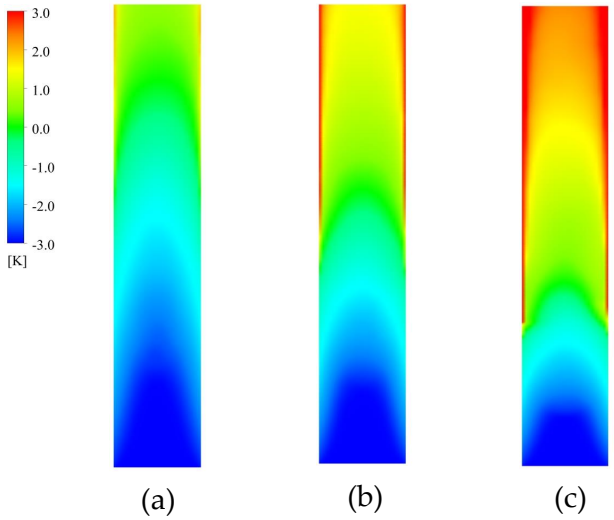

Figure 5.10: Distribution of the time-averaged liquid superheating temperatur for a) case1 ($\Delta T_{sup} = 8$ K) b) case2 ($\Delta T_{sup} = 10$ K) c) case3 ($\Delta T_{sup} = 12$ K).

5.2.2 Effect of flow morphologies on the wall heat transfer coefficient

For thermal-hydraulic analysis of the flow boiling, the temporal wall heat transfer coefficient, h_w, the GasD and GasC void fractions (α_D and α_C) are plotted in Figure 5.11 along a vertical line on the wall at $t = 2$ s. The distribution of GasT void fraction, α_T, in the middle plane of the pipe is shown as well. In case1 (Figure 5.11a) with the lowest wall superheat, α_T is low and consequently h_w is almost

constant in the lower part (axial position lower than $z = 0.2$ m). In other words, in this region, the boiling process has not been significantly initiated and single-phase forced convection from the heating wall to the liquid phase is the dominant heat transfer mechanism. Further down the pipe, where GasC is accumulated at the heating wall the liquid film is fully consumed (at positions (a) and (b)) and a sharp decrease occurs in the value of h_w. The formation of GasC structures also significantly reduces h_w [138]. Like the region between positions (c) and (d) where a dryout is formed. This notable reduction is due to the single-phase convection from the heating wall to GasC, which is greatly smaller than phase-change heat transfer. By increasing the wall superheat in case2, the GasD void fraction starts to increase from the pipe inlet which results in an increase of h_w. Similar to case1, the GasC coverage on the wall decreases h_w (positions (a) and (c) in Figure 5.11b). It is also observed that h_w increases in the regions where no GasC structures are found, that is, where GasD is formed on the heating wall. For instance, at positions (b) and (d) in case2 (Figure 5.11b). It demonstrates that dispersed bubbles formation on the heating wall supports the heat transfer. These increases and decreases in h_w due to GasD and GasC formation on the heating wall can also be observed in case3 (Figure 5.11c).

5.2.3 Comparison of GENTOP and Eulerian-Eulerian two-fluid models

The mechanistic bubble dynamics and heat-partitioning models from Chapter 3 and 4 were implemented in the well-established and frequently used E-E two-fluid framework. The results obtained by the E-E two-fluid and GENTOP models are compared. For the simulation of case1, case2, and case3 in the E-E two-fluid framework, the iMUSIG model including two GasD and a continuous liquid phase were employed. For both models the same grid size was used. For GasD interaction forces and turbulence modelling, the ”baseline” and BIT models introduced in Section 2.3.4 were used.

Figure 5.12 illustrates the distribution of total void fraction at $t = 2$ s for case1, case2, and case3. The E-E two-fluid model does not capture the interfacial structures due to averaging the probability of each phase in time and space. In the regions near the inlet section, GasD is only generated with a low void fraction due to the high condensation rate. Thus, the distributions predicted by both approaches are almost the same. However, by proceeding further along the pipe, larger bubbles and slugs are formed, which can not be modelled by the E-E two-fluid model.

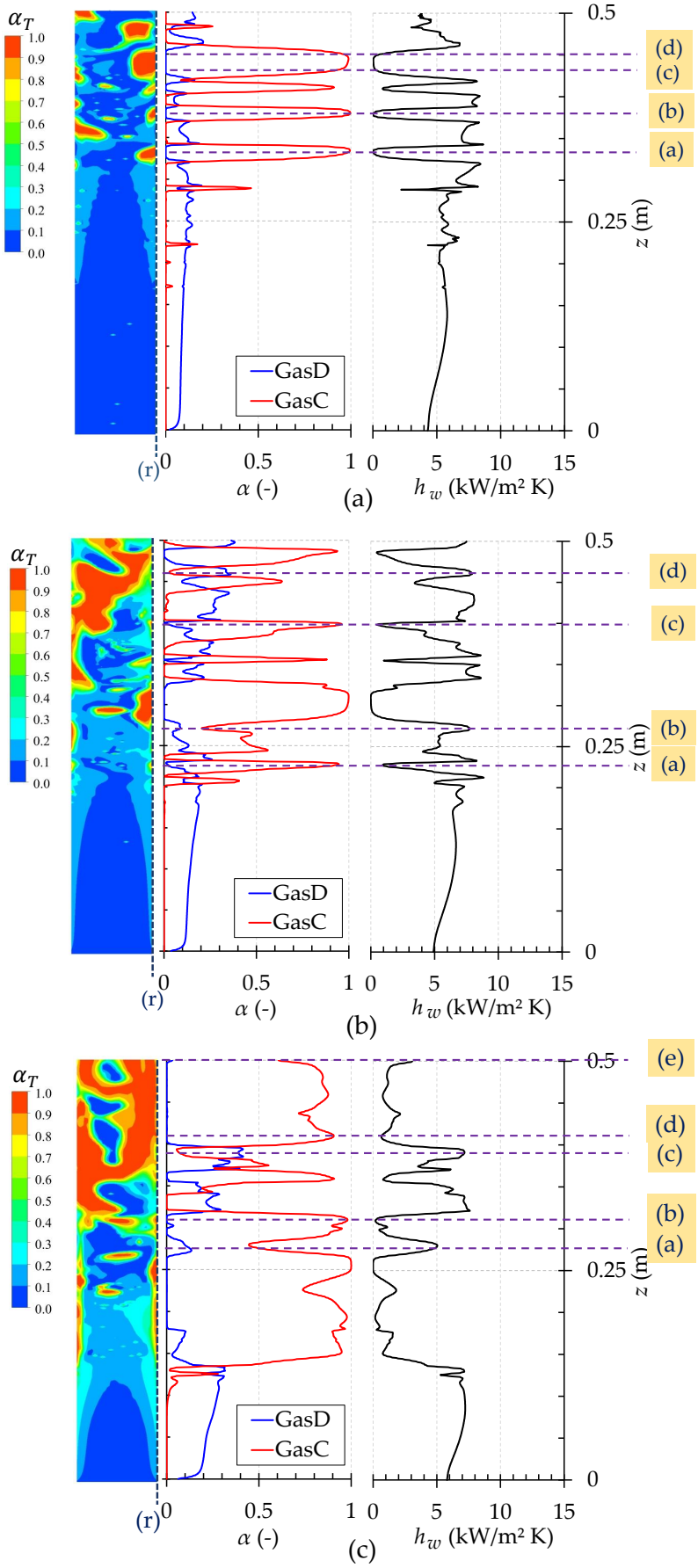

Figure 5.11: Temporal distributions of GasD and GasC void fractions as well as wall heat transfer coefficient for a) case1 ($\Delta T_{sup} = 8$ K) b) case2 ($\Delta T_{sup} = 10$ K) c) case3 ($\Delta T_{sup} = 12$ K) at $t = 2$ s.

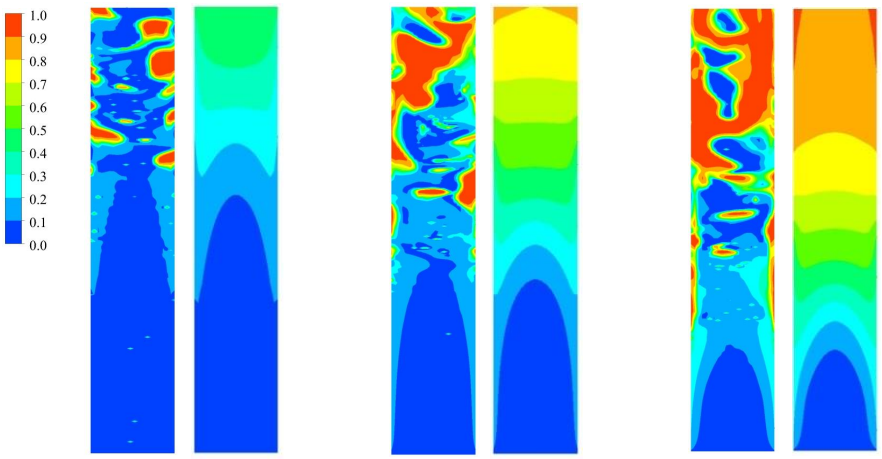

Figure 5.12: Distribution of total void fraction calculated by GENTOP and E-E models (left and right side) for a) case1 ($\Delta T_{sup} = 8$ K) b) case2 ($\Delta T_{sup} = 10$ K) c) case3 ($\Delta T_{sup} = 12$ K).

In order to investigate the impact of flow patterns on the wall heat transfer, azimuthally and time-averaged values of GasC and GasD void fraction as well as h_w calculated by both GENTOP and E-E two-fluid models are plotted in Figure 5.13. In the GENTOP results, h_w increases from the pipe's inlet until the GasC formation points ($z = 0.22$, 0.18, and 0.08 m for case1, case2, and case3), which is because of GasD formation on the wall or in other words phase-change heat transfer. For these regions, the predictions of both models for GasD void fraction and h_w are equal as expected. After the points of GasC formation, the results diverge which is due to the inability of the E-E two-fluid model to predict the GasC structures formation and consequently their effects on the wall heat transfer coefficient. In the GENTOP results, the GasC formation causes a significant reduction in the value of h_w which is due to the lower amount of single-phase convection from the heating wall to GasC compared to the phase-change heat transfer. In case2 and case3 more GasC is formed on the wall compared to case1 and consequently this decrease is more obvious in these cases. By going further along the pipe when GasC void fraction starts to decrease a noticeable enhancement in the values of h_w is observed as well. Compared to the GENTOP model, the E-E model predicts higher h_w, which comes from the fact that GasC presence on the wall is not considered in this model.

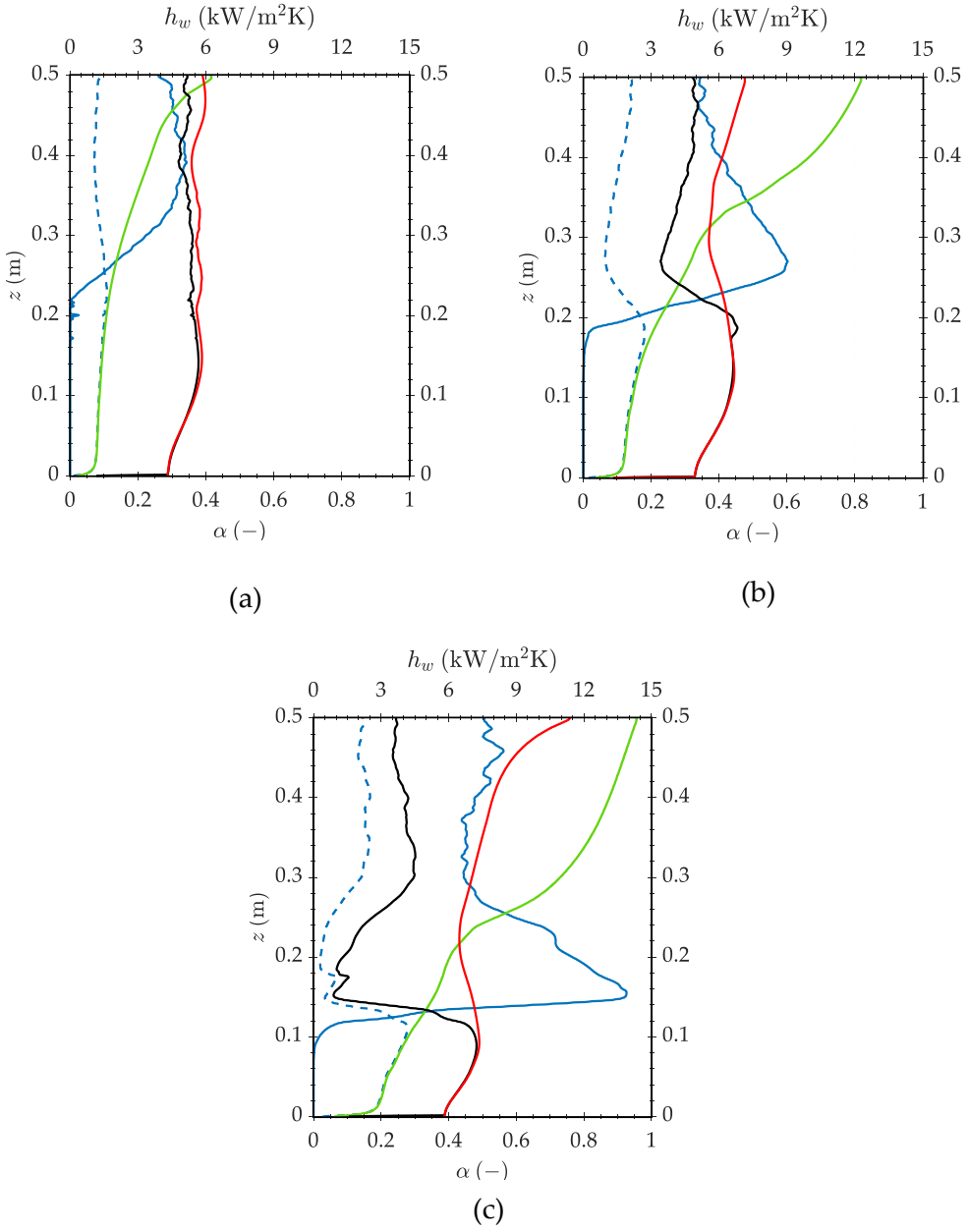

Figure 5.13: Time-averaged distributions of wall heat transfer coefficient, GasD and GasC void fractions obtained by GENTOP and E-E models for a) case1 ($\Delta T_{sup} = 8$ K) b) case2 ($\Delta T_{sup} = 10$ K) c) case3 ($\Delta T_{sup} = 12$ K) (legend: α_D, GENTOP α_C, GENTOP α_D, E-E h_w, GENTOP h_w, E-E).

Figure 5.14 shows the cross sectional and time-averaged values of the total void fraction calculated by both GENTOP and E-E models. Until GasC formation (see Figure 5.7b) both models obtain the same results. As soon as the GasC structures are formed, the results diverge. The E-E model predicts a higher averaged total void fraction than the GENTOP model which is because of this fact that also h_w is predicted higher (see Figure 5.13).

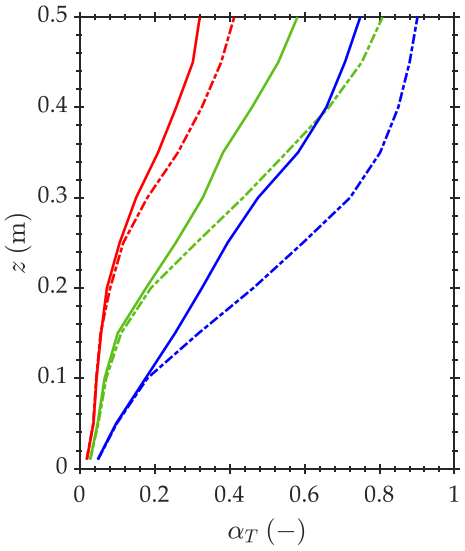

Figure 5.14: Cross-sectional and time-averaged profiles of total void fraction calculated by GENTOP and E-E models for a) case1 ($\Delta T_{sup} = 8$ K) b) case2 ($\Delta T_{sup} = 10$ K) c) case3 ($\Delta T_{sup} = 12$ K)(legend: — case1, GENTOP - - - case1, E-E — case2, GENTOP - - - case2, E-E — case3, GENTOP - - - case3, E-E).

5.2.4 Effect of subcooling on the flow boiling transition patterns

Figure 5.15 shows the time course of the averaged volume fractions of GasD, GasC, GasT and liquid for case2, case4, and case5 ($\Delta T_{sub} = 3, 4$, and 5 K respectively). For increased subcooling (decreasing inlet temperature) less gas is generated and GasC is formed later (0.25 s, 1 s and 1.5 s for case2, case4, and case5). This is due to the fact that raising the subcooling enhances the condensation rate on the bubble cap leading to bubbles shrinkage and low void fraction.

Figure 5.16a exhibits the cross-sectional and time-averaged values of GasT void fraction along the pipe for the case2, case4, and case5. For case2, there is a very low void fraction area ($\alpha < 0.1$) at axial positions lower than 0.14 m. Nevertheless, in case4 and case5 the subcooling enhancement leads to a longer distance (0.18 and 0.32 m respectively). The cross-sectional and time-averaged values of GasC void fraction along the pipe is shown in Figure 5.16b. GasC originates at axial positions of 0.16 m, 0.24 m and 0.32 m for case2, case4, and case5, respectively. This can be explained by the fact that increasing inlet subcooling leads to a higher condensation rate at the bubbles interface and consequently the later formation of GasC. The cross-sectional and time-averaged values of the liquid temperature are plotted in Figure 5.16c. Increasing the subcooling in case4 and case5, causes that the averaged temperatures reaches saturation at axial positions of 0.24 m and 0.35 m while for case5 the averaged temperature remains lower than the saturation one.

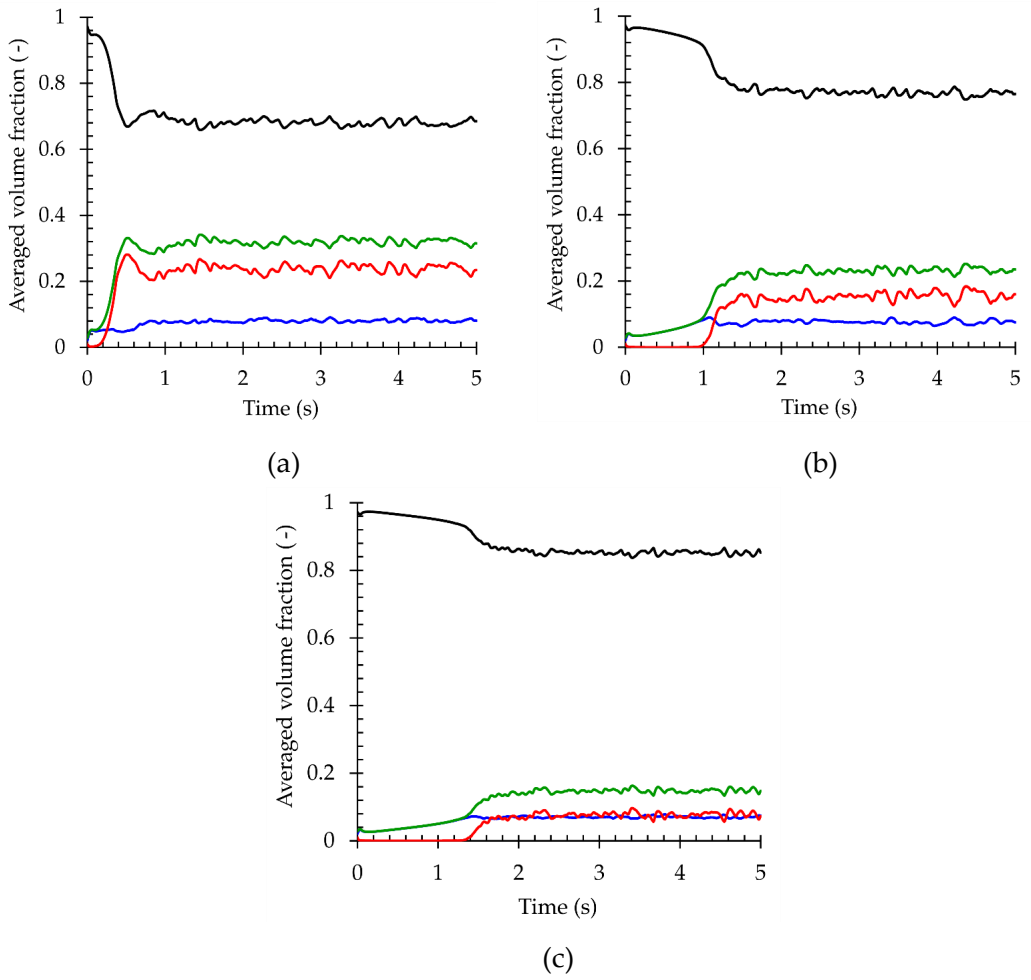

Figure 5.15: Averaged volume fractions of GasD, GasC, GasT and liquid for a) case2 ($\Delta T_{sub} = 3$ K) b) case4 ($\Delta T_{sub} = 4$ K) c) case5 ($\Delta T_{sub} = 5$ K (legend: GasD GasC GasT Liquid).

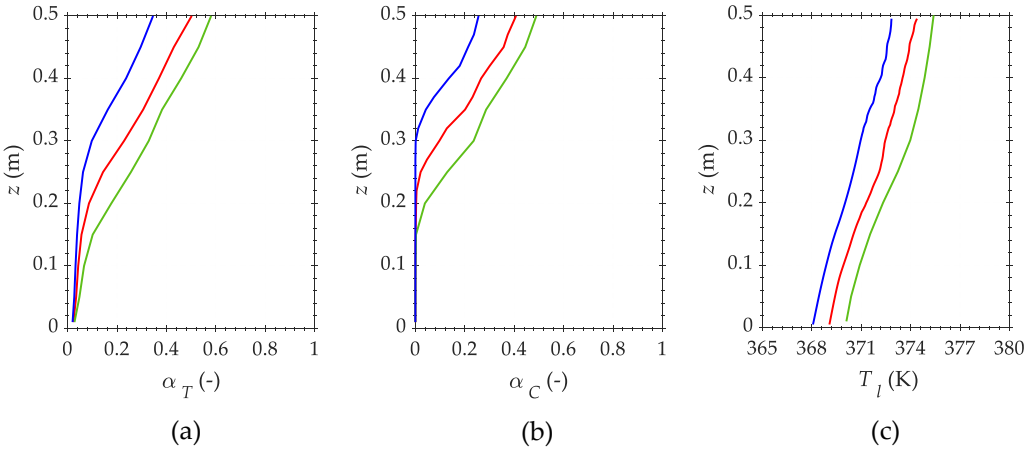

Figure 5.16: Distribution of cross-sectional and time-averaged values of a) GasT void fraction b) GasC void fraction c) liquid temperature for case2 ($\Delta T_{sub} = 3$ K), case4 ($\Delta T_{sub} = 4$ K) and case5 ($\Delta T_{sub} = 5$ K)(legend: case2 case4 case5).

Figure 5.17 shows the iso-surface velocity of GasC for five cases after 2 s. It can be seen in 3D that, as expected, the GasC formation point goes further upstream with increasing wall superheat. The comparison of case2, case4, and case5 proves that by increasing the inlet subcooling the GasC formation point is elevated.

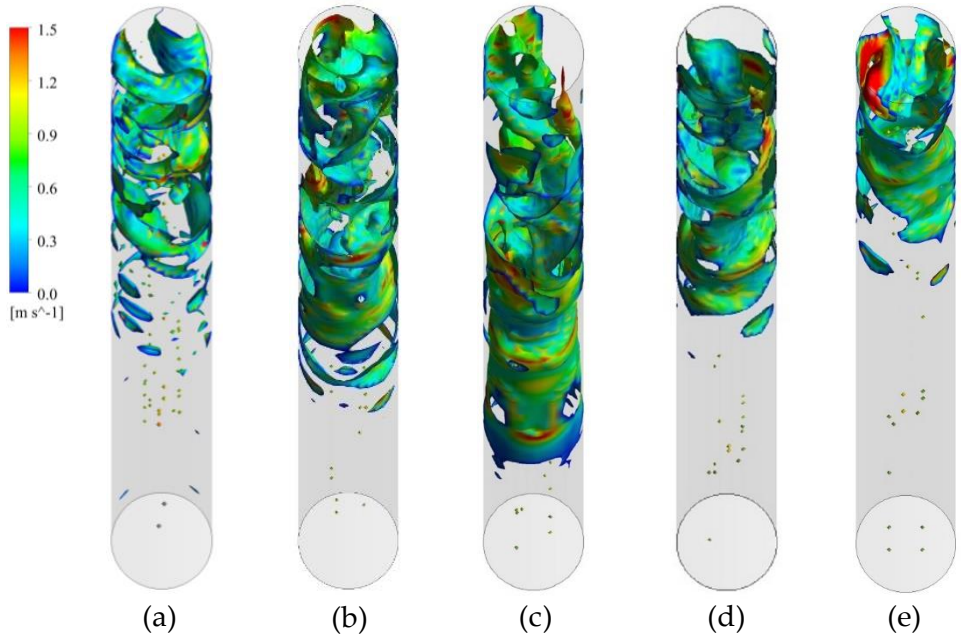

Figure 5.17: Iso-surface velocity of GasC for a) case1 ($\Delta T_{sub} = 3$ K, $\Delta T_{sup} = 8$ K) b) case2 ($\Delta T_{sub} = 3$ K, $\Delta T_{sup} = 10$ K) c) case3 ($\Delta T_{sub} = 3$ K, $\Delta T_{sup} = 12$ K) d) case4 ($\Delta T_{sub} = 4$ K, $\Delta T_{sup} = 10$ K) e) case5 ($\Delta T_{sub} = 5$ K, $\Delta T_{sup} = 10$ K) at $t = 2$ s.

5.2.5 Effect of inlet fluid velocity on the flow boiling transition patterns

Figure 5.18a shows the cross-sectional and time-averaged values of GasT void fraction along the pipe for the case2, case6, and case7. The low void fraction area ($\alpha < 0.1$) occurs at axial positions of 0.14, 0.16 and 0.18 m for case2, case6, and case7 respectively. Like the effect of subcooling temperature on the GasT void fraction, this can be explained by the fact that increasing inlet velocity results in higher interface heat transfer coefficient leading to higher condensation rate and consequently lower void fraction. Figure 5.18b exhibits the cross-sectional and time-averaged values of GasC void fraction along the pipe. GasC originates at axial position 0.16 m for case2. Nevertheless, in case6 and case7 the inlet velocity increase leads to a longer distance (0.2 and 0.22 m respectively).The cross-sectional and time-averaged values of the liquid temperature are plotted in Figure 5.18c. Inlet velocity enhancement in case2, case6, and case7 causes that the averaged

temperatures reaches saturation at an axial position of 0.24, 0.28 and 0.33 m respectively.

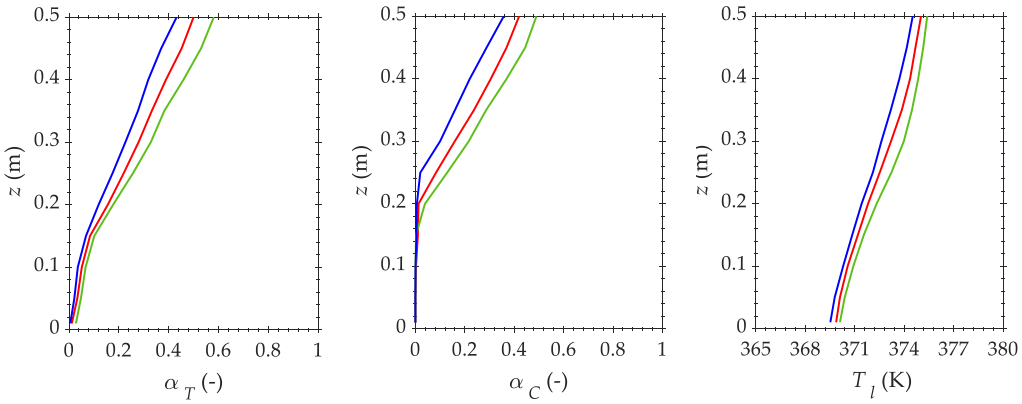

Figure 5.18: Distribution of cross-sectional and time-averaged values of a) GasT void fraction b) GasC void fraction c) liquid temperature for case2 ($\boldsymbol{U}_{in} = 0.2\ \frac{\mathrm{m}}{\mathrm{s}}$), case6 ($\boldsymbol{U}_{in} = 0.3\ \frac{\mathrm{m}}{\mathrm{s}}$) and case7 ($\boldsymbol{U}_{in} = 0.4\ \frac{\mathrm{m}}{\mathrm{s}}$) (legend: case2 case6 case7).

5.3 Summary

This chapter provides the application of GENTOP model for the modelling of flow transition patterns during the upward subcooled boiling inside a vertical heating pipe. The bubble dynamics model introduced in Chapter 3 was implemented in the GENTOP framework as a sub-model. The heat-partitioning model introduced in Chapter 4 was adopted for high void fraction. This adaptation considers the presence of continuous gas structure on the heating wall during flow boiling. The impacts of wall superheat, inlet subcooling and velocity on the flow boiling transition patterns were investigated. The effects of flow boiling morphologies on the wall heat transfer coefficient were assessed as well. In the end, the results obtained by GENTOP and the E-E two-fluid models for flow patterns transition and wall heat transfer coefficient were compared.

6 Conclusions and outlook

6.1 Conclusions

Flow boiling occurs in PWRs and BWRs as well as in their passive safety systems. Safety systems of the new generation of nuclear power plants are no longer confined to active components which need electrical power in the event of an accident in the plant. They also use passive safety cooling loops that do not require any external power supplies or manual intervention. These loops remove the decay heat from the reactor core through natural circulation. One of the major research directions in reactors safety systems has been stability analyses of flow boiling occurring in their passive safety loops in recent decades. Instabilities of flow boiling in these cooling circuits may cause flow oscillations. These oscillations can lead to insufficient local cooling and mechanical vibrations which threaten the reactor's safety. The stability of flow boiling in these safety loops is highly dependent on the parameters such as void fraction, bubble departure size, heat transfer coefficient as well as flow transition patterns. Therefore, these thermal-hydraulic parameters need to be accurately predicted.

Computational methods and specifically the E-E two-fluid model have shown tremendous success in flow boiling modelling. However, the effectiveness of this model for flow boiling modelling is affected by the uncertainties of empirical and mechanistic models, which are used to predict bubble dynamics parameters. Considering the uncertainties of available empirical and mechanistic models for bubble dynamics, the major aim of this thesis has been the development of a mechanistic model to implement in CFD codes for flow boiling modelling. Overall, the major contributions of this research are given below.

A mechanistic bubble dynamics model based on the force balance on a growing bubble is presented. It requires no recalibration of parameters to predict bubble growth and detachment. It was formulated based on the physics of a nucleated bubble and several well-developed models and theories to cover the whole bubble life cycle including inertia-controlled, thermal diffusion-controlled periods and departure. It includes the contributions of microlayer evaporation, superheated layer and condensation to the bubble growth. As a novel idea, the bottleneck in the late bubble growth period was modelled. In addition, the consideration of dynamic

contact and inclination angles makes the model applicable under different thermal-hydraulic and geometric conditions without using recalibration factors. The model was successfully validated against four different experimental cases from the literature. The experimental data covered different mass fluxes, heat fluxes, subcooling, pressure, heating wall orientation angle, pipe designs and working fluids. The average deviation for the prediction of bubble lift-off diameter was 26%, which proves the good predictability of the present model. To gain reliability and an in-depth analysis of the proposed approach, a sensitivity analysis was performed. It proved that the model can accurately predict the dependency of bubble departure and lift-off diameters on different parameters such as mass flux, heat flux, subcooling, pressure and heating wall orientation angle. The summary of sensitivity analysis is given as:

- Drag and lift forces increase with mass flux enhancement, which decreases bubble lift-off diameter.
- Heat flux from the heating wall determines the growth speed of the bubble, which may increase or decrease the bubble departure diameter.
- Subcooling temperature affects the departure diameter due to condensation. Higher liquid subcooling reduces bubble departure and lift-off diameters.
- Pressure significantly increases the vapor to liquid density ratio, which results in departure diameter decrease.

The previously developed bubble dynamics model was implemented in the E-E framework as a sub-model to improve the accuracy of flow boiling modelling and reduce the case dependency. The developed model is dependent on the wall superheat. Therefore, the implementation extends the current nucleation site activation and heat-partitioning model. For this purpose, the activated nucleation sites were classified into different groups with different superheat and bubble dynamics parameters were calculated for each group. These parameters were calculated based on the function of wall superheat, subcooling temperature and fluid velocity by a separate code and then implemented in ANSYS CFX 18.2. The implementation was coupled with a PBM model. With this novel modelling approach, the impact of bubble sliding on the wall heat transfer, which has been rarely considered in other modelling approaches, was analyzed. However, bubble coalescence on the wall during sliding was not considered in this model and so it should be a subject for future studies. For validation of modelling results, ten experimental test cases including subcooled flow boiling in a vertical pipe and an annulus were chosen. These experiments cover a wide range of operating parameters such as wall heat flux, fluid velocity, subcooling temperature and pressure. The void fraction, bubble diameter, bubble velocity, IAD, bubble passing frequency, liquid and wall temperature were

validated against the experimental data at different locations of heating pipes. The good agreement with the experimental data proved the successful applicability of this models' implementation in the E-E two-fluid framework for simulation of subcooled boiling flows.

Prediction of flow patterns transition during subcooled boiling has been a critical topic since these patterns have a significant impact on the heat and mass transfer rates. For this purpose, the developed bubble dynamics model was coupled with the GENTOP concept for the modelling of flow boiling regimes. The GENTOP concept is based on the iMUSIG model in the E-E framework and a GasC is added, i.e., the fluid flow domain is divided into two GasD, a GasC and continuous liquid phases. The GasC was detected by the newest version of AIAD model and its interfacial transfers including mass and momentum was accordingly modelled. The proposed heat-partitioning model was adopted for application in the GENTOP framework. This adaptation for high void fractions considered the effect of GasC structures formation on the wall heat transfer. Seven generic test cases including transient subcooled flow boiling in a vertical heating pipe with different wall superheats, subcooling temperatures, and inlet velocities were performed by using ANSYS CFX 18.2. There was a good convergence behavior for different operating conditions and the major results can be summarized as follows:

- Increasing wall superheat accelerates the GasC formation (in the lower part of the pipe) and conversely increasing the subcooling and inlet velocity delays it (in the upper part of the pipe).

- The bubble formation on the heating wall enhances the local heat transfer and conversely, the presence of GasC structures significantly reduces it due to the lower convection from the heating wall to GasC compared to the boiling heat transfer.

- The time-averaged and temporal void fractions obtained with the GENTOP were compared to the E-E two-fluid model. As expected, the interfacial structures could not be detected in E-E two-fluid model due to the averaging process.

- The relation between time-averaged void fractions and wall heat transfer coefficient obtained from both E-E two-fluid and GENTOP results was investigated. As long as no GasC is formed in the flow domain, both models obtain the same results. However, the formation of GasC structures diverges the results which is due to the inability of E-E two fluid model for flow patterns modelling and their effects on the wall heat transfer.

– The formation of GasC structures on the heating wall significantly reduces the wall heat transfer coefficient. The E-E two-fluid model is unable to model these structures, so it predicts a higher wall heat transfer coefficient and, as a result, a higher total void fraction than the GENTOP model does.

6.2 Outlook

In this thesis, a mechanistic bubble dynamics model was developed and implemented into an E-E CFD framework for subcooled flow boiling modelling. This model was formulated based on some well-developed models and theories and successfully validated against four different experimental cases. However, it needs further improvements. The first one is the base diameter expansion hypothesis. Although it is a commonly accepted approach, it lacks physical support. Therefore, this hypothesis needs to be critically assessed and developed to improve the accuracy of the model prediction. The second one is bubble coalescence on the heating wall during sliding, which was not considered in this model. Consequently, it should the subject of future studies.

The bubble dynamics model was also implemented in the GENTOP framework for simulation of flow boiling transition patterns. However, due to the lack of experimental data, this part was merely confined to numerical simulations for generic cases. Experimental data with high resolution in time and space is necessary to quantitatively validate the numerical results. Last but not least, the transition of flow boiling patterns in a heating pipe at different angles of inclination can be the subject of future investigations.

References

[1] Patricia Fry Godley. “The state of play and future of fossil fuels”. In: *Natural Resources & Environment* 11.3 (1997), pp. 3–6 (cit. on p. 1).

[2] N Aksan, H Choi J, J Chung Y, et al. “Passive safety systems and natural circulation in water cooled nuclear power plants”. In: (2009) (cit. on p. 1).

[3] Paul Breeze. *Power generation technologies*. Newnes, 2019 (cit. on p. 1).

[4] Machimontorn Promtong. “Development of mechanistic approach for wall heat flux partitioning in subcooled boiling flows”. PhD thesis. RMIT University, 2018 (cit. on p. 1).

[5] Stephen Goldberg and Robert Rosner. “Nuclear reactors: Generation to generation”. In: American academy of arts and sciences Cambridge. 2011 (cit. on p. 1).

[6] Giovanni Giustini. “Modelling of boiling flows for nuclear thermal hydraulics applicationsA brief review”. In: *Inventions* 5.3 (2020), p. 47 (cit. on p. 1).

[7] S Mostafa Ghiaasiaan. *Two-phase flow, boiling, and condensation: in conventional and miniature systems*. Cambridge University Press, 2007 (cit. on p. 1).

[8] Gian Piero Celata and Andrea Mariani. *Critical heat flux, post dry-out and their augmentation*. Tech. rep. ENEA, 1999 (cit. on p. 2).

[9] Amirhosein Moonesi Shabestary, Frances Viereckl, Yu Zhang, et al. “Modelling of Passive Heat Removal Systems: A Review with Reference to the Framatome KERENA BWR Reactor: Part I”. In: *Energies* 13.1 (2019), p. 35 (cit. on pp. 2–4).

[10] AK Nayak and PK Vijayan. “Flow instabilities in boiling two-phase natural circulation systems: a review”. In: *Science and Technology of nuclear installations* 2008 (2008) (cit. on pp. 3, 4).

[11] JA Boure, AE Bergles, and LS Tong. “Review of two-phase flow instability”. In: *Nuclear engineering and design* 25.2 (1973), pp. 165–192 (cit. on p. 3).

[12] Gonella V Durga Prasad, Manmohan Pandey, and Manjeet S Kalra. “Review of research on flow instabilities in natural circulation boiling systems”. In: *Progress in Nuclear Energy* 49.6 (2007), pp. 429–451 (cit. on pp. 3, 4).

[13] Zoran V Stosic, Werner Brettschuh, and Uwe Stoll. “Boiling water reactor with innovative safety concept: The Generation III+ SWR-1000”. In: *Nuclear Engineering and Design* 238.8 (2008), pp. 1863–1901 (cit. on pp. 3, 5).

[14] DORIS Neumann. “The passive safety systems of the SWR 1000”. In: (2001) (cit. on pp. 3, 4).

[15] Rafał Bryk, Thomas Mull, and Holger Schmidt. “Experimental investigation of LWR passive safety systems performance at the INKA test facility”. In: *E3S Web of Conferences*. Vol. 137. EDP Sciences. 2019, p. 01035 (cit. on pp. 3, 4).

[16]André Bieberle, Amirhosein Moonesi Shabestary, Thomas Geissler, et al. “Flow morphology and heat transfer analysis during high-pressure steam condensation in an inclined tube part I: experimental investigations”. In: *Nuclear Engineering and Design* 361 (2020), p. 110553 (cit. on pp. 4, 5).

[17]René Manthey, Frances Viereckl, Amirhosein Moonesi Shabestary, et al. “Modelling of Passive Heat Removal Systems: A Review with Reference to the Framatome BWR Reactor KERENA: Part II”. In: *Energies* 13.1 (2019), p. 109 (cit. on pp. 4, 6, 7).

[18]Elias Amselem Abecasis. “Analysis of boiling water reactor design and operating conditions effect on stability behaviour”. In: (2010) (cit. on p. 4).

[19]AK Nayak, PK Vijayan, V Jain, D Saha, and RK Sinha. “Study on the flow-pattern-transition instability in a natural circulation heavy water moderated boiling light water cooled reactor”. In: *Nuclear engineering and design* 225.2-3 (2003), pp. 159–172 (cit. on p. 4).

[20]Yixiang Liao, Dirk Lucas, Eckhard Krepper, and Roland Rzehak. “CFD Simulation of Flashing Boiling Flow in the Containment Cooling Condensers (CCC) System of KERENA Reactor”. In: *International Conference on Nuclear Engineering*. Vol. 55805. American Society of Mechanical Engineers. 2013, V003T10A039 (cit. on p. 4).

[21]Werner Brettschuh and Dieter Schneider. “Modern Light Water Reactors-EPR and SWR 1000. Present status and possibilities of development and application”. In: (2002) (cit. on p. 5).

[22]Gretar Tryggvason and Jiacai Lu. “Direct numerical simulations of multiphase flows: Opportunities and challenges”. In: *AIP Conference Proceedings*. Vol. 2293. 1. AIP Publishing LLC. 2020, p. 030002 (cit. on p. 7).

[23]Andrea Prosperetti and Grétar Tryggvason. *Computational methods for multiphase flow*. Cambridge university press, 2009 (cit. on p. 7).

[24]W Friz. “Maximum volume of vapor bubbles”. In: *Physic. Zeitschz.* 36 (1935), pp. 379–354 (cit. on pp. 8, 41).

[25]Novak Zuber. “The dynamics of vapor bubbles in nonuniform temperature fields”. In: *International Journal of Heat and Mass Transfer* 2.1-2 (1961), pp. 83–98 (cit. on pp. 8, 15, 18, 20).

[26]VI Tolubinsky and DM Kostanchuk. “Vapour bubbles growth rate and heat transfer intensity at subcooled water boiling”. In: *International Heat Transfer Conference 4*. Vol. 23. Begel House Inc. 1970 (cit. on pp. 8, 41, 85).

[27]Susann Hänsch, Dirk Lucas, Eckhard Krepper, and Thomas Höhne. “A multi-field two-fluid concept for transitions between different scales of interfacial structures”. In: *International Journal of Multiphase Flow* 47 (2012), pp. 171–182 (cit. on pp. 8, 44, 46, 49, 50, 118).

[28]Frank Kreith and Raj M Manglik. *Principles of heat transfer*. Cengage learning, 2016 (cit. on p. 13).

[29]Yih-Yun Hsu and Robert W Graham. “Transport processes in boiling and two-phase systems”. In: (1986) (cit. on p. 14).

[30]Lord Rayleigh. “VIII. On the pressure developed in a liquid during the collapse of a spherical cavity”. In: *The London, Edinburgh, and Dublin Philosophical Magazine and Journal of Science* 34.200 (1917), pp. 94–98 (cit. on p. 15).

[31]Yeong-Cheng Lien. “Bubble growth rates at reduced pressure.” PhD thesis. Massachusetts Institute of Technology, 1969 (cit. on p. 15).

[32]James Anthony Robinson. “Bubble growth dynamics in boiling”. PhD thesis. 2002 (cit. on p. 15).

[33]Ho Sung Lee. “Vapor bubble dynamics in microgravity”. PhD thesis. University of Michigan, 1993 (cit. on p. 15).

[34]M So Plesset and So A Zwick. “The growth of vapor bubbles in superheated liquids”. In: *Journal of applied physics* 25.4 (1954), pp. 493–500 (cit. on pp. 15, 20).

[35]H_K Forster and Novak Zuber. “Growth of a vapor bubble in a superheated liquid”. In: *Journal of Applied Physics* 25.4 (1954), pp. 474–478 (cit. on p. 15).

[36]Peter Griffith. *Bubble growth rates in boiling*. Tech. rep. Cambridge, Mass.: Massachusetts Institute of Technology, Division of, 1956 (cit. on p. 15).

[37]P Savic. “Discussion on bubble growth rates in boiling”. In: *Trans. ASME J. Heat Tr ansfer* 80 (1958), pp. 726–728 (cit. on p. 15).

[38]BB Mikic, WM Rohsenow, and P Griffith. “On bubble growth rates”. In: *International Journal of Heat and Mass Transfer* 13.4 (1970), pp. 657–666 (cit. on pp. 15, 17, 20, 55, 57).

[39]Andrea Prosperetti and Milton S Plesset. “Vapour-bubble growth in a superheated liquid”. In: *Journal of Fluid Mechanics* 85.2 (1978), pp. 349–368 (cit. on pp. 16, 20).

[40]DA Labuntsov. “State of the art of the nucleate boiling mechanism of liquids”. In: *Heat Transfer and Physical Hydrodynamics, Moskva, Nauka, in Russian* (1974), pp. 98–115 (cit. on pp. 16, 55, 57).

[41]MG Cooper and AJP Lloyd. “The microlayer in nucleate pool boiling”. In: *International Journal of Heat and Mass Transfer* 12.8 (1969), pp. 895–913 (cit. on pp. 16, 20, 55, 58).

[42]SJD Van Stralen, MS Sohal, R Cole, and WM Sluyter. “Bubble growth rates in pure and binary systems: combined effect of relaxation and evaporation microlayers”. In: *International Journal of Heat and Mass Transfer* 18.3 (1975), pp. 453–467 (cit. on p. 16).

[43]James F Klausner, Renwei Mei, DM Bernhard, and LZ Zeng. “Vapor bubble departure in forced convection boiling”. In: *International journal of heat and mass transfer* 36.3 (1993), pp. 651–662 (cit. on pp. 17–20, 55, 60, 62, 64, 72–79, 84).

[44]Glen E Thorncroft and James F Klausner. “Bubble forces and detachment models”. In: *Multiphase Science and Technology* 13.3&4 (2001) (cit. on pp. 18, 56, 62–64).

[45]Rong Situ, Takashi Hibiki, Mamoru Ishii, and Michitsugu Mori. “Bubble lift-off size in forced convective subcooled boiling flow”. In: *International Journal of Heat and Mass Transfer* 48.25-26 (2005), pp. 5536–5548 (cit. on pp. 18, 20, 72, 74, 78, 79, 81–84).

[46]GH Yeoh, Sherman CP Cheung, JY Tu, and Mark KM Ho. “Fundamental consideration of wall heat partition of vertical subcooled boiling flows”. In: *International Journal of Heat and Mass Transfer* 51.15-16 (2008), pp. 3840–3853 (cit. on pp. 18, 20).

[47]Wen Wu, Peipei Chen, Barclay G Jones, and Ty A Newell. “A study on bubble detachment and the impact of heated surface structure in subcooled nucleate boiling flows”. In: *Nuclear engineering and design* 238.10 (2008), pp. 2693–2698 (cit. on pp. 18, 20).

[48]Rosie Sugrue and Jacopo Buongiorno. “A modified force-balance model for prediction of bubble departure diameter in subcooled flow boiling”. In: *Nuclear Engineering and Design* 305 (2016), pp. 717–722 (cit. on pp. 18, 20, 78).

[49]Byong-Jo Yun, Andrew Splawski, Simon Lo, and Chul-Hwa Song. “Prediction of a subcooled boiling flow with advanced two-phase flow models”. In: *Nuclear engineering and design* 253 (2012), pp. 351–359 (cit. on pp. 18, 19, 75, 76).

[50]Deqi Chen, Liang-ming Pan, and Song Ren. “Prediction of bubble detachment diameter in flow boiling based on force analysis”. In: *Nuclear Engineering and Design* 243 (2012), pp. 263–271 (cit. on pp. 18, 55, 60–63).

[51]Marco Colombo and Michael Fairweather. “Prediction of bubble departure in forced convection boiling: A mechanistic model”. In: *International Journal of Heat and Mass Transfer* 85 (2015), pp. 135–146 (cit. on pp. 18–20, 77, 78).

[52]Sumit Raj, Manabendra Pathak, and Mohd Kaleem Khan. “An analytical model for predicting growth rate and departure diameter of a bubble in subcooled flow boiling”. In: *International Journal of Heat and Mass Transfer* 109 (2017), pp. 470–481 (cit. on pp. 19, 20, 77).

[53]Thomas Mazzocco, Walter Ambrosini, R Kommajosyula, and E Baglietto. “A reassessed model for mechanistic prediction of bubble departure and lift off diameters”. In: *International Journal of Heat and Mass Transfer* 117 (2018), pp. 119–124 (cit. on pp. 19, 20).

[54]S Lo. “Application of the MUSIG model to bubbly flows”. In: *AEAT-1096, AEA Technology* 230 (1996), pp. 8216–8246 (cit. on p. 23).

[55]Eckhard Krepper, Dirk Lucas, Thomas Frank, Horst-Michael Prasser, and Phil J Zwart. “The inhomogeneous MUSIG model for the simulation of polydispersed flows”. In: *Nuclear Engineering and Design* 238.7 (2008), pp. 1690–1702 (cit. on p. 24).

[56]Guan Heng Yeoh and Jiyuan Tu. *Computational techniques for multiphase flows*. Butterworth-Heinemann, 2019 (cit. on pp. 25, 39).

[57]WE Ranz and WR Marshall. “Evaporation from droplets”. In: *Chem. Eng. Prog* 48.3 (1952), pp. 141–146 (cit. on pp. 26, 56, 58, 101).

[58]GA Hughmark. “Mass and heat transfer from rigid spheres”. In: *AIChE Journal* 13.6 (1967), pp. 1219–1221 (cit. on pp. 26, 118).

[59]Yixiang Liao, Roland Rzehak, Dirk Lucas, and Eckhard Krepper. “Baseline closure model for dispersed bubbly flow: Bubble coalescence and breakup”. In: *Chemical Engineering Science* 122 (2015), pp. 336–349 (cit. on p. 28).

[60]Michael J Prince and Harvey W Blanch. “Bubble coalescence and break-up in air-sparged bubble columns”. In: *AIChE journal* 36.10 (1990), pp. 1485–1499 (cit. on pp. 30, 92, 118).

[61]Hean Luo and Hallvard F Svendsen. “Theoretical model for drop and bubble breakup in turbulent dispersions”. In: *AIChE Journal* 42.5 (1996), pp. 1225–1233 (cit. on pp. 30, 31, 92, 118).

[62]Roland Rzehak, Thomas Ziegenhein, Sebastian Kriebitzsch, Eckhard Krepper, and Dirk Lucas. “Unified modeling of bubbly flows in pipes, bubble columns, and airlift columns”. In: *Chemical Engineering Science* 157 (2017), pp. 147–158 (cit. on pp. 32, 35).

[63]Mamoru Ishii and Novak Zuber. “Drag coefficient and relative velocity in bubbly, droplet or particulate flows”. In: *AIChE journal* 25.5 (1979), pp. 843–855 (cit. on p. 32).

[64]Akio Tomiyama, Hidesada Tamai, Iztok Zun, and Shigeo Hosokawa. “Transverse migration of single bubbles in simple shear flows”. In: *Chemical Engineering Science* 57.11 (2002), pp. 1849–1858 (cit. on pp. 33, 101).

[65]Shigeo Hosokawa, Akio Tomiyama, Shinji Misaki, and Tomoyuki Hamada. “Lateral migration of single bubbles due to the presence of wall”. In: *Fluids Engineering Division Summer Meeting*. Vol. 36150. 2002, pp. 855–860 (cit. on p. 34).

[66]Alan D Burns, Thomas Frank, Ian Hamill, Jun-Mei Shi, et al. “The Favre averaged drag model for turbulent dispersion in Eulerian multi-phase flows”. In: *5th international conference on multiphase flow, ICMF*. Vol. 4. ICMF. 2004, pp. 1–17 (cit. on p. 34).

[67]Y Sato, M Sadatomi, and K Sekoguchi. “Momentum and heat transfer in two-phase bubble flowI. Theory”. In: *International Journal of Multiphase Flow* 7.2 (1981), pp. 167–177 (cit. on p. 35).

[68]David C Wilcox. “Reassessment of the scale-determining equation for advanced turbulence models”. In: *AIAA journal* 26.11 (1988), pp. 1299–1310 (cit. on p. 35).

[69]Yixiang Liao and Dirk Lucas. “Poly-disperse simulation of condensing steam-water flow inside a large vertical pipe”. In: *International Journal of Thermal Sciences* 104 (2016), pp. 194–207 (cit. on p. 35).

[70]D Lucas, T Frank, C Lifante, P Zwart, and A Burns. “Extension of the inhomogeneous MUSIG model for bubble condensation”. In: *Nuclear Engineering and Design* 241.11 (2011), pp. 4359–4367 (cit. on p. 37).

[71]N Kurul and Michael Z Podowski. “Multidimensional effects in forced convection subcooled boiling”. In: *International Heat Transfer Conference Digital Library*. Begel House Inc. 1990 (cit. on pp. 38, 39, 88).

[72]RL Judd and KS Hwang. “A comprehensive model for nucleate pool boiling heat transfer including microlayer evaporation”. In: (1976) (cit. on pp. 38, 39).

[73]Brahim Mohamedi, Salah Hanini, Abdelrahmane Ararem, and Nacim Mellel. “Simulation of nucleate boiling under ANSYS-FLUENT code by using RPI model coupling with artificial neural networks”. In: *()* 26.4 (2015), pp. 40601–040601 (cit. on p. 38).

[74]Xiang Zhang, Ting Yu, Tenglong Cong, and Minjun Peng. “Effects of interaction models on upward subcooled boiling flow in annulus”. In: *Progress in Nuclear Energy* 105 (2018), pp. 61–75 (cit. on p. 38).

[75]BA Kader. “Temperature and concentration profiles in fully turbulent boundary layers”. In: *International journal of heat and mass transfer* 24.9 (1981), pp. 1541–1544 (cit. on p. 38).

[76]DBR Kenning et al. “Fully-developed nucleate boiling: overlap of areas of influence and interference between bubble sites”. In: *International Journal of Heat and Mass Transfer* 24.6 (1981), pp. 1025–1032 (cit. on p. 39).

[77]Richard Francis Gaertner. *Population of active sites in nucleate boiling heat transfer*. University of Illinois at Urbana-Champaign, 1959 (cit. on p. 40).

[78]DB Kirby and JW Westwater. “Bubble and vapor behavior on a heated horizontal plate during pool boiling near burnout”. In: *Chemical Engineering Progress Symposium Series*. Vol. 61. 57. 1965, pp. 238–248 (cit. on p. 40).

[79]M Lemmert et al. “Influence of Flow Velocity on Surface Boiling Heat Transfert Coefficient”. In: (1972) (cit. on pp. 40, 41, 77, 78, 85, 93).

[80]G Kocamustafaogullari and M Ishii. “Interfacial area and nucleation site density in boiling systems”. In: *International Journal of Heat and Mass Transfer* 26.9 (1983), pp. 1377–1387 (cit. on p. 40).

[81]Nilanjana Basu, Gopinath R Warrier, and Vijay K Dhir. “Onset of nucleate boiling and active nucleation site density during subcooled flow boiling”. In: *J. Heat Transfer* 124.4 (2002), pp. 717–728 (cit. on p. 40).

[82]Novak Zuber. *Hydrodynamic aspects of boiling heat transfer (thesis)*. 4439. United States Atomic Energy Commission, Technical Information Service, 1959 (cit. on p. 41).

[83]Han Chi-Yeh and Peter Griffith. “The mechanism of heat transfer in nucleate pool boilingPart I: Bubble initiaton, growth and departure”. In: *International Journal of Heat and Mass Transfer* 8.6 (1965), pp. 887–904 (cit. on p. 41).

[84]Davood Farajisarir. “Growth and collapse of vapour bubbles in convective subcooled boiling of water”. PhD thesis. University of British Columbia, 1993 (cit. on p. 41).

[85]Robert Cole. “A photographic study of pool boiling in the region of the critical heat flux”. In: *AIChE Journal* 6.4 (1960), pp. 533–538 (cit. on p. 41).

[86]Karl Stephan. *Heat transfer in condensation and boiling*. Springer, 1992 (cit. on p. 41).

[87]G Kocamustafaogullari and M Ishii. “Foundation of the interfacial area transport equation and its closure relations”. In: *International Journal of Heat and Mass Transfer* 38.3 (1995), pp. 481–493 (cit. on p. 41).

[88]Eckhard Krepper, Roland Rzehak, Conxita Lifante, and Thomas Frank. “CFD for subcooled flow boiling: Coupling wall boiling and population balance models”. In: *Nuclear engineering and design* 255 (2013), pp. 330–346 (cit. on pp. 41, 45, 77, 78, 92, 93, 101).

[89] Etienne Manon. “Contribution à l’analyse et à la modélisation locale des écoulements bouillants sous-saturés dans les conditions des réacteurs à eau sous pression”. PhD thesis. Châtenay-Malabry, Ecole centrale de Paris, 2000 (cit. on pp. 41, 90).

[90] Eckhard Krepper, Bostjan Končar, and Yury Egorov. “CFD modelling of subcooled boilingconcept, validation and application to fuel assembly design”. In: *Nuclear engineering and design* 237.7 (2007), pp. 716–731 (cit. on p. 41).

[91] Eckhard Krepper and Roland Rzehak. “CFD for subcooled flow boiling: Simulation of DEBORA experiments”. In: *Nuclear Engineering and Design* 241.9 (2011), pp. 3851–3866 (cit. on p. 41).

[92] SZ Rouhani and MS Sohal. “Two-phase flow patterns: A review of research results”. In: *Progress in Nuclear Energy* 11.3 (1983), pp. 219–259 (cit. on p. 43).

[93] Lixin Cheng, Gherhardt Ribatski, and John R Thome. “Two-phase flow patterns and flow-pattern maps: fundamentals and applications”. In: *Applied Mechanics Reviews* 61.5 (2008) (cit. on p. 43).

[94] Jaco Dirker, Diksha Juggurnath, Alihan Kaya, et al. “Thermal energy processes in direct steam generation solar systems: Boiling, condensation and energy storage–A review”. In: *Frontiers in Energy Research* 6 (2019), p. 147 (cit. on p. 43).

[95] D Bestion. “Applicability of two-phase CFD to nuclear reactor thermalhydraulics and elaboration of Best Practice Guidelines”. In: *Nuclear Engineering and Design* 253 (2012), pp. 311–321 (cit. on pp. 43, 46).

[96] B Hasanpour, MS Irandoost, M Hassani, and R Kouhikamali. “Numerical investigation of saturated upward flow boiling of water in a vertical tube using VOF model: effect of different boundary conditions”. In: *Heat and Mass Transfer* 54.7 (2018), pp. 1925–1936 (cit. on p. 43).

[97] A Tomiyama. “Modeling and hybrid simulation of bubbly flow”. In: *Multiphase Sci. Technol.* 18 (2006), pp. 73–110 (cit. on p. 43).

[98] Gregor Cerne, Stojan Petelin, and Iztok Tiselj. “Coupling of the interface tracking and the two-fluid models for the simulation of incompressible two-phase flow”. In: *Journal of computational physics* 171.2 (2001), pp. 776–804 (cit. on p. 43).

[99] Akio Tomiyama and Naoki Shimada. “A numerical method for bubbly flow simulation based on a multi-fluid model”. In: *J. Pressure Vessel Technol.* 123.4 (2001), pp. 510–516 (cit. on pp. 43, 44).

[100] Munenori Maekawa, Naoki Shimada, Akira Sou, and Akio Tomiyama. “Numerical simulation of poly-dispersed bubbly flow using a multi-fluid model”. In: *Journal of Fluid Science and Technology* 2.2 (2007), pp. 502–512 (cit. on p. 44).

[101] Kai Yan and Defu Che. “A coupled model for simulation of the gas–liquid two-phase flow with complex flow patterns”. In: *International Journal of Multiphase Flow* 36.4 (2010), pp. 333–348 (cit. on p. 44).

[102] Christophe Vallée, Thomas Höhne, Horst-Michael Prasser, and Tobias Sühnel. “Experimental investigation and CFD simulation of horizontal stratified two-phase flow phenomena”. In: *Nuclear Engineering and Design* 238.3 (2008), pp. 637–646 (cit. on p. 44).

[103]Philip J Zwart, Alan D Burns, and Paul F Galpin. “Coupled algebraic multigrid for free surface flow simulations”. In: *International Conference on Offshore Mechanics and Arctic Engineering*. Vol. 4269. 2007, pp. 655–664 (cit. on p. 44).

[104]Amirhosein Moonesi Shabestary, André Bieberle, Daniel von der Cron, et al. “Flow morphology and heat transfer analysis for high-pressure steam condensation in an inclined tube part II: Numerical investigations”. In: *Nuclear Engineering and Design* 362 (2020), p. 110580 (cit. on p. 44).

[105]Thomas Höhne and Christophe Vallée. “Experiments and numerical simulations of horizontal two-phase flow regimes using an interfacial area density model”. In: *The Journal of Computational Multiphase Flows* 2.3 (2010), pp. 131–143 (cit. on p. 44).

[106]Thomas Höhne, Dirk Lucas, et al. “Numerical simulations of counter-current two-phase flow experiments in a PWR hot leg model using an interfacial area density model”. In: *International journal of heat and fluid flow* 32.5 (2011), pp. 1047–1056 (cit. on p. 44).

[107]Thomas Höhne and Jan-Peter Mehlhoop. “Validation of closure models for interfacial drag and turbulence in numerical simulations of horizontal stratified gas–liquid flows”. In: *International Journal of Multiphase Flow* 62 (2014), pp. 1–16 (cit. on pp. 44, 51, 118).

[108]Gustavo Montoya, Dirk Lucas, Eckhard Krepper, Susann Hänsch, and Emilio Baglietto. “Analysis and applications of a generalized multi-field two-fluid approach for treatment of multi-scale interfacial structures in high void fraction regimes”. In: *Proc. Int. Congress on Adv. on Nucl. Power Plants. ICAPP2014-14230, USA*. 2014 (cit. on pp. 44, 49, 118).

[109]T Höhne, E Krepper, G Montoya, and D Lucas. “CFD-simulation of boiling in a heated pipe including flow pattern transitions using the GENTOP concept”. In: *Nuclear Engineering and Design* 322 (2017), pp. 165–176 (cit. on pp. 44–46, 49, 50, 118, 120).

[110]Thomas Höhne, Paul Porombka, and Senen Moya Sáez. “Validation of AIAD Sub-Models for Advanced Numerical Modelling of Horizontal Two-Phase Flows”. In: *Fluids* 5.3 (2020), p. 102 (cit. on pp. 47, 48, 118).

[111]P Porombka and T Höhne. “Drag and turbulence modelling for free surface flows within the two-fluid Euler–Euler framework”. In: *Chemical Engineering Science* 134 (2015), pp. 348–359 (cit. on p. 48).

[112]Jeremiah U Brackbill, Douglas B Kothe, and Charles Zemach. “A continuum method for modeling surface tension”. In: *Journal of computational physics* 100.2 (1992), pp. 335–354 (cit. on pp. 49, 50, 118).

[113]Jingsen Ma, Assad A Oberai, Donald A Drew, Richard T Lahey Jr, and Mark C Hyman. “A comprehensive sub-grid air entrainment model for RaNS modeling of free-surface bubbly flows”. In: *The Journal of Computational Multiphase Flows* 3.1 (2011), pp. 41–56 (cit. on pp. 51, 118).

[114]Alejandro M Castro, Jiajia Li, and Pablo M Carrica. “A mechanistic model of bubble entrainment in turbulent free surface flows”. In: *International journal of multiphase flow* 86 (2016), pp. 35–55 (cit. on p. 51).

[115]Thomas Höhne, Thomas Geissler, André Bieberle, and Uwe Hampel. “Numerical modeling of a horizontal annular flow experiment using a droplet entrainment model”. In: *Annals of Nuclear Energy* 77 (2015), pp. 351–360 (cit. on pp. 51, 52).

[116]Y Egorov and F Menter. *Experimental implementation of the RPI boiling model in CFX-5.6*. Tech. rep. Technical Report ANSYS/TR-04-10, 2004 (cit. on p. 52).

[117]Hamed Setoodeh, Wei Ding, Dirk Lucas, and Uwe Hampel. “Prediction of bubble departure in forced convection boiling with a mechanistic model that considers dynamic contact angle and base expansion”. In: *Energies* 12.10 (2019), p. 1950 (cit. on pp. 55, 57, 58, 61).

[118]Wei Ding, Eckhard Krepper, and Uwe Hampel. “Evaluation of the microlayer contribution to bubble growth in horizontal pool boiling with a mechanistic model that considers dynamic contact angle and base expansion”. In: *International Journal of Heat and Fluid Flow* 72 (2018), pp. 274–287 (cit. on pp. 57, 63, 68).

[119]Yaohua Zhao and Takaharu Tsuruta. “Prediction of bubble behavior in subcooled pool boiling based on microlayer model”. In: *JSME International Journal Series B Fluids and Thermal Engineering* 45.2 (2002), pp. 346–354 (cit. on pp. 58, 70).

[120]Yoshio Utaka, Yuki Kashiwabara, and Michio Ozaki. “Microlayer structure in nucleate boiling of water and ethanol at atmospheric pressure”. In: *International Journal of Heat and Mass Transfer* 57.1 (2013), pp. 222–230 (cit. on p. 58).

[121]Frank P Incropera, David P DeWitt, Theodore L Bergman, Adrienne S Lavine, et al. *Fundamentals of heat and mass transfer*. Vol. 6. Wiley New York, 1996 (cit. on pp. 59, 60, 70).

[122]Roland Clift, John R Grace, and Martin E Weber. “Bubbles, drops, and particles”. In: (2005) (cit. on p. 61).

[123]DW Moore. “The boundary layer on a spherical gas bubble”. In: *Journal of Fluid Mechanics* 16.2 (1963), pp. 161–176 (cit. on p. 61).

[124]WGJ Van Helden, CWM Van Der Geld, and PGM Boot. “Forces on bubbles growing and detaching in flow along a vertical wall”. In: *International journal of heat and mass transfer* 38.11 (1995), pp. 2075–2088 (cit. on p. 62).

[125]Timothy Robert Auton. “Dynamics of bubbles, drops, and particles in motion in liquids.” PhD thesis. University of Cambridge, 1984 (cit. on p. 63).

[126]Abhijit Mukherjee and Satish G Kandlikar. “Numerical study of single bubbles with dynamic contact angle during nucleate pool boiling”. In: *International Journal of Heat and Mass Transfer* 50.1-2 (2007), pp. 127–138 (cit. on p. 63).

[127]Yuehua Yuan and T Randall Lee. “Contact angle and wetting properties”. In: *Surface science techniques*. Springer, 2013, pp. 3–34 (cit. on pp. 65, 79).

[128]V Prodanovic, D Fraser, and M Salcudean. “Bubble behavior in subcooled flow boiling of water at low pressures and low flow rates”. In: *International Journal of Multiphase Flow* 28.1 (2002), pp. 1–19 (cit. on pp. 72, 74, 78, 79, 84).

[129]Rosemary M Sugrue. “The effects of orientation angle, subcooling, heat flux, mass flux, and pressure on bubble growth and detachment in subcooled flow boiling”. PhD thesis. Massachusetts Institute of Technology, 2012 (cit. on pp. 73–76, 79–84).

[130]Craig Gerardi, Jacopo Buongiorno, Lin-wen Hu, and Thomas McKrell. “Study of bubble growth in water pool boiling through synchronized, infrared thermometry and high-speed video”. In: *International Journal of Heat and Mass Transfer* 53.19-20 (2010), pp. 4185–4192 (cit. on p. 73).

[131]Gang Hong, Xiao Yan, Yan-hua Yang, Tian-zhou Xie, and Jian-jun Xu. “Bubble departure size in forced convective subcooled boiling flow under static and heaving conditions”. In: *Nuclear engineering and design* 247 (2012), pp. 202–211 (cit. on p. 77).

[132]Hamed Setoodeh, Wei Ding, Dirk Lucas, and Uwe Hampel. “Modelling and simulation of flow boiling with an Eulerian-Eulerian approach and integrated models for bubble dynamics and temperature-dependent heat partitioning”. In: *International Journal of Thermal Sciences* 161 (2021), p. 106709 (cit. on pp. 85, 87).

[133]Wei Ding, Eckhard Krepper, and Uwe Hampel. “The Implementation of an Activated Temperature-Dependent Wall Boiling Model in an Eulerian-Eulerian Computational Fluid Dynamics Approach for Predicting the Wall Boiling Process”. In: *Nuclear Technology* 205.1-2 (2019), pp. 23–32 (cit. on pp. 87, 93).

[134]Michael Z Podowski and Raf M Podowski. “Mechanistic multidimensional modeling of forced convection boiling heat transfer”. In: *Science and Technology of Nuclear Installations* 2009 (2009) (cit. on p. 87).

[135]Nilanjana Basu, Gopinath R Warrier, and Vijay K Dhir. “Wall heat flux partitioning during subcooled flow boiling: Part 1model development”. In: *J. Heat Transfer* 127.2 (2005), pp. 131–140 (cit. on p. 89).

[136]In-Cheol Chu, Seung-Jun Lee, Young Jung Youn, et al. “Experimental evaluation of local bubble parameters of subcooled boiling flow in a pressurized vertical annulus channel”. In: *Nuclear Engineering and Design* 312 (2017), pp. 172–183 (cit. on pp. 90, 102, 103, 111).

[137]Hamed Setoodeh, Amirhosein Moonesi Shabestary, Wei Ding, Dirk Lucas, and Uwe Hampel. “CFD-Modelling of Boiling in a Heated Pipe Including Flow Pattern Transition”. In: *Applied Thermal Engineering* (2021), p. 117962 (cit. on pp. 115, 116).

[138]Sung-Min Kim and Issam Mudawar. “Review of databases and predictive methods for heat transfer in condensing and boiling mini/micro-channel flows”. In: *International Journal of Heat and Mass Transfer* 77 (2014), pp. 627–652 (cit. on p. 125).

List of Figures

List of Tables

Declaration

I hereby certify that I have authored this thesis entitled *Development of a Multi-field Two-fluid Approach for Simulation of Boiling Flows* independently and without undue assistance from third parties. No other than the resources and references indicated in this thesis have been used. I have marked both literal and accordingly adopted quotations as such. They were no additional persons involved in the spiritual preparation of the present thesis. I am aware that violations of this declaration may lead to subsequent withdrawal of the degree.

Dresden, 2022

Hamed Setoodeh